Molecular Spintronic Devices: from Molecular Spin Valves to Spin-OLEDs

Instituto de Ciencia Molecular
Universitat de València

Memoria presentada por Sara Gómez Miralles para aspirar al grado de
Doctor en Nanociencia y Nanotecnología (programa ref. 3045)

Abril 2017

Dirigida por el Dr. Eugenio Coronado Miralles y la Dra. Helena Prima García

D. EUGENIO CORONADO MIRALLES, catedrático del Departamento de Química Inorgánica de la Universitat de València y Dña. HELENA PRIMA GARCÍA, doctora por la Freie Universität von Berlin y actualmente investigadora en el Instituto de Ciencia Molecular de la Universitat de València,

CERTIFICAN:

Que la memoria presentada por Dña. Sara Gómez Miralles con título: *Molecular Spintronic Devices: from Molecular Spin Valves to Spin-OLEDs* corresponde a su Tesis Doctoral y ha sido realizada bajo su dirección en el Instituto de Ciencia Molecular, autorizando mediante este escrito la presentación de la misma para optar al grado de Doctor.

En Paterna, a 10 de Abril de 2017

Dr. Eugenio Coronado Miralles

Dra. Helena Prima García

Sara Gómez Miralles

Agradecimientos

Este manuscrito no habría llegado a buen término sin la ayuda y el apoyo de muchas personas. En primer lugar, me gustaría dar las gracias a Eugenio por recibirme así y convertir un mal giro en buena suerte, dándome la oportunidad de doctorarme en su grupo; también por la confianza, la libertad científica y la puerta siempre abierta del despacho. Admiro tu capacidad para llevar tantas líneas de investigación y tu ilusión en no dejar de seguir innovando. Estoy también muy agradecida a Helena, que me incluyó nada más llegar en el islote, cada día más grande, que somos los físicos en el RTMM. Gracias a ella he crecido muchísimo como científica y probablemente ésa sea la cosa más importante que me llevo de esta etapa.

Me gustaría dar las gracias también al personal técnico del grupo, sobre el que me he apoyado en innumerables ocasiones. En particular a Jose, Eva, Chimo, Álex, Manuel, Jorge, Estela y Paco, por los pedidos, las medidas, el código, los envíos, el cacharreo y los trámites administrativos. También a Chema y a Gloria, por las medidas de SQUID y los dewars de He. A Marian por cuidarnos tanto y tan bien. Pero de entre todos, estoy especialmente agradecida a Ángel y a Ale. Ángel, esta tesis no existiría sin todo lo que has aportado. Ha sido un honor trabajar contigo y aprender tantas cosas de tí (recordaré con mucho cariño los meses del PEIE). Te voy a echar mucho de menos. Ale, trabajar contigo es una gozada. Gracias por la paciencia, las síntesis, las medidas y los mimos: eres un sol.

También estoy muy agradecida a los investigadores del grupo con los que he podido colaborar directamente, en especial a Juanpi. Fue una suerte enorme em-

pezar contigo en el laboratorio, y todo lo que hemos ido viviendo después, espero que no nos perdamos la pista (*els pots s'assemblen a les olles*). Los imanes moleculares son entes menos raros para mí gracias a Álex, Walter, Guille y José Jaime. Álex, a veces he pensado en cambiarme a los qubits solo para poder trabajar más contigo, porque todo parece ir cuesta abajo. Muchas gracias por las correcciones y las conversaciones. Walter ha formado parte también del despacho 2.10.3, que ha sido un oasis de buen humor sin importar lo mal que iban algunos días los experimentos, muchas gracias por todas las risas y la química. En ese cuadrilátero de alta densidad, donde nunca colgamos el saco de boxeo, destaco a Michele, al que le agradezco los productos de alta gama del badulaque y maravillosos ratos en las escaleras al Sol. También a Samuel, entre otras cosas por apagarme tantas veces el compresor en domingo y los buenos ratos en Logroño. Y a Ramón, por ayudarme a entender mejor a los químicos, aguantarme los chistes malos y por las fotos con esmalte de uñas que algún día venderé. No me olvido de los que estuvieron al principio allí: Julia, Efrén y Elena (os hemos echado de menos), ni de los que han llegado a mitad: Marta y Marco (me ha gustado mucho compartir ese espacio con vosotros). Y a Amparo y sus visitas a media mañana, siempre de buen humor. A Ali, gracias por ser un gran referente, a Francisco por toda la química que me ha enseñado sobre los *prussian blue*, a Gonzalo y Jorge por los magnetocapacitores, a Yan por los dibujos de los POMs, a Carlos y Sergio por las críticas, a los teóricos Salva y Modesto por los conceptos, a Enrico y Karina (fundamentales en los últimos meses), a Michele por las conversaciones tan importantes sobre OLEDs y a Henk por compartir su experiencia con nosotros. Por último en el ICMol, a las chicas de *Nosotras Científicas*, por estar haciendo estas cosas tan necesarias, tan cerca (Lorena, gracias por venir). El ambiente que se respira en el grupo es inmejorable y es culpa de todos vosotros.

Durante este periodo he tenido la suerte de realizar dos estancias de investigación. He pasado unos meses fantásticos y pasados por agua en Nanogune (Donostia). Luis y Amilcar, muchas gracias por todo, aprendí un montón y lo pasé muy bien. Luis, gracias también por esas llamadas para resolver tantas dudas. Me he traído mucho más que ciencia de vuelta al Mediterráneo. *Xiangnan, it was great to share so many evaporations with you.* Libe, Mano, Luca y Oihana, *eskerrik asko!* Y

al subconjunto catalán: Roger, Fèlix y sobre todo Saül (*van ser molt guais aquelles nits de sincrotró*).

The second research stay was at ISMN-CNR. Alek, I felt very much at home in Bologna, thanks for making it possible. It was a very enriching period. Alberto, its been really nice to work with you, there and later. Thank you for sharing your insights and experience, I have learned so much. Patrizio, thank you for all the LSMO. Lorenzo and Betta, it was great to be in the lab with you. And Eugenio, I feel so lucky that you have been mentoring this. I admire your high capabilities, humility and sense of humor (you've been my favorite book). I hope that we can continue playing with the magnetic field and photons for a long time.

Besides, I was lucky to have two productive collaborations. Mirko, thanks a lot for the UPS data, it became a very important part of the research carried out. And Zhi-Gang, thank you very much for the Hanle theoretical framework that adds value to the experiments.

Y a las amigas, las de verdad (ese mar de fueguitos), por hacer malabares para juntarnos, reírnos, querernos y cuidarnos; por intentar entender nuestros mundos distintos y apoyarnos. Y de entre ellas: Sonia, sin tu música esto hubiera sido otra cosa mucho más sosa.

Fer, gracias por la cobertura, los menús y los golpes en la espalda. Eres el tío más guay, e Irene la tía más molona. A Juan-Luis por noble, justo y valiente. Y a Lola, por ser como es, e ir y venir tantas veces sin perder la sonrisa. Habéis sido un apoyo muy grande. Gracias a los cuatro por estar ahí siempre.

Y finalmente, a mis chicos favoritos. Quique, fuego grande y sereno, gracias por entender y pertenecer a este mundo sin sentido donde a veces no hay ni bajas, ni horarios pero sí repercusión en el entorno más cercano (ahora nos toca un rato para nosotros). Y a Pilo, por llegar, reestructurarlo todo y colocarlo en un sitio mejor.

A Quique, Pilo, Juan-Luis y Lola

Abstract

The investigation herein described belongs to the molecular spintronics field and it has been motivated by the desire to deepen in the knowledge of molecular spin valves and spin-OLED devices, through the incorporation of new materials and the study of spin precession in the molecular layers.

This manuscript outlines the research carried out during the PhD period and it is divided into six chapters. The basic concepts in molecular spintronics are reviewed in the first chapter of the dissertation. There, the notions that will be relevant in the following chapters are emphasized.

Chapter two is devoted to the study of thin films of five new molecular compounds based on quinolines: Na[Y(5,7Cl_2q)$_4$], Na[Tb(5,7Cl_2q)$_4$], Na[Dy(5,7Cl_2q)$_4$], NEt_4[Dy(5,7Cl_2q)$_4$], and $K_{0.5}(NEt_4)_{0.5}$[Dy(5,7Cl_2q)$_4$], where 5,7Cl_2q = 5,7-dichloro--8-hydroxiquinoline. For clarity reasons they are renamed: NaYClq, NaTbClq, NaDyClq, NEtDyClq and KNEtDyClq. An exhaustive multi-technique analysis formed by thermogravimetry, elemental analysis, infrared spectroscopy, mass spectrometry and ac magnetometry demonstrates that only the sodium derivaties NaYClq, NaTbClq and NaDyClq are thermally stable and can be sublimated retaining their molecular integrity and magnetic properties. Such a feature has allowed us to prepare films of these sodium derivatives showing low roughness values and high substrate coverage that make them suitable for their incorporation into molecular spintronic devices. Finally, the magnetic sublimable molecules are deposited as thin films on ferromagnetic substrates. Interestingly, a molecular blocking is observed in the FC-

ZFC curves probably caused by the activation of the single molecule magnet behavior induced by the ferromagnetic substrate.

In the third chapter of this dissertation we have fabricated spin valves using these sublimable sodium derivatives as spin collector layer. Thus, negative magnetoresistance is observed with the compounds NaYClq and NaDyClq as molecular layers. The two configurations of the devices studied are Co (15 nm) / AlO_x (1 nm) / NaYClq / NiFe (15 nm) and Co (15 nm)/ AlO_x (1 nm) / NaDyClq / NiFe (15 nm) where the molecular layers nominal thicknesses are in the range [8, 25] nm. We demonstrate that the interfacial spin polarization and magnetoresistance in a molecular spin valve can be modified by specific details of the metal-molecule interaction. The positive MR observed in the device with structure NiFe (15 nm)/ AlO_x (1 nm) / NaDyClq / Co (15 nm) confirms that the spinterface is NaDyClq / NiFe. The hybridization has been studied by means of X-ray absorption spectroscopy.

Chapter four deals with the study of two spin valves based on polyoxometalates formed by stacks of LSMO (20 nm) / $DODA_3PMo_{12}O_{40}$ (100 nm) / Co (25 nm) and LSMO (20 nm) / $DODA_3PMo_{12}O_{40}$ (80 nm) / MoO_x (3 nm) / Co (25 nm). Both types of devices are designed taken into account the energy level alignment at the interfaces, determined by UPS spectroscopy. The thickness of the MoO_x layer has been chosen taking into account the spin-polarized UPS spectra. The incorporation of the MoO_x layer has resulted in a considerable improvement of the device performance since magnetoresistance signal remains up to voltages as high as 3.5 V.

In chapter five we design and study a spin-OLED with the configuration: LSMO (20 nm) / PEIE (1 nm) / F8BT (45 nm) / MoO_x (3 nm) / Co (25 nm) where PEIE $=$ polyethylenimine ethoxylated and F8BT $=$ poly(9,9-dioctylfluorene-alt-benzothiadiazole). All the layers are formed by commercial materials. In addition, the interfaces between the magnetic electrodes and the organic semiconductor emitting layer have been carefully engineered to have a proper energetic band alignment. The device shows MEL effect in a wide range of temperatures and voltages with a maximum of 2.4 % at 9 V at 20 K.

The Hanle effect constitutes the main subject of chapter six. This effect is con-

sidered the litmus test to demonstrate that the magnetoresistance in molecular spin valves origins in spin polarized currents. The spin-OLED is a suitable device to study spin precession by means of the Hanle effect since the light emission ensures that the spin-polarized charge is being transported through the frontier orbitals (HOMO and LUMO) of the molecular semiconductor. Remarkably, we measure the absence of Hanle effect in the light and resistance of the spin-OLED: LSMO (20 nm) / ZnO (1.8 nm) / N965 (1 nm) / F8BT (65 nm) / MoO_x (3 nm) / Co (15 nm) at different temperatures, voltages and angles. Our results give us a strong hint of exchange as spin transport mechanism in molecular materials.

This dissertation should give rise to the following publications:

Design of Molecular Spintronics Devices Containing Molybdenum Oxide as Hole Injection Layer, Juan Pablo Prieto-Ruíz, Sara G. Miralles, Nicolas Grossmann, Martin Aeschlimann, Mirko Cinchetti, Helena Prima-García and Eugenio Coronado, *Advanced Electronic Materials, 3, 1600366, 2017*.

Controlling Singlet-Triplet Ratio in OLEDs by Spin Polarised Currents, Juan Pablo Prieto-Ruíz,* Sara G. Miralles,* Helena Prima-García, Alberto Riminucci, Patrizio Graziosi, Mirko Cinchetti, Martin Aeschlimann, Valentin Alek Dediu and Eugenio Coronado, *submitted to Nature Materials*.

Interface-Assisted Sign Inversion of Magnetoresistance in Spin Valves based on Novel Lanthanide Quinoline Molecules, Amilcar Bedoya-Pinto,* Sara G. Miralles,* Saül Vélez, Pierluigi Gargiani, Manuel Valvidares, Fèlix Casanova, Eugenio Coronado and Luis E. Hueso, *submitted to Advanced Functional Materials*.

Sublimable Single-Ion Magnets Based on Chloroquinolinate Lanthanoid Complexes: Deposition on Ferromagnetic Substrates, Sara G. Miralles, Amilcar Bedoya-Pinto, José J. Baldoví, Walter Cañon-Mancisidor, Yoann Prado, Alejandro Gaita-Ariño, Guillermo Mínguez-Espallargas, Luis E. Hueso and Eugenio Coronado, *submitted to Chemical Science*.

Lanthanide Quinolinate Complexes: SMM Film Behavior Study, Walter Cañon-Mancisidor, Sara G. Miralles, Guillermo Mínguez-Espallargas, José J. Baldoví, Alejandro Gaita-Ariño and Eugenio Coronado, *in preparation*.

Polyoxometalate-Based Molecular Spin Valves: Magnetoresistance at High Voltage, Sara G. Miralles, Helena Prima-García, Marco Calbucci, Mirko Cinchetti, Martin Aeschlimann, Patrizio Graziosi, Valentin Alek Dediu and Eugenio Coronado, *in preparation*.

Study of the Hanle Effect in a Spin-OLED, Sara G. Miralles, Helena Prima-García, Alberto Riminucci, Zhi-Gang Yu, Eugenio Lunedei, Patrizio Graziosi, Valentin Alek Dediu and Eugenio Coronado,*in preparation*.

Abbreviations

A	absorbance
ac	alternating current
AF	antiferromagnetic
AFM	atomic force microscopy
Alq_3	tris(8-hydroxyquinoline)aluminum
AMR	anisotropic magnetoresistance
AP	antiparallel
B	magnetic induction (flux)
B_{Raman}	Raman relaxation mechanism parameter
c	speed of light
CSA	channel spark ablation
d	layer thickness
d_{eff}	effective layer thickness
d_{nom}	nominal layer thickness
D	diffusion coefficient
D	zero-field splitting parameter
dc	direct current
DF	delayed fluorescence
DOS	density of states

e	electron charge
e^-	electron
E	energy
E	electric field
$E_{Binding}$	binding energy
E_F	Fermi level
E_k	kinetic energy
EA	electron affinity
EDX	energy dispersive X-ray
EIL	electron injection layer
EL	electroluminescence
EML	emissive layer
EQE	external quantum efficiency
ESI-MS	electrospray ionization mass spectrometry
EtOH	ethanol
F	fluorescence
F8BT	poly(9,9-dioctylfluorene-alt-benzothiadiazole)
FM	ferromagnetic
g	g-factor
GMR	giant magnetoresistance
h	Planck's constant
h^+	hole
H	magnetic field strength
H_c	coercive field
H_{dc}	static magnetic field
HI	hyperfine interaction
HIL	hole injection layer
HOMO	highest occupied molecular orbital
HyLED	hybrid organic inorganic light emitting diode

H_Z	non-collinear magnetic field
I	current
I	light intensity
IC	internal conversion
IE	ionization energy
IR	infrared
ISC	intersystem crossing
ITO	indium tin oxide
IV	current-voltage
IVL	current-voltage-luminescence
J	current density
k_B	Boltzmann constant
KNEtDyClq	$K_{0.5}(NEt_4)_{0.5}$[Dy(5,7-dichloro-8-hydroxiquinolate)$_4$]
L	luminescence
lb	leaky barrier
LB	Langmuir-Blodgett
Ln	lanthanide
LSMO	lanthanum strontium manganite
LT	low temperature
LUMO	lowest unoccupied molecular orbital
m	mass
m_e	electron rest mass
M	magnetization
M	magnetic moment
M_S	saturation magnetization
MALDI-TOF	matrix-assisted laser desorption ionization
MEL	magneto-electroluminescence
MF	magnetic field
ML	monolayer

Mn_{12}	$Mn_{12}O_{12}(CH_3COO)_{16}(H_2O)_4$
MOKE	magneto-optic Kerr effect
MR	magnetoresistance
MSC	molecular semiconductor
MSV	molecular spin valve
MTJ	magnetic tunnel junction
n	density of carriers
n_{Raman}	Raman relaxation mechanism exponent
N^{up}	majority photoemitted electrons
N^{down}	minority photoemitted electrons
NaDyClq	Na[Dy(5,7-dichloro-8-hydroxiquinolate)$_4$]
NaTbClq	Na[Tb(5,7-dichloro-8-hydroxiquinolate)$_4$]
NaYClq	Na[Y(5,7-dichloro-8-hydroxiquinolate)$_4$]
NEt_4	tetraethylammonium
NEtDyClq	NEt_4[Dy(5,7-dichloro-8-hydroxiquinolate)$_4$]
N965	bis(4,4'-tridecyl-2,2'-bipyridine)-(4,4'-dicarboxy-2,2'-bipyridine) ruthenium(II)-bis(chloride)
OLED	organic light emitting diode
OMAR	organic magnetoresistance
OMEL	organic magneto-electroluminescence
OMR	ordinary magnetoresistance
OSC	organic semiconductor
P	parallel
P	polarization
P	phosphorescence
P	pressure
$\boldsymbol{P_{base}}$	base pressure
PEIE	ethoxylated polyethylenimine
PES	photoelectron spectroscopy

POM	polyoxometalate
PP	polaron pair
PPMS	physical property measurement system
QTM	quantum tunneling magnetization
R	resistance
R_{AP}	resistance of the antiparallel state
R_P	resistance of the parallel state
RMS	root mean squared
RT	room temperature
RTMM	Research Team on Molecular Materials
s	spin density
S	spin
S	singlet
SCLC	space charge limited current
SEM	scanning electron microscopy
SIM	single-ion magnet
SMM	single-molecule magnet
SO	spin-OLED
SOC	spin-orbit coupling
SQUID	superconducting quantum interference device
STO	strontium titanate
$t_{transit}$	transit time
T	temperature
T	triplet
T	transmittance
T_b	blocking temperature
T_N	Néel temperature
T_C	Curie temperature
T_6	sexithienyl

$T_{sublimation}$	sublimation temperature
TGA	thermogravimetric analysis
TMR	tunneling magnetoresistance
ToF	time of flight
TTA	triplet-triplet annihilation
U_{eff}	effective energy barrier
UHV	ultra high vacuum
UPS	ultraviolet photoelectron spectroscopy
UV	ultraviolet
UV-Vis	ultraviolet-visible
v	drift velocity
v	mean velocity
V	voltage
V_{ON}	turn on voltage
VB	valence band
XAS	X-ray absorption spectroscopy
XPS	X-ray photoelectron spectroscopy
z	sample height
Z	atomic number
α	Cole-Cole parameter
α_a	absorption coefficient
γ	gyromagnetic ratio
Δ	vacuum level shift
η	number of tunneling events
θ	angle between H_z and P
κ	extinction coefficient
λ	wavelength
λ_s	spin diffusion length
μ	mobility

μ_B	Bohr's magneton
ν	frequency
ρ	roughness
ρ_{ptp}	peak to peak roughness
ρ_{RMS}	root mean squared roughness
σ	Gaussian width
τ	relaxation time
τ_{s}	spin relaxation time
τ_0	Arrhenius pre-exponential factor
ϕ	work function
ϕ_{eff}	effective energy barrier
χ	magnetic susceptibility
χ_{S}	adiabatic magnetic susceptibility
χ_{T}	isothermal magnetic susceptibility
χ'	in phase magnetic susceptibility
χ''	out of phase magnetic susceptibility
ψ_{bi}	built in potential
ω	angular frequency
ω_{L}	Larmor frequency

Contents

1 Introduction

1.1 Molecular Spintronics

Molecular spintronics,[1–4] also referred as organic spintronics, is a young and fascinating field that designs and studies molecular-based electronic devices where the spin is manipulated and controlled. Indeed, it is the confluence of three different disciplines: spintronics, molecular electronics and molecular magnetism; and it takes the advantage of chemical and electric benefits of the molecules.

In fact, molecular materials, rich in carbon atoms, present low hyperfine interaction (HI) and spin-orbit coupling (SOC), which constitute the main sources of spin depolarization.[4,5] The HI comes from the interaction between the spin of the electron and the nuclear spin. Since the charge transport in molecules takes place along the carbon chains, the contact hyperfine is typically negligible as C^{12}, with an abundance amounting to 99 %, has zero nuclear spin. Thus, in contrast with conventional inorganic solids, the HI in molecular materials is limited to the weak dipolar interaction

with the nuclei of the hydrogen atoms. Furthermore, the SOC originates from the interaction between the spin of the electron and its movement in the atomic orbit being proportional to Z^4. Therefore, as organic materials are mainly composed of light elements, a small SOC and HI result leading to long spin diffusion lengths.[6]

In fact, molecular spintronics has not been limited to imitate the inorganic semiconductors but to give rise to new phenomena and to fabricate novel devices formed by one or few molecules in the race towards miniaturization. Analogously to molecular electronics, the molecular spintronics field can be divided in two sub-branches: molecular nanospintronics and molecular-based spintronics. In molecular nanoespintronics,[7] a unique or a few molecules constitute the spintronic device where the spins are manipulated individually.[8–10] The manipulation of single molecules is experimentally a big challenge and theoretical studies have taken the lead.[11] One of the most interesting possibilities within molecular nanospintronics is the use of magnetic molecules in quantum computing not only as magnetic storage units or bits but also as readers of superposition of quantum states or spin qubits.[12,13]

The research described in this manuscript belongs to molecular-based spintronics which was born in 2002 with the incorporation of an organic semiconductor in a spintronic structure.[14] Since then, many molecular materials have been integrated in spintronic heterostructures giving rise to the second generation spintronic devices: molecular spin valves,[15] spin-OLEDs[16,17] and magnetic solar cells.[18–20]

1.1.1 Inorganic Spintronics

Spintronics or spin-electronics,[21,22] which uses both the electrical and magnetic properties of electrons, is a relatively young field. It is constructed based upon the imbalance in the density of states (DOS) sub-bands at the Fermi level for spin-up and spin-down carriers, characteristic of ferromagnetic metals, as illustrated in Figure 1.1. As a result, the electric current injected from a ferromagnetic electrode is spin-polarized.

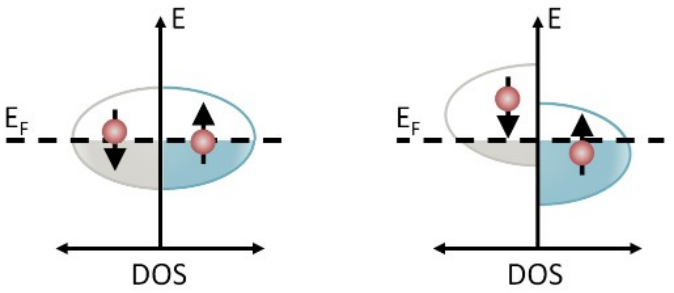

Figure 1.1 Schematic of the density of states at the Fermi level in a metal (left) and in a ferromagnetic metal (right). In the latter, the density of states at the Fermi level is unbalanced for spin-up and spin-down branches.

The origins of spintronics can be traced back to the experiments on magnetic tunnel junctions made by Jullière in the 1970s.[23] But the field of spintronics emerged in 1988 with the discovery of giant magnetoresistance (GMR) in superlattices of Fe-Cr.[24] In this system, thin layers of magnetic and non-magnetic metals are alternated forming multilayers. The magnetic coupling between layers is ferromagnetic or antiferromagnetic depending on the thickness of the non-magnetic films. Thus, the electrical resistance of the structure depends on the magnetization of the layers. The resistance percentage of variation is known as GMR due to the high values observed. At low temperatures 50 % giant magnetoresistance was measured.

The GMR made a huge breakthrough in improving data storage density on hard drive disks and in extending the hard disk technology to consumer electronics. Only nine years elapsed since the finding and the launch by IBM of the first hard disk based on GMR in 1997.[25] Rarely the transfer of technology between the investigation and the mass production is so fast. Then, twenty years later, the 2007 Nobel Prize in Physics was awarded jointly to Albert Fert and Peter Grünberg for the discovery of GMR.[26,27]

The variation of the electrical resistance in a magnetic field is known generally as magnetoresistance (MR), where GMR is a particular case. MR may have different origins and it can be observed in single layers or in multilayered structures.

Magnetoresistance occurs in all metals where it is termed ordinary magnetoresistance (OMR) and it is rooted in the Hall effect and the Lorentz force.[28] For non-magnetic metals, the percentage is small at low field values, although it may become large at high magnetic fields. If the metal is ferromagnetic the resistance variation in a magnetic field is called anisotropic magnetoresistance (AMR) and stems from spin-orbit coupling. AMR was discovered by Lord Kelvin in 1856 when he measured different electric currents in iron substrates depending on the angle between the magnetic field and the current. And there is an analogous to AMR in organic and molecular materials which is known as organic magnetoresistance (OMAR).[29] However, it seems that the OMAR effect stems from the hyperfine interaction and the influence of the external magnetic field on polaron pairs (PP).[30]

As the superlattices of Fe-Cr[24] showed, multilayer structures can exhibit magnetoresistance, being the spin valves the prototypic device.[31] In this case the MR is termed giant magnetoresistance (GMR). Vertical spin valves consist on two ferromagnetic electrodes and a spacer layer, named spin collector layer, assembled in a sandwich-like structure. The resistance modulation is caused by the scattering that the charge carriers overcome depending on their spin polarization while entering the second electrode. By contrast, if the carriers do not travel in the spacer layer but tunnel between electrodes the device is a magnetic tunnel junction (MTJ) and the magnetoresistance is termed tunneling magnetoresistance (TMR).[32]

1.1.2 Molecular Electronics

The molecular electronics or organic electronics field brings molecular materials in classical electronics. The term organic has been extensive employed although many compounds, rather than organic (namely carbon-based and containing only oxygen, nitrogen, sulfur, phosphorus, boron, or halogens) include metal atoms and correspondingly, molecular suits best.

There are fundamental differences between inorganic semiconductors and molecular materials that establish the divergences in the physics of both fields. Firstly, inor-

ganic semiconductors show low band gaps (for example E_{gap}(Ge) = 0.7 eV, E_{gap}(GaAs) = 1.4 eV or E_{gap}(Si) = 1.1 eV), contrary to molecular semiconductors (MSCs).[33] Additionally, the conductivities of classical semiconductors stay in the range [10^{-8}, 10^{-2}] Ω^{-1} cm^{-1} being orders of magnitude higher than the conductivities of molecular materials (for example the conductivity of Alq_3 is around 10^{-15} $\Omega^{-1}cm^{-1}$).[34] Also, the dielectric constants of inorganic semiconductors are larger, so the Coulombic forces between electrons and holes are not important, as opposed to molecular semiconductors, where electron and hole have a Coulomb interaction energy in the range [0.5, 1] eV. Besides, most molecular semiconductors are based on carbon chains where single and double bonds between carbon atoms are alternated, which is known as π-conjugation and where the electrical conduction properties of these materials rely on. Each carbon atom has three sp^2 orbitals in the plane that form frontal sigma bonds overlapping with the neighboring carbon and hydrogen atoms and one p_z orbital out of the plane that bonds to the neighboring p_z orbitals. Charge carriers can travel along the entire electronic π cloud and therefore are delocalized along the molecule. The electrons occupy the π-bonding orbitals and give rise to the highest occupied molecular orbital (HOMO) while the anti-bonding orbitals are empty and conform the lowest unoccupied molecular orbital (LUMO). In principle, molecular materials are closer to an electrical insulator than to a conductor since its energy gap (energy difference between HOMO and LUMO) is around 3 eV. However, they conduct electricity when charges are injected from neighboring electrodes, by doping or photoexcitation.[35]

Molecular compounds can be classified into molecules or polymers depending on their structure.[36] The latter are formed by repeat units whose replication produces the complete polymer chain. Besides, the molecular films can be amorphous and disordered, or crystalline when they form a molecular crystal, while polymers give rise to amorphous layers. The molecular materials studied in this dissertation form disordered thin films since they have been deposited by solution processing techniques or vacuum deposition methods on disordered substrates. It is assumed that the density of states in their HOMO and LUMO follows a Gaussian distribution with a width of about $\sigma = 100$ meV.[35,37] The charge transport in the molecular layer occurs by hopping between localized sites in the molecules or polymer chains. Due

to the differences in terms of charge transport, the mobilities of molecular semiconductors are several orders of magnitude smaller than the mobilities of inorganic semiconductors.[36]

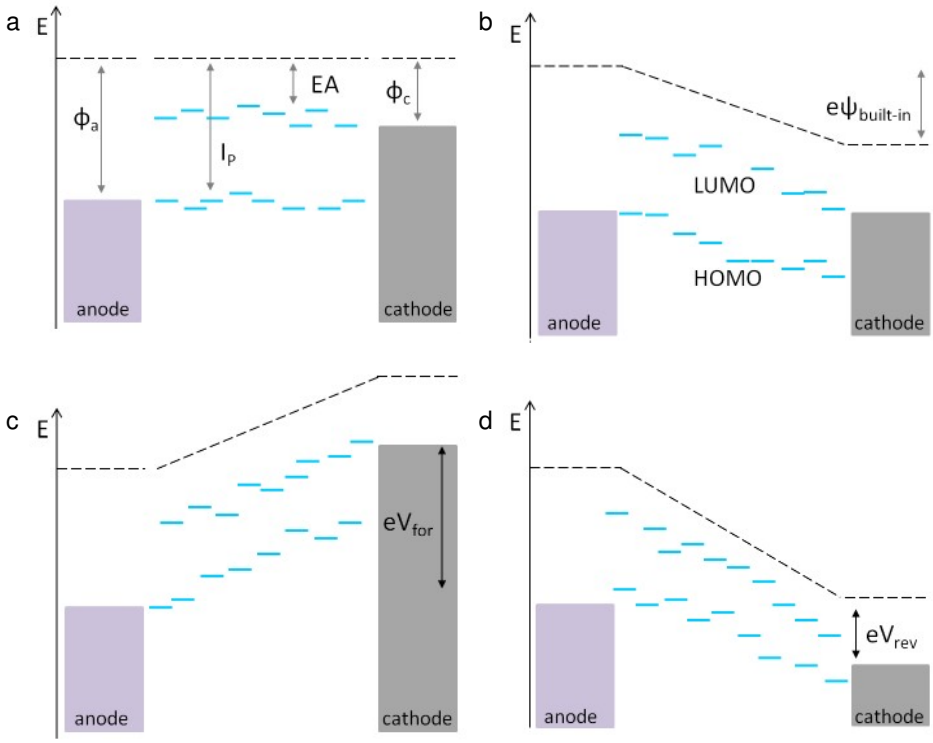

Figure 1.2 Energy level alignment of a metal/molecular semiconductor/metal junction. a) Open circuit condition where there is no current flow. b) Short circuit condition where the flow of charge modifies the vacuum, HOMO and LUMO levels. The built-in potential is defined as the difference in vacuum levels between the electrodes. c) Forward bias condition. When the buit-in potential is overcome, electrons and holes flow in the MSC. d) Reverse bias. There is no current flow in an ideal device. The vacuum level is represented by a dashed black line. The anode (cathode) is a high (low) work function metal. Adapted from the work of Köhler et al.[35]

The basic model of a molecular electronics device consists of two metallic electrodes and a molecular interlayer. The charge injection and extraction depends

mainly on the energy level alignment of the different materials.[35,38,39] Figure 1.2 shows the energy level diagram of a metal / molecular semiconductor / metal junction where four different electric situations are depicted.

In principle, electrical conduction can be carried by electrons, holes or both, depending on the energetic alignment between layers. Here we consider that the conduction is bipolar. The high work function metal is responsible of hole injection whereas the low work function metal is accountable for electron injection. The work function (ϕ) of the electrodes is defined as the minimum energy needed to extract an electron to the vacuum level. The electron affinity (EA) is defined as the amount of energy obtained by moving an electron from the vacuum to the LUMO of the MSC. The ionization potential (I_P) is defined as the energy required to extract an electron from the HOMO. Note that electrons move towards lower energy levels while holes, since they are virtual particles signifying a lack of electron in the HOMO, seek higher energies.[35]

Figure 1.2a shows the open circuit state. In it, as the electrodes are not electrically contacted there is no charge transfer between the different layers. Besides, there is no potential drop inside the device and thus, HOMO and LUMO have the same energetic value throughout the bulk of the molecular material which is known as the flat band condition. HOMO and LUMO are commonly represented by lines, however, here we depict them by discrete levels in a more realistic illustration.

Figure 1.2b depicts the short circuit condition where the electrodes are put in contact. The electrons flow from the low work function metal (cathode) to the high work function metal (anode) until the Fermi level is equilibrated in the device. This creates a potential gradient across the junction and within the molecular layer where the potential drop creates a gradient in the HOMO and LUMO levels. If the built in potential (ψ_{bi}) is applied to the device, the flat band condition is obtained.

Figure 1.2c illustrates the forward bias state. A voltage bias is applied to the two electrodes so that the inclination of HOMO and LUMO is reversed compared to the short-circuit situation. When the voltage is high enough, the cathode injects electrons into the LUMO and the anode injects holes in the HOMO. At this stage, an

electric current flows in the device. Charges move within the molecular material due to the internal electric field which is the potential gradient.

Finally, the reverse bias situation is depicted in Figure 1.2d. In this case the voltage at the electrodes is added to the ψ_{bi}. In an ideal device, there is no current flow. However, in a amorphous film device there is a intermediate set of energetic states between HOMO and LUMO caused by impurities or traps.[40] This is also the reason why in the forward bias condition an electric current appears before the built in potential has been exceeded.

In general the work function (ϕ) of the cathode does not coincide energetically with the LUMO and similarly the work function of the anode has not the same energetic value than the HOMO. This generates energetic barriers at the metal / molecular interfaces that need to be overcome.[35] The difference between the work function of the electrode and the electron affinity (EA) of the molecular semiconductor is known as the electron injection barrier. Similarly, the difference between the metal work function and the ionization energy (IE) of the molecular semiconductor (MSC) is known as the hole injection barrier. These two barriers constitute the device gateway and they can be decreased by the deposition of thin layers that tune the electrodes work functions by the formation of interfacial dipoles.[41]

1.2 Molecular Spin Valves

1.2.1 Working Principles

A molecular spin valve (MSV) is mainly formed by three layers: a molecular semiconductor (MSC) placed in between two ferromagnetic (FM) electrodes, named spin injector and spin detector.[15] The MSC, or spin collector, has the function to transport the spin carriers pumped by the spin injector to the detector. Besides, both ferromagnets are chosen to have different coercive fields that will give rise to two

magnetic orientations between electrodes: parallel and antiparallel alignment.

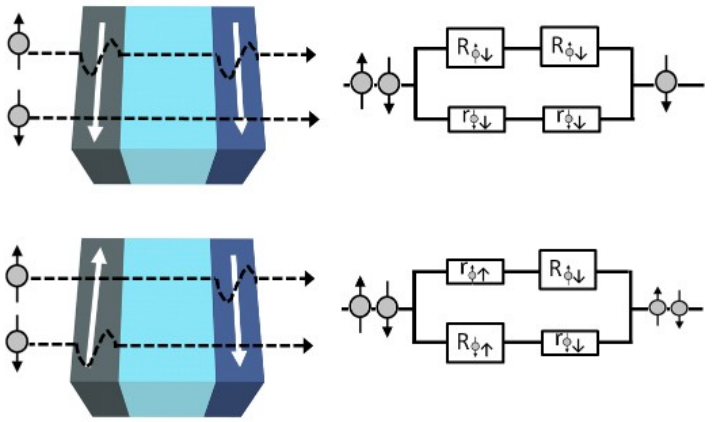

Figure 1.3 Parallel (top panel) and antiparallel (bottom panel) states in a molecular spin valve. Carriers encounter high or low scattering depending on their spin orientation compared with the magnetization direction of the electrodes. On the right hand side the equivalent circuit for each situation is depicted (R (r) stands for the high (low) equivalent resistance). White arrows point to the magnetization direction of the electrodes while black arrows and gray circles indicate the spin-up and spin-down charge carriers. Adapted from the work of Camarero et al.[42]

As pointed in section 1.1, in a current flow, the carriers find more or less scattering depending on their spin polarization when being injected into the second FM electrode. Hence, various scenarios lead to different equivalent circuits based on Motts model,[43] as illustrated in Figure 1.3. In a first approximation, the equivalent circuit is composed by two channels, one for the spin-up and the other for the spin-down carriers. A MSV with the two FM electrodes magnetically oriented in the same direction is shown in the top panel of the figure. This situation is known as the parallel (P) state. When traversing the device, a carrier oriented spin-up will find high scattering at both electrodes, unlike a carrier-oriented spin-down what is reflected in the magnitude of the resistances of the equivalent circuit. Consequently, the spin-up population is depleted. The bottom of the figure depicts the antiparallel (AP) state where the electrodes have opposing magnetization directions. In this case both spin-up and spin-down carriers encounter many scattering processes and both spin-up and spin-down populations are attenuated, as illustrated by the reduced size spin-up

and spin-down population arrows.

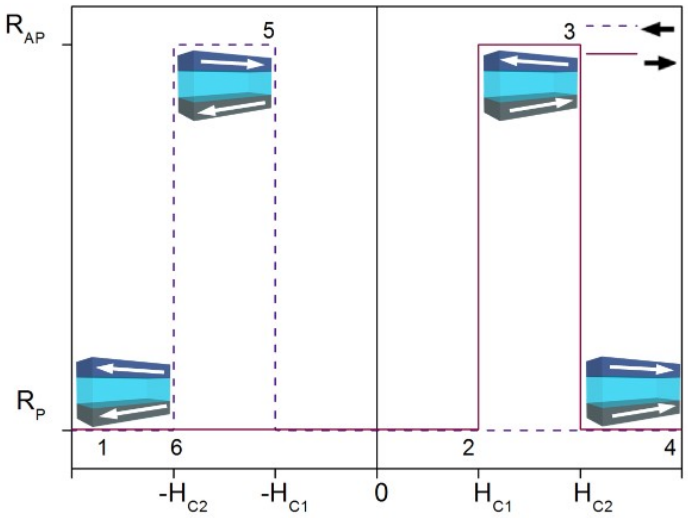

Figure 1.4 Illustration of the magnetoresistance measurement procedure where R_P and R_{AP} stand for the resistances of the parallel and antiparallel states respectively and $H_{c1(c2)}$ is the coercive field of the soft (hard) magnetic electrode. See the text for details.

Thus, two resistance states can be observed at a fixed voltage or at a constant current applied, in a magnetic field sweep, what gives rise to the magnetoresistance curves. Two resistance states are established in the device due to the distinct values of the coercive fields (H_c). The measurement is usually initiated in a high negative field (stage 1 and red solid line in Figure 1.4) where bot electrodes are aligned. Then the field is decreased progressively until its direction is changed by making it positive. When the soft magnet coercive field is reached (H_{c1}) it flips its magnetization and the resistance switches to the resistance of the AP state. The spin valve remains in the high resistance state only until the hard magnet is oriented parallel, what happens at stage 3. At this point the resistance of the P state is recovered since both electrodes have again the same magnetization direction (stage 4). The dashed purple line shows the equivalent measurement in the backward sweep direction with the changes between P and AP states at the stages 5 (H_c of the soft magnet) and

6 (H_c of the hard magnet). The percentage of giant magnetoresistance or usually termed just magnetoresistance is calculated as:

$$GMR = \frac{R_{AP} - R_P}{R_P} \tag{1.1}$$

Besides, the GMR can be related to the polarization of the electrodes (*P* and *P'*) by the modified Jullière formula:[23,44]

$$GMR = \frac{2PP' \cdot exp(-d/\lambda_s)}{1 + PP' \cdot exp(-d/\lambda_s)} \tag{1.2}$$

where d is the molecular layer thickness and λ_s is the spin diffusion length of the MSC. The polarizations of the electrodes are a function of the number of spin-up (N^{up}) and spin-down carriers (N^{down}):

$$P = \frac{N^{up} - N^{down}}{N^{up} + N^{down}} \tag{1.3}$$

At first glance, GMR and tunneling magnetoresistance (TMR) are indistinguishable since the difference resides in the type of charge transport. Carriers can pass from one electrode to the other without traveling in the molecular material by means of the tunnel effect which is the case of magnetic tunnel junctions (MTJs).[45] Commonly they present the configuration FM / insulator / FM where the insulating layer is thin enough to let carriers tunnel across the device, since the tunneling probability is inversely proportional to the exponential of the layer thickness.

In 2002 Dediu and coworkers[14] designed a LSMO / T_6 / LSMO junction that varied the electrical resistance in a magnetic field. However, the identical LSMO electrodes showed equal coercive fields which precluded the MR measurement. Later in 2004, a magnetoresistance curve was measured for the first time in a vertical molecular spin valve designed by Xiong et al.[31] They reported 40 % at 11 K in a LSMO / Alq_3 / Co junction. Since then much progress has been made in this kind

of molecular spintronics devices.[15,46,47] In most cases, the device comprises inorganic electrodes that sandwich a molecular layer but a fully molecular spin valve was reported recently[48] with the structure V[TCNE]$_x$ / rubrene / V[TCNE]$_x$. Besides, MSVs are also evolving to multifunctionality and a photoresponsive spin valve with four different resistance states and based on F_{16}CuPC was reported in 2016.[49]

Most MSVs, apart from the two electrodes and the spin collector, include insulating barriers, being the most common the alumina barrier (Al_2O_3). These barriers contribute considerably to the overall resistance of the junction but they help with the high short circuit statistics, which constitutes an ongoing issue in the molecular spintronics field. Also, it has been demonstrated that the adhesion of Alq_3 is improved when deposited on an oxide layer. Besides Al_2O_3, other type of barriers have been tested such as LiF.[50]

1.2.2 The Spinterface

A priori, the MR of a spin valve is positive which simply means that the resistance of the AP state is higher than the resistance of the P state. However, many groups reported negative MR, that is, the resistance of the AP state is smaller than the resistance of the P state (see Figure 1.5).[31,51,52] This MR sign inversion is possible because at one of the interfaces the majority carriers become the minority carriers and vice versa. In the parallel state the electrodes are aligned in the same direction, but when carriers reach the second electrode they encounter high scattering. Therefore, the state of the resistance is high (see Figure 1.5). An analogous situation is encountered in the AP state where the magnetization of the electrodes is antiparallel but the carriers encounter low scattering when reaching the spin detector.

One of the possibilities to achieve negative MR is by antiferromagnetic (AF) coupling, since an AF layer will invert the majority and minority spins. For instance, negative MR has been measured in MTJs where Ciudad and coworkers[50] demonstrated that the inversion in their devices was due to a chemical reaction caused by the LiF. An CoF_2 AF layer was produced being the responsible of the MR sign

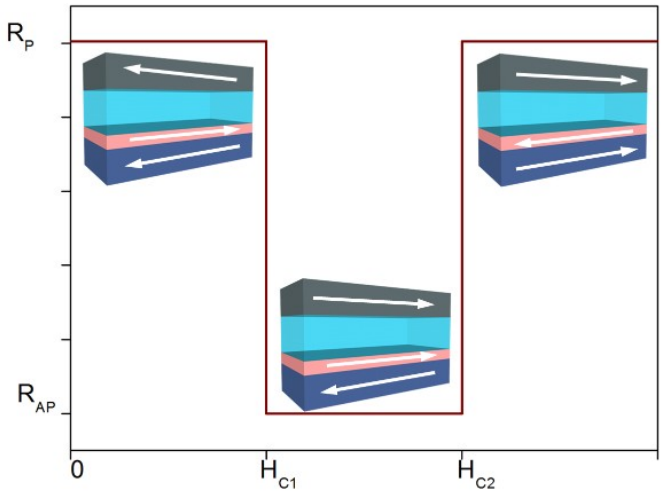

Figure 1.5 Illustration of one of the MR branches in the case of negative magnetoresistance where the resistance of the P (AP) state is high (low). At one of the interfaces the spin polarization of the current is inverted. When the relative orientation of the electrodes is P (AP) the carriers encounter high (low) scattering, contrary to the case of positive MR.

inversion.

Molecules are also capable to invert the sign of the magnetoresistance without reacting chemically with the electrodes, but by orbital overlap or hybridization. In their case, the spin filtering is due to the fact that the localized molecular levels broaden when put in contact with metals, and the broadening is different for spin-up and spin-down branches when the metal is ferromagnetic (see Figure 1.6). This situation generates preferential channels near the Fermi level, allowing passing more spin-up or spin-down carriers. Furthermore, the first molecular layer makes an additional selection of the spin polarization, changing the spin polarization coming from FM. Thus, the spin filtering has to be studied individually for the interface given a couple of materials.

The direct demonstration of spin filtering was given by Atodiresei et al[53] at the Fe / H_2Pc interface. Nevertheless the model was firstly proposed by Barraud et al[54]

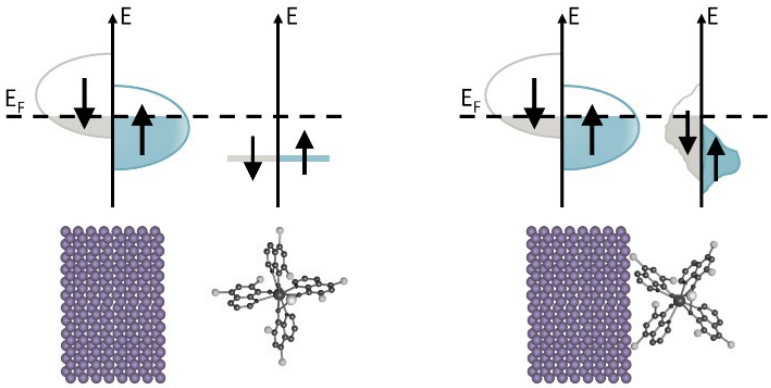

Figure 1.6 Density of states at the Fermi level for a FM metal and a molecule at a certain distance (left) and in contact (right). In the latter, the molecular levels broaden and relocate opening the possibility that the spin filtering occurs at the interface, inverting the spin polarization. Adapted from the work of Sanvito.[55]

in 2010. Later, this ability of a metal / molecule interface to invert the sign of the magnetoresistance was named spinterface by Sanvito.[55]

1.3 Spin-OLEDs

1.3.1 Working Principles

Spin-OLEDs[16,17] are multifunctional devices that behave at the same time as organic light emitting diodes and molecular spin valves. Basically the structure of a spin-OLED is alike the configuration of an OLED in which the metallic electrodes are replaced by ferromagnetic metals. Or, seen another way, a spin-OLED is a MSV where transport takes place in the HOMO and LUMO of the molecular semiconductor enabling recombination and light emission.

OLEDs,[56] that were invented in the 1980s, transform the electrical current in

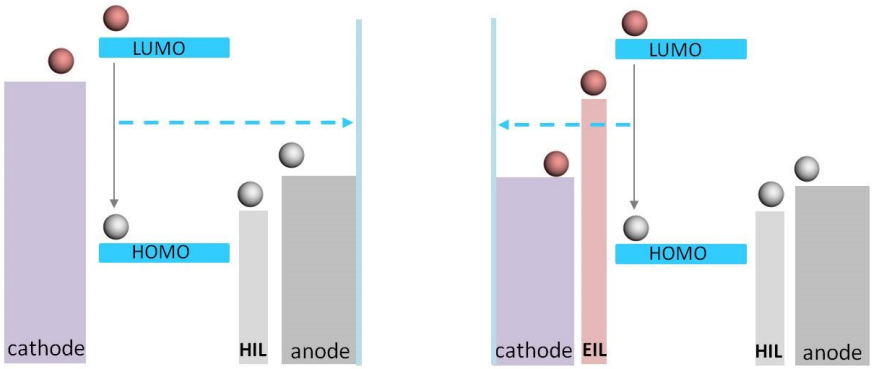

Figure 1.7 Energy level alignment and hole and electron injection in OLEDs (left) and HyLEDs (right). In HyLEDs the low work function and reactive cathode is replaced by a high work function and stable metal thanks to an electron injection layer (EIL). Electrons (holes) are represented as red (gray) balls. The light comes out through the glass substrate (blue layer).

visible light using molecular materials. Nowadays they are implemented in most displays and form part of our daily life.[57] OLED devices are built in sandwich-type structures where the two electrodes inject positive (holes) and negative (electrons) charge carriers into one or various organic semiconductors, where recombination of charges and light emission takes place. As standard, the anode is made from indium thin oxide (ITO) that is deposited on a transparent glass substrate allowing light to exit the device through this side. On the other side, the cathode is a low work function metal (hence very reactive), such as Ba, Ca or Li, that is typically capped with Ag or Al for corrosion protection.

The energy level and band alignment of an OLED is illustrated on the left side of Figure 1.7. The low work function cathode injects electrons into the molecular semiconductor thanks to the good alignment between the work function of the metal and the LUMO. Holes are injected from the anode through a hole injection layer (HIL) that is placed between the anode and the emissive layer.

Hybrid organic-inorganic light emitting diodes (HyLEDs) are a particular case of OLEDs.[58,59] They were designed to circumvent the corrosion problems and avoid the

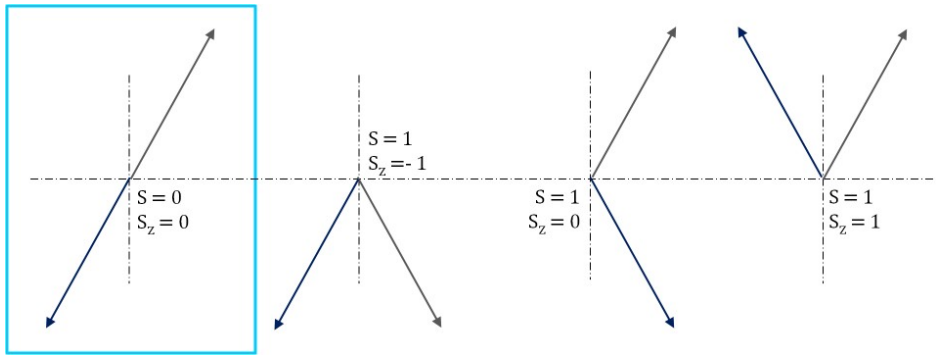

Figure 1.8 One singlet (S = 0) and three triplets (S = 1) are generated in a OLED represented in a $S_z(S_x)$ coordinate axis by combining hole and electron spins. If the spin of the electron (gray arrow) and hole (purple arrow) point up, the exciton will be in the T_1 triplet state (S_z = 1). Contrary, if both point down, the T_{-1} triplet state will be formed (S_z= –1). In addition, if the spin polarizations of hole and electron have opposite directions, the triplet T_0 or the singlet S_0 will have 1/2 probability to be formed (S_z= 0).

encapsulation that OLEDs require. HyLEDs incorporate an electron injection layer (EIL) which makes unnecessary the use of reactive cathodes of low work function. An illustration of the energy levels and band alignment in a HyLED is depicted on the right of Figure 1.7. In HyLEDs, electron injection takes place from the cathode to the LUMO through the conduction band of the EIL. And similarly to OLEDs, holes are injected into the HOMO through the conduction band of the HIL. The EIL improves the stability of the sample and also makes encapsulation unnecessary.[58] Besides, the layer deposition order is inverted compared to regular OLEDs, favoring light emission as recombination takes place in most cases near the cathode, since in most cases, the mobility of holes is higher than the mobility of electrons.

Contrary to OLEDs or HyLEDs, the spin polarization of the charge carriers in spin-OLEDs is controlled by an external magnetic field. In particular, the orientation of the magnetization of the electrodes affects the intensity of the light emitted by the device thanks to the dominion of the relative populations of singlets and triplets.[60]

The radiative recombination process cascade can start in the same or neighbor-

ing molecules. Initially, the electron and hole are attracted and bound coulombically to form a polaron pair, when their wave functions overlap. Then, when the electron and hole are in the same molecule, the exciton is formed which is the first step of recombination and light emission.

The spin of a two particle system (electron and hole) can be in four different spin states, one singlet (S) and three triplets (T):[61]

$$
\begin{aligned}
|S_0\rangle &= \frac{1}{\sqrt{2}}\{|\uparrow\downarrow\rangle - |\downarrow\uparrow\rangle\} \\
|T_{-1}\rangle &= |\downarrow\downarrow\rangle \\
|T_0\rangle &= \frac{1}{\sqrt{2}}\{|\uparrow\downarrow\rangle + |\downarrow\uparrow\rangle\} \\
|T_1\rangle &= |\uparrow\uparrow\rangle
\end{aligned}
\tag{1.4}
$$

where the arrows indicate the spin polarization of the electron or hole spins. S_0 stands for the ground state singlet, while T_{-1} is the low energy triplet, T_0 is the middle energy triplet and T_1 is the high energy triplet.

In a regular OLED all four configurations (S_0, T_{-1}, T_0 and T_1) have the same probability to be formed since the electrodes are injecting random spin orientations (see Figure 1.8). In a first approximation, the singlet exciton is the main responsible of light emission because the transition from the singlet to the ground state is allowed. So theoretically, the rate electron to photon conversion or external quantum efficiency (EQE) is limited to 25 % in OLEDs.[62]

In contrast to OLEDs, the FM electrodes in the spin-OLED inject spins aligned parallel or antiparallel depending on the orientation of the electrodes magnetization. When the electrodes inject charges with opposite spin polarization the singlet ratio is increased since, theoretically, only the S_0 and T_0 configurations can be formed. Both S_0 and T_0 have 1/2 probability and thus, the maximum EQE is increased to 50 % in a spin-OLED.

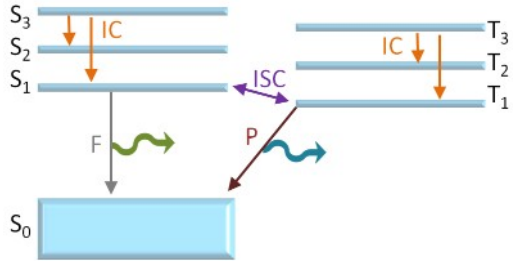

Figure 1.9 Jablonski diagram. Singlets or triplets can relax by internal conversion (orange arrows), intersystem crossing (purple arrow) or by radiative processes such as fluorescence (gray arrow) or phosphorescence (brown arrow).

Singlets and triplets can deactivate by different mechanisms, provided that the spin selection rules are not broken. Figure 1.9 shows the Jablonski diagram where the relaxation mechanisms to the ground state (S_0) for singlets and triplets are depicted. The transitions from the excited singlets S_3 to S_2 or S_1 are achieved by internal conversion (IC) where the excess of energy is lost as phonons. Also, the first excited singlet can non-radiatively transform into the lowest triplet state by intersystem crossing (ISC). The origin of ISC lies in the spin-orbit coupling and consequently it is most common in molecules that contain heavy atoms. Besides, the smaller the energy difference between S_1 and T_1, the greater the ISC probability. The electroluminescence spectrum of these devices shows the wavelength dependence characteristic of the molecular semiconductor film.

The singlet exciton can recombine radiatively since its total spin is zero, just like the total spin of the ground state, what is known as fluorescence (**F**). The triplet exciton decay can occur with or without light emission (radiatively or non-radiatively). The radiative emission of triplets gives rise to phosphorescence (**P**). In the case of phosphorescence the energy is trapped in the triplet for longer times, compared to **F**, since the transition to the ground state is forbidden. Besides, light can also origin from triplet-triplet annihilation (TTA) which is known as delayed fluorescence (**DF**).[63] In this process two molecules in the triplet state interact and produce one singlet state that deactivates directly. Thus, the fluorescence and the delayed fluorescence spectra coincide and the only difference is the longer lifetime for the **DF**.

1.3.2 The MEL Effect

The polaron pair formed in the spin-OLED will be in a singlet or triplet state depending on the relative orientation of the magnetization of the FM electrodes. Figure 1.10 sketches the ferromagnetic electrodes (gray and purple cones) that determine the spin polarization of electrons (gray arrows) and holes (purple arrows). The exciton is formed in the molecular semiconductor, here represented by the blue axis of coordinates. Depending on the electrodes relative magnetic orientation, singlets or triplets will be formed. In the ideal situation, in the AP state only the T_0 and S_0 are possible and the singlet-triplet ratio increases to 1:1 with a maximum theoretical EQE of 50 %. Contrary, in the parallel state depicted in Figure 1.10b, where both electrodes are aligned there is no light emission.

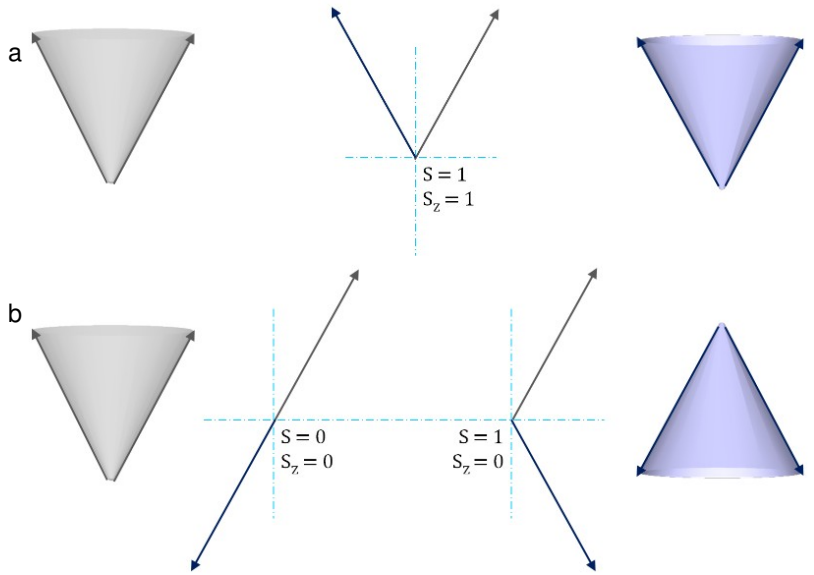

Figure 1.10 Illustration of the singlets and triplets formation in the two states of a spin-OLED. a) In the AP state the electroluminescence quantum efficiency is increased up to a maximum of 50 %. b) In the P state, the triplet population is favored.

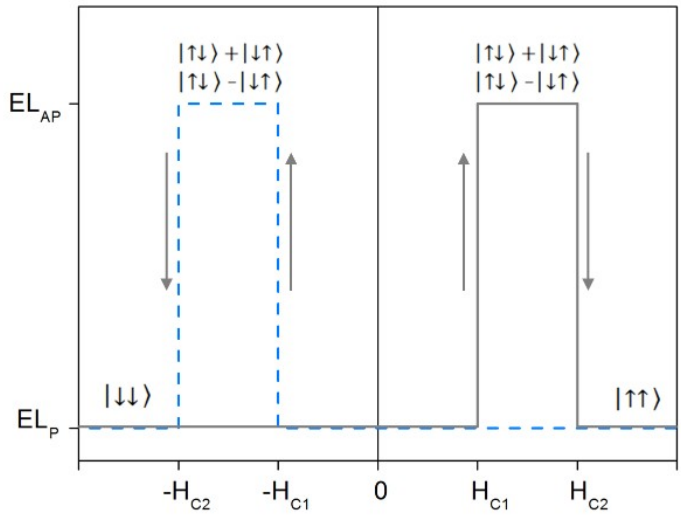

Figure 1.11 MEL effect curve. The measurement protocol is analogous to the MR. The magnetic field is varied while a constant voltage is applied or a constant current flows in the device. The electroluminescence intensity changes depending on the magnetic alignment of the electrodes and the singlets and triplets relative populations. In the AP state, the S_0 singlet and the T_0 triplet can be formed and the light intensity increases because the singlet is the main responsible of light emission. On the contrary, when both electrodes are aligned in the same direction, the light intensity decreases due to an increase of the triplet population.

Similar to magnetoresistance, the variation of the intensity of the light emitted by the device is registered as a function of magnetic field. In the AP state the intensity of light increases due to the increase in the population of singlets. On the contrary, in the P state the light decreases due to the increase of the triplet population. The magneto-electroluminescence (MEL) effect is registered in a similar way as for the MR and at the same time. The measurement usually starts at high negative magnetic field and the intensity of light remains constant until the coercive field of the soft magnet is reached (see Figure 1.11). At this point, the AP state has been achieved and the light emission increases since the singlet relative population has been raised. When the MF equals the coercive field of the hard magnet, the triplet population is enhanced and the light intensity decreases. The backward MEL curve

(blue dashed curve in Figure 1.11) is registered similarly. The percentage of MEL effect is quantified as:

$$MEL(\%) = \frac{EL_{AP} - EL_P}{EL_P} \tag{1.5}$$

where EL_{AP} and EL_P are the electroluminescence in the antiparallel and parallel states respectively.

Although the origin of the MR is at the scattering that spin carriers encounter when crossing the device and the origin of the MEL effect stems from the variation of singlets and triplets relative populations, they are coupled effects both related to the spin-polarized current. Analogously to MR, the MEL effect can be negative if an interface reverses the spin polarization. Therefore, it should be noted that MR and MEL effect must show the same sign in the same device. That is, if the MR is positive (negative), the light intensity will be higher (smaller) in the AP state generating a positive (negative) MEL response.

1.4 Spin Precession in Molecular Spin Valves

1.4.1 Spin Injection in Molecular Spin Valves

Although spin injection in molecular materials has been demonstrated recently by two-photon photoemission[64] and muon spin rotation,[65] none of the techniques demonstrates that the magnetoresistance of a molecular spin valve is caused by spin-polarized currents in the molecular layer.

Since the pioneering works[14,31] many groups have reported magnetoresistance in molecular spin valves.[15,46,47] A priori, it is assumed that the magnetoresistance originates from the scattering that the spin polarized current overcomes when entering the spin collector electrode from the molecular material, i.e., the devices show GMR. But the MR could be the consequence of the scattering that the carriers encounter at the second electrode when tunneling from the spin injector without spin

transport in the molecular layer, i.e., devices showing tunneling magnetoresistance (TMR). Both effects, GMR and TMR, give rise to the same type of magnetoresistance curves and are beforehand indistinguishable.

Even though the molecular layer thicknesses often exceed the hundreds of nanometers and thus the tunneling regime is hostile, the nominal thicknesses are in general much higher than the real thicknesses due to the formation of ill-defined layers.[46] The top electrode is usually deposited by evaporation techniques and impacts violently on the soft molecular layer causing interdiffusion or metallic inclusions as shown in Figure 1.12. In an ill-defined layer, carriers can tunnel between electrodes through thin regions giving rise to TMR in a device that was intended to show GMR. Some possible strategies to overcome this problem are to evaporate the first metallic nanometers at low deposition rates[46,66] or to insert insulating barriers between the molecular layer and the top electrode[52] although in most cases, these do not provide the desired results.

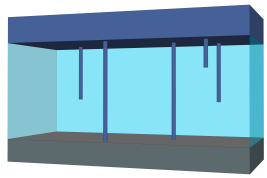

Figure 1.12 Illustration of an ill-defined layer. The top electrode penetrates in the molecular layer creating metallic inclusions. Thus, the charge carriers may travel through pinholes or tunnel through the thin zones.

1.4.2 The Hanle Effect

The Hanle effect consists on forcing the spins to precess once they are inside the molecular material by applying a small non-collinear magnetic field to randomize the spins. It is considered the litmus test of spin injection in molecular spin valves since it will demonstrate that their magnetoresistance is caused by spin-polarized currents in the molecular layer.[67–70]

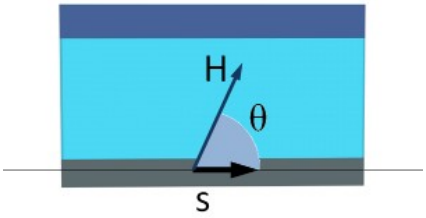

Figure 1.13 θ is defined as the angle between the non-collinear magnetic field and the magnetization of the electrodes.

The Johnson and Silsbee model[71] described below quantitatively explains the Hanle effect. The spin density (s) follows the drift-diffusion equation:[72]

$$\frac{\partial s}{\partial t} = D\frac{\partial^2 s}{\partial x^2} - v\frac{\partial s}{\partial x} - \frac{s}{\tau_s} \tag{1.6}$$

where D is the diffusion coefficient in cm^2/s, v is drift velocity and τ_s is the spin relaxation time. The solution to this drift-diffusion equation is a Gaussian distribution that travels at a velocity v towards the spin detector in the x axis:

$$s(x,t) = \frac{1}{2\sqrt{\pi D t}} exp\left(-\frac{(x-vt)^2}{4Dt}\right) exp\left(-\frac{t}{\tau_s}\right) \tag{1.7}$$

The initial spin polarization injected in the molecular layer by the FM electrode can be described by the vector:

$$S_0 = \begin{pmatrix} 0 & sin\theta & cos\theta \end{pmatrix} \tag{1.8}$$

where θ is the angle between H_z and the magnetization of the electrode (see Figure 1.13). The non-collinear magnetic field will force the spins to precess at the Larmor frequency:

$$\omega_L = \frac{egH_z}{2m_e} \tag{1.9}$$

where e is the electron charge, g is the g-factor and m_e is the electron rest mass.

Furthermore, the rotation matrix around the z-axis is described by:

$$R_z = \begin{pmatrix} cos(\omega_L t) & -sin(\omega_L t) & 0 \\ sin(\omega_L t) & cos(\omega_L t) & 0 \\ 0 & 0 & 1 \end{pmatrix} \tag{1.10}$$

Thus, the spin polarization at a time t in the presence of H_z will be:

$$S_t = \begin{pmatrix} -sin\theta sin(\omega_L t) & sin\theta sin(\omega_L t) & cos\theta \end{pmatrix} \tag{1.11}$$

Finally, the GMR measured in the device will be proportional to the sum of all the projections $S_0 \cdot S_t$ weighted by the diffusion transport:

$$GMR \propto \int_0^\infty \frac{1}{2\sqrt{\pi D t}} [sin^2\theta cos(\omega_L t) + cos^2\theta] exp\left(-\frac{(x-vt)^2}{4Dt}\right) exp\left(-\frac{t}{\tau}\right) dt \tag{1.12}$$

The Hanle effect has been measured in inorganic spin valves,[73,74] where the transport is coherent and each precession is reflected in an oscillation in the value of the resistance[71] and also in graphene-based spin valves.[75] In both cases the carrier mobilities are orders of magnitude higher than the characteristic mobilities of molecular materials.

Contrary, in molecular semiconductors the transport is incoherent. Then, the integral in Equation 1.12 with the term $cos\omega_L t$ vanishes and the GMR is proportional to $cos^2\theta$.[69] In MSVs, the Hanle effect is measured by applying a magnetic field perpendicular to the magnetization of the electrodes (H_z), as sketched in Figure 1.14. Consequently, $\theta = \pi/2$ and the magnetoresistance should be quenched. H_z is small enough not to affect the polarization of the electrodes.

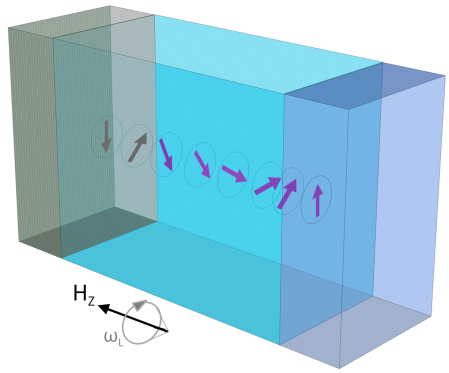

Figure 1.14 Illustration of the spin precession (Hanle effect) in a molecular spin valve (H_z at $\theta = \pi/2$ quenches the MR). When the spins are injected in the molecular layer, they precess around the magnetic field H_z at the Larmor frequency so that the resistance is no longer the resistance of the antiparallel state. An analogous situation is encountered by the parallel state.

Unfortunately, the scientific community is not keen on publishing negative results and only a few works reported MSVs where no Hanle effect could be measured.[69,76] The reasons for the absence of Hanle effect in MSVs may be several. In the worst case, transport is not occurring through the molecular material and therefore the spins cannot precess in it, since there is no spin current in the molecular layer. But if indeed, there is transport in the molecular material, the absence of Hanle effect may arise from the difference in terms of spin transport mechanisms between molecular and inorganic materials. In the former, the spin can travel much faster decoupled from the electric charge through exchange.[67] In consequence, the pure spin currents can preclude the quenching of the MR and the observation of the Hanle effect.

1.5 Bibliography

[1] V. A. Dediu, L. E. Hueso, I. Bergenti, and C. Taliani. “Spin routes in organic semiconductors”. Nature Materials 8.9 (2009), pp. 707–716.

[2] S. Sanvito. “Molecular spintronics”. Chemical Society Reviews 40.6 (2011), pp. 3336–3355.

[3] P. Ruden. “Organic spintronics: Interfaces are critical”. Nature Materials 10.1 (2011), pp. 8–9.

[4] Z. V. Vardeny. Organic spintronics. CRC Press, 2010.

[5] Editorial. “Why going organic is good”. Nature Materials 8.691 (2009).

[6] Z. G. Yu. “Spin-orbit coupling, spin relaxation, and spin diffusion in organic solids”. Physical Review Letters 106.10 (2011), p. 106602.

[7] J. Bartolomé, F. Luis, and J. F. Fernández. “Molecular Magnets”. Physics and Applications (2014).

[8] S. Schmaus, A. Bagrets, Y. Nahas, T. K. Yamada, A. Bork, M. Bowen, E. Beaurepaire, F. Evers, and W. Wulfhekel. “Giant magnetoresistance through a single molecule”. Nature Nanotechnology 6.3 (2011), pp. 185–189.

[9] L. Bogani and W. Wernsdorfer. “Molecular spintronics using single-molecule magnets”. Nature Materials 7.3 (2008), pp. 179–186.

[10] R. Vincent, S. Klyatskaya, M. Ruben, W. Wernsdorfer, and F. Balestro. “Electronic read-out of a single nuclear spin using a molecular spin transistor”. Nature 488.7411 (2012), pp. 357–360.

[11] E. Coronado and M. Yamashita. “Molecular spintronics: the role of coordination chemistry”. Dalton Transactions 45.42 (2016), pp. 16553–16555.

[12] J. Lehmann, A. Gaita-Ariño, E. Coronado, and D. Loss. “Spin qubits with electrically gated polyoxometalate molecules”. Nature Nanotechnology 2.5 (2007), pp. 312–317.

[13] S. Thiele, F. Balestro, R. Ballou, S. Klyatskaya, M. Ruben, and W. Wernsdorfer. “Electrically driven nuclear spin resonance in single-molecule magnets”. Science 344.6188 (2014), pp. 1135–1138.

[14] V. Dediu, M. Murgia, F. Matacotta, C. Taliani, and S. Barbanera. “Room temperature spin polarized injection in organic semiconductor”. Solid State Communications 122.3 (2002), pp. 181–184.

[15] J. Devkota, R. Geng, R. C. Subedi, and T. D. Nguyen. “Organic spin valves: a review”. Advanced Functional Materials 26.22 (2016), pp. 3881–3898.

[16] T. D. Nguyen, E. Ehrenfreund, and Z. V. Vardeny. “Spin-polarized light-emitting diode based on an organic bipolar spin valve”. Science 337.6091 (2012), 204–209.

[17] J. Prieto-Ruiz, S. G. Miralles, H. Prima-García, A. Riminucci, P. Graziosi, M. Cinchetti, M. Aeschlimann, V. A. Dediu, and E. Coronado. “Controlling singlet-triplet ratio in OLEDs by spin polarised currents”. arXiv:1612.00633 (2016).

[18] X. Zhang, S. Mizukami, T. Kubota, Q. Ma, M. Oogane, H. Naganuma, Y. Ando, and T. Miyazaki. “Observation of a large spin-dependent transport length in organic spin valves at room temperature”. Nature Communications 4 (2013), p. 1392.

[19] H. Cho, S.-H. Jeong, M.-H. Park, Y.-H. Kim, C. Wolf, C.-L. Lee, J. H. Heo, A. Sadhanala, N. Myoung, S. Yoo, et al. “Overcoming the electroluminescence efficiency limitations of perovskite light-emitting diodes”. Science 350.6265 (2015), pp. 1222–1225.

[20] C. Zhang, D. Sun, C. Sheng, Y. Zhai, K. Mielczarek, A. Zakhidov, and Z. V. Vardeny. “Magnetic field effects in hybrid perovskite devices”. Nature Physics 11.5 (2015), pp. 427–434.

[21] I. Zutic, J. Fabian, and S. D. Sarma. “Spintronics: Fundamentals and applications”. Reviews of Modern Physics 76.2 (2004), p. 323.

[22] S. Wolf, D. Awschalom, R. Buhrman, J. Daughton, S. Von Molnar, M. Roukes, A. Y. Chtchelkanova, and D. Treger. “Spintronics: a spin-based electronics vision for the future”. Science 294.5546 (2001), pp. 1488–1495.

[23] M. Jullière. “Tunneling between ferromagnetic films”. Physics Letters A 54.3 (1975), pp. 225–226.

[24] M. N. Baibich, J. M. Broto, A. Fert, F. N. Van Dau, F. Petroff, P. Etienne, G. Creuzet, A. Friederich, and J. Chazelas. “Giant magnetoresistance of (001) Fe/(001) Cr magnetic superlattices”. Physical Review Letters 61.21 (1988), p. 2472.

[25] E. Grochowski and D. A. Thompson. “Outlook for maintaining areal density growth in magnetic recording”. IEEE Transactions on Magnetics 30.6 (1994), pp. 3797–3800.

[26] A. Fert. “Origin, development, and future of spintronics (Nobel Lecture)”. Angewandte Chemie International Edition 47.32 (2008), pp. 5956–5967.

[27] P. A. Grünberg. “From spinwaves to Giant Magnetoresistance (GMR) and beyond”. Nobel Lectures in Physics (2006–2010) 3 (2014), p. 166.

[28] T. McGuire and R. Potter. “Anisotropic magnetoresistance in ferromagnetic 3d alloys”. IEEE Transactions on Magnetics 11.4 (1975), pp. 1018–1038.

[29] W. Wagemans and B. Koopmans. “Spin transport and magnetoresistance in organic semiconductors”. Physica Status Solidi B 248.5 (2011), pp. 1029–1041.

[30] V. Prigodin, J. Bergeson, D. Lincoln, and A. Epstein. “Anomalous room temperature magnetoresistance in organic semiconductors”. Synthetic Metals 156.9 (2006), pp. 757–761.

[31] Z. Xiong, D. Wu, Z. V. Vardeny, and J. Shi. “Giant magnetoresistance in organic spin-valves”. Nature 427.6977 (2004), pp. 821–824.

[32] R. Lin, F. Wang, J. Rybicki, M. Wohlgenannt, and K. Hutchinson. “Distinguishing between tunneling and injection regimes of ferromagnet/organic semiconductor/ferromagnet junctions”. Physical Review B 81.19 (2010), p. 195214.

[33] S. M. Sze and K. K. Ng. Physics of semiconductor devices. John Wiley & Sons, 2006.

[34] M. Era, Y. Ikeda, H. Tokuhisa, and T. Tsutsui. “Electric conduction of electroluminescent metal chelate thin films”. Molecular Crystals and Liquid Crystals 327.1 (1999), pp. 171–174.

[35] A. Köhler and H. Bässler. Electronic processes in organic semiconductors. John Wiley & Sons, 2015.

[36] V. Coropceanu, J. Cornil, D. A. da Silva Filho, Y. Olivier, R. Silbey, and J. L. Brédas. “Charge transport in organic semiconductors”. Chemical Reviews 107.4 (2007), pp. 926–952.

[37] N. Tessler, Y. Preezant, N. Rappaport, and Y. Roichman. “Charge transport in disordered organic materials and its relevance to thin-film devices: A tutorial review”. Advanced Materials 21.27 (2009), pp. 2741–2761.

[38] H. Ishii, K. Sugiyama, E. Ito, and K. Seki. “Energy level alignment and interfacial electronic structures at organic/metal and organic/organic interfaces”. Advanced Materials 11.8 (1999), pp. 605–625.

[39] W. Brütting. Physics of Organic Semiconductors. Wiley-VCH, 2006.

[40] Z. G. Yu. “Impurity-band transport in organic spin valves”. Nature Communications 5 (2014), p. 4842.

[41] N. Koch, N. Ueno, and A. T. S. Wee. The molecule-metal interface. John Wiley & Sons, 2013.

[42] J. Camarero and E. Coronado. “Molecular vs. inorganic spintronics: the role of molecular materials and single molecules”. Journal of Materials Chemistry 19.12 (2009), pp. 1678–1684.

[43] N. F. Mott. “Electrons in transition metals”. Advances in Physics 13.51 (1964), pp. 325–422.

[44] J. MacLaren, X. Zhang, and W. Butler. “Validity of the Jullière model of spin-dependent tunneling”. Physical Review B 56.18 (1997), p. 11827.

[45] J. S. Moodera and G. Mathon. “Spin polarized tunneling in ferromagnetic junctions”. Journal of Magnetism and Magnetic Materials 200.1 (1999), pp. 248–273.

[46] D. Sun, E. Ehrenfreund, and Z. V. Vardeny. “The first decade of organic spintronics research”. Chemical Communications 50.15 (2014), pp. 1781–1793.

[47] H. Gu, X. Zhang, H. Wei, Y. Huang, S. Wei, and Z. Guo. “An overview of the magnetoresistance phenomenon in molecular systems”. Chemical Society Reviews 42.13 (2013), pp. 5907–5943.

[48] B. Li, C. Y. Kao, J. W. Yoo, V. N. Prigodin, and A. J. Epstein. “Magnetoresistance in an all-organic-based spin valve”. Advanced Materials 23.30 (2011), pp. 3382–3386.

[49] X. Sun, A. Bedoya-Pinto, Z. Mao, M. Gobbi, W. Yan, Y. Guo, A. Atxabal, R. Llopis, G. Yu, Y. Liu, et al. “Active morphology control for concomitant long distance spin transport and photoresponse in a single organic device”. Advanced Materials (2016).

[50] D. Ciudad, M. Gobbi, C. J. Kinane, M. Eich, J. S. Moodera, and L. E. Hueso. “Sign control of magnetoresistance through chemically engineered interfaces”. Advanced Materials 26.45 (2014), pp. 7561–7567.

[51] H. Vinzelberg, J. Schumann, D. Elefant, R. Gangineni, J. Thomas, and B. Büchner. “Low temperature tunneling magnetoresistance on (La,Sr)MnO_3/Co junctions with organic spacer layers”. Journal of Applied Physics 103.9 (2008), p. 093720.

[52] V. Dediu, L. Hueso, I. Bergenti, A. Riminucci, F. Borgatti, P. Graziosi, C. Newby, F. Casoli, M. De Jong, C. Taliani, et al. “Room-temperature spintronic effects in Alq_3-based hybrid devices”. Physical Review B 78.11 (2008), p. 115203.

[53] N. Atodiresei, J. Brede, P. Lazi, V. Caciuc, G. Hoffmann, R. Wiesendanger, and S. Blügel. “Design of the local spin polarization at the organic-ferromagnetic interface”. Physical Review Letters 105.6 (2010), p. 066601.

[54] C. Barraud, P. Seneor, R. Mattana, S. Fusil, K. Bouzehouane, C. Deranlot, P. Graziosi, L. Hueso, I. Bergenti, V. Dediu, et al. “Unravelling the role of the interface for spin injection into organic semiconductors”. Nature Physics 6.8 (2010), pp. 615–620.

[55] S. Sanvito. “Molecular spintronics: The rise of spinterface science”. Nature Physics 6.8 (2010), pp. 562–564.

[56] J. Kalinowski. Organic light-emitting diodes: Principles, characteristics & processes. CRC press, 2004.

[57] R. Sprengard, K. Bonrad, T. K. Daeubler, T. Frank, V. Hagemann, I. Köhler, J. Pommerehne, C. R. Ottermann, F. Voges, and B. Vingerling. “OLED devices for signage applications: a review of recent advances and remaining challenges”. Optical Science and Technology, the SPIE 49th Annual Meeting. International Society for Optics and Photonics. 2004, pp. 173–183.

[58] M. Sessolo and H. J. Bolink. “Hybrid organic–inorganic light-emitting diodes”. Advanced Materials 23.16 (2011), pp. 1829–1845.

[59] H. J. Bolink, H. Brine, E. Coronado, and M. Sessolo. “Phosphorescent hybrid organic–inorganic light-emitting diodes”. Advanced Materials 22.19 (2010), pp. 2198–2201.

[60] I. Bergenti, V. Dediu, E. Arisi, T. Mertelj, M. Murgia, A. Riminucci, G. Ruani, M. Solzi, and C. Taliani. “Spin polarised electrodes for organic light emitting diodes”. Organic Electronics 5.6 (2004), pp. 309–314.

[61] J. J. Sakurai, S. F. Tuan, and E. D. Commins. Modern quantum mechanics, revised edition. AAPT, 1995.

[62] P. Ball. “Material witness: A new twist for OLEDs”. Nature Materials 15.8 (2016), pp. 822–822.

[63] A. Hayer, H. Bässler, B. Falk, and S. Schrader. “Delayed fluorescence and phosphorescence from polyphenylquinoxalines”. The Journal of Physical Chemistry A 106.46 (2002), pp. 11045–11053.

[64] M. Cinchetti, K. Heimer, J.-P. Wüstenberg, O. Andreyev, M. Bauer, S. Lach, C. Ziegler, Y. Gao, and M. Aeschlimann. “Determination of spin injection and transport in a ferromagnet/organic semiconductor heterojunction by two-photon photoemission”. Nature Materials 8.2 (2009), pp. 115–119.

[65] A. J. Drew, J. Hoppler, L. Schulz, F. Pratt, P. Desai, P. Shakya, T. Kreouzis, W. Gillin, A. Suter, N. Morley, and V. Malik. “Direct measurement of the electronic spin diffusion length in a fully functional organic spin valve by low-energy muon spin rotation”. Nature Materials 8.2 (2009), pp. 109–114.

[66] S. Majumdar, H. S. Majumdar, R. Laiho, and R. Österbacka. “Organic spin valves: effect of magnetic impurities on the spin transport properties of polymer spacers”. New Journal of Physics 11.1 (2009), p. 013022.

[67] Z. G. Yu. “Suppression of the Hanle effect in organic spintronic devices”. Physical Review Letters 111.1 (2013), p. 016601.

[68] S. Sanvito and V. A. Dediu. “Spintronics: News from the organic arena”. Nature Nanotechnology 7.11 (2012), pp. 696–697.

[69] A. Riminucci, M. Prezioso, C. Pernechele, P. Graziosi, I. Bergenti, R. Cecchini, M. Calbucci, M. Solzi, and V. Alek Dediu. “Hanle effect missing in a prototypical organic spintronic device”. Applied Physics Letters 102.9 (2013), p. 092407.

[70] Z. G. Yu. “Spin transport and the Hanle effect in organic spintronics”. Nanoelectronics and Spintronics 1.1 (2015), pp. 1–18.

[71] M. Johnson and R. H. Silsbee. “Interfacial charge-spin coupling: Injection and detection of spin magnetization in metals”. Physical Review Letters 55.17 (1985), p. 1790.

[72] B. Huang and I. Appelbaum. “Spin dephasing in drift-dominated semiconductor spintronics devices”. Physical Review B 77.16 (2008), p. 165331.

[73] M. Johnson and R. Silsbee. “Coupling of electronic charge and spin at a ferromagnetic-paramagnetic metal interface”. Physical Review B 37.10 (1988), p. 5312.

[74] S. P. Dash, S. Sharma, R. S. Patel, M. P. de Jong, and R. Jansen. “Electrical creation of spin polarization in silicon at room temperature”. Nature 462.7272 (2009), pp. 491–494.

[75] J. J. van den Berg, W. Strupinski, and B. J. van Wees. “Observation of anomalous Hanle spin precession line shapes resulting from interaction with localized states”. Physical Review B 91.8 (2015), p. 081403.

[76] M. Grünewald, R. Göckeritz, N. Homonnay, F. Würthner, L. Molenkamp, and G. Schmidt. “Vertical organic spin valves in perpendicular magnetic fields”. Physical Review B 88.8 (2013), p. 085319.

2

Chloroquinoline-based Molecules as Thin Films

2.1 Introduction

Single-molecule magnets or SMMs[1–3] have commanded the scientific community attention in the last two decades due to their unique magnetic behavior. They constitute the smallest molecular unit for magnetic data storage. But, contrary to what happens in classical magnets, the magnetic memory is not a cooperative effect, as it arises from the single molecule.

SMMs can be seen as superparamagnetic molecules with a spin S that relaxes slowly below a certain temperature, still in this mesoscopic regime, this classical effect coexists with quantum effects.[4] The first generation of SMMs reported were based in molecules containing a cluster of exchange-coupled transition metal ions bridged by simple ligands such as oxides. Among them, the Mn_{12} with a total giant

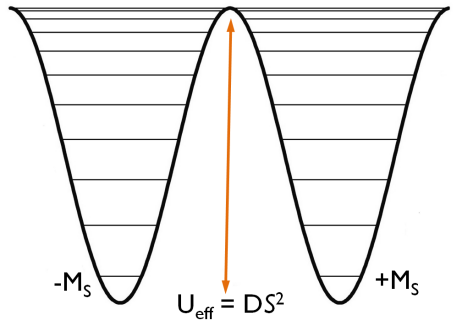

Figure 2.1 Energy levels as a function of the M_S quantum number whose up and down orientations are separated by a magnetic anisotropy barrier (U_{eff}) in the double-well potential. The classical projections of S are quantized into $2M_S+1$ energetic states.

spin of S = 10 has been the most studied.[5]

The classical relaxation of the magnetization in these systems is due to the presence of a superparamagnetic energy barrier (U_{eff}) caused by a negative spin anisotropy which stabilizes the highest M_S value (see Figure 2.1). The larger the barrier, the longer the time the magnetization is retained. The U_{eff} magnitude depends on the total spin S and on the axial anisotropy, quantified by *D* which is known as the zero-field splitting parameter.[1] Besides this classical process, the spin can relax by quantum tunneling through the magnetization barrier (QTM). Both mechanisms compete below a certain temperature. In the latter, the spin flips from $-M_S$ to $+M_S$, or through an intermediate spin projection, without overcoming the barrier.

The second generation of SMMs is constituted by single-ion magnets (SIMs) based on coordination compounds where a central lanthanide ion is the source of magnetic anisotropy. The unique magnetic and quantum properties together with the electronic robustness of their magnetic state rely on the occupancy of the f-orbitals, which have more internal character than the d-orbitals. Owing to the participation of f-electrons, the lanthanides exhibit high total magnetic moments, high spin-orbit coupling and large magnetic anisotropy.[4]

In principle, the potential of single-ion magnets in the field of molecular spintronics lies in the possibility of introducing in the spin collector layer large magnetic moments, which may be spin polarized through dipolar interactions with the ferromagnetic electrode, in particular in the vicinity of the hybrid molecular/inorganic interface. In this chapter we study thin films of a new family of SIMs. The major difficulty with these coordination complexes is to make them thermally stable in order to be able to sublimate them on the ferromagnetic substrates. We evaluate this possibility by means of a multi-technique process. The sublimable SIM molecules will be deposited on different substrates and the films will be studied by SQUID magnetometry.

2.2 Results and Discussion

2.2.1 Molecular Structure of the Compounds

Among all the molecular compounds used in molecular spintronics, Alq_3 (aluminum tris-8-hydroxyquinoline) has played the main role.[6,7] A few years ago, when this quinoline-based compound was introduced in the molecular spintronics field,[8] it was already a well-known molecule in molecular electronics, as it had been extensively used in different devices such as organic light emitting diodes,[9–11] organic solar cells[12,13] or organic field effect transistors.[14]

Inspired by the long experience acquired by the molecular spintronics community, two families of quinoline-based molecules similar to Alq_3 were synthesized in our group. The first, the Ln_3q_9 family[15] is constituted by trinuclear molecules and quinoline-based ligands in a bidimensional geometry (see Figure 2.2c). Recently, they have been implemented in spin valves demonstrating their potential for spintronic devices.[16]

The second family of lanthanide quinoline-based compounds is studied in this

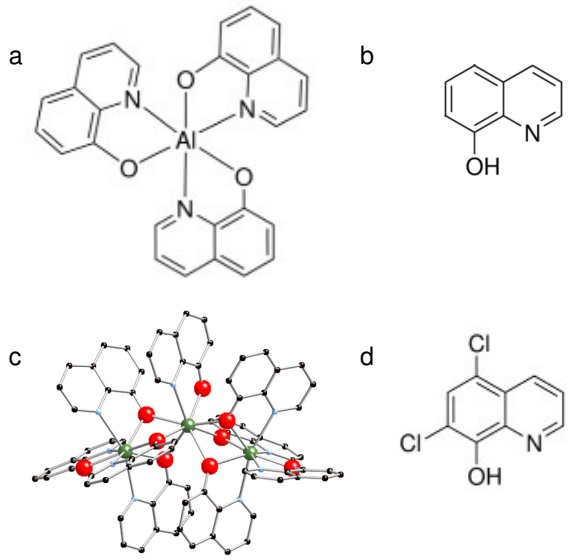

Figure 2.2 Molecular structure of a) Alq_3 (aluminum tris-8-hydroxyquinoline). b) The ligand q = 8-hydroxyquinoline of Alq_3 and Ln_3q_9. c) The Ln_3q_9 family where the lanthanoid (Ln) is depicted in green, oxygen in red, carbon in black and nitrogen in blue. d) The ligand $5,7Cl_2q$ = (5,7-dichloro-8-hydroxyquinoline) of the molecular compounds NaLnClq, NEtLnClq and KNEtLnClq, studied in this chapter.

chapter. They are analogous complexes to Alq_3 where a lanthanide atom replaces the central Al and the three ligands of Alq_3 become four chlorine-substituted quinolines (see Figure 2.2).

The quinoline-based complexes studied in this chapter have the chemical formula $A[Ln(5,7Cl_2q)_4]$ (where A = Na^+, NEt_4^+, $K_{0.5}(NEt_4)_{0.5}^+$; Ln = Y^{III}, Tb^{III}, Dy^{III} and $5,7Cl_2q$ = 5,7-dichloro-8-hydroxyquinoline). Hereafter these five compounds are named for simplicity NaYClq, NaTbClq, NaDyClq, NEtDyClq and KNEtDyClq, specifying the cation and the lanthanoid center.

Figure 2.3 shows the molecular structure of the three different families of compounds, which differ only in the cation used to counterbalance its negative charge. In all compounds, each lanthanoid is coordinated to four $5,7Cl_2q$ ligands, each of

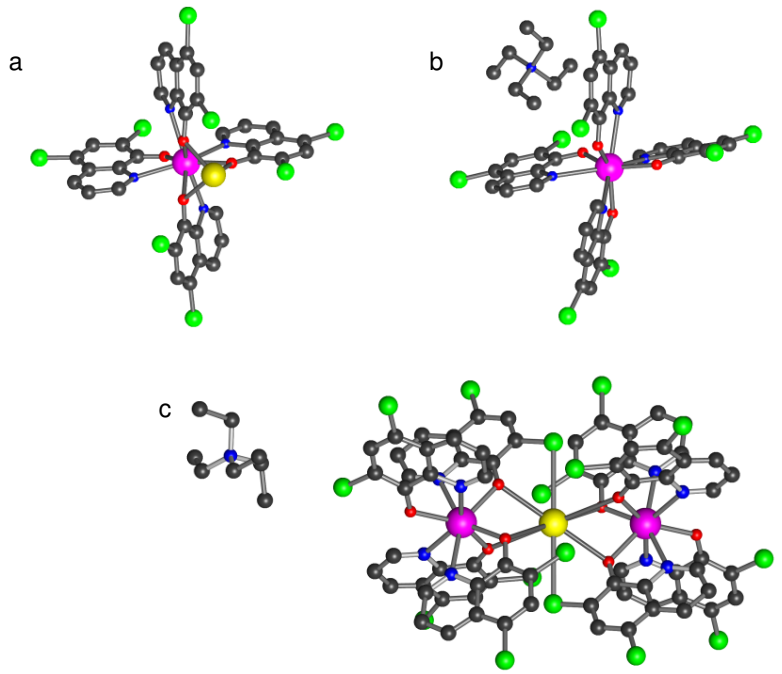

Figure 2.3 Molecular structure of the compounds. a) NaLnClq with Ln = Y , Tb or Dy. b) NEtDyClq. c) KNEtDyClq. The central lanthanoid ion is in pink, oxygen in red, nitrogen in blue, carbon in black, chlorine in green and sodium (in a) and potassium (in c) in yellow.

them acting as a bidentate ligand via the nitrogen and oxygen atoms. It can be appreciated that the inorganic core, which is the main responsible of the magnetic properties, is surrounded by a shell of organic ligands that isolate it. All compounds are mononuclear except KNEtDyClq which is dinuclear as it contains two lanthanide centers linked by the K^+.

The mononuclear compounds have a spherical shape while the dinuclear species are oval-shaped. Furthermore, in the Na^+ derivatives, this cation is in close contact with the lanthanide in such a way that they form the ionic pair well separated from the other ionic pairs in the structure. A priori, these molecular features (weight

of the molecular species, contacts between the anionic lanthanoid complexes and the counter-ions and intermolecular interactions) could be relevant in terms of sublimation capability because spherical molecules might be more likely to retain their molecular structure upon sublimation.

2.2.2 Magnetic Properties of the Compounds

The responsible of the magnetic properties associated to the compounds studied in this chapter are the Tb^{3+} and Dy^{3+} ions. The diamagnetic molecule NaYClq hosts an Y^{3+} ion, with the same charge an similar radius but with no f-electrons and therefore diamagnetic (just like Alq_3).

Figure 2.4 shows the static magnetic measurements of all the magnetic compounds plotted as χT vs T.[4] They show values near to those expected for the $^7F_6$ and $^6H_{15/2}$ multiplets of Tb^{III} (11.82 emu K mol^{-1}) and Dy^{III} (14.17 emu K mol^{-1}).[2] The

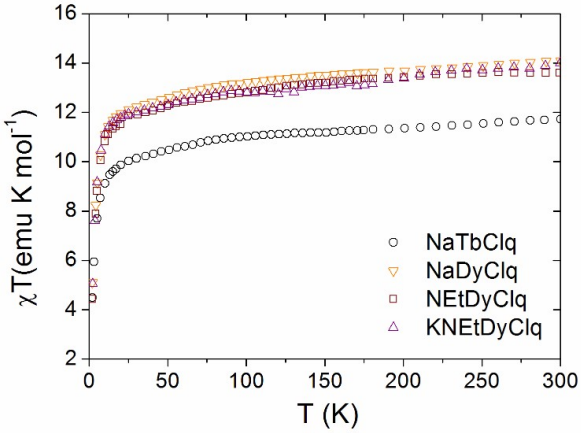

Figure 2.4 χT product of the compounds.The χT values at 300 K in the four complexes are near those expected for Tb^{III} (11.81 emu K mol^{-1}) and Dy^{III} (14.17 emu K mol^{-1}).

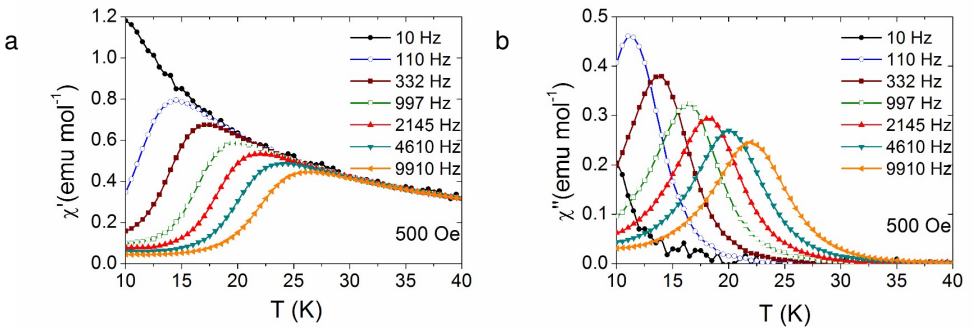

Figure 2.5 Temperature dependence of the in-phase (a) and the out-of-phase (b) components of the magnetic susceptibility of bulk NaDyClq at the frequencies indicated and in a dc field of 500 Oe. NaDyClq presents the highest T_m = 22 K at 9910 Hz.

characteristic decay observed at low temperatures is caused by the depopulation of the excited stark levels, which is typical of lanthanoid centers.

In SIMs, the slow relaxation of the magnetization can be quantified using alternating current (ac) susceptibility measurements.[17] The ac magnetic field (H) is a cosine function that oscillates at frequency ω ($H = H_0 cos(\omega t)$). Furthermore, the ac magnetic susceptibility can be decomposed in a real, or in-phase component (χ'), and an imaginary, or out-of-phase component (χ''), related to energy dissipation The magnetic moment of the SIM is unable to follow the oscillations of the external field and this causes a maximum (T_m) in both the in-phase and the out of phase ac susceptibility components which are frequency dependent. From this dependence one can estimate the energy barrier (U_{eff}) being also related with the blocking temperature (T_b), i.e., the temperature at which the magnetic hysteresis loop opens up.

We checked the SMM behavior by measuring the frequency-dependent signal of the out of phase magnetic susceptibility, χ''. Similarly to other lanthanoid systems, the maximum in χ'' is only observed when applying an external dc field, possibly due to the presence of a fast relaxation of the magnetization through a quantum tunneling mechanism. This is commonly observed in the so called field-induced

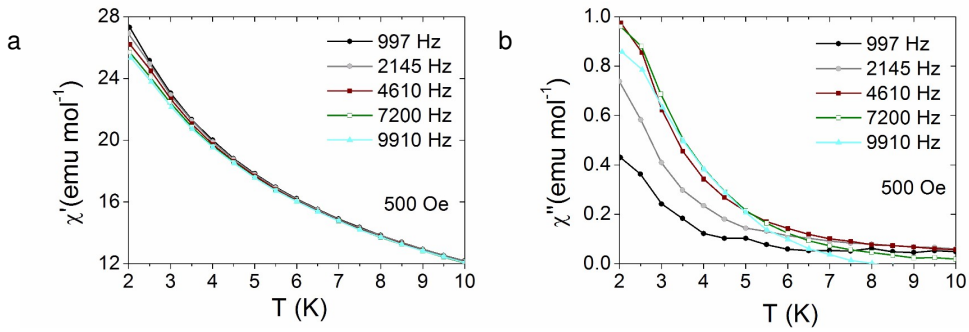

Figure 2.6 Magnetic susceptibilities in phase (χ') and out of phase (χ'') at H_{dc} = 500 Oe for the NaTbClq compound. The dependence of χ'' with the frequency can be intuited. Unfortunately the maxima locate below 2 K which is out of the equipment temperature range.

SIMs. The fast tunneling can be easily removed with the application of a dc field that drives the levels away from the hyperfine avoided crossing region.[1]

T_m is defined as the temperature of the χ'' maximum at the highest frequency. The NaDyClq compound shows the highest T_m = 22 K at 9910 Hz as seen in Figure 2.5. Conversely, the NaTbClq maxima locate below 2 K (see Figure 2.6) and cannot be observed. The NEtDyClq compound presents a T_m = 4.5 K at 9910 Hz and finally the KNEtDyClq molecule shows a T_m = 13 K at 997 Hz (see Figures 2.7 and 2.8).

Henceforth, we focus in the NaDyClq compound to analyze its magnetization relaxation mechanism by means of Cole-Cole plots. The rationale behind such a decision is that the NaDyClq molecule is the only compound that shows SMM behavior at high temperatures together with stability upon sublimation, as will be demonstrated in the following sections.

In lanthanide-based SIMs, the relaxation of the magnetization is typically governed by single-ion factors rather than magnetic exchange or thermal relaxation processes.[18] The number of relaxation mechanisms can be obtained from Cole-Cole plots.[19] These plots are Argand-type diagrams constructed from the maxima of χ'

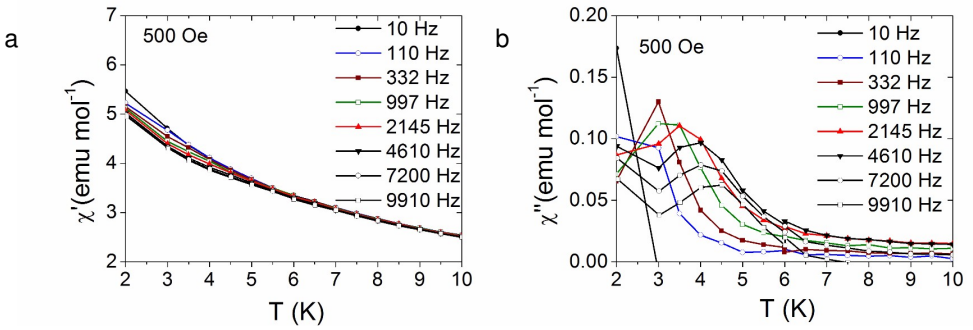

Figure 2.7 ac magnetic measurements. Magnetic susceptibilities in phase (χ') and out of phase (χ'') at H_{dc} = 500 Oe of bulk NEtDyClq at different frequencies. The T_m amounts to 4.5 K at 9910 Hz. The out-of-phase magnetic susceptibility is frequency dependent manifesting the single-molecule magnet behavior.

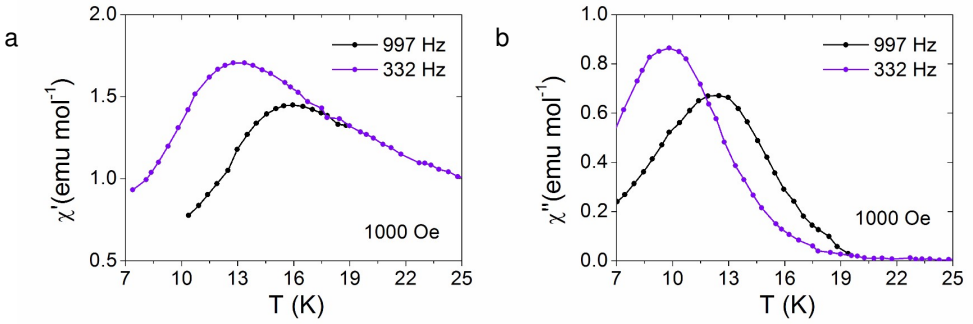

Figure 2.8 Frequency dependence of χ' and χ'' with a dc field of 1000 Oe for bulk KNEtDyClq. The T_m amounts to 14 K at 997 Hz. The KNEtDyClq compound shows the second highest T_m: (T_m (NaDyClq, 997 Hz) = 16 K, T_m (KNEtDyClq, 997 Hz) = 14 K and T_m (NEtDyClq, 997 Hz) = 3.5 K).

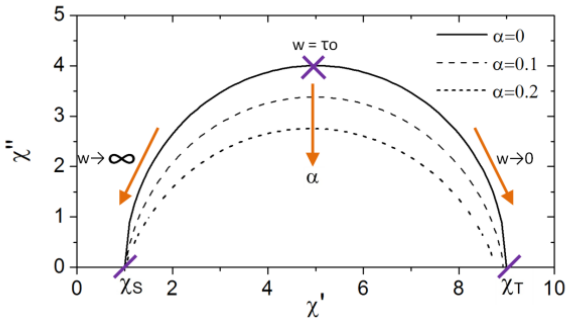

Figure 2.9 Simulated Cole-Cole curves plotted from Equation 2.1 with χ_T = 9 and χ_S = 1. For α = 0 all the (χ', χ") pairs belong to the perfect semicircle with radius (χ_T-χ_S)/2 indicating that the system magnetically relaxes by a dominant relaxation process.

and χ'' and fitted to the equation:

$$\chi''(\chi') = \frac{-\chi_T - \chi_S}{2tan\left((1-\alpha)\frac{\pi}{2}\right)} + \sqrt{(\chi' - \chi_S)(\chi_T - \chi') \frac{(\chi_T - \chi_S)^2}{2tan^2\left((1-\alpha)\frac{\pi}{2}\right)}} \tag{2.1}$$

where $0 < \alpha < 1$ is related to the number of relaxation mechanisms, χ_T is the isothermal susceptibility and χ_S is the adiabatic susceptibility. If the parameter α = 0, the Cole-Cole curve is a perfect semicircle indicating one dominant relaxation process. Whereas as α increases, various relaxation mechanisms compete (see Figure 2.9). Besides, the intersections of the Cole-Cole curve with the x axis give the values of χ_T and χ_S. χ' tends to the isothermal susceptibility when $\omega \to 0$ whilst when $\omega \to \infty$, χ' tends to the adiabatic susceptibility.

The Cole-Cole fits for compound NaDyClq present in all cases low α values indicating one dominant relaxation mechanism with a unique energy barrier (see Figure 2.10 where H_{dc} = 500 Oe and Figures A.1c (H_{dc} = 150 Oe), A.2c (H_{dc} = 425 Oe), A.3c (H_{dc} = 750 Oe) and A.4c (H_{dc} = 1000 Oe) in Appendix A).

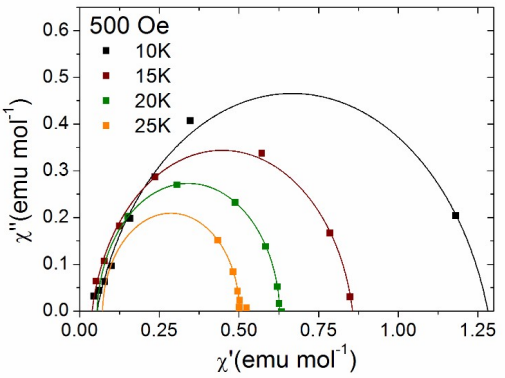

Figure 2.10 Cole-Cole plot for compound NaDyClq at the temperatures indicated and a dc magnetic field of 500 Oe. The fits to equation 2.1 are plotted as solid lines while the experimental data constructed after Figure 2.5 is represented by points. The parameter α obtained from the fit in each case is: α (10 K) = 0.17 $\pm$ 0.04, α (15 K) = 0.11 $\pm$ 0.01, α (20 K) = 0.03 $\pm$ 0.01 and α (25 K) = 0.02 $\pm$ 0.01.

As relaxation mechanism, we can have two possibilities, namely Orbach and Raman processes. The former has been systematically implemented in the lanthanoid-based SIMs and it is well understood in the case of the first generation SMMs where there are plenty of magnetic levels available. The Orbach mechanisms is a thermal dependent process that follows the Arrhenius law seen in Equation 2.2 where τ = 2 π/ω^{-1}, T is the temperature corresponding to the maxima in the χ''(T) curves, U_{eff} is the energy barrier, k_B is the Boltzmann constant and the pre-exponential factor, τ_0, depends on the environment of the individual molecules.

$$\tau = \tau_0 \exp\left[\frac{-U_{eff}}{k_B T}\right] \tag{2.2}$$

Alternatively, the Raman mechanism is a two-phonon process in which relaxation is taking place through an exchange of energy by lattice vibrations via a virtual level. It is described by the Equation 2.3 where the n_{Raman} exponent is expected to be 1/9 for a Kramers ion (odd number of 4f electrons, $[Dy^{3+}]$ = [Xe] $4f^9$).

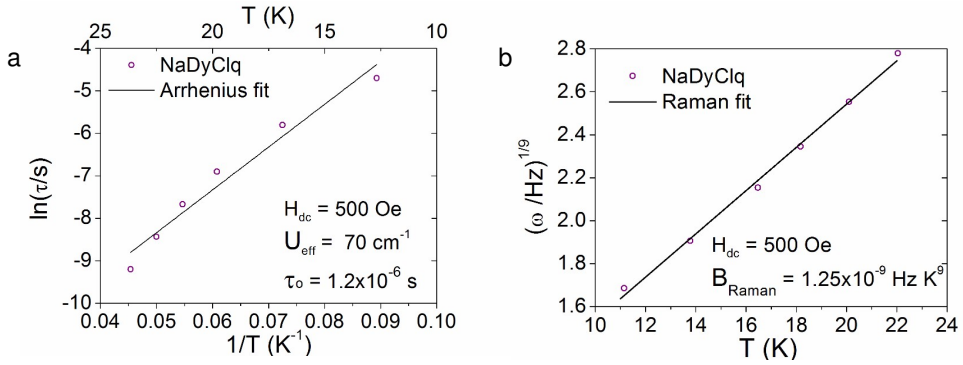

Figure 2.11 Arrhenius (a) and Raman (b) plots for the NaDyClq compound at H_{dc} = 500 Oe. The energy barrier and pre-exponential factor obtained from the Arrhenius fit are U_{eff} = 70 cm^{-1} and $\tau_0 = 1.2 \cdot 10^{-6}$ s. The Raman parameter B_{Raman} =$1.25 \cdot 10^{-9}$ Hz K^9. The Raman equation fits better to the experimental data.

$$\tau^{-1} = B_{Raman} T^{n_{Raman}} \tag{2.3}$$

Figures 2.11, A.1-4d and A.1-4e in Appendix A depict the experimental data tested as either a Raman or an Orbach mechanism hypothesis.[20] At first sight, the Raman linear fits seem to agree better with the experimental points in all cases. Contrary, the high temperature points in the Arrhenius plots locate below the linear fit, while the low temperature points locate above, which may indicate that the equation is not appropriate to the data. However, we evaluate the values of the coefficient of determination (R^2) obtained from the fits to both relaxation mechanisms as seen in Table 2.1 to dig deeper into this issue. The closer R^2 is to 1, the better the experimental data fits to the model. The Raman process fits better than the Orbach hypothesis in all cases, as seen in Table 2.1.

The energy barrier and Raman constant at zero dc field can be calculated by fitting linearly the dependence of U_{eff} and B_{Raman} with the applied dc field as seen in Figure 2.12. The extrapolation gives $U_{eff}(H_{dc}{=}0) = 60.1$ cm^{-1} and $B_{Raman}(H_{dc}{=}0) = 9.3 \cdot 10^{-10}$ Hz K^9.

H_{dc}(Oe)	R^2 (Raman)	R^2 (Orbach)
150	0.997	0.983
425	0.996	0.957
500	0.995	0.954
750	0.997	0.966
1000	0.996	0.985

Table 2.1 Coefficient of determination, R^2, of the fits to the Raman and Orbach terms showing a best fit for the Raman relaxation process for all dc fields.

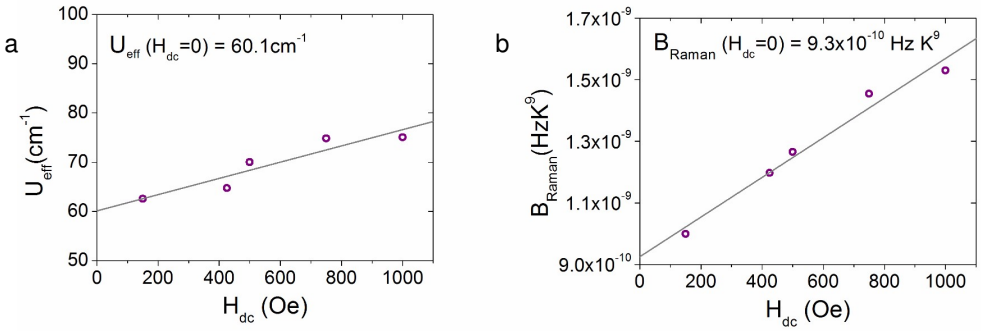

Figure 2.12 a) Extrapolation of the effective energy barrier (U_{eff} = 60.1 cm^{-1}) at zero dc magnetic field for bulk NaDyClq. b) Extrapolation of B_{Raman} at zero dc field of $B_{Raman} = 9.3 \cdot 10^{10}$ Hz K^9.

Furthermore, the energetic distance between the ground and first excited states hast been theoretically calculated in our group by means of the SIMPRE software.[21] The first excited state is found at 126 cm^{-1} and the effective energy barrier at zero dc field obtained through the Arrhenius fit amounts to 60.1 cm^{-1} (see Figure 2.12a). This value is much lower than the energy difference between the basal and first excited states, thus confirming that the relaxation mechanism must be related to a virtual level by means of a Raman-type relaxation mechanism.

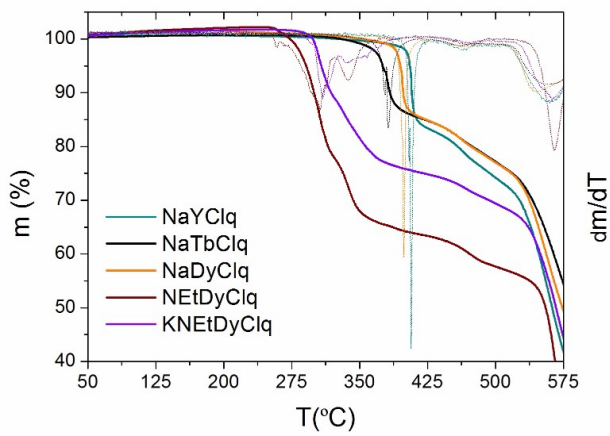

Figure 2.13 Thermogravimetric analysis of the compounds. The dashed lines magnify the changes of slope in m(T) since they are the derivatives dm/dT. Thermal stability is found for the Na-based compounds up to 400 ºC and up to 300 ºC in the case of NEtDyClq and KNEtDyClq.

2.2.3 Molecule Sublimation Study

Magnetic molecules based on coordination chemistry have not yet fulfilled their potential in molecular spintronics because most of them are extremely delicate and undergo redox reactions with metallic electrodes. Furthermore, they are not thermally stable and decompose when heated.

In very few cases these molecular complexes can be sublimated. Thus, a current focus of interest in molecular spintronics is that of depositing magnetic molecules on the appropriate substrates (ferromagnetic electrodes in particular) in order to study the properties of these hybrid interfaces. Besides, this constitutes the initial step towards the integration of these molecules in spintronic devices.[22–26]

Here we prepare films of the sublimable compounds described in the previous section. In a second step we use a combination of techniques to analyze which molecules maintain their structure upon sublimation. These techniques are: thermogravimetric analysis (TGA), energy-dispersive X-ray spectroscopy analysis (EDX),

infrared spectroscopy (IR), electrospray ionization mass spectrometry (ESI-MS) and matrix-assisted laser desorption/ionization time-of-flight (MALDI-TOF).

Thermogravimetric analysis enabled us to study the thermal stability of all compounds as seen in Figure 2.13. An abrupt change of slope in the TGA curves (highlighted by the corresponding derivative curves) might indicate a phase change while a smooth change of slope might point to decomposition. A quasi-vertical change of slope is observed for all the sodium compounds which also present higher thermal stability, above 350 °C. An abrupt change of slope is symptomatic of stability upon sublimation. However, this is a necessary but not a sufficient condition.

Thus, the five compounds were investigated with the use of a thermal evaporator (P_{base} = 10^{-6} mbar, $T_{sublimation}$ = [260, 340] °C). This resulted in the formation of yellowish solids. Subsequently, different techniques were used to compare the bulk compounds to the sublimated materials to discern which of them are suitable for their deposition as thin films.

		alkali / Ln		Cl / Ln	
		calc.	found	calc.	found
NaYClq	bulk	1	0.85	8	8.25
	film		0.81		8.01
NaTbClq	bulk	1	0.89	8	7.71
	film		0.91		7.64
NaDyClq	bulk	1	0.91	8	7.36
	film		0.94		7.57
NEtDyClq	bulk	-	-	8	7.23
	film		-		7.63
KNEtDyClq	bulk	0.5	0.38	16	17.28
	film		0.55		14.26

Table 2.2 Atomic ratios calculated and found from the EDX analysis in the bulk compounds and films, where alkali = Na, K and Ln = Y, Tb, Dy.

Firstly, the energy dispersive X-ray (EDX) analysis was performed. This technique allows to find the atomic proportions in a sample. Table 2.2 shows that Na/Ln, K/Ln and Cl/Ln proportions obtained by the EDX measurements are maintained in

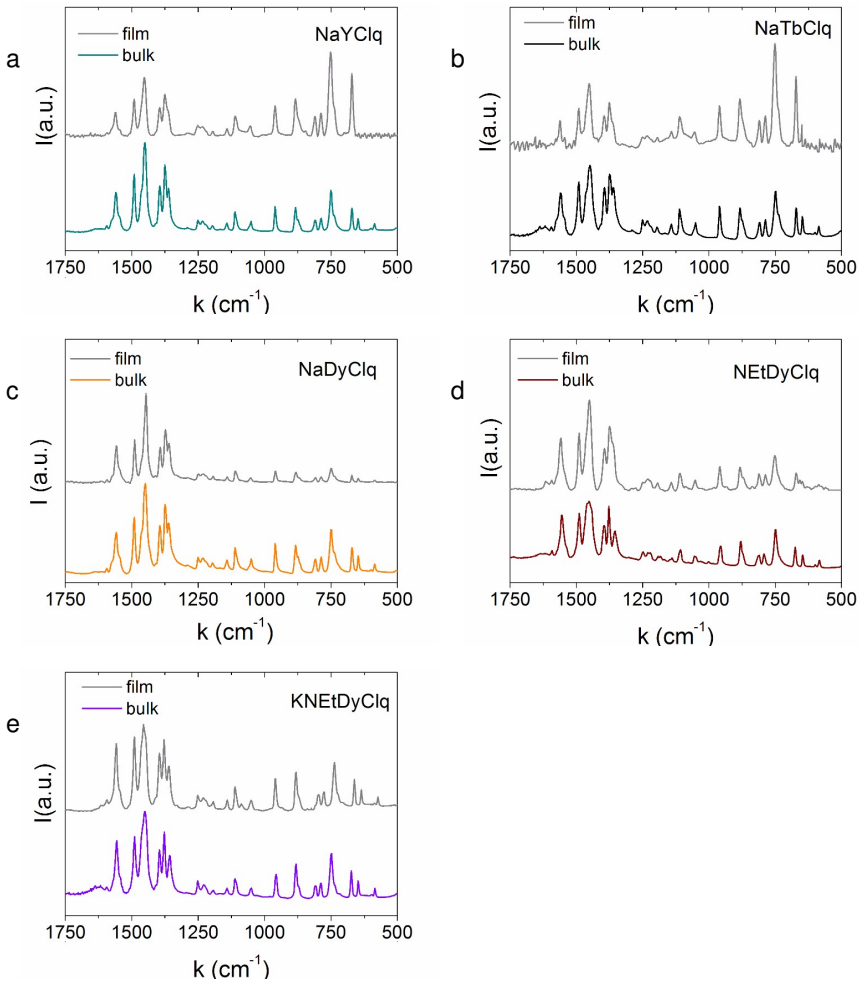

Figure 2.14 IR transmission spectra for the bulk compounds compared with the deposited films where the ligand vibrations can be detected. The range [1600, 1300] cm^{-1} corresponds to the C=N and C=C vibration frequencies (ring stretching) whereas C−O stretching is located at 1100 cm^{-1}.The range [958, 954] cm^{-1} is attributed to the C−Cl vibrations (see the text for details). Accordingly, all the sublimated materials retain the ligand structure upon evaporation.

all sublimated molecules except for the Cl/Dy ratio in the case of the KNEtDyClq film that is a bit lower than expected.

Then, the transmission IR spectra of the powdered compounds are compared with the films finding an excellent agreement in all cases (see Figure 2.14). The characteristic vibration modes of the molecules are in the range [1700, 500] cm^{-1}. The bands in the range [1600, 1300] cm^{-1} are mainly attributed to C=N and C=C vibration frequencies (ring stretching) while the band at 1100 cm^{-1} is related to the C−O stretching.[27] The C−Cl vibration locates in the range [958, 954] cm^{-1}. Thus, the IR spectroscopy has allowed us to verify that the ligand is intact after the sublimation process, as expected since the ligand is a precursor in the synthesis of all compounds.

Subsequently, we compare bulk materials to films by means of mass spectrometry, in particular electrospray ionization mass spectrometry (ESI-MS) and matrix-assisted laser desorption-ionization time of flight (MALDI-TOF) techniques. Both ESI-MS and MALDI-TOF belong to the known as soft-ionization techniques and allow the identification of the charged species of a compound. ESI-MS can be used to analyze powdered compounds but not films. Contrary, MALDI-TOF uses a laser to ionize molecules on a surface and thus, it is suitable for films.

Electrospray ionization mass spectrometry has been performed for all bulk compounds to check the quality of the synthesis. For the five cases the main signal corresponds to the relation mass/charge (m/z) of the anionic molecule: $[Dy[(5,7Cl_2q)_4]]^-$. On the right hand side of Figure 2.15 the pattern of the main signal is compared to the theoretical pattern, matching in all cases. The secondary signals are attributed to fragmentations of the molecules caused by the technique itself.

Contrary, in the case of the MALDI-TOF measurements of the films, the pattern appears for all layers except for KNEtDyClq and NEtDyClq as shown in Figure 2.16. The absence of the correct pattern in the MALDI-TOF spectra for NEtDyClq and KNEtDyClq films reveals that they are not suitable for film formation.

The different sublimation ability experimentally observed in these compounds

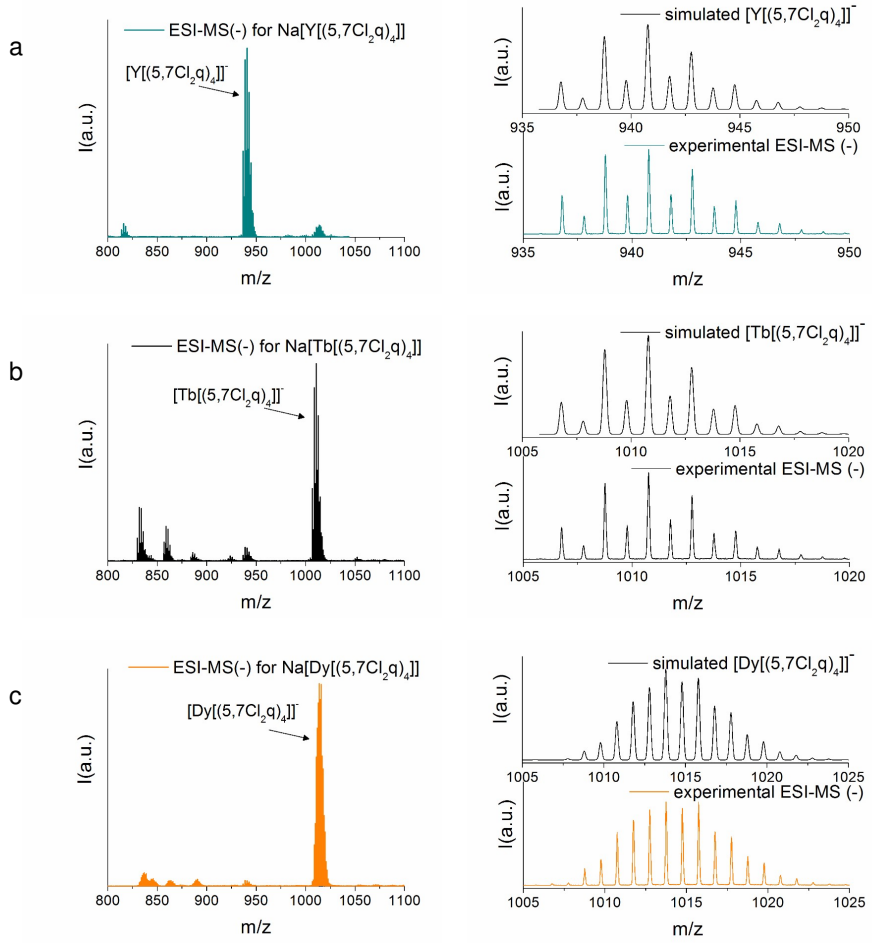

Figure 2.15 Electrospray ionization mass spectrometry (ESI-MS) for the bulk compounds in negative mode. a) NaYClq. b) NaTbClq. c) NaDyClq. The main signals are highlighted with arrows. The secondary signals are attributed to fragmentations of the molecules caused by the technique.

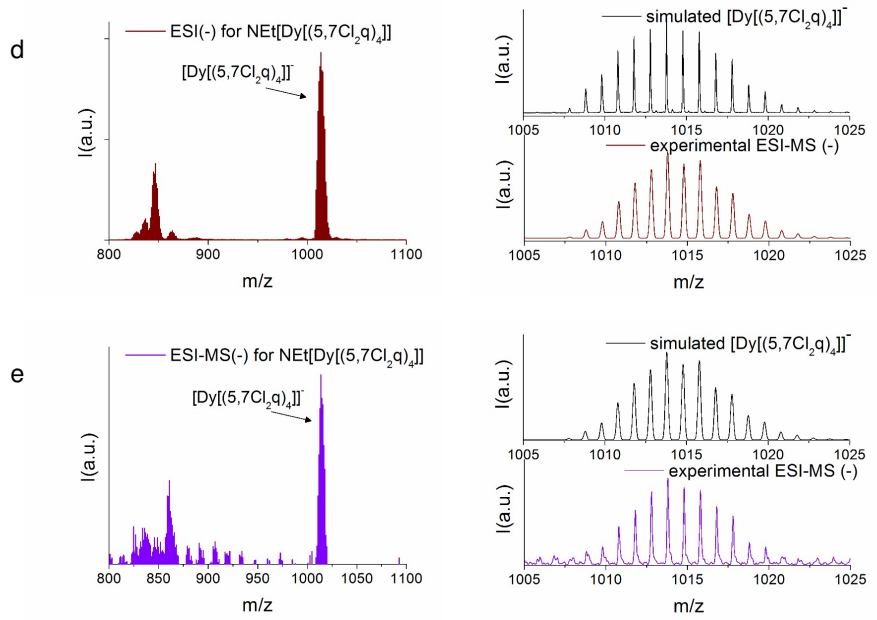

Figure 2.15 (continuation) Electrospray ionization mass spectrometry (ESI-MS) for the bulk compounds in negative mode. d) NEtDyClq. e) KNEtDyClq.

can be rationalized by close inspection of the molecular structures. In NaLnClq compounds, the sodium cation is tightly bound (tridentate oxygen coordination) to the $[Ln(Cl_2q)_4]^-$ anion, thus yielding a neutral molecule that can sublime as a whole entity (see the molecular structure illustrated in Figure 2.3). On the contrary, both NEtDyClq and KNEtDyClq are formed by charged species, which might be the cause of their inability to sublime. In the case of NEtDyClq, the organic cation NEt^{4+} is only very weakly bound to the $[Ln(Cl_2q)_4]^-$ anion, meaning they cannot easily sublime together. For KNEtDyClq, we do find a tightly bound K^+ cation, again with tridentate oxygen coordination, but it is equally shared between two $[Ln(Cl_2q)_4]^-$ moieties. This results in a large (supra)molecular anion which is again only very weakly bound to its neighboring $NEt_4{}^+$ cation.

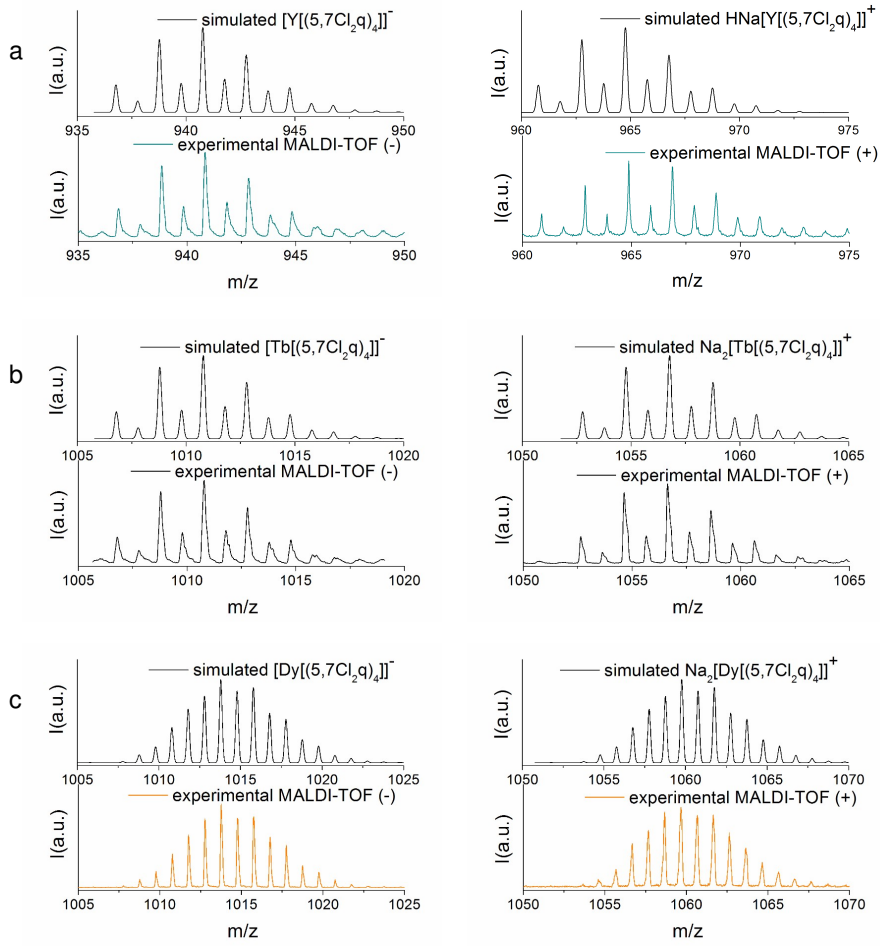

Figure 2.16 MALDI-TOF in negative and positive modes for films of a) NaYClq, b) NaTbClq and c) NaDyClq. The experimental pattern was not found for films of NEt-DyClq and KNEtDyClq.

2.2.4 Magnetic Properties of the Films

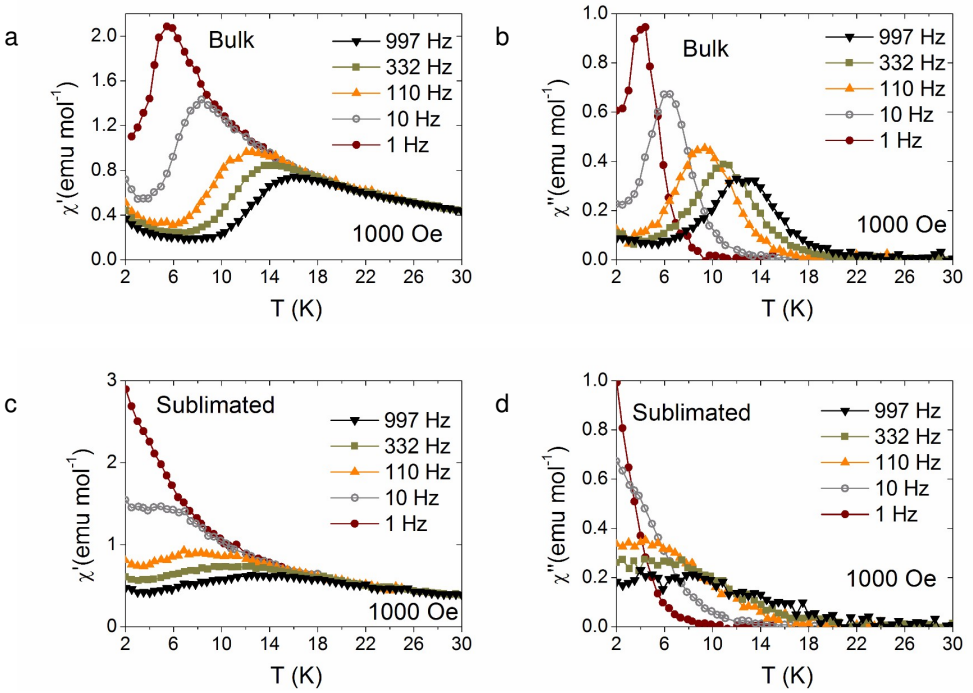

Figure 2.17 Comparison of the ac magnetic measurements for NaDyClq as bulk and as film showing the preservation of the slow relaxation of the magnetization at $H_{dc} = 1000$ Oe. a) Frequency dependence of the in phase and b) out of phase magnetic susceptibilities of the bulk compound at 1000 Oe external dc field. c) χ' and d) χ'' of the NaDyClq film.

The multi-technique process of the last section indicates that only the Na-based films maintain the molecular integrity upon sublimation. Among them, only NaDyClq exhibits SMM behavior and a high blocking temperature enabling the comparison between the ac magnetometry of the bulk material and the film. Figure 2.17 shows the ac measurements for bulk and sublimated NaDyClq measured by SQUID magnetometry performed in a external magnetic field of 1000 Oe. We notice that the slow relaxation of the magnetization is also preserved in the film. Still, the maxima

in χ'' are shifted towards lower temperatures in the film indicating that the barrier is slightly reduced.[28]

2.2.5 Deposition of the Magnetic Molecules on FM Substrates

The NaDyClq and NaYClq compounds have been evaporated on different substrates. The morphology of the films has been studied by means of atomic force microscopy (AFM). Figure 2.18 shows the images of bilayers of NiFe (8 nm) / NaYClq (10 nm), NiFe (8 nm) / NaDyClq (10 nm) and Co (10 nm) / NaDyClq (15 nm) on Si-SiO_2. The topography images show good coverage in all cases. Both NaDyClq and NaYClq show low peak to peak and RMS roughness for the films of 10 nm on NiFe (ρ_{ptp}(NaDyClq) = 2.93 nm and ρ_{RMS}(NaDyClq) = 0.32 nm whereas ρ_{ptp}(NaYClq) = 3.79 nm and ρ_{RMS}(NaYClq) = 0.39 nm). Besides, the surfaces are grain structured and uniform. For a thicker NaDyClq the surface is smoother and less grain structured, the ρ_{RMS} is still very low despite the appearance of aggregations that increase the ρ_{ptp} considerably. These very low roughness values below 1 nm make these molecules potential materials to be included in multilayered devices.

The magnetic properties of the bilayers have been studied by SQUID magnetometry. Figure 2.19 depicts the field cooled (FC) and zero-field cooled (ZFC) curves for the bilayers Al_2O_3 (1.5 nm) / NaTbClq (10 nm) and Au (10 nm) / NaDyClq (10 nm). In the FC curve, the sample is cooled in an external field of 500 Oe and then measured while warming it up in a small field of 50 Oe. The individual magnetic moments go from a disordered state (canceling each other out over the sample) to being aligned in a common direction (parallel to the field) as temperature decreases so that the magnetization (M) measured increases. Meanwhile, in the ZFC curve, the sample is cooled down in the absence of a magnetic field. Then the bilayer is warmed up while measured also in a small field of 50 Oe. The thermal dependence of the magnetization resembles the paramagnetic behavior of the bilayers.

The behavior of the bilayers changes when the molecular layer is grown on NiFe

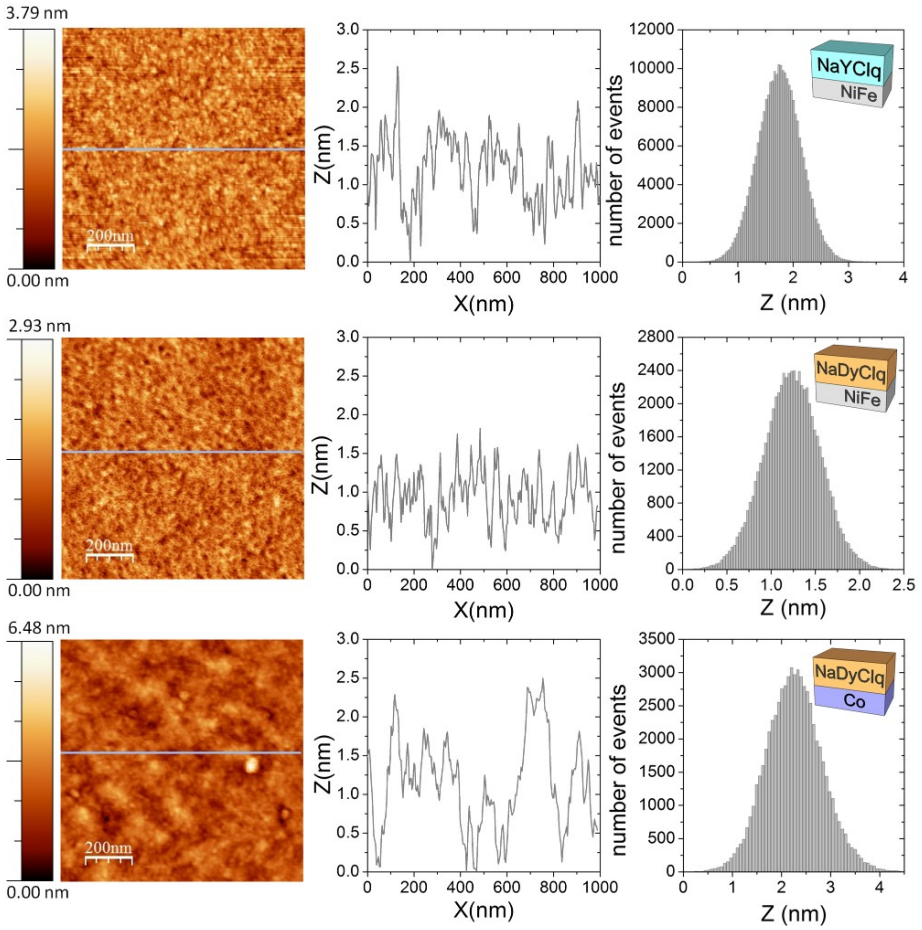

Figure 2.18 AFM topography images, profiles at medium high and histograms of the bilayers: NiFe (8 nm) / NaYClq (10 nm) on top panel (ρ_{RMS} = 0.39 nm and ρ_{ptp} = 3.79 nm), NiFe (8 nm) / NaDyClq (10 nm) in the central panel (ρ_{RMS} = 0.32 nm and ρ_{ptp} = 2.93 nm) and Co (10 nm) / NaDyClq (15 nm) on the bottom panel (ρ_{RMS} = 0.58 nm and ρ_{ptp} = 6.48 nm). All of them are grown on Si-SiO_2 substrates with initial RMS roughness $\approx$ 0.5 nm. All the layers show very low RMS roughnesses below 1 nm . NaDyClq shows lower peak to peak and RMS roughness than the NaYClq which may indicate a better molecular packing.

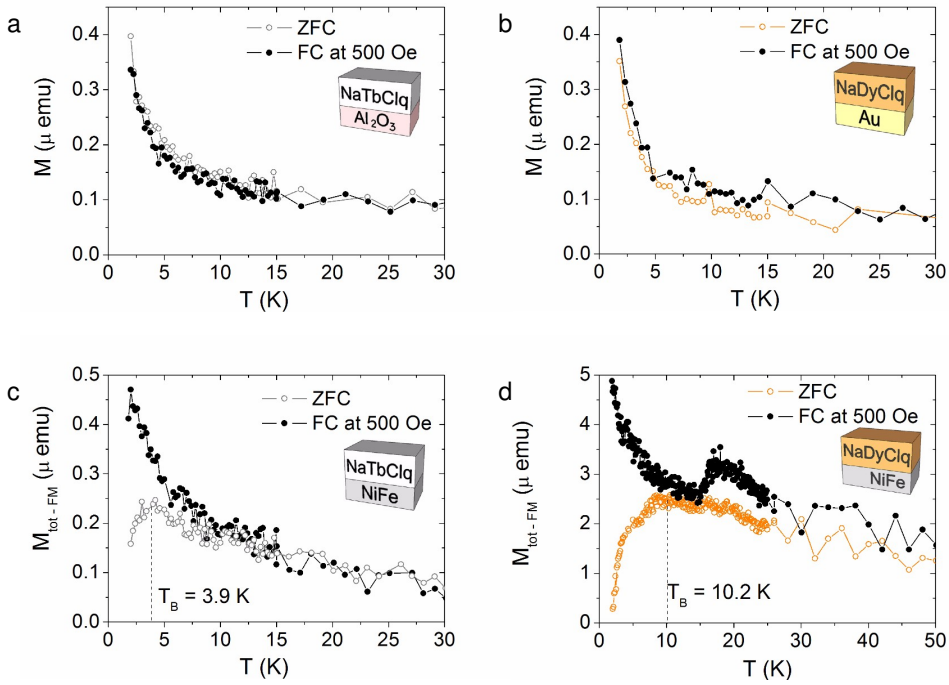

Figure 2.19 Thermal dependence of the magnetization. a) 10 nm of NaTbClq grown on 1.5 nm of Al_2O_3. b) 10 nm of NaDyClq grown on 10 nm of Au. c) 10 nm of NaTbClq grown on 10 nm of NiFe. d) 10 nm of NaDyClq grown on 10 nm of NiFe.

as seen in Figure 2.19. A cusp appears at low temperature in the zero-field cooled scan indicating the presence of an energy barrier. When increasing temperature, and increase in the magnetization is measured, going from blocked to paramagnetic behavior, being able to align with the small external field. As temperature is further increased, the random fluctuations from thermal energy begin to dominate and the spins become randomly oriented once again. The magnetic blocking behavior is probably due to an activation of the single molecule magnet behavior induced by the NiFe substrate or as a result of the interface coupling between the ferromagnet and the paramagnetic Tb / Dy spins. The blocking temperatures amount to 3.9 K (NaTbClq / NiFe) and 10.2 K (NaDyClq / NiFe). There is a second feature in the

field-cooled scan around around 20 K in the NaDyClq / NiFe curve, which implies a change in the susceptibility and which can be an indication of an antiferromagnetic phase created at the hybrid interface.

2.3 Conclusions and Perspectives

In this chapter we have studied the magnetic properties of the single ion magnets NaDyClq, NaTbClq, NEtDyClq and KNEtDyClq. Among them, the NaDyClq compound has shown a high blocking temperature, which has allowed us to study its spin relaxation mechanisms. We have understood by means of Cole-Cole plots that the system relaxes through a Raman-type mechanism.

However, the main objective of the chapter was to study the potential of the molecular family members to be incorporated in molecular spintronic devices. Through various experimental techniques, we have been able to conclude that the Na derivatives preserve intact their molecular structure upon sublimation and therefore they are suitable for deposition as thin films to be included in heterostructures. In these cases, the TGA analysis showed a vertical drop while EDX pointed out that sublimated materials preserved the alkali:Cl:lanthanide ratios. The IR spectra demonstrated that the ligands remained intact in all films. The definitive proof has been the MALDI-TOF spectra where the molecular pattern can be observed only for the Na-based films. Accordingly, the NaDyClq films maintained a SIM behavior with an out-of-phase magnetic susceptibility dependence on the frequency.

Finally, the magnetic molecules have been deposited on different substrates, studied by atomic force microscopy and analyzed by SQUID magnetometry. The influence of the ferromagnetic substrates on the magnetic molecules has been observed by a magnetic blocking at low temperature as indicator of an energy barrier.

The conclusion is that, Na-based compounds are suitable to be included in spintronic devices, which will become the main topic of next chapter.

2.4 Experimental Details

All materials and reagents were purchased from Sigma-Aldrich and used as received, except for the ligand 5,7-dichloro-8-hydroxyquinoline ($5,7Cl_2q$) which was recrystallized in chloroform.

The synthesis of $Na[Ln(5,7Cl_2q)_4]$ (where $Ln = Tb^{III}$, Dy^{III}, Y^{III}) was performed as follows: 856 mg (4 mmol) of $5,7Cl_2q$ were dissolved in 80 ml of absolute ethanol at 50 ℃. A solution of 160 mg of NaOH (4 mmol) dissolved in 40 ml of absolute ethanol at 50 ℃ was added. Then, a solution of hot absolute ethanol (50 ℃) containing $LnCl_3 \cdot 6H_2O$ (0.6 mmol) was added drop-wise and kept under stirring at 50 ℃ during 1 hour and then cooled down to room temperature. The yellow precipitate was filtered on a sintered-glass filter and washed with milli-Q water and 10 ml of a cold mixture of 1:1 EtOH:H_2O. Phase purity was established by X-ray powder diffraction.

$NEt_4[Dy(5,7Cl_2q)_4]$ was synthesized in the following way: 856 mg (4 mmol) of $5,7Cl_2q$ and 662 mg (4 mmol) of NEt_4Cl were dissolved in 80 ml of absolute ethanol at 50 ℃ under stirring. 556 ml (4 mmol) of Et_3N were added. Then, a solution of hot absolute ethanol (50 ℃) containing $DyCl_3 \cdot 6H_2O$ (0.6 mmol) was added drop-wise and kept under stirring at 50 ℃ during 1 hour and then cooled to room temperature. The yellow precipitate was filtered on a sintered-glass filter and washed with milli-Q water and 10 ml of a cold mixture of 1:1 EtOH:milli-Q water.

The synthesis of $K_{0.5}(NEt_4)_{0.5}[Dy(5,7Cl_2q)_4]$ was made as follows: 856 mg (4 mmol) of $5,7Cl_2q$, 331 mg (2 mmol) of NEt_4Cl and 200 mg (2 mmol) of KNO_3 were dissolved in 80 ml of absolute ethanol at 50 ℃ under stirring. 556 ml (4 mmol) of Et_3N were added. Then, a solution of hot absolute ethanol (50 ℃) containing $DyCl_3 \cdot 6H_2O$ (0.6 mmol) was added drop-wise and kept under stirring at 50 ℃ during 1 hour and then cooled to room temperature. The yellow precipitate was filtered on a sintered-glass filter and then washed with milli-Q water and 10 ml of a cold mixture of 1:1 EtOH:H_2O. Phase purity was established by X-ray powder diffraction.

	formula	molecular weight (g/mol)
NaYClq	$C_{36}H_{16}O_4N_4Cl_8YNa$	964.06
NaTbClq	$C_{36}H_{16}O_4N_4Cl_8TbNa$	1034.08
NaDyClq	$C_{36}H_{16}O_4N_4Cl_8DyNa$	1037.65
NEtDyClq	$C_{44}H_{36}O_4N_5Cl_8Dy$	1144.91
KNEtDyClq	$C_{80}H_{52}O_8N_9Cl_{16}Dy_2K$	2198.67

Table 2.3 Formula and molecular weight of the compounds.

The thermogravimetric analysis were performed using a thermal analyzer model Mettler Toledo TGA/SDTA 851e that operates in the range [25, 1100] ℃ and has a sensibility of 0.1 μg.

The Energy-dispersive X-ray spectroscopy was measured with a FEI/Philips XL-30 Field Emission ESEM for the five powdered compounds.

The infrared spectra of the powdered compounds and layers were recorded in transmission mode in a Nicolet 5700 FT-IR spectrometer.

Electrospray ionization mass spectrometry was analyzed with a Waters Micromass ZQ spectrometer. The isotopic patterns were analyzed using the mMass software. The films of Na[Ln(5,7Cl_2q)$_4$] were analyzed in a 5800 MALDI TOF/TOF (AB-Sciex) in negative (and positive) reflection mode (3000 shots every position) in a mass range of [800, 5500] m/z where no matrix was used.

The magnetic measurements were performed in a Quantum Design Physical Property Measurement System (PPMS) in the frequency range [10, 9910] Hz and in a Quantum Design MPMS XL-5 SQUID magnetometer operating in the frequency range [0.1, 1] KHz. The AC susceptibility magnetic measurements were performed at different frequencies under a oscillating eld of amplitude 3.95 Oe.

Prior to metal and molecule layers deposition the $Si-SiO_2$ substrates were cleaned with ethanol. The Na[Ln(5,7Cl_2q)$_4$] (Ln=Tb, Dy)/metal hybrid layers were fabricated in a dual-chamber evaporator (P_{base} = 10^{-10} mbar). The metallic layers (NiFe, Co) were deposited via e-beam evaporation, while the molecular layers were sublimated

thermally from conventional effusion cells, at evaporation temperatures ranging between [260, 340] ℃. Many NaDyClq films deposited on glass were scratched in order to have enough mass to measure it in the SQUID magnetometer. In the bilayer cases, the metallic layer thickness was set to [8, 10] nm, and the NaLnClq molecular layer thickness has been varied between 10 and 15 nm.

The surface topographies were imaged using an Atomic Force Microscopes Agilent 5500, operating in tapping mode with a tip frequency of 342 kHz. Cantilevers were from silicon, with a spring constant of 40 Nm^{-1}. The image area amounts to 1 μm x 1 μm.

The magnetic properties of the hybrid layers have been characterized in a state-of-the-art SQUID magnetometer (Quantum Design MPMS), with a sensitivity of 5 x 10^{-8} emu. The SQUID measurements were performed at Cic-Nanogune in close collaboration with A. Bedoya and L. Hueso.

2.5 Bibliography

[1] G. A. Craig and M. Murrie. “3d single-ion magnets”. Chemical Society Reviews 44.8 (2015), pp. 2135–2147.

[2] O. Kahn. Molecular magnetism. 1993.

[3] D. Gatteschi, R. Sessoli, and J. Villain. Molecular nanomagnets. Vol. 5. Oxford University Press, 2006.

[4] H. L. Feltham and S. Brooker. “Review of purely 4f and mixed-metal nd-4f single-molecule magnets containing only one lanthanide ion”. Coordination Chemistry Reviews 276 (2014), pp. 1–33.

[5] L. Bogani and W. Wernsdorfer. “Molecular spintronics using single-molecule magnets”. Nature Materials 7.3 (2008), pp. 179–186.

[6] V. Dediu, L. Hueso, I. Bergenti, A. Riminucci, F. Borgatti, P. Graziosi, C. Newby, F. Casoli, M. De Jong, C. Taliani, et al. “Room-temperature spintronic effects in Alq_3-based hybrid devices”. Physical Review B 78.11 (2008), p. 115203.

[7] S. Sanvito. “Molecular spintronics: The rise of spinterface science”. Nature Physics 6.8 (2010), pp. 562–564.

[8] Z. Xiong, D. Wu, Z. V. Vardeny, and J. Shi. “Giant magnetoresistance in organic spin-valves”. Nature 427.6977 (2004), pp. 821–824.

[9] D. Garbuzov, V. Bulovi, P. Burrows, and S. Forrest. “Photoluminescence efficiency and absorption of aluminum-tris-quinolate (Alq_3) thin films”. Chemical Physics Letters 249.5-6 (1996), pp. 433–437.

[10] V. Bulovi, V. Khalfin, G. Gu, P. Burrows, D. Garbuzov, and S. Forrest. “Weak microcavity effects in organic light-emitting devices”. Physical Review B 58.7 (1998), p. 3730.

[11] M. D. Halls and H. B. Schlegel. “Molecular orbital study of the first excited state of the OLED material tris (8-hydroxyquinoline) aluminum (III)”. Chemistry of materials 13.8 (2001), pp. 2632–2640.

[12] Q. Song, F. Li, H. Yang, H. Wu, X. Wang, W. Zhou, J. Zhao, X. Ding, C. Huang, and X. Hou. “Small-molecule organic solar cells with improved stability”. Chemical Physics Letters 416.1 (2005), pp. 42–46.

[13] P. Peumans, A. Yakimov, and S. R. Forrest. “Small molecular weight organic thin-film photodetectors and solar cells”. Journal of Applied Physics 93.7 (2003), pp. 3693–3723.

[14] F. Cicoira and C. Santato. “Organic light emitting field effect transistors: advances and perspectives”. Advanced Functional Materials 17.17 (2007), 342-1–3434.

[15] N. F. Chilton, G. B. Deacon, O. Gazukin, P. C. Junk, B. Kersting, S. K. Langley, B. Moubaraki, K. S. Murray, F. Schleife, M. Shome, et al. “Structure, magnetic behavior, and anisotropy of homoleptic trinuclear lanthanoid 8-quinolinolate complexes”. Inorganic chemistry 53.5 (2014), pp. 2528–2534.

[16] A. Bedoya-Pinto, H. Prima-García, F. Casanova, E. Coronado, and L. E. Hueso. “Spin-polarized hopping transport in magnetically tunable rare-earth quinolines”. Advanced Electronic Materials 1.6 (2015).

[17] C. Benelli and D. Gatteschi. Introduction to molecular magnetism: From transition metals to lanthanides. John Wiley & Sons, 2015.

[18] R. J. Blagg, L. Ungur, F. Tuna, J. Speak, P. Comar, D. Collison, W. Wernsdorfer, E. J. McInnes, L. F. Chibotaru, and R. E. Winpenny. “Magnetic relaxation pathways in lanthanide single-molecule magnets”. Nature Chemistry 5.8 (2013), pp. 673–678.

[19] M. Gonidec, R. Biagi, V. Corradini, F. Moro, V. De Renzi, U. del Pennino, D. Summa, L. Muccioli, C. Zannoni, D. B. Amabilino, et al. “Surface supramolecular organization of a terbium (III) double-decker complex on graphite and its single molecule magnet behavior”. Journal of the American Chemical Society 133.17 (2011), pp. 6603–6612.

[20] S. Gómez-Coca, A. Urtizberea, E. Cremades, P. J. Alonso, A. Camón, E. Ruiz, and F. Luis. “Origin of slow magnetic relaxation in Kramers ions with non-uniaxial anisotropy”. Nature Communications 5 (2014).

[21] J. J. Baldoví, S. Cardona-Serra, J. M. Clemente-Juan, E. Coronado, A. Gaita-Ariño, and A. Palii. “SIMPRE: A software package to calculate crystal field parameters, energy levels, and magnetic properties on mononuclear lanthanoid complexes based on charge distributions”. Journal of Computational Chemistry 34.22 (2013), pp. 1961–1967.

[22] L. Malavolti, L. Poggini, L. Margheriti, D. Chiappe, P. Graziosi, B. Cortigiani, V. Lanzilotto, F. B. de Mongeot, P. Ohresser, E. Otero, et al. “Magnetism of TbPc 2 SMMs on ferromagnetic electrodes used in organic spintronics”. Chemical Communications 49.98 (2013), pp. 11506–11508.

[23] L. Malavolti, V. Lanzilotto, S. Ninova, L. Poggini, I. Cimatti, B. Cortigiani, L. Margheriti, D. Chiappe, E. Otero, P. Sainctavit, F. Totti, A. Cornia, M. Mannini, and R. Sessoli. “Magnetic bistability in a submonolayer of sublimated Fe 4 single-molecule magnets”. Nano Letters 15.1 (2015), pp. 535–541.

[24] D. Klar, A. Candini, L. Joly, S. Klyatskaya, B. Krumme, P. Ohresser, J.-P. Kappler, M. Ruben, and H. Wende. “Hysteretic behaviour in a vacuum deposited submonolayer of single ion magnets”. Dalton Transactions 43.28 (2014), 106-86–10689.

[25] A. Cornia, M. Mannini, P. Sainctavit, and R. Sessoli. “Chemical strategies and characterization tools for the organization of single molecule magnets on surfaces”. Chemical Society Reviews 40.6 (2011), pp. 3076–3091.

[26] E. Kiefl, M. Mannini, K. Bernot, X. Yi, A. Amato, T. Leviant, A. Magnani, T. Prokscha, A. Suter, R. Sessoli, et al. “Robust magnetic properties of a sublimable single-molecule magnet”. ACS Nano 10.6 (2016), pp. 5663–5669.

[27] H. Aly, F. A. Kerim, and A. Kandil. “IR spectra of lanthanide 8-hydroxyquinoline complexes”. Journal of Inorganic and Nuclear Chemistry 33.12 (1971), pp. 4340–4344.

[28] J. Dreiser. “Molecular lanthanide single-ion magnets: from bulk to submonolayers”. Journal of Physics: Condensed Matter 27.18 (2015), p. 183203.

3

Molecular Spin Valves Based on Chloroquinolines: Negative MR

3.1 Introduction

As pointed in chapter one, the molecular spin valve or MSV[1,2] is the prototype device in molecular spintronics. The device consists of two ferromagnetic electrodes with different coercive fields and an intermediate molecular layer that transports the spin polarized current between electrodes while decouples them magnetically. Thus, the resistance of the MSV shows two states, high and low, depending on the relative magnetic orientation of the electrodes which is known as giant magnetoresistance (GMR) or, straightforwardly, magnetoresistance (MR).

Tremendous progress has been reached in studying and understanding the underlying physics of these devices since the first MSV was reported.[3,4] The molecular compounds studied as spin collector layers provided flexibility, chemical tunability,

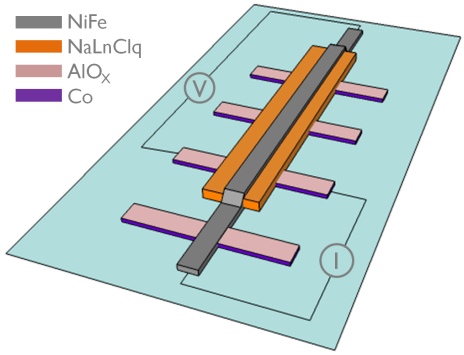

Figure 3.1 Sketch of half chip with three molecular junctions and one reference junction that does not contain NaLnClq. The contacts are drawn in a four-probe configuration.

cost efficiency and new phenomena.[5,6] The first molecular compound studied in a MSV was sexithienyl (T_6).[3] It was included in a lateral spin valve formed by LSMO / T_6 / LSMO that showed MR at room temperature which was attributed to the spin polarized current injection from the LSMO electrode into the organic.

Since then, a vast amount of molecular compounds and polymers has been studied, such as fullerene,[7] bathocuproine,[8] graphene,[9] or P3HT.[10] However, among all, the most popular has been Alq_3.[4,11–13] Although it was incorporated to the molecular spintronics field only a few years ago, this quinoline-based compound is an old acquaintance in optoelectronics.[14]

In this chapter we consider two types of MSVs assembled with two out of the three sublimable molecular compounds studied in chapter two. Both are morphologically very similar to Alq_3: the Na[Dy(5,7-dichloro-8-hydroxiquinolate)] or NaDyClq which behaves as single ion magnet[15] and the Na[Y(5,7-dichloro-8-hydroxiquinolate)] or NaYClq which, as Alq_3, is diamagnetic.

Here the initial idea is to compare both types of devices (NaDyClq-based and NaYClq-based) in terms of spin transport. As a matter of principle, if the elevated magnetic moment of the NaDyClq molecule was polarized in the presence of the fer-

romagnetic electrodes, the spin injection would be affected, whereas no interaction was expected in the case of the diamagnetic molecule. This could lead to significant differences in the measured MR. However, it should be taken into account that HOMO and LUMO of quinoline-based compounds are usually located spatially in the ligands,[16] far from the central atom, and consequently the spin transport might be unaffected by the magnetism of these particular layers.

3.2 Results and Discussion

3.2.1 Design of the Molecular Spin Valves

The MSVs were assembled using NaLnClq (where Ln = Dy or Y) molecules as spin collector layers and cobalt and permalloy as bottom and top ferromagnetic electrodes respectively. Besides, while NiFe is in direct contact with the molecular layer, a thin barrier of partially oxidized aluminum (AlO_x or leaky barrier) is placed between the molecular material and the Co electrode. The molecular spin valves stack order is:

Co / AlO_x / NaLnClq / NiFe

The use of barriers is a common tool in the design of molecular spin valves,[8] being the most studied barrier in molecular spintronics the alumina barrier which consists on a completely oxidized aluminum layer (Al_2O_3).[11,13,17] This insulating barrier reduces the probability of short circuit but at the same time it contributes considerably to the overall resistance of the junction.[5] In terms of charge transport, one basic disadvantage of the use of the alumina is that it is not easy to distinguish whether carriers are traveling in the molecular material or tunneling between electrodes. In both cases, and due to the insulating character of Al_2O_3, the resistance of the device is high ($\sim M\Omega$). To circumvent this problem, we use a leaky barrier, produced by oxidizing Al in a controlled manner (see the experimental section for a detailed

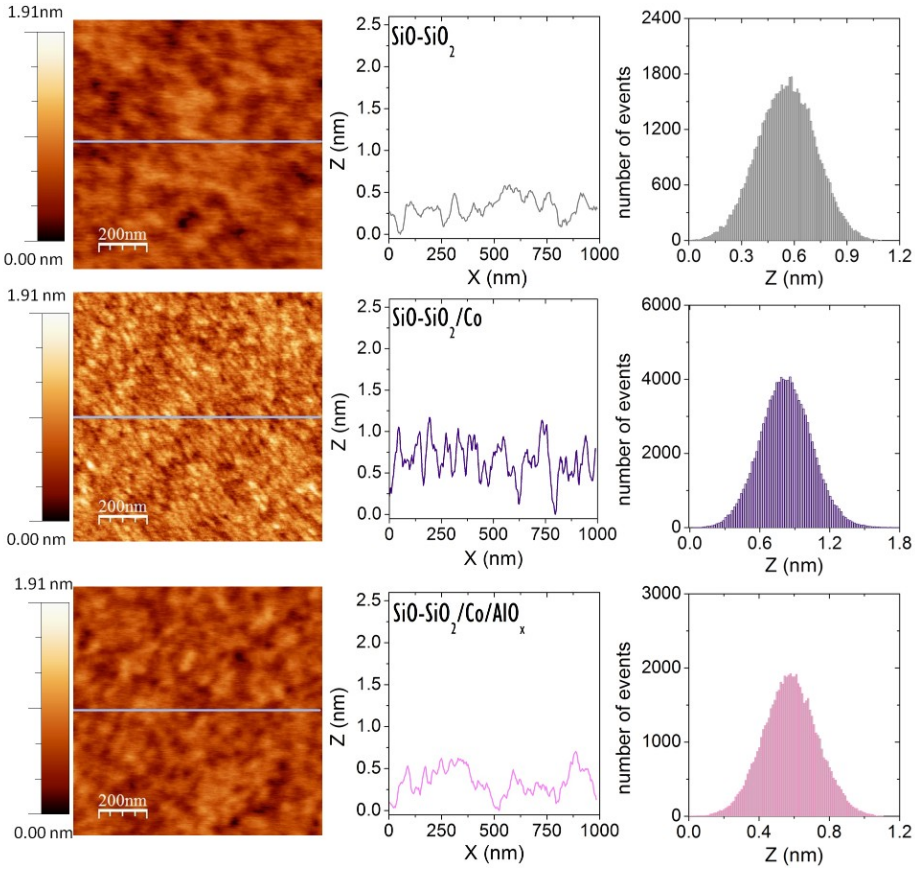

Figure 3.2 AFM topography images, profiles and histograms of $Si-SiO_2$ substrate (top panel), 15 nm of Co evaporated on the $Si-SiO_2$ substrate (central panel) and 1 nm of AlO_X evaporated on the $Si\text{-}SiO_2/Co$ layers (bottom panel). The leaky barrier shows a similar morphology to the $Si-SiO_2$ substrate.

description). This kind of partially oxidized Al barrier has been used before in some works providing excellent results.[7,8]

The morphology of the leaky barrier was characterized by means of atomic force microscopy (AFM). Figure 3.2 shows the images of 1 μm x 1 μm scan size acquired in tapping mode for the $SiO-SiO_2$ substrate (top panel), 15 nm of Co evaporated on the substrate (medium panel) and 1 nm of AlO_X deposited on $Si-SiO_2$ / Co (bottom panel). The profiles at a medium height (gray lines) are shown in the center and the histograms on the right of the figure show the distribution of heights. The peak to peak roughness and the RMS values are:

$$\rho_{RMS}(Si-SiO_2) = 0.16 \text{ nm}$$
$$\rho_{RMS}(Si-SiO_2 \text{ / Co}) = 0.22 \text{ nm}$$
$$\rho_{RMS}(Si-SiO_2 \text{ / Co / } AlO_x) = 0.15 \text{ nm}$$
$$\rho_{ptp}(Si-SiO_2) = 1.10 \text{ nm}$$
$$\rho_{ptp}(Si-SiO_2 \text{ / Co}) = 1.91 \text{ nm}$$
$$\rho_{ptp}(Si-SiO_2 \text{ / Co / } AlO_x) = 1.11 \text{ nm}$$

In general, all the layers show very low roughness values. The RMS roughness is similar for the $Si-SiO_2$ substrate and the leaky barrier. Moreover, the morphology of both is comparable and distinct from the morphology of the cobalt layer. Consequently, the leaky barrier may be favoring the growth of the organic layer as the surface is smoother and not grain structured. However, we should note that the AFM images were recorded in air atmosphere and that the oxidation of AlO_x might have changed the topography.

On each $Si-SiO_2$ chip, eight junctions are assembled and one of them does not include a molecular layer and serves as reference junction (see the illustration of half chip in Figure 3.1). This is achieved through management of shadow masks in the evaporation process. In every chip, we verify that the reference junction (Co / AlO_x / NiFe) shows very low resistance and a metallic behavior, as shown in Figure 3.3, what ensures that the aluminum barrier is not completely oxidized.

The AFM study of the molecular layers in the devices with thicknesses $Si-SiO_2$

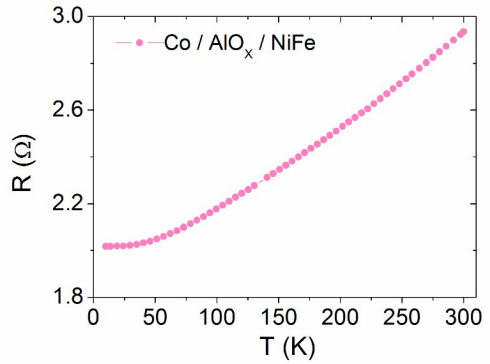

Figure 3.3 Resistance dependence on temperature of the reference junction Co / AlO_X (lb) / NiFe showing a metallic behavior.

(substrate) / Co (15 nm) / AlO_x (1 nm) / NaYClq (15 nm) / NiFe (15 nm) and Si-SiO_2 (substrate) / Co (15 nm) / AlO_x (1 nm) / NaDyClq (15 nm) / NiFe (15 nm) is shown in Figure 3.4. The imaging is possible because the different layers are accessible to the AFM tip in some regions of the substrate. The RMS roughness show low values and both molecular layers exhibit high quality in terms of smooth surface. The average height for the NaDyClq layer is 1 nm while for the NaYClq image it is 3.5 nm as shown in the histograms on the right of the figure.

$$\rho_{\text{RMS}}(\text{Si}-\text{SiO}_2 \text{ / Co / AlO}_x \text{ / NaDyClq}) = 0.29 \text{ nm}$$
$$\rho_{\text{RMS}}(\text{Si}-\text{SiO}_2 \text{ / Co / AlO}_x \text{ / NaYClq}) = 0.58 \text{ nm}$$
$$\rho_{\text{ptp}}(\text{Si}-\text{SiO}_2 \text{ / Co / AlO}_x \text{ / NaDyClq}) = 3.18 \text{ nm}$$
$$\rho_{\text{ptp}}(\text{Si}-\text{SiO}_2 \text{ / Co / AlO}_x \text{ / NaYClq}) = 4.69 \text{ nm}$$

The AFM analysis predicts that the NaYClq layers will need to be thicker than the NaDyClq layers to avoid short-circuited junctions. This fact is probably related with the higher roughness and packing of the diamagnetic compound as the AFM images show.

The optical band gap can be calculated by linearly fitting the tail of the absorbance curve, as shown in Figure 3.5. The wavelength of the absorbance onset corresponds to the energy of the first photon absorbed by the molecules, which con-

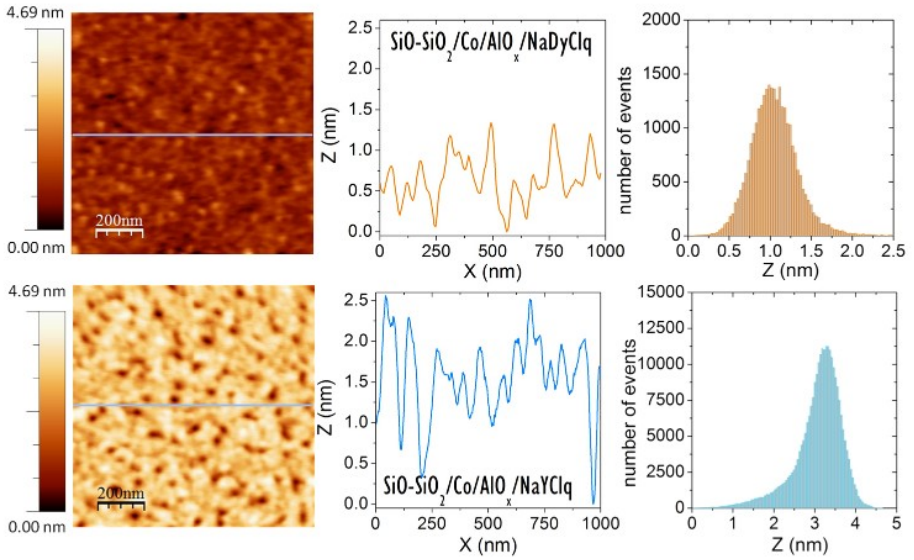

Figure 3.4 AFM topography images, profiles at medium high and histograms. Top panel: Si−SiO_2 / Co (15 nm) / AlO_x (1 nm) / NaDyClq (15 nm) The RMS roughness is 0.29 nm and the peak to peak roughness is 3.18 nm. The medium height is 1.1 nm. Bottom panel: Si−SiO_2 / Co (15 nm) / AlO_x (1 nm) / NaYClq (15 nm). The RMS roughness is 0.58 nm and the peak to peak roughness is 4.69 nm. A non-symmetric histogram points to two different mean heights coupled. The NaYClq compound shows higher roughness pointing to a different packing between both compounds.

stitutes an estimation of the HOMO-LUMO energetic distance.[18] We calculated the optical band gap of NaYClq and NaDyClq by measuring the absorbance of molecular solutions in ethanol. The energy gaps (E_{gap} = hc / λ_{onset}) obtained amount to 2.78 eV and 2.73 eV respectively. These E_{gap} values are similar to the band gaps of Alq_3[18] or Tb_3q_9.[19] As we have previously stated, in the quinoline-based molecular compounds, HOMO and LUMO are located in the ligands and this might be the reason of the very similar HOMO-LUMO distance.

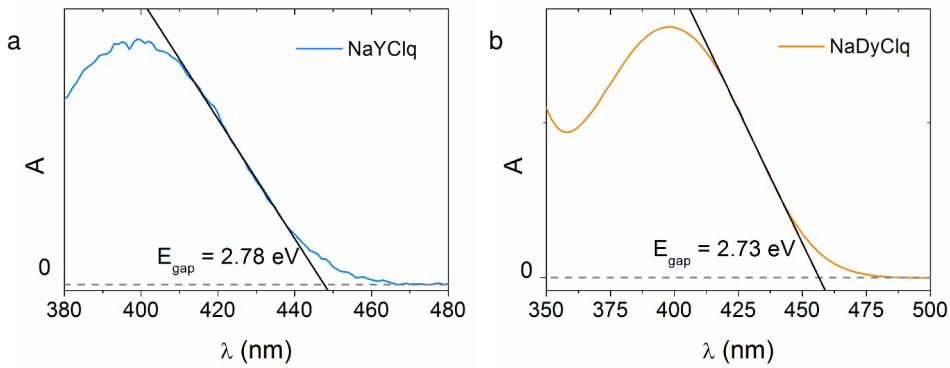

Figure 3.5 Absorbance of the molecular compounds, the optical gap is obtained from the onset of the absorbance curve. a) NaYClq (E_{gap} = 2.78 eV) and b) NaDyClq (E_{gap} = 2.73 eV).

3.2.2 Multi-Step Tunneling

In preliminary studies, the thicknesses of the electrodes and the leaky barrier were fixed while the thicknesses of the molecular layers were progressively reduced until a magnetoresistance response was observed. The NaYClq and NaDyClq spin valves which meet this requirement are reported in this chapter and have the following configurations and thicknesses:

Co (15 nm) / AlO_x (1 nm) / NaYClq (15 nm) / NiFe (15 nm)
Co (15 nm) / AlO_x (1 nm) / NaDyClq (8 nm) / NiFe (15 nm)

We measured the thermal dependence of the current-voltage (IV) curves to understand the charge transport mechanisms in the devices. Transport measurements were made in a four probe set-up as (see and illustration in Figure 3.1). In this configuration, two probes supply current while the other two measure the voltage. In this way, the voltage drop at the electrodes is not taken into account. This arrangement is especially useful when the resistance of the electrodes is similar to the resistance

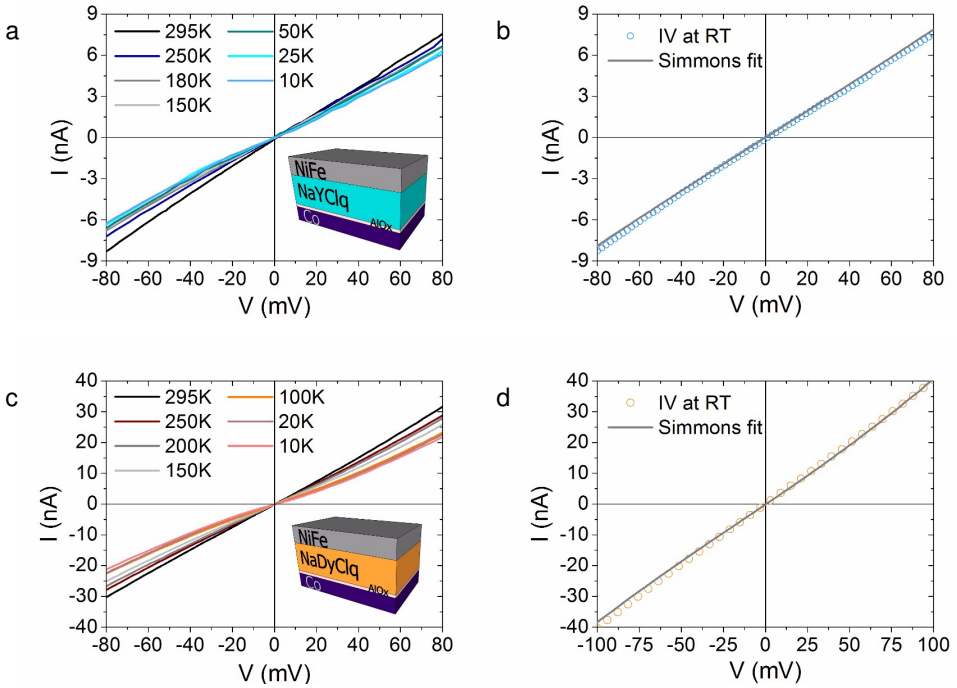

Figure 3.6 a) Current-voltage curves at different temperatures of the NaYClq spin valve showing a weak thermal dependence characteristic of the tunneling regime. b) The Simmons fit of the IV curve at room temperature gives an effective energy barrier and molecular layer effective thickness: $\phi_{eff} = (1.9 \pm 0.1)$ eV and $d_{eff} = (2.3 \pm 0.1)$ nm, the nominal thickness is $d_{nom} = 15$ nm. c) Current-voltage curves at different temperatures of the NaDyClq spin valve. d) The energy barrier and molecular layer effective thickness obtained from the Simmons formalism are: $\phi_{eff} = (1.2 \pm 0.1)$ eV and $d_{eff} = (2.6 \pm 0.1)$ nm, the nominal thickness is $d_{nom} = 8$ nm.

of the junction.

The thermal dependence of the IV curves of the spin valves is shown in Figures 3.6a and 3.6c. The antisymmetric IV curves show a weak temperature dependence characteristic of tunneling transport. While hopping is a thermally activated process in which carriers travel in the molecular layer, in the tunneling regime, they straight-

forwardly penetrate the isolating barrier. The tunnel probability is high for thin layers ($<$ 10 nm), since electron wavefunction shows an exponential decay inside the barrier.[17,20,21]

Due to top contact interpenetration,[1] the real thicknesses of the molecular layers are smaller than the thicknesses measured upon evaporation (nominal thicknesses). We estimated the effective tunnel barriers (ϕ_{eff}) and effective thicknesses (d_{eff}) by means of the Simmons model,[22] where the current flowing through a tunneling barrier at a metal / insulation / metal junction is described by the following formula:

$$J = \frac{e}{2\pi h}\frac{1}{d_{eff}}\left\{\left(\phi_{eff} - \frac{eV}{2}\right)\exp\left[-\frac{4\pi\sqrt{2m}}{h}d_{eff}\sqrt{\phi_{eff} - \frac{eV}{2}}\right] - \left(\phi_{eff} - \frac{eV}{2}\right)\exp\left[-\frac{4\pi\sqrt{2m}}{h}d_{eff}\sqrt{\phi_{eff} + \frac{eV}{2}}\right]\right\} \quad (3.1)$$

where e is the electron charge, h is Planck's constant, m is the electron rest mass and V is the applied voltage. The formula applies as long as the energy associated with the bias voltage is lower than the energy barrier.[22] The Simmons fits at room temperature for both MSVs are shown in Figures 3.6b and 3.6d. The effective energy barrier of the NaYClq spin valve is slightly higher than the obtained for the NaDyClq device (ϕ_{eff} (NaYClq) $= 1.9 \pm 0.1$ eV and ϕ_{eff} (NaDyClq) $= 1.2 \pm 0.1$ eV). The effective thicknesses obtained are thinner than the nominals: NaDyClq $\rightarrow$ $d_{\text{nom}} = (8.0 \text{ nm} \pm 0.1) \ll d_{\text{eff}} = (2.3 \pm 0.1)$ nm and NaYClq $\rightarrow$ $d_{\text{nom}} = (15.0 \pm 0.1) \ll d_{\text{eff}} = (2.6 \pm 0.1)$ nm.

To further explore the tunneling transport mechanism in the MSVs, we evaluated if the charge carries tunnel directly between electrodes (direct tunneling) or require intermediate stops at states near the Fermi level (multi-step tunneling) as a function of the molecular layer thickness. We applied the model described by Schoonus et al.[23] The transition from direct to multi-step tunneling is found by inspecting the semilogarithmic plot of $1/J$ versus the effective thickness obtained by the Simmons fits. The change of slope or multi-step tunneling onset can be observed in Figure 3.7 and occurs for an effective thickness of approximately d_{eff} = 2.6 nm. The slopes of the linear curves are proportional to the extinction coefficient κ of the electronic

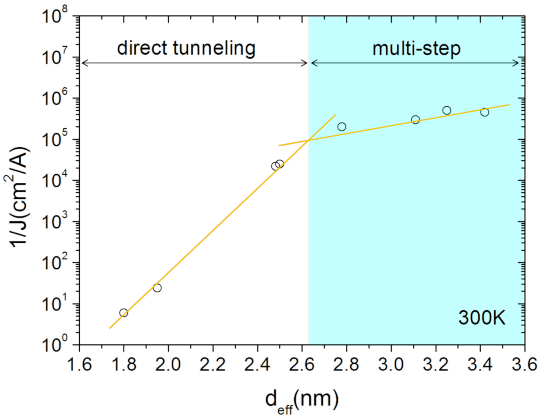

Figure 3.7 Semi-logarithmic plot of $1/J$ versus the effective thickness of the molecular layers obtained from the Simmons model of the devices Co / AlO_x / NaLnClq / NiFe. The onset of multi-step tunneling locates at $\sim$2.6 nm.

wavefunction in the molecular barrier ($1/J$ -$\propto$ exp (κd_{eff})), which amounts in our case to 3.4 nm^{-1} in the direct tunneling regime. In the multi-step tunneling regime $1/J \propto \exp(\kappa d_{eff}/\eta)$, where η is the number of total tunneling events. We infer a slope $-\kappa/\eta = 1.36$, corresponding to 2 to 3 tunneling events.

3.2.3 Negative Magnetoresistance

The magnetoresistance curves are measured by applying a constant voltage to the device in a sweep of magnetic field. The polarized carriers encounter greater or less difficulty in traversing the device, depending on the relative orientation of the magnetization of the electrodes (antiparallel or parallel). Consequently, the resistance shows two states, high and low.

The measurement starts usually at high negative magnetic field. The voltage is fixed and the current is measured while the field increases. In our devices, the voltage is defined as positive when current flows from Co to NiFe (cobalt is the

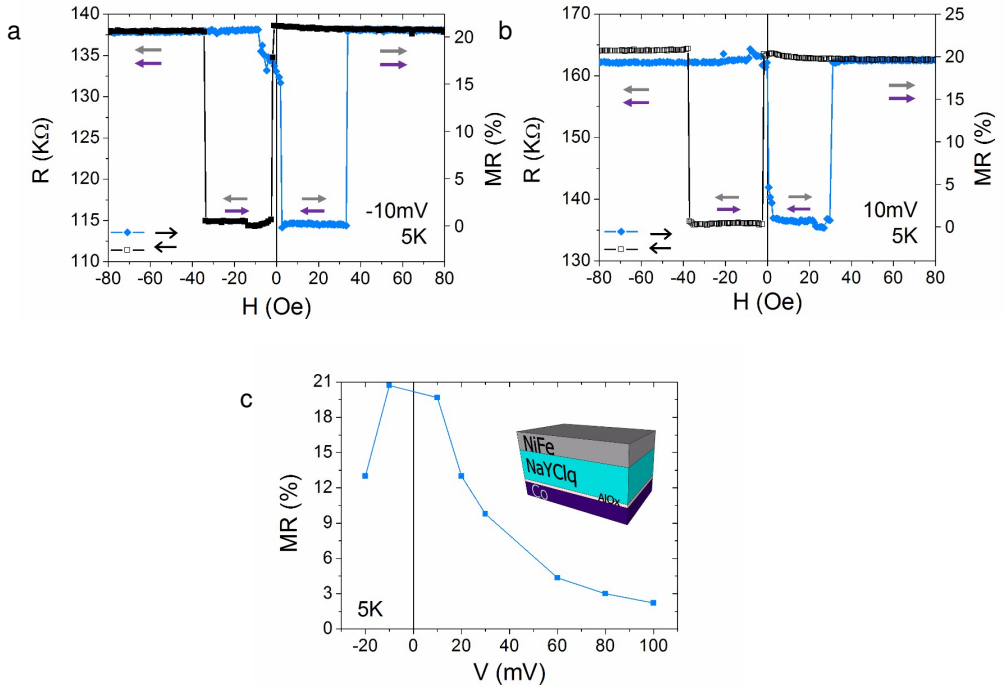

Figure 3.8 Magnetoresistance of the NaYClq spin valve with nominal thicknesses: Co (15 nm) / AlO_x (1 nm) / NaDyClq (15 nm) / NiFe (15 nm). a) MR = 21 % at -10 mV. b) MR $=$ 20 % at 10 mV. c) Dependence of the MR with voltage at 5 K. The device layers are: Co (15 nm) / AlO_x (1 nm) / NaYClq (15 nm) / NiFe (15 nm). The black arrows indicate the sweep directions whereas the purple and gray arrows note the magnetization direction of the Co and NiFe electrodes respectively.

positive and NiFe the negative electrode). The current switches when the applied field reaches the coercive field (H_c) of the soft magnet (NiFe). Ideally, it remains constant until the coercive field of the hard magnet (Co) is reached when a second switch returns it to their original value. Finally, the magnetic field sweep is reversed. The resulting MR curves resemble the shape of a butterfly.

In an antiparallel (parallel) electrode alignment, the resistance is R_{AP} (R_P). The MR percentage is quantified as: MR (%) $=$ ($R_{AP} - R_P$) / R_P and if $R_{AP} > R_P$ the MR

is positive whereas if $R_{AP} < R_P$ it is negative.

Figure 3.8 shows the magnetoresistance curves at different voltages at a temperature of 5 K measured in the diamagnetic NaYClq spin valve. The sharp switches at 3 Oe and 30 Oe are indicators of clean and smooth interfaces and the plateaus show that both electrodes are well spatially and magnetically decoupled.

However, the most surprising fact is that the magnetoresistance is negative, i.e., the resistance of the AP state is smaller than the resistance of the P state. This is due to the fact that majority carriers are inverting the spin polarization at some point while they traverse the device. Figure 3.8c depicts the dependence of the MR response with the bias voltage at 5 K. This bias dependence shape is commonly observed in this kind of devices.[5]

Contrary to what one may predict, the negative MR is not related with the magnetic character of the molecular layer, as the magnetic transport measurements in the NaDyClq spin valve described in the following paragraphs will demonstrate.

The MR measured in the spin valve based on the magnetic NaDyClq is also negative as seen in Figure 3.9. The maximum MR registered amounts to 32 % at 5 K. Here we also observe sharp switches indicating smooth and clean interfaces since they are a consequence of the magnetization reversal process. Figure 3.9c shows a similar voltage dependence to the NaYClq MSV. At these low voltages, conduction does not take place in the HOMO or LUMO of the molecular compounds but through an intermediate trap band[24] where the multi-step sites may be located. The thermal dependence of the MR can be observed in Figure 3.9d. As expected, MR decreases upon heating and disappears at temperatures higher than 150 K.[5]

The negative MR could be originated in the partially oxidize aluminum layer by the formation of Al quantum well states.[25,26] To rule out this possibility we assembled devices without molecular layers and studied their magnetoresistance. The magnetic tunnel junctions consist on a stack of Co / Al (x nm) / Al_2O_3 ($1.3 - 2$ nm) / NiFe. The thickness of the Al_2O_3 layer is calculated by subtracting the effective thickness obtained from the Simmons model[22] fitting to the nominal thicknesses. The configu-

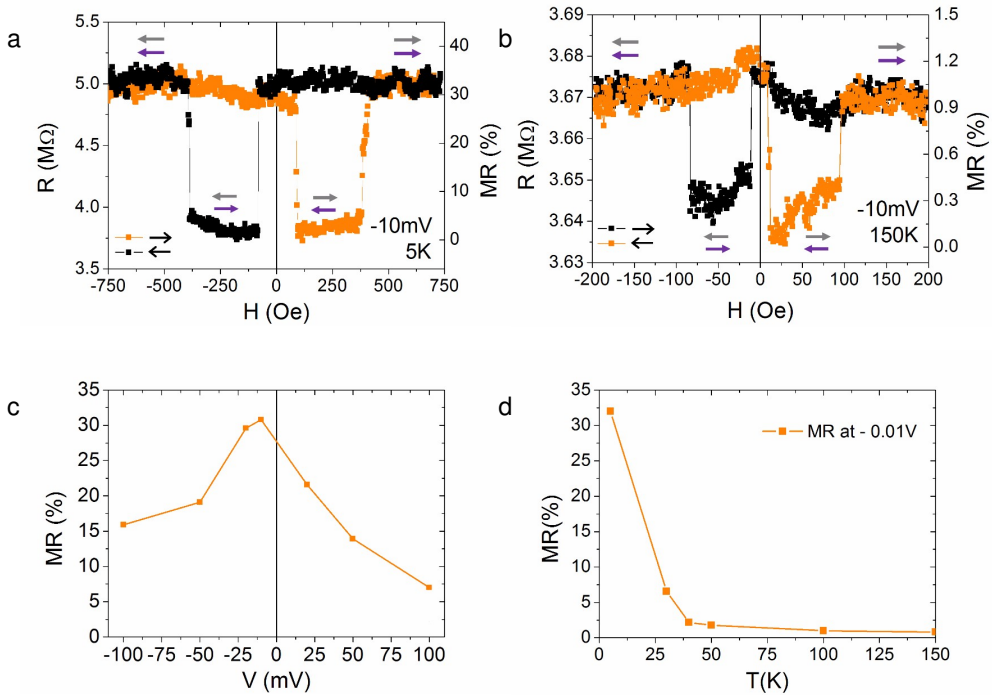

Figure 3.9 Magnetoresistance of the NaDyClq spin valve with nominal thicknesses: Co (15 nm) / AlO_x (1 nm) / NaDyClq (8 nm) / NiFe (15 nm). a) Maximum MR measured of MR = 32 % at 5 K and −10 mV. b) MR = 0.9 % MR at 150 K and −10 mV. c) Voltage dependence of the MR at 5 K. d) Thermal dependence of the MR. The black arrows indicate the sweep direction whereas the purple and gray arrows note the magnetization direction of the Co and NiFe electrodes respectively.

ration and thicknesses obtained in the MTJs are:

MTJ1: Co (15 nm) / Al_2O_3 (1.5 nm) / NiFe (15 nm)
MTJ2: Co (15 nm) / Al (0.7 nm) / Al_2O_3 (1.3 nm) / NiFe (15 nm)
MTJ3: Co (15 nm) / AlO_x (1 nm) / Al_2O_3 (1.5 nm) / NiFe (15 nm)
MTJ4: Co (15 nm) / Al (1 nm) / Al_2O_3 (2 nm) / NiFe (15 nm)

Figure 3.10a shows the experimental IV curves of the four devices at room temperature and the Simmons fits represented as solid lines. As depicted in Figure

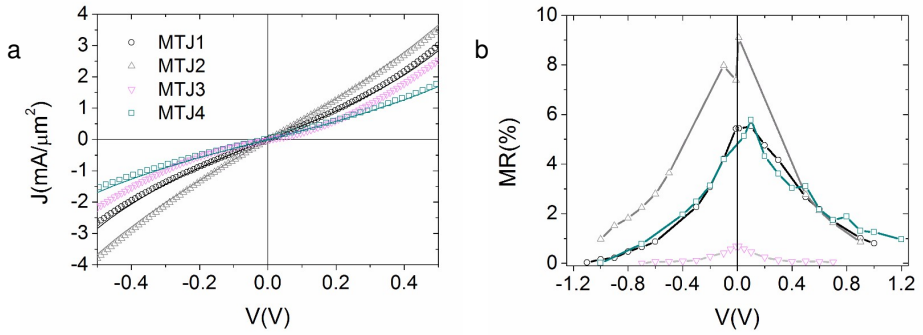

Figure 3.10 a) JV curves of the four magnetic tunnel junctions. Solid lines are obtained by fitting the experimental data to the Simmons model. b) Voltage dependence of the magnetoresistance for the four devices. No negative MR is observed in any of the MTJ.

3.10b, none of the MTJs shows negative MR. Therefore, we can rule out that aluminum is responsible for MR sign inversion.

3.2.4 The NaLnClq / NiFe Spinterface

In the MSVs we have studied in the previous sections, the leaky barrier isolates the Co from the molecular layer while the molecule and the NiFe are in direct contact. In this section, we study a new MSV configuration where we swap the ferromagnetic electrodes to reverse this situation. Thus, in the new stack order the NiFe is isolated from the molecular material by means of the leaky barrier. The objective is to see if the NaLnClq / NiFe interface is the responsible of the MR inversion. The structure and thicknesses of the molecular spin valve with the FM reversed is:

NiFe (15 nm) / AlO_x (1 nm) / NaDyClq (25 nm) / Co (15 nm)

The weak thermal dependence of the current-voltage curves indicates that the device is also in the tunneling regime (see Figure 3.11a). Besides, the Simmons fit

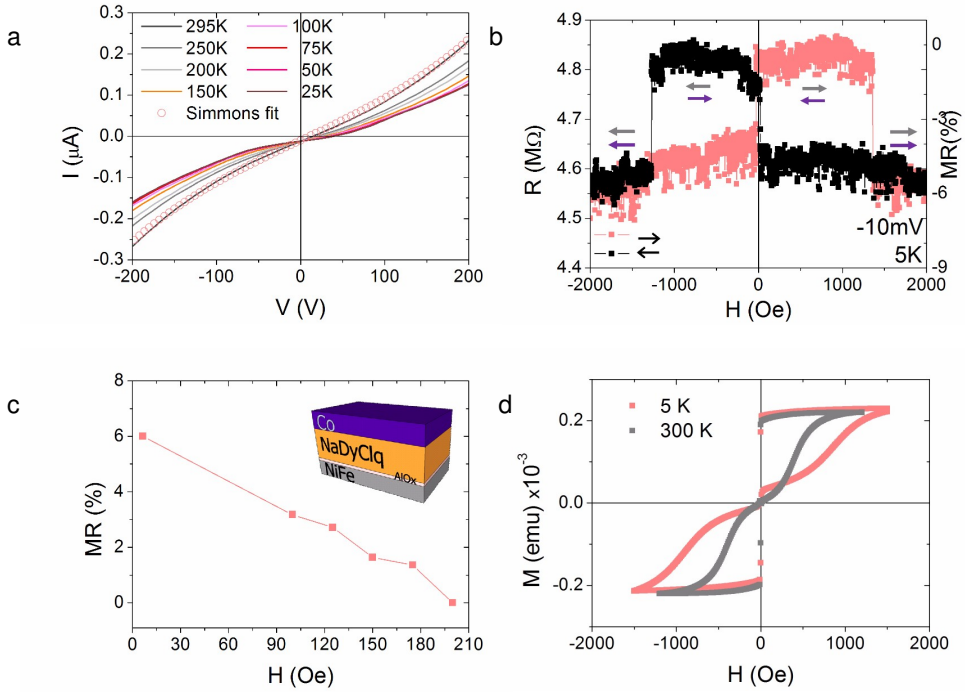

Figure 3.11 Magnetic characterization of NiFe (15 nm) / AlO_x (1 nm) / NaDyClq (25 nm) / Co (15 nm). a) IV curves and Simmons fit at room temperature with $d_{eff} = 2.7 \pm 0.1$ nm and $\phi_{eff} = 1.1 \pm 0.1$ eV. b) Maximum MR of 6 % at -10 mV and 5 K. c) Thermal evolution of the MR signal. d) Hysteresis loops at 5 K and 300 K of the MSV.

to the IV curve at room temperature gives an effective thickness of d_{eff} = 2.7 $\pm$ 0.1 nm, in contrast with the nominal thickness of 25 nm, and an effective energy barrier ϕ_{eff} = 1.1 $\pm$ 0.1 eV. The hysteresis loop measured in the device at 5 K and 300 K is shown in Figure 3.11d where the coercitivities of the FM electrodes can be observed as they correspond to the switches of the MR curves.

The MR observed now is positive and demonstrates that the molecule / NiFe interface is inverting the spin polarization in the molecular spin valves: Co / AlO_x / NaLnClq / NiFe. Besides, in the present spin valve, the magnetoresistance signal is

lost at 200 K, unlike the magnetic signal loss at 150 K in the initial configuration (see Figures 3.9d and 3.11c) indicating that they are not governed by the same magnetic mechanisms.

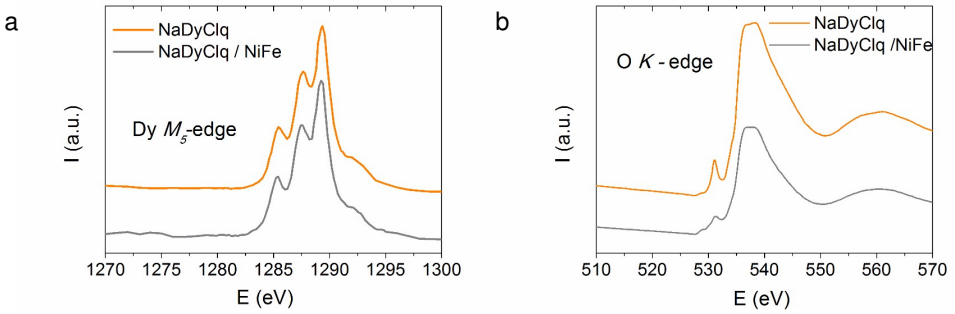

Figure 3.12 X-ray absorption spectroscopy before and after NiFe deposition on top of the molecular layer NaDyClq. a) Dy M_5-edge. b) O K-edge. Both edges are unaffected upon the metal deposition.

The inversion of the MR in inorganic magnetic tunnel junctions has been ascribed to bonding effects at the interface.[27] It has been demonstrated that the inversion of the spin polarization can occur in an oxide / FM interface if the oxide layer (or a layer product of the chemical reaction between the oxide and the metal) is antiferromagnetically coupled to the FM electrode.[28] Nevertheless, the case of the spinterface is different. In this case the molecule remains intact and the inversion is due to an overlapping between the metallic and molecular orbitals (hybridization). The molecular levels broaden when put in contact with the ferromagnet and the broadening is different for spin-up and spin-down, allowing the first molecular layers to filter the spin.[6,29] We have ruled out that the MR inversion at the NaDyClq / NiFe interface is due to a chemical reaction, rather to a molecule / metal hybridization, by X-ray absorption spectroscopy (XAS).

XAS is a synchrotron technique based on the photoelectric effect in which X-rays are absorbed by the sample promoting core level electrons out of the atoms. The synchrotron radiation source provides tunable and intense X-rays, the photon energy is adjusted by a monochromator to the energetic range where core electrons

can be excited. For every element, the XAS spectrum shows a sharp rise when the photon energy is equal to the binding energy of the electron shell (K, L, M). The edge refers to the minimum energy at which a vacancy is created. Besides, the name of the edges indicates the excited electron orbit (n = 1 (K), 2 (L), 3 (M)). The spectrum is commonly divided into two zones: XANES (X-ray absorption near edge spectroscopy) and EXAFS (extended X-ray absorption fine-structure spectroscopy). XANES, the spectral zone near the absorption edge, is specially sensitive to the oxidation state and coordination environment, while EXAFS is related to the neighboring atoms.[30]

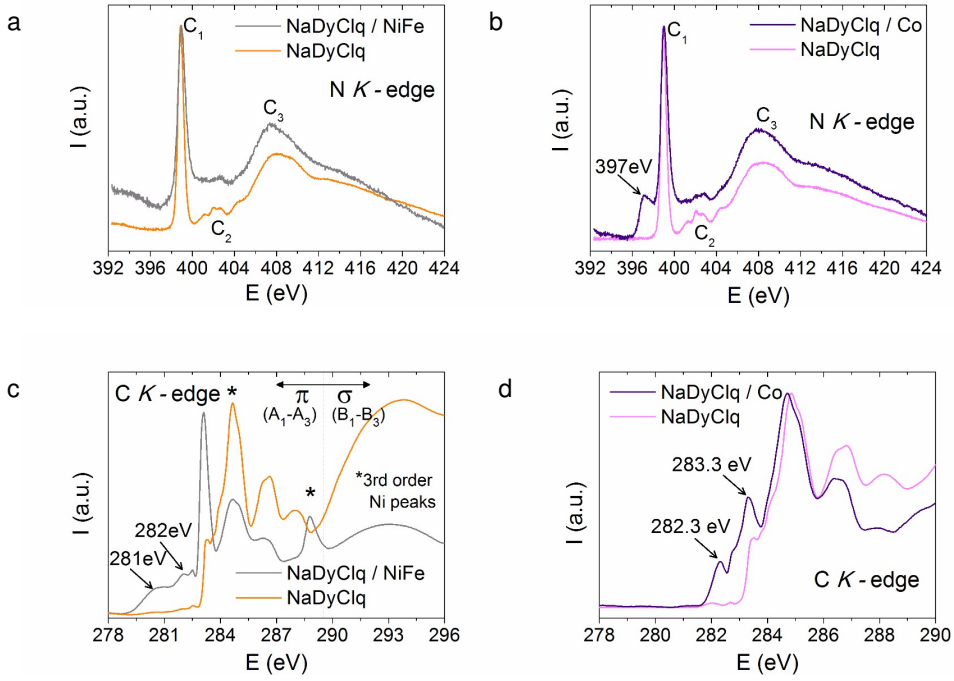

Figure 3.13 Nitrogen K-edge before and after NiFe (a) and Co (b) depositions on top of the NaDyClq molecular layer. Carbon K-edge before and after NiFe (c) and Co (d) depositions on top of the NaDyClq molecular layer. The spectra corresponding to the NaDyClq/NiFe spinterface (NaDyClq/Co interface) depict the molecular layer spectrum in orange (pink).

The molecular layers were sublimated in situ in an evaporator connected to the end of the beamline at the synchrotron facilities, where the sample fabrication conditions are equivalent to the conditions in the device fabrication. Besides, the UHV conditions (base pressure 10^{-10} mbar) ensure that no residual oxygen is present in the experiments.

The NaDyClq molecular compound is formed by six different atoms: Dy, O, Cl, Na, N and C (see an illustration of the molecular structure in Figure 2.3a in Chapter 2). The XAS spectra of Dy and O in Figure 3.12 show that they are not affected by the deposition of NiFe on top of the molecular layer, so we can rule out that they participate in any chemical reaction. Unfortunately, the Na and Cl XAS spectra exhibit low signal-to-noise ratio after metal deposition due to a low absorption cross section preventing the comparison of the spectra before and after NiFe sublimation. However, Na^+ is totally inert and does not react with Ni or Fe. Thus, the antiferromagnetic products of an hypothetic chemical reaction between NiFe and Cl would be $NiCl_2$, $FeCl_2$and $FeCl_3$, but they cannot be the origin of the negative MR effect since all of them have Nèel temperatures below 150 K, which is the temperature above which the MR signal is lost in our devices ($T_{Nèel}$($NiCl_2$) = 50 K, $T_{Nèel}$($FeCl_2$) = 24 K and $T_{Nèel}$($FeCl_3$) = 10 K).[31–33]

The XAS spectra of N and C immediately before and after NiFe or Co deposition on the molecular layer are shown in Figure 3.13 where it is found that each metal leads to a different interaction with the NaDyClq orbitals.

The N k-edge of the pristine molecule shows three characteristic peaks corresponding to the transitions $\pi(C_1)$ and $\sigma(C_2$ and $C_3)$.[16] The deposition of NiFe does not affect the N k-edge as seen in Figure 3.13a. However, after Co sublimation a new peak located at 397 eV can be observed (see Figure 3.13b). A similar situation has been observed in the spectrum of MnPc molecules on a cobalt substrate where the increase on the spectral weight was ascribed to hybrid Co-N states.[34] In this respect, it is noted that the NaDyClq / Co interface is not responsible of the MR sign inversion.

The C k-edge of the pristine molecule (in orange in Figure 3.13c and in pink

in Figure 3.13d) shows three characteristic peaks that are ascribed to the LUMO and LUMO+1 transitions localized at the carbon rings of the ligands.[16] The two peaks highlighted with a star in Figure 3.13c correspond to a high order replica of the Ni signal and do not belong to the molecule / metal interaction. The C k-edge is modified upon either metal sublimation but the interaction is different in any case and more intense in the case of NiFe. Two new peaks located at 282.3 eV and 283.3 eV are observed in the NaDyClq / Co spectrum shown in Figure 3.13d.

In the case of NaDyClq / NiFe, two new peaks appear also at the pre-edge region approximately at 281 eV and 282 eV. These peaks that lie in the HOMO-LUMO gap contribute to the electronic transport (see Figure 3.13c) and can be ascribed to the hybrid states responsible of the MR sign inversion.

3.3 Conclusions and Perspectives

In this chapter we have designed molecular spin valves based on two sublimable compounds described in the chapter two. Although both compounds have different magnetic behavior (one is paramagnetic, based on Dy^{3+}, while the other is diamagnetic, based on Y^{3+}), no differences could be attributed in terms of magnetotransport. This issue could be tackled if the reproducibility problem is solved, which constitutes nowadays one of the big issues within the molecular spintronics devices.

Interestingly, both molecular spin valves invert the sign of the MR when the molecular material is in direct contact with the permalloy ferromagnetic electrode. This hybridized molecule / FM spinterface[6,35] has been identified by isolating one of the ferromagnetic electrodes from the molecular material. The result has been a reversal in the sign of the magnetoresistance, which changes from positive (when the spinterface is absent; case of the NaDyClq / Co interface) to negative (in presence of a NaDyClq / NiFe spinterface).

X-ray absorption spectroscopy has been used to demonstrate the different interactions of the molecule with Co an NiFe at the interface. The spectra show different

features in each case, pointing to distinct interactions between the molecules and the FM metals. However, we do not know specifically the origin of spin filtering in the NaDyClq / NiFe interface.

As perspectives of the future work, if the reproducibility problem is solved, many interesting combinations could be studied. For instance, a monolayer of magnetic molecules could enhance the spin injection in a diamagnetic layer. Also both molecules could be simultaneously evaporated at different rates what would enlighten the role of the magnetic atom in the spin transport.

3.4 Experimental Details

All this work was performed at Cic-Nanogune in close collaboration with A. Bedoya and L. Hueso.

The Co / AlO_x / NaLnClq / NiFe and NiFe / AlO_x / NaLnClq / Co vertical spin valves were fabricated at UHV in an in-situ dual chamber Theva evaporator at a base pressure of 10^{-10} mbar. The ferromagnetic electrodes were sublimated via electron beam evaporation. The bottom electrode was evaporated at a rate of 1 Å/s while the first nanometers of the top electrode were evaporated at a rate of 0.1 Å/s. The aluminum layer was e-beam evaporated at $0.1-0.2$ Å/s and oxidized in a controlled atmosphere in the loadlock of the evaporator at 0.1 mbar (O_2 pressure) during 20 minutes to conform the leaky barrier (AlO_x). The molecular layers were sublimated thermally from conventional effusion cells, at evaporation temperatures ranging between [345, 355] ℃, keeping the substrate at a constant temperature of 24 ℃. Metals were 99.99 % purity (Lesker). Eight junctions were assembled on each $Si-SiO_2$ chip. The active device areas were in the range 300 μm x 600 μm to 200 μm x 300 μm due to the masks design.

The absorbance spectra were recorded by means of an Agilent UV/VIS HP 8453 spectrometer while the molecular compounds were diluted in ethanol solutions.

The surface topographies were imaged using the atomic force microscope Agilent 5500, operating in tapping mode with a tip frequency of 342 kHz. Cantilevers were from silicon, with a spring constant of 40 Nm^{-1}. The image area amounts to 1 μm x 1 μm. The image processing was done with the WSxM software.[36]

The electric and magnetic measurements were performed in vacuum with a magnetic-field equipped Lakeshore Probe Station in which temperature can vary in the range [5, 300] K. For the current-voltage and magnetoresistance curves a Keithley 4200 semiconductor analyzer was used.

The X-ray absorption spectroscopy measurements were carried out at the beamlines I1011 in Max Lab Synchrotron (Lund) and BOREAS in ALBA Synchrotron (Barcelona) equipped with in-situ preparation chambers (10^{-10} mbar) where the NaDyClq / metal layers were prepared. The molecules were grown from effusion cells and the NiFe and Co metals were e-beam evaporated, under the same conditions as for the device fabrication. The X-ray absorption measurements were taken in total electron yield, with the spectra normalized to a freshly sputtered Au-grid.

3.5 Bibliography

[1] D. Sun, E. Ehrenfreund, and Z. V. Vardeny. “The first decade of organic spintronics research”. Chemical Communications 50.15 (2014), pp. 1781–1793.

[2] H. Gu, X. Zhang, H. Wei, Y. Huang, S. Wei, and Z. Guo. “An overview of the magnetoresistance phenomenon in molecular systems”. Chemical Society Reviews 42.13 (2013), pp. 5907–5943.

[3] V. Dediu, M. Murgia, F. Matacotta, C. Taliani, and S. Barbanera. “Room temperature spin polarized injection in organic semiconductor”. Solid State Communications 122.3 (2002), pp. 181–184.

[4] Z. Xiong, D. Wu, Z. V. Vardeny, and J. Shi. “Giant magnetoresistance in organic spin-valves”. Nature 427.6977 (2004), pp. 821–824.

[5] J. Devkota, R. Geng, R. C. Subedi, and T. D. Nguyen. “Organic spin valves: a review”. Advanced Functional Materials 26.22 (2016), pp. 3881–3898.

[6] C. Barraud, P. Seneor, R. Mattana, S. Fusil, K. Bouzehouane, C. Deranlot, P. Graziosi, L. Hueso, I. Bergenti, V. Dediu, et al. “Unravelling the role of the interface for spin injection into organic semiconductors”. Nature Physics 6.8 (2010), pp. 615–620.

[7] M. Gobbi, F. Golmar, R. Llopis, F. Casanova, and L. E. Hueso. “Room-temperature spin transport in C60-based spin valves”. Advanced Materials 23.14 (2011), pp. 1609–1613.

[8] X. Sun, M. Gobbi, A. Bedoya-Pinto, O. Txoperena, F. Golmar, R. Llopis, A. Chuvilin, F. Casanova, and L. E. Hueso. “Room-temperature air-stable spin transport in bathocuproine-based spin valves”. Nature Communications 4 (2-013).

[9] E. Cobas, A. L. Friedman, O. M. vant Erve, J. T. Robinson, and B. T. Jonker. “Graphene as a tunnel barrier: graphene-based magnetic tunnel junctions”. Nano Letters 12.6 (2012), pp. 3000–3004.

[10] S. Majumdar, H. S. Majumdar, R. Laiho, and R. Österbacka. “Organic spin valves: effect of magnetic impurities on the spin transport properties of polymer spacers”. New Journal of Physics 11.1 (2009), p. 013022.

[11] V. Dediu, L. Hueso, I. Bergenti, A. Riminucci, F. Borgatti, P. Graziosi, C. Newby, F. Casoli, M. De Jong, C. Taliani, et al. “Room-temperature spintronic effects in Alq_3-based hybrid devices”. Physical Review B 78.11 (2008), p. 115203.

[12] F. J. Wang, Z. H. Xiong, D. Wu, J. Shi, and Z. V. Vardeny. “Organic spintronics: The case of Fe/Alq_3/Co spin-valve devices”. Synthetic Metals 155.1 (2005), pp. 172–175.

[13] T. Santos, J. Lee, P. Migdal, I. Lekshmi, B. Satpati, and J. Moodera. “Room-temperature tunnel magnetoresistance and spin-polarized tunneling through an organic semiconductor barrier”. Physical Review Letters 98.1 (2007), /iu-pac0|1|6|6|0|1.

[14] J. Kalinowski. Organic light-emitting diodes: Principles, characteristics & processes. CRC press, 2004.

[15] L. Bogani and W. Wernsdorfer. “Molecular spintronics using single-molecule magnets”. Nature Materials 7.3 (2008), pp. 179–186.

[16] A. DeMasi, L. Piper, Y. Zhang, I. Reid, S. Wang, K. Smith, J. Downes, N. Peltekis, C. McGuinness, and A. Matsuura. “Electronic structure of the organic semiconductor Alq_3 (aluminum tris-8-hydroxyquinoline) from soft X-ray spectroscopies and density functional theory calculations”. The Journal of chemical physics 129.22 (2008), p. 224705.

[17] R. Lin, F. Wang, J. Rybicki, M. Wohlgenannt, and K. Hutchinson. “Distinguishing between tunneling and injection regimes of ferromagnet/organic semiconductor/ferromagnet junctions”. Physical Review B 81.19 (2010), p. 195214.

[18] M. M. Duvenhage, M. Ntwaeaborwa, H. G. Visser, P. J. Swarts, J. C. Swarts, and H. C. Swart. “Determination of the optical band gap of Alq_3 and its derivatives for the use in two-layer OLEDs”. Optical Materials 42 (2015), pp. 193–198.

[19] A. Bedoya-Pinto, H. Prima-García, F. Casanova, E. Coronado, and L. E. Hueso. “Spin-polarized hopping transport in magnetically tunable rare-earth quinolines”. Advanced Electronic Materials 1.6 (2015).

[20] J. Jiang, J. Pearson, and S. Bader. “Absence of spin transport in the organic semiconductor Alq_3”. Physical Review B 77.3 (2008), p. 035303.

[21] T. Tran, T. Q. Le, J. G. Sanderink, W. G. van der Wiel, and M. P. de Jong. “The multistep tunneling analogue of conductivity mismatch in organic spin valves”. Advanced Functional Materials 22.6 (2012), pp. 1180–1189.

[22] J. G. Simmons. “Generalized formula for the electric tunnel effect between similar electrodes separated by a thin insulating film”. Journal of Applied Physics 34.6 (1963), pp. 1793–1803.

[23] J. Schoonus, P. Lumens, W. Wagemans, J. Kohlhepp, P. Bobbert, H. Swagten, and B. Koopmans. “Magnetoresistance in hybrid organic spin valves at the onset of multiple-step tunneling”. Physical Review Letters 103.14 (2009), 14-6601.

[24] Z. G. Yu. “Impurity-band transport in organic spin valves”. Nature Communications 5 (2014), p. 4842.

[25] J. S. Moodera and G. Mathon. “Spin polarized tunneling in ferromagnetic junctions”. Journal of Magnetism and Magnetic Materials 200.1 (1999), pp. 248–273.

[26] S. Jiang, B. Chen, P. Wang, Y. Zhou, Y. Shi, F. Yue, H. Ding, and D. Wu. “Voltage polarity manipulation of the magnetoresistance sign in organic spin valve devices”. Applied Physics Letters 104.26 (2014), p. 262402.

[27] J. M. De Teresa, A. Barthelemy, A. Fert, J. P. Contour, F. Montaigne, and P. Seneor. “Role of metal-oxide interface in determining the spin polarization of magnetic tunnel junctions”. Science 286.5439 (1999), pp. 507–509.

[28] D. Ciudad, M. Gobbi, C. J. Kinane, M. Eich, J. S. Moodera, and L. E. Hueso. “Sign control of magnetoresistance through chemically engineered interfaces”. Advanced Materials 26.45 (2014), pp. 7561–7567.

[29] S. Sanvito. “Molecular spintronics: The rise of spinterface science”. Nature Physics 6.8 (2010), pp. 562–564.

[30] D. Koningsberger and R. Prins. X-ray absorption: principles, applications, techniques of EXAFS, SEXAFS, and XANES. John Wiley and Sons, 1988.

[31] M. Lines. “Magnetic properties of $CoCl_2$ and $NiCl_2$”. Physical Review 131.2 (1963), p. 546.

[32] R. Birgeneau, W. Yelon, E. Cohen, and J. Makovsky. “Magnetic properties of $FeCl_2$ in zero field. I. excitations”. Physical Review B 5.7 (1972), p. 2607.

[33] E. R. Jones Jr, O. Morton, L. Cathey, T. Auel, and E. Amma. “Low-temperature magnetic susceptibility of $FeCl_3$”. The Journal of Chemical Physics 50.11 (1969), pp. 4755–4757.

[34] S. Javaid, M. Bowen, S. Boukari, L. Joly, J.-B. Beaufrand, X. Chen, Y. Dappe, F. Scheurer, J.-P. Kappler, J. Arabski, et al. “Impact on interface spin polarization of molecular bonding to metallic surfaces”. Physical Review Letters 105.7 (2010), p. 077201.

[35] F. Djeghloul, F. Ibrahim, M. Cantoni, M. Bowen, L. Joly, S. Boukari, P. Ohresser, F. Bertran, P. Le Fèvre, P. Thakur, et al. “Direct observation of a highly spin-polarized organic spinterface at room temperature”. Scientific Reports 3.1272 (2013).

[36] I. Horcas, R. Fernández, J. Gomez-Rodriguez, J. Colchero, J. Gómez-Herrero, and A. Baro. “WSXM: a software for scanning probe microscopy and a tool for nanotechnology”. Review of Scientific Instruments 78.1 (2007), p. 013705.

4

Molecular Spin Valves Based on Polyoxometalates: MR at High Voltage

4.1 Introduction

Polyoxometalates[1,2] (in short POMs) constitute an extensive class of molecular metal oxides with wide electronic versatility and structural variety.[3] Regarding its molecular composition, they are formed by metal cations and oxo anions in high symmetry configurations. POMs are described by the general formula $[X_xM_yO_z]^{n-}$ where X is known as the heteroatom and M is a transition metal. They present different tridimensional structures such as Lindqvist ($M_6O_{19}{}^{2-}$), Anderson ($XM_6O_{24}{}^{n-}$), Keggin ($XM_{12}O_{40}{}^{n-}$), Dawson ($X_2M_{18}O_{62}{}^{n-}$) or Preyssler ($NaP_5W_{30}O_{110}{}^{14-}$) as illustrated in Figure 4.1.

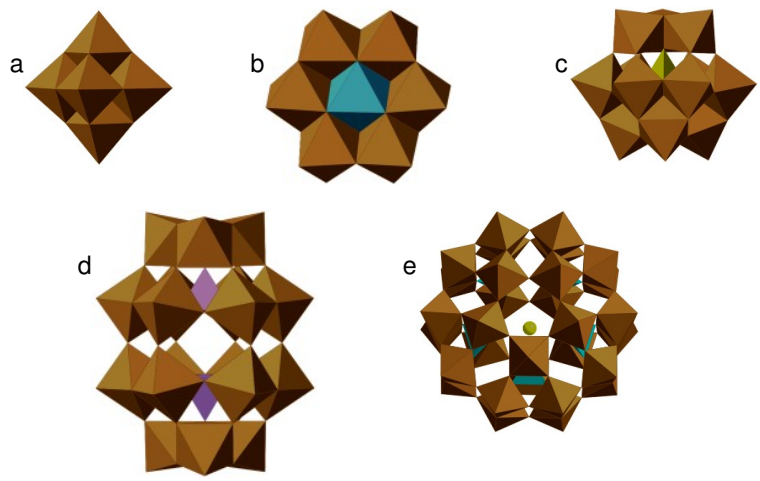

Figure 4.1 Polyhedral representations of some structures of POMs. a) Lindqvist anion $[M_6O_{19}]^{2-}$. b) Anderson anion $[XM_6O_{24}]^{n-}$. c) Keggin anion $[XM_{12}O_{40}]^{n-}$. d) Wells-Dawson anion $[X_2M_{18}O_{62}]^{n-}$. e) Preyssler anion $[NaP_5W_{30}O_{110}]^{14-}$. Brown octahedra, MO_6; green octahedron, XO_6; yellow tetrahedra, XO_4; and yellow sphere, Na^+. The M atoms are located in the center of the octahedron

Nowadays POMs have a broad variety of applications in different fields such as medicine, catalysis or quantum computing.[4–6] Commonly, their potential is grounded in the ability that they have in solution to accept several electrons with minimal structural changes. Besides, POMs are stable and soluble in both aqueous and non-aqueous solvents. Concerning molecular spintronics, POMs offer a unique opportunity to compare properties between family members as they constitute a very large collection of versatile, robust and chemically tunable compounds.

Among countless POMs,[7] we choose the phosphomolybdate $[PMo_{12}O_{40}]^{3-}$, historically the first POM discovered. It was found in 1783 by the D'Elhuyar brothers when they showed that the reaction of phosphoric acid with ammonium molybdate produced a yellowish powder that would turn out to be the ammonium phosphomolybdate ($(NH_4)_3PMo_{12}O_{40}$). Some years later, in 1826 Berzelius reported it as the phosphomolybdic acid for the first time. However, it was not until 1933 when the molecular structure was solved by X-ray diffraction by Keggin.[8]

The properties of molecular spin valves (MSVs) strongly depend on the spin-polarized charge injection at the metal-molecular interfaces. In this kind of devices, a careful engineering of the inorganic / organic interfaces is required. Most of the MSVs reported added a thin inorganic layer placed between one of the electrodes and the molecular material, such as LiF, Al_2O_3 or MgO)[9,10] but thin organic layers (such as dipolar amine molecules) have also been tested.[11] The advantages of these interfacial barriers include the prevention of the top electrode penetration in the molecular layer,[12] or the modification of the electrode work function, resulting in an improvement of the charge injection.[13,14]

In this chapter we introduce for the first time a POM in a molecular spin valve. Normally POMs are deposited on substrates by the Langmuir-Blodgett technique[15] but we are able to deposit relatively thick layers up to 100 nm by means of spin coating using as counter-ions sulfactant molecules. This has made it possible to study and compare two kind of devices: a MSV without any kind of barrier and an equal structure in which a thin MoO_x barrier was included. Molybdenum oxide is a very commonly used barrier in optoelectronic devices, but the requirements that this kind of interfacial barrier should fulfill in a spintronic device are more severe since the current must preserve its spin polarization along the device.

4.2 Results and Discussion

4.2.1 Thin Films of Phosphomolybdate

The molecular structure of the phosphomolybdate anion with formula $[PMo_{12}O_{40}]^{3-}$ is shown in Figure 4.2 where a central $PO_4{}^{3-}$ phosphate anion is surrounded by 12 MO_6 in a Keggin-type structure.

Although the $H_3PMo_{12}O_{40}$ exhibits good solubility in a wide variety of solvents, it tends to aggregate when deposited on substrates. To solve this problem, POMs are

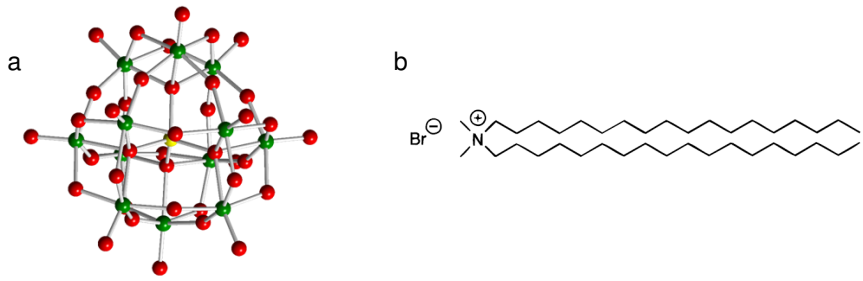

Figure 4.2 a) Molecular structure of the $[PMo_{12}O_4]^{3-}$ Keggin anion in the ball-and-stick representation where P is in yellow, Mo in green and O in red. b) Molecular structure of of DODABr or dimethyldioctadecylammonium bromide ($[CH_3(CH_2)_{17}]_2N(Br)(CH_3)_2$).

usually deposited by the Langmuir-Blodgett (LB) technique where a layer of dimethyldioctadecylammonium (DODA) and a POM layer are alternated.[16] However, the films obtained by LB are too thin. Thus, in order to obtain thicker films, we made a POM-DODA solution to form films by means of spin coating. The DODA cation stabilizes the film avoiding aggregation. The resulting homogeneous films have a salt-type amorphous structure in which DODA moieties are surrounding the POM anions.

The structure of the DODABr is shown in Figure 4.2c. We have checked its isolating character, otherwise characteristic of aliphatic compounds, by depositing thin films on an interdigitated electrode with a 5 μm bandgap. The resistances measured were above 20 GΩ. Thus, in principle we can electrically see the film as a set of POM semiconductive islands in a DODA insulating matrix.

Thin layers are deposited from a yellow solution of $DODA_3PMo_{12}O_{40}$. Initially, two solutions of $H_3PMo_{12}O_{40}$ in H_2O and DODABr in chloroform are placed in a separating funnel. The two phases exchange an ion upon forceful stirring, the POM is transferred to the organic phase while the bromide moves to the aqueous phase. After a while, when the two phases separate again the organic part is collected. Subsequently it is used to spin coat thin layers on the substrates. Then, film characterization was performed by means of infrared (IR) spectroscopy, profilometry, atomic force microscopy (AFM) and absorption measurements.

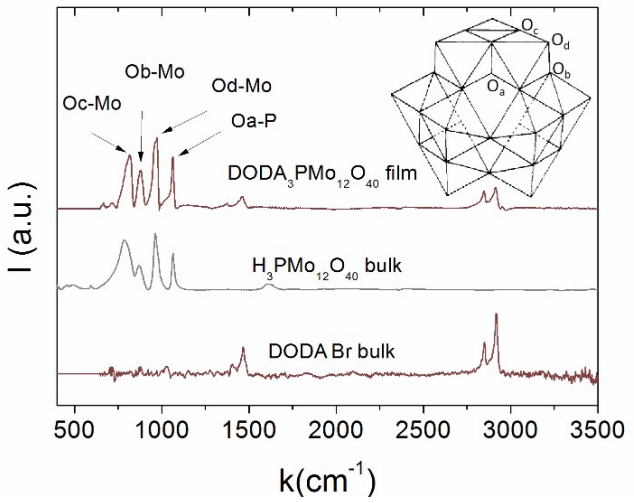

Figure 4.3 IR spectrum of a $DODA_3PMo_{12}O_{40}$ film compared to IR spectra of DODABr and $H_3PMo_{12}O_{40}$ in KBr. The contribution in the range [2000, 2500] cm^{-1} of CO_2 has been subtracted from all spectra. The four different O sites in the Keggin structure are illustrated in the inset.

Figure 4.3 shows the IR spectrum of a $DODA_3PMo_{12}O_{40}$ film compared to the spectra of DODABr and $H_3PMo_{12}O_{40}$ in KBr. The characteristic vibration modes of the POM locate in the range [1100, 750] cm^{-1}.[17] Oxygen atoms occupy four inequivalent sites (a, b, c and d) in the Keggin structure as illustrated in the inset of Figure 4.3. The peak located around 1064 cm^{-1} is associated to the $P-O_a$ vibration whereas the peak located at 961 cm^{-1} corresponds to the $Mo-O_d$ vibration. The peak located at 871 cm^{-1} coincides with the interaction $Mo-O_b$ and the interaction $Mo-O_c$ is located around 785 cm^{-1}.[18] Concerning the DODABr IR signal, the peaks around 1500 cm^{-1} can be assigned to the interaction of the CH_2 groups with N^+. Also, the vibration bands near 3000 cm^{-1} are ascribed to the antisymmetric and symmetric stretching modes of the $=CH_2$ vibration.[19] The contribution of CO_2 located in the range [2400, 2300] cm^{-1} has been removed from all spectra.

The thickness of the layers is determined by profilometry with a prior scratching of

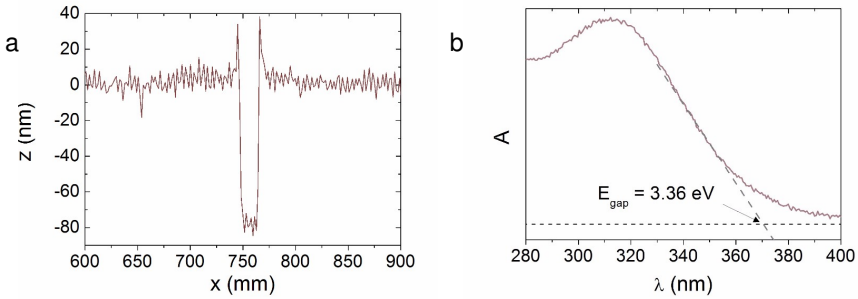

Figure 4.4 a) Profilometry of a 80 nm film of $DODA_3PMo_{12}O_{40}$. b) Absorbance of a $DODA_3PMo_{12}O_{40}$ film of 80 nm and optical bandgap calculation.

the molecular layer with a wooden toothpick, which is possible thanks to the softness of the POM-DODA film. As an example, Figure 4.4a shows the profile measured of a $DODA_3PMo_{12}O_{40}$ film of 80 nm.

Alternatively, the quality of the surfaces is examined by means of atomic force microscopy (AFM) as depicted in Figure 4.5 where the topography image of a zone of 500 μm 500 x μm, the profile at medium height (gray line) and the histogram are shown. The RMS roughness of the AFM topography image amounts to 4.4 nm whereas the peak to peak roughness is 31 nm, values which are relatively low for a 100 nm thick film. The histogram reveals that the medium grain height is around 16 nm.

In summary, we confirmed that the $DODA_3PMo_{12}O_{40}$ films are formed and deposited properly. Besides, they show good substrate coverage and uniformity so that they can be included in multi-layered sandwich-type structures such as molecular spin valves.

In terms of HOMO-LUMO energetic distance, a gap of 2.03 eV was calculated theoretically for the isolated $[PMo_{12}O_{40}]^{3-}$ anion.[7] As expected, this value differs from the HOMO-LUMO gap of the POM-DODA film determined experimentally by means of the onset of the absorbance curve.[20] Figure 4.4b shows the absorbance spectrum of the $DODA_3PMo_{12}O_{40}$ film where an energetic gap of 3.36 eV is ob-

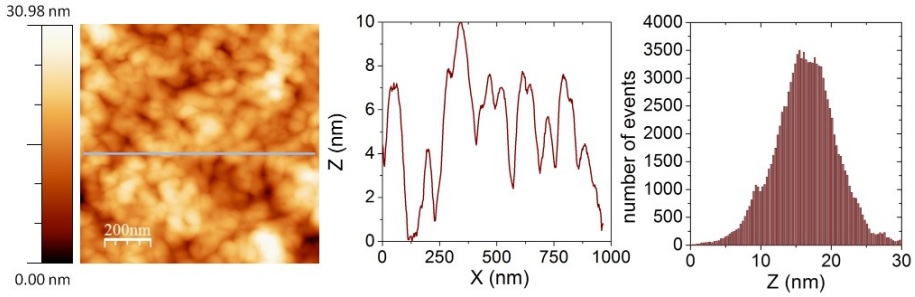

Figure 4.5 AFM topography image (left), profile at medium high (center) and histogram (right) of a 100 nm film of $DODA_3PMo_{12}O_{40}$. The RMS roughness is 4.4 nm and the peak to peak roughness amounts to 31 nm.

tained. Although the absorbance tail provides a good estimation of the HOMO-LUMO distance, note that the electrical bandgap is higher. In principle, the Coulombic interaction makes the optical bandgap in general smaller than the electrical bandgap, since the photogenerated electron-hole pair is strongly bounded. In the electrical bandgap case, the addition of an electron to the LUMO (reduction) or a hole to the HOMO which is equivalent to remove an electron (oxidation), does not create a bounded electron-hole pair and the energetic distance or electric bandgap is higher.[21]

4.2.2 Design of the Molecular Spin Valves

The first POM-based MSV studied in this chapter is designed without any kind of thin barrier and with $La_{0.7}Sr_{0.3}MnO_3$ (lanthanum strontium manganite or LSMO) and cobalt as bottom and top electrodes respectively in the structure:

$$LSMO / DODA_3PMo_{12}O_{40} / Co$$

The POM-based layers are deposited by means of solution methods and thus an air-stable ferromagnetic bottom electrode as LSMO is needed. LSMO exhibits a

perovskite structure consisting on a lanthanum manganite where some of the lanthanum atoms have been substituted by strontium atoms. But its real potential for spintronics relies in its half metal behavior. Ideally, the LSMO acts as electrical conductor for the majority spins and as insulator for minority spins, thus injecting 100 % spin polarized current. In practice, the LSMO spin polarization at the Fermi level is very high compared to cobalt or permalloy (P_{Co}, $P_{NiFe} \approx 40$ % whereas $P_{LSMO} \approx 80-95$ %).[22,23] However, one of the disadvantages of the LSMO is that its Curie temperature is well below the cobalt and permalloy Curie temperatures (T_C(LSMO) = 325 K, T_C(Co) = 1388 K, T_C(NiFe) = 870 K).[12,24,25]

The energy level alignment between the different interfaces in the MSV will determine the device performance. The energy difference between Fermi level (E_F) and vacuum level is known as the ionization energy (IE), i.e., the minimum amount of energy needed to remove an electron from the material that, in case of metals, coincides with the metal work function (ϕ). In our device, the LSMO work function is located at -4.4 eV whereas the work function of Co is located at -5 eV.[26]

The energetic position of the highest occupied molecular orbital (HOMO) of the POM-DODA film has been measured by ultraviolet photoemission spectroscopy[27] or UPS which is based on the photoelectric effect and the Einstein relation:

$$h\nu = E_{\text{Binding}} + E_{\text{k}} \tag{4.1}$$

where hν is the energy of the incident photons (21.2 eV for He I and 40.8 eV for He II), $E_{Binding}$ is the energy necessary to extract an electron from the material to the vacuum level and E_k is the kinetic energy of the photoelectron.

Since the photon energy is fixed, the electrons with the highest kinetic energy come from the Fermi level while the electrons at the cut-off edge are the slowest electrons with $E_k = 0$ after leaving the surface. Thus, the metal work function can be calculated as the difference between the energy of the incident photons and the cut-off at high binding energy. In the case of molecular layers, the maximum kinetic energy in the UPS spectrum belongs to electrons in the HOMO level of the semicon-

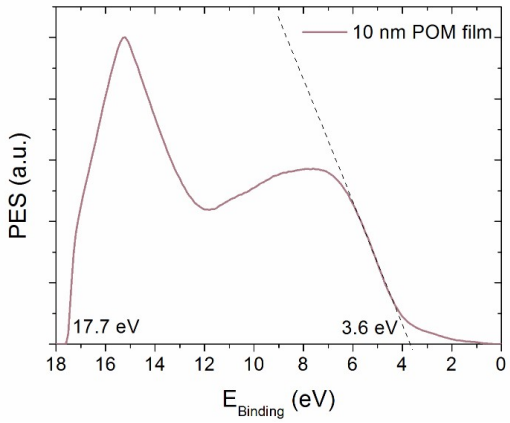

Figure 4.6 UPS spectrum of a 10 nm POM-DODA film.The position of the HOMO with respect to the vacuum level is -7.1 eV.

ductor ($\epsilon^{F}{}_{vac}$) referenced to the E_F of the underlying metallic reference. The energy of the HOMO level (E_{HOMO}), referenced to the vacuum level, can be calculated from:

$$E_{\text{HOMO}} = \epsilon^{F}{}_{v} + \epsilon^{F}{}_{\text{vac}} \tag{4.2}$$

where $\epsilon^{F}{}_{v}$ is the onset of the spectrum referenced to the E_F of the metal and $\epsilon^{F}{}_{vac}$ = hν - $E_{cut\text{-}off}$.

Figure 4.6 shows the UPS spectrum of a 10 nm POM-DODA film on a gold substrate. The origin of binding energy coincides with the Fermi level of an underlying the gold reference sample. The spectrum was generated by integrating the whole reciprocal event horizon, because the set-up is not limited in detection angle, which results in a less pronounced low energy cut-off. The valence band onset of the molecular film is located at 3.6 eV with respect to the Fermi level of the metal and the $E_{cut\text{-}off}$ is 17.7 eV, leading to a $E_{HOMO} = -7.1$ eV.

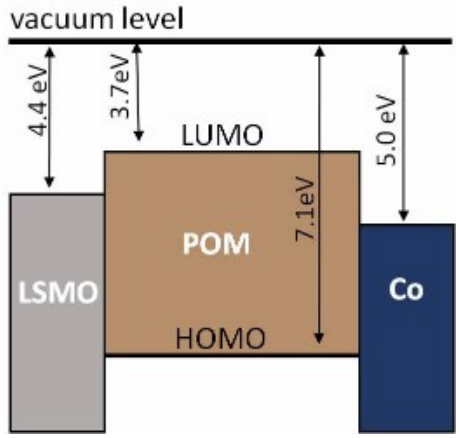

Figure 4.7 Energy level alignment in the molecular spin valves: LSMO (20 nm) / POM (100 nm) / Co (25 nm).

4.2.3 MR of the LSMO / POM / Co Spin Valve

Figure 4.7 shows the structure and energy level alignment in the devices. The HOMO of the POM-DODA film is located at -7.1 eV while the LUMO is at -3.7 eV, as calculated from the optical bandgap obtained from the absorbance onset. The charge transport is expected to be carried by electrons rather than hole since both work functions of the electrodes are closer to the LUMO of the POM layer. The thicknesses of the layers are:

$$\text{LSMO (20 nm) / } \text{DODA}_3\text{PMo}_{12}\text{O}_{40} \text{ (100 nm) / Co (25 nm)}$$

The IV curve at 290 K is shown in Figure 4.8a with a resistance value of 55 kΩ, this value is low for a 100 nm molecular layer, indicating that the top electrode created thin molecular regions. Besides, the Simmons fit gives an effective molecular layer thickness of 3.3 $\pm$ 0.1 nm which is much thinner than the nominal thickness (100 nm). This molecular layer reduction is caused by the impact of the cobalt electrode upon evaporation. Although the effective energy barrier obtained from the fit

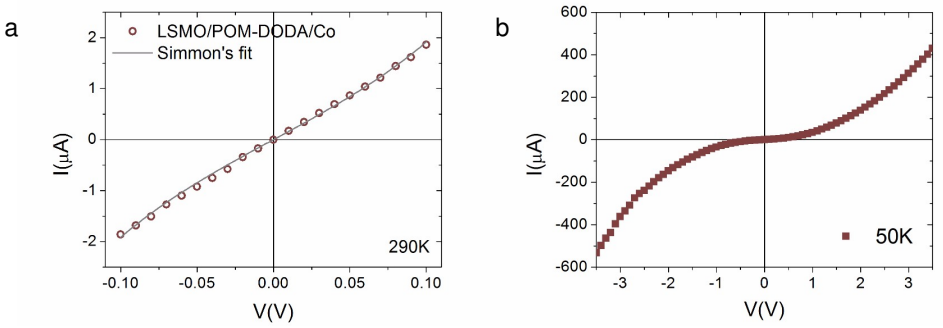

Figure 4.8 IV curve measured at 290 K for the device LSMO / POM-DODA / Co with a nominal molecular thickness of 100 nm and the fit to the Simmons model (solid line).[28] The fit parameters obtained are ϕ_{eff} = 0.6 $\pm$ 0.1 eV and an effective thickness d_{eff} = 3.3 $\pm$ 0.1 nm. b) IV curve at 50 K.

amounts only to 0.6 $\pm$ 0.1 eV, the tunnel probability is high for molecular layers thinner than 10 nm.[29] In fact, the tunneling regime is confirmed with the weak thermal dependence of the resistance as seen when comparing the IV curves at 290 K (Figure 4.8a) and 50 K (Figure 4.8b). Besides, the barrier height obtained by Simmons is similar to the equivalent barrier obtained from the energy level alignment (LUMO$-\phi_{LSMO} = 0.7$ eV), which shows the goodness of the fit.

Moreover, most MSVs tend to break for applied voltages above 1.5 V. However, the IV curve at 50 K is measured up to $\pm$3.5 V demonstrating the robustness of the junction. At these high voltages if there were small conductive channels or pinholes, they would burn, and the sample would be short-circuited or in a very high resistance state, which are not the cases.

Figure 4.9 shows the magnetic characterization of the device at 50 K. A maximum magnetoresistance response of 7.5 % has been measured at 0.1 V. This MR value is very similar to the 7.4 % measured at $-$0.1 V. The magnetoresistance curves follow the coercive fields of the electrodes (see the hysteresis loop measured in Figure 4.9f). The coercive field of LSMO is around 50 Oe. However, the high coercive field of cobalt ($\approx$1000 Oe) may be indicating the presence of cobalt oxide and/or high

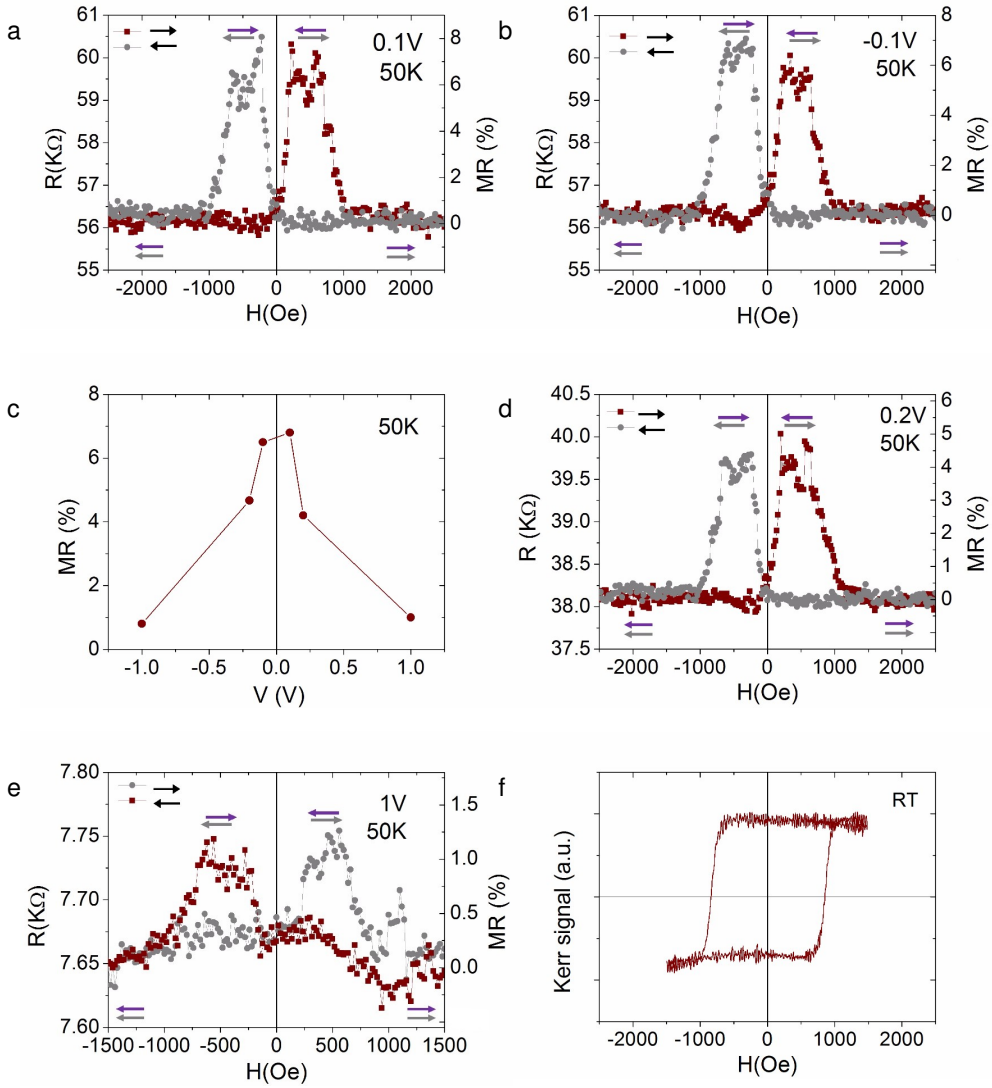

Figure 4.9 Electric and magnetic characterization at 50 K of the LSMO / POM-DO-DA / Co device. a) Maximum MR measured at 0.1 V of 7.5 %. b) MR=7.4 % at −0.1 V. c) Voltage dependence of the MR. d) MR=4 % at 0.2 V. e) MR=1 % at 1 V. f) Hysteresis loop of the cobalt layer in the MSV at room temperature where the coercive field can be appreciated. In the MR curves the LSMO signal has been subtracted as explained in appendix B.

roughness of the Co layer.

When the voltage is increased, the magnetoresistance shows a strong dependence with voltage, as in most MSVs and magnetic tunnel junctions reported, and above 1 V the MR signal is lost (see Figure 4.9c). The strong voltage dependence is commonly attributed to magnons.[30] The resistance of the antiparallel state drops more abruptly with the voltage compared to the resistance of the parallel state. This, known as zero bias anomaly, causes the MR to be higher at voltages close to zero bias and to decrease abruptly at voltages below 1 V. The zero bias anomaly can not be attributed to the fact that the carriers have overcame the insulating barrier, since the voltages at which it occurs are too low. Under a bias voltage, electrons with energies above the Fermi level (termed "hot electrons") are responsible for the low voltage quenching of the MR by producing local collective excitations at the interfaces between the insulating layer and the ferromagnetic electrodes.[30]

4.2.4 The Molybdenum Oxide Barrier

Molybdenum oxide[31] is a well known material in the molecular electronics field.[31,32] It has been used as hole injection layer (HIL) in molecular optoelectronic devices,[33–37] due to its deep conduction band, which shows energies ranging from -5.5 to -6.7 eV, depending on the deposition conditions and surface contaminations.[13] In fact, it has been recently demonstrated that MoO_x creates an interfacial dipole in the M / MoO_x interface (where M = Au, Al, Co) that increases the metal work function enhancing the device performance.[14]

Prior to the incorporation of the MoO_x in the spintronic devices we have performed X-ray photoemission spectroscopy (XPS) and spin resolved ultraviolet photoemission spectroscopy[38] (UPS) in a Co / MoO_x bilayer to evaluate the oxidation states in the MoO_x layers and the modification of the Co work function together with the spin polarization. Both XPS and UPS are based on the photoelectric effect but the information obtained from each technique is different. Besides, the penetration depth is around 10 nm for XPS while UPS is more surface sensitive.[39] XPS is a

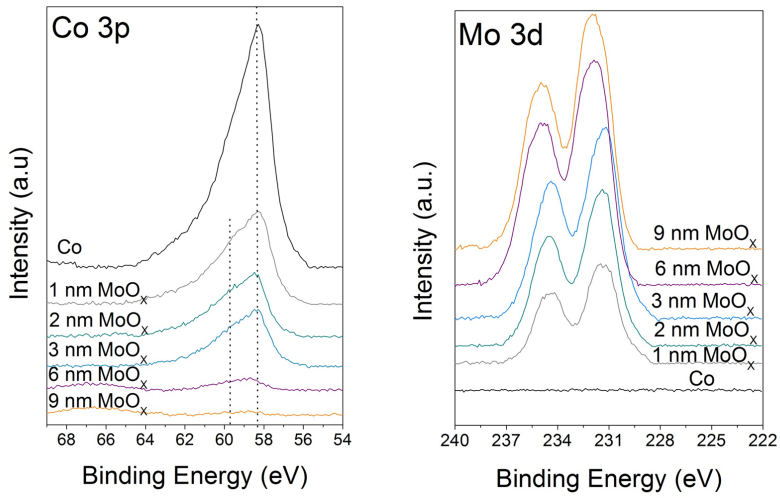

Figure 4.10 XPS study of Co / MoO_x bilayers with MoO_x nominal thicknesses of 0, 1, 2, 3, 6 and 9 nm. The evolution of the Co 3p core level as a function of MoO_x thickness is shown on the left and the evolution of the Mo 3d core level spectra for the same samples is shown on the right. The oxidation of the Co caused by the MoO_x can be inferred by the emergence of the peak located at 59.7 eV.

powerful technique to determine the oxidation states of the atoms in a film where incident X-rays provoke the emission of photoelectrons. The difference between the energy of the incident photon and the kinetic energy of the photoelectron is the binding energy characteristic of each element.

In a first step, MoO_x layers with different thicknesses (y = 0, 1, 2, 3, 6, 9 nm) were thermally evaporated in high vacuum on a $Si-SiO_2$ / Co (25 nm) substrate and characterized via XPS measurements. Figure 4.10 shows the Co 3p spectra for increasing thicknesses of MoO_x. The peaks located at 58.3 and 59.7 eV are associated with pristine cobalt and cobalt oxide respectively. The analysis of the spectra reveals that after 1 nm of MoO_x deposition, the cobalt layer is partially oxidized. The same layers are evaluated in the Mo 3d region as seen in Figure 4.11. We observe three different oxidation states of molybdenum located[40] at 229.8 (Mo^{4+}), 231.2 (Mo^{5+})

and 232.6 (Mo^{6+}) eV. In layers with MoO_x thicknesses below 1 nm only Mo^{4+} and Mo^{5+} are present. This molybdenum reduction is related with the cobalt oxidation at the interface. Besides, the interfacial cobalt oxide layer avoids oxygen diffusion and reaction.

In a second step we have performed the spin-resolved ultraviolet photoemission spectroscopy (UPS) experiments to investigate both the electronic structure at the Co / MoO_x interface, as well as the effect of the MoO_x barrier on the spin polarization of the magnetic electrode.

The UPS experiment was done for the same MoO_x thicknesses used in the XPS analysis, with the aim of evaluating the impact of this parameter on the properties previously mentioned. The same MoO_x material employed for the fabrication of the device and XPS study was evaporated directly on top of the Co without breaking the vacuum. The thickness of the MoO_x layer was increased stepwise from 0 to 9 nm. Figure 4.12a shows the UPS spectra recorded for increasing MoO_x thickness. The spectra present two main features: a peak located at -0.4 eV that corresponds to a Co$-$3d bulk transition, and spectroscopic features located between -3 eV and -10 eV, that correspond to O$-$2p derived states in the valence band structure of MoO_x. For increasing MoO_x thickness, we observe an exponential decrease of the Co-3d bulk peak intensity. This is a reasonable value for the inelastic mean free path of electrons with kinetic energy of approximately 20 eV in an insulating material such MoO_x, thus giving strong indication for homogeneous layer-by-layer growth of the MoO_x layer on the cobalt surface. The MoO_x valence band features, on the other hand, are clearly resolved in the UPS spectra above the nominal thickness of 1 nm, and their spectral weight progressively increases for increasing MoO_x thickness.

Figure 4.12b shows the low-energy cut-off of the UPS spectra that reflects the work function of the sample. By deposition of MoO_x on top of the cobalt surface, we observe a progressive shift of the low-energy cut-off towards the Fermi level, corresponding to a progressive increase of the work function. For the nominal thickness of MoO_x of 9 nm, we observe an increase of 1.37 eV. This effect is in total accordance with previously reported works on UPS studies of this particular system.[14]

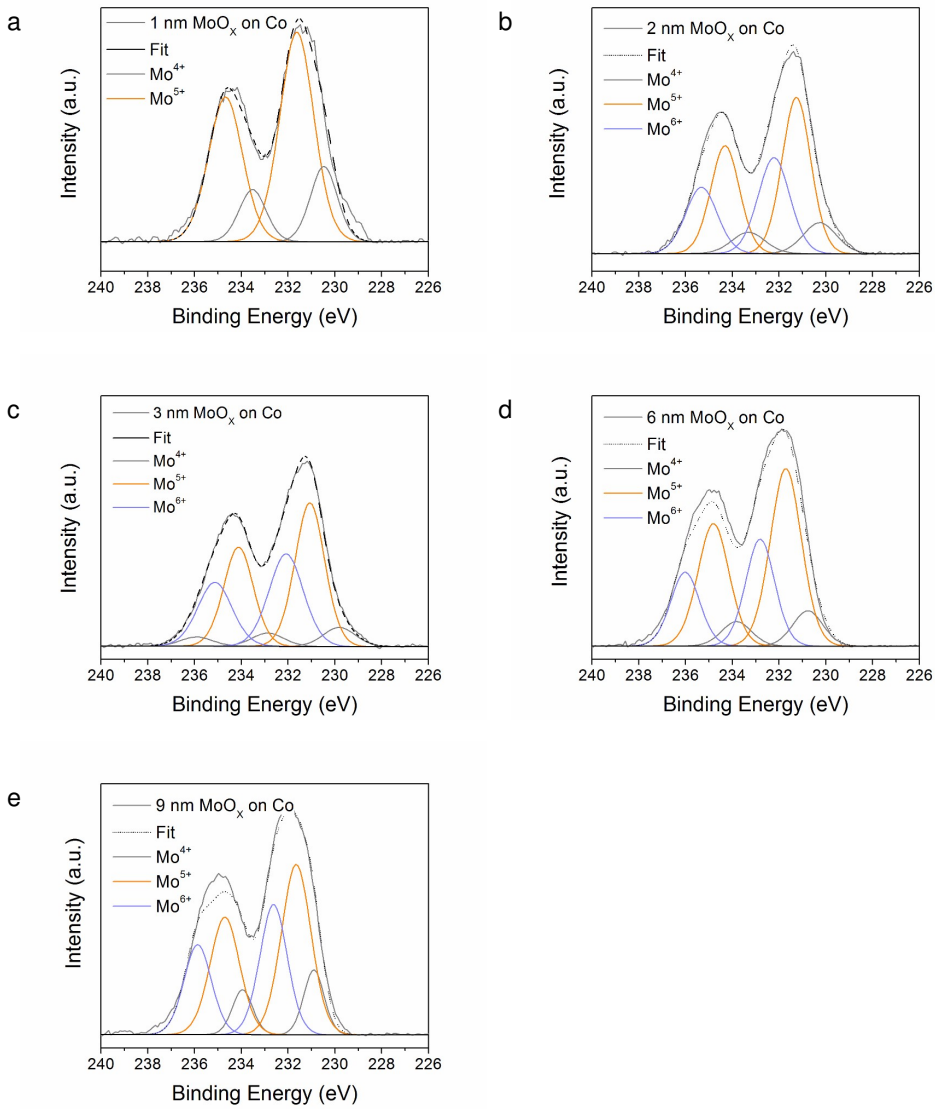

Figure 4.11 XPS study of Co / MoO_x bilayers with different MoO_x nominal thicknesses. a) 1 nm MoO_x. b) 2 nm MoO_x. c) 3 nm MoO_x. d) 6 nm MoO_x. e) 9 nm MoO_x. The oxidation states of molybdenum are located at 229.8 (Mo^{4+}), 231.2 (Mo^{5+}) and 232.6 (Mo^{6+}) eV.[40]

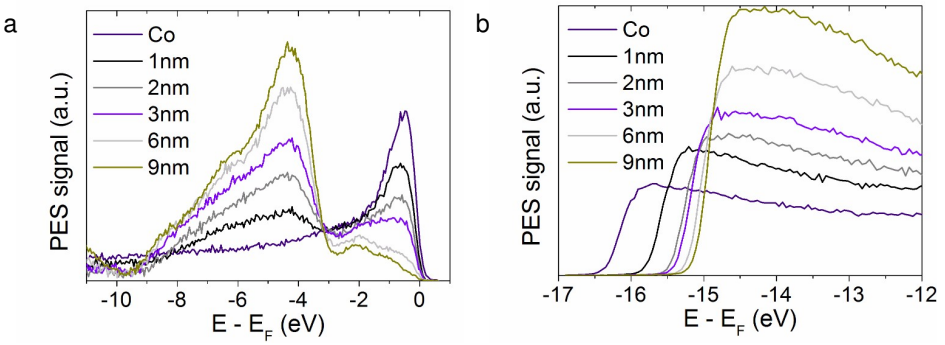

Figure 4.12 a) UPS spectra of a Co / MoO_x interface as a function of the MoO_x thickness (from 0 nm to 9 nm) in which the secondary electron background has been subtracted. b) Low-energy cut-off of the UPS spectra without subtraction of the secondary electron background. The Co work function for a MoO_x thickness of 3 nm is $\phi_{Co} = h\nu - E_{cut\text{-}off} = -5$ eV.

The formation of an interface dipole with its negative terminal pointing to the MoO_x can be ascribed to this overall vacuum level shifting. From the perspective of the device, this important upward shifting in the vacuum level is translated into a reduction of the hole injection barrier, when using this oxide as a buffer layer.

In the field of optoelectronics there are many works focused on the understanding of the interface between MoO_x and molecular semiconductors. It has been shown how, thanks to its deep conduction band, MoO_x interacts via the formation of charge transfer states by accepting electrons from the HOMO of the molecular material. These mechanisms create a doped injection layer that is responsible for the enhanced hole injection properties of MoO_x in molecular electronic devices.

This effect of the oxide buffer layer on the interface with a molecular semiconductor was confirmed by comparing the photoemission spectroscopy (PES) signal of an Alq_3 layer on top of pristine Co and onto Co / MoO_x. There is a clear shifting of all molecular states 0.75 eV towards the Fermi level (see Figure 4.13). Thus, the presence of the MoO_x at the interface is reducing the hole injection barrier from

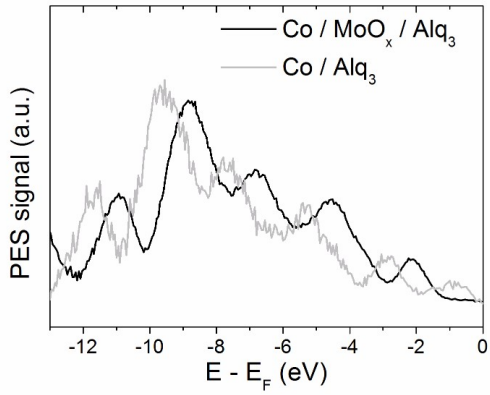

Figure 4.13 Comparison of the UPS spectra of Alq_3 on Co (black curve) and Alq_3 on Co / MoO_x (gray curve).

Co to Alq_3 which is translated into a shifting of all molecular states to lower binding energies previously reported for other molecular semiconductors.

Finally, we performed spin-resolved UPS on the samples with the objective of choosing the proper thickness of molybdenum oxide when including it in a spintronic device. Figure 4.14 shows the results of the spin-resolved UPS measurements, where we determine the number of photoemitted majority and minority electrons, N^{up} and N^{down} respectively. In particular, we measure the spin component along the direction of the cobalt easy axis. The definition of majority and minority electrons is the same for the Co substrate and the Co / MoO_x system. The spin polarization P at the energy $E - E_F$ is then calculated from N^{up} and N^{down} as:

$$P(E - E_F) = \frac{N^{up}(E - E_F) - N^{down}(E - E_F)}{N^{up}(E - E_F) + N^{down}(E - E_F)} \tag{4.3}$$

The shape and value of the measured spin polarization give information about the changes in the magnetic properties of the Co electrode as the MoO_x layer is deposited on top. Up to a nominal MoO_x thickness of 3 nm, the spin polarization close

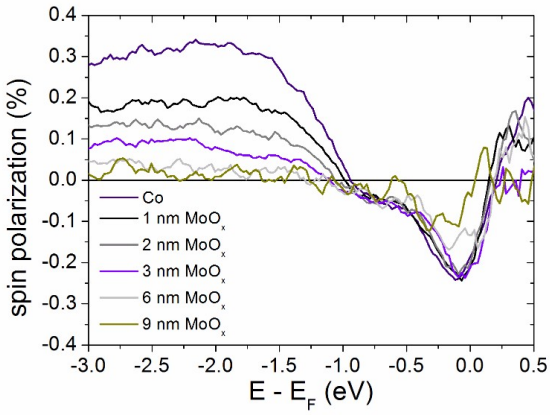

Figure 4.14 Spin polarization of the Co / MoO_x system as a function of MoO_x thickness (varied between 0 nm and 9 nm).

to the Fermi level is virtually unaffected by the presence of MoO_x. When the thickness of MoO_x was higher than 3 nm, we observe a progressive reduction of the spin polarization close to the Fermi level. For 9 nm MoO_x thickness the measurements exhibit a very poor signal-to-noise ratio, due to the extremely low photoelectron yield at this energy. The spin polarization for energies below -1 eV shows a different behavior: here, the absolute value of P decreases progressively with increasing MoO_x thickness. We explain the different behavior in this energy region with the presence of unpolarized electrons in the photoemission spectra originating from MoO_x.

We conclude that the optimal thickness of the MoO_x layer for our devices is 3 nm. Note that it is a much thinner layer than the one commonly used in optoelectronics.

4.2.5 MR of the LSMO / POM / MoO_x / Co Spin Valve

The second type of molecular spin valves studied in this chapter incorporate a 3 nm layer of molybdenum oxide between the molecular layer and the top electrode. The structure and layer thicknesses are:

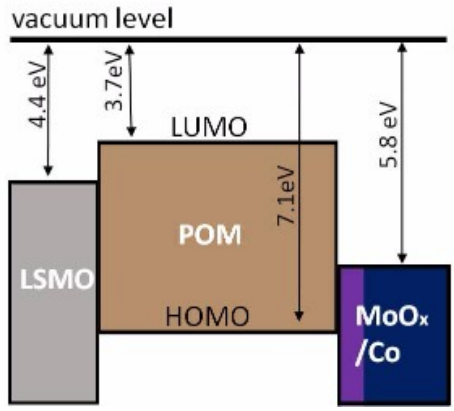

Figure 4.15 Energy level alignment in the molecular spin valve with nominal thicknesses and structure: LSMO (20 nm) / POM (80 nm) / MoO_x (3 nm) / Co (25 nm).

LSMO (20 nm) / $DODA_3PMo_{12}O_{40}$ (80 nm) / MoO_x (3 nm) / Co (25 nm)

In most MSVs reported, a thin oxide barrier is deposited between one of the ferromagnetic electrodes and the molecular layer with the objective to enhance the device performance.[41] In general, the oxide barrier modifies the work function of the electrode on which it is deposited, in a manner similar to MoO_x and Co.[21] Besides, if the thin oxide layer is placed on the bottom electrode, it serves as seed layer where the molecular material may grow better. While if the barrier is placed between the molecular material and the top electrode, it helps to avoid the formation of an ill-defined layer by preventing the interpenetration of the top electrode upon sublimation.[42]

The alignment of the energy levels of the different layers obtained from the UPS measurements is shown in Figure 4.15. The LSMO work function is aligned with the LUMO of the molecular layer whereas the MoO_x / Co is aligned with the HOMO facilitating the bipolar transport by holes and electrons. However, the current flowing through the junction at high as shown in Figure 4.16a. Thus, the electrical transport measurements indicate that carriers tunnel between electrodes, without hopping transport in the molecular material.

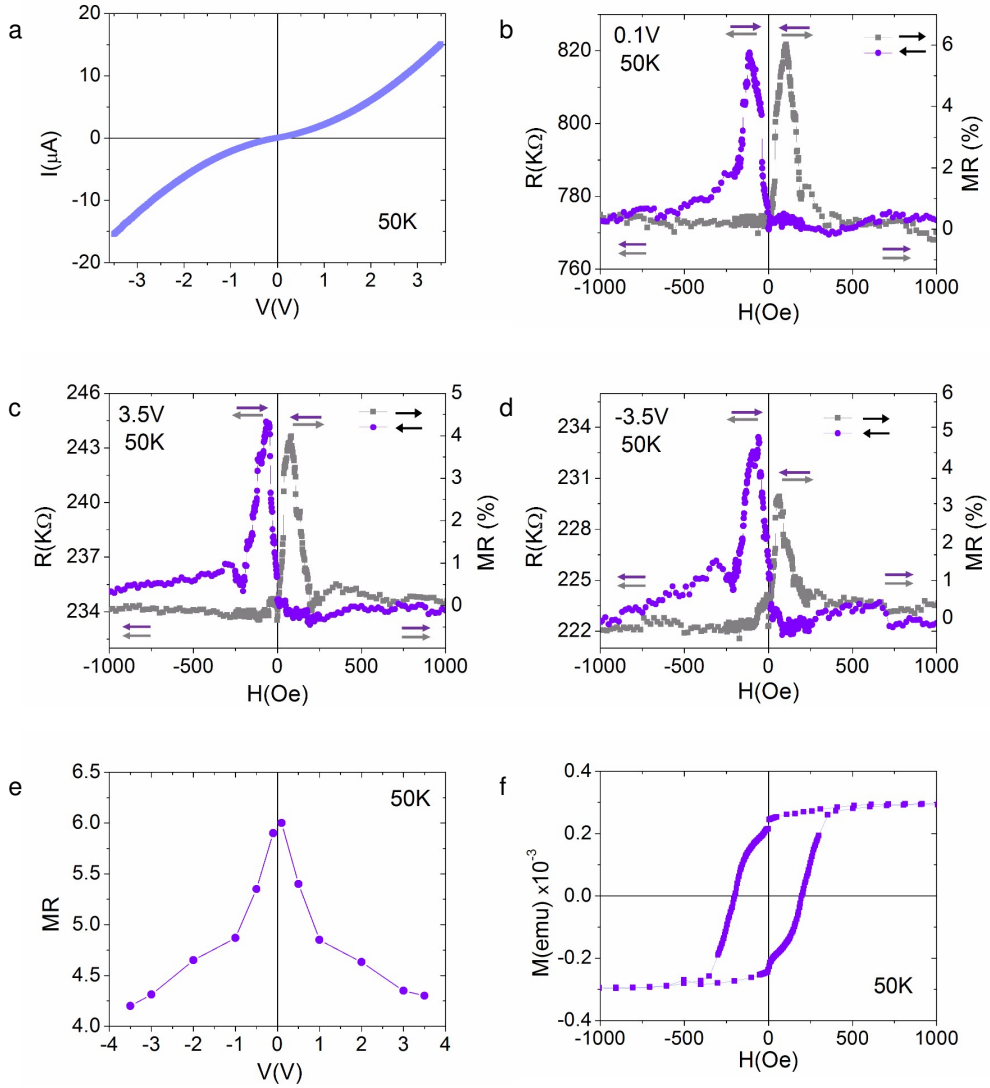

Figure 4.16 Electric and magnetic measurements at 50 K in the device LSMO / POM-DODA / MoO_x / Co. a) IV curve. b) MR = 6 % at 0.1 V. c) MR = 5.9 % at −0.1 V. d) MR = 3.2 % at −3.5 V. e) MR = 3.6 % at 3.5 V. f) Hysteresis loop at 50 K where the coercive fields of LSMO (20 Oe) and cobalt (210 Oe) can be appreciated. In the MR curves the LSMO signal has been subtracted as explained in appendix B.

An analogous characterization at 50 K to the LSMO / POM / Co spin valve shown in Figure 4.9 has been performed for the LSMO / POM / MoO_x / Co spin valve as seen in Figure 4.16. The MR curves follow the coercive fields of the electrodes (see Figure 4.16f). Although the XPS data demonstrated that the cobalt layer is oxidized and consequently, the coercive field should be high, the H_c of cobalt in the MSV with MoO_x is smaller than the H_c of cobalt in the MSV without MoO_x. Apart from that, the value of the MR = 6 % at 0.1 V is lower than the MR measured in the MSV without MoO_x (7.5 %) probably due precisely to the spin depolarization that the MoO_x layer introduces.

However, the most surprising fact is that the MR does not fall abruptly with the voltage, as it usually does in MTJs[30] and MSVs.[41] This behavior has been previously reported in a molecular nanojunction with the structure LSMO / $CH_3(CH_2)_{11}PO_3H_2$ / Co.[43] The transport in their device is also governed by tunneling and the TMR is maintained up to 2 V. They conclude that the orbital matching might be the reason for the MR at high voltage.

Moreover, a similar MR voltage dependence has been observed in a bipolar MSVs with the structure LSMO / D-DOO-PPV / LiF / Co where the LiF layer played the role of the MoO_x.[44,45]

In our case, the MSV without molybdenum oxide loses the MR signal at low voltage ($\approx$1 V), while the MSV with MoO_x shows MR signal up to $\pm$3.5 V. This seems to indicate that the modification of the Co work function is related to the MR at high voltage, even though carriers tunnel between electrodes.

4.3 Conclusions and Perspectives

In this chapter we have studied two molecular spin valves based on the polyoxometalate phosphomolybdate, which constitute the first example of MSVs based on POMs. Both types of MSVs studied differ only in the MoO_x barrier. There is a twofold objective for these devices: the incorporation for the first time of a POM-

based molecular layer in a MSV and the study of the role of the MoO_x barrier. The energy levels of the layers in the devices and the optimum thickness of the molybdenum oxide layer have been studied by UPS.

With regard to MR, we should stress that the LSMO / POM / MoO_x / Co spin valve shows magnetoresistance up to $\pm$3.5 V. Although the reasons for the maintenance of the MR signal up to high voltages are not completely understood, the sheer fact is very interesting in terms of applications.

In the next chapter of this manuscript it is demonstrated that the MR at high voltage is intimately related to the bipolar transport in the device together with a proper energy alignment of the interfaces.

4.4 Experimental Details

All the materials employed for the fabrication of the spin valves are commercial and were used directly as received from the provider. Prior to device fabrication a cleaning procedure is followed. Samples are rubbed in a solution of the liquid alkaline detergent Mucasol in distilled water during 5 minutes. After that, substrates are sonicated in three different solutions during 10 minutes each time: Mucasol-distilled water, isopropanol and distilled water. Later they are dried in a N_2 gas flow.

The $H_3PMo_{12}O_{40}$ is dissolved in 50 ml of milli-Q water and the DODABr in 50 ml of chloroform, in proportion $H_3PMo_{12}O_{40}$ [1:3] DODABr. The POM solution is yellow and the DODA solution is colorless. The solutions are united in a separating funnel and stirred vigorously during 5 minutes. The two phases are mixed and come in contact enough for ion exchange. The $PMo_{12}O_{40}{}^{3-}$ moves to the organic phase while the Br is transferred to the aqueous phase. When the two phases separate again the organic phase is collected. The 20 nm thick LSMO electrode was grown by channel spark ablation (CSA)[46] on (100) oriented double-side polished $SrTiO_3$ substrates. Molecular layers are deposited by means of a spin coater model KW-4A from Chemat Technologies at rotation speeds of 2000 rpm and 1700 rpm for the 80

nm and the 100 nm films respectively. The MoO_x barrier, Co electrode and Au protective layers are thermally evaporated using shadow masks at a base pressure of 10^{-6} mbar. The active area amounts to 1.5 mm x 500 μm. The $[CH_3(CH_2)_{17}]_2N(Br)(CH_3)_2$ films were spin coated from a solution in chloroform on G-IDEAU5 interdigitated Au electrodes from DropSens with 125 x 2 digits, a digit length of 6760 μm and a 5 μm bandgap.

X-ray photoelectron spectroscopy (XPS) was performed at the facilities of the Universidad de Alicante. A XPS, K-ALPHA Thermo Scientific was used to analyze the films. Spectra were collected using $Al - K\alpha$ radiation (1486.6 eV) with a twin crystal monochromator and yielding a focused X-ray spot (elliptical in shape with a major axis length of 400 μm) at 3 mA C and 12 kV. The alpha hemispherical analyzer was operated in the constant energy mode with survey scan pass energies of 200 eV to measure the whole energy band and 50 eV in a narrow scan to selectively measure the particular elements. The Avantage software was used to analyze the spectra. All spectra were calibrated using the adventitious C1s peak with a fixed value of 284.5 eV. After the calibration, the background was subtracted for each spectrum using a Shirley-type background in order to remove most of the extrinsic loss structure.[47]

Infrared spectra were collected on a Nicolet 5700 FT-IR spectrometer. A Nanoscope Multimode (Veeco) atomic force microscope (AFM) in tapping mode operation was used in the morphological study of all the layers composing the device. WSxM software was used for image processing.[48] The absorbance of the films deposited on quartz substrates was measured with a Cary 300 UV-Vis spectrometer.

The UPS measurements were recorded at the University of Kaiserslautern in collaboration with prof. Mirko Cinchetti from the Ultrafast Phenomena at Surfaces research group at the Department of Physics and research center OPTIMAS. For the photoemission studies, we have deposited 5.4 nm cobalt on a Cu(001) single crystal by electron beam epitaxy with an Omicron EFM-3 evaporator. Deposition was done at a pressure of 10^{-10} mbar. Afterwards the sample was annealed at 370 K. This results in a metastable tetragonally distorted Co fcc film with an in-plane magnetic uniaxial anisotropy along the (110) direction of copper.[49] To detect the spin-

dependent electronic structure of the Co / MoO_x bilayer, we performed spin-resolved ultraviolet photoemission spectroscopy (UPS) in the setup described in Droguetti work.[38] Shortly, the excitation source is an Omicron HIS 13 vacuum ultraviolet lamp, operated at the He I line ($h\nu$ = 21.2 eV). The light incident angle is 45°. The emitted photoelectrons are analyzed in energy and spin by a Focus SPLEED detector mounted on a cylindrical sector analyzer (Focus CSA). The acceptance angle of the detector system is $\pm$ 13° and the energy resolution is 0.22 eV. All presented measurements were performed at room temperature. In the presented UPS spectra of the Co / MoO_x bilayer, the secondary electron background has been removed for a more accurate determination of the peak position, following the procedure described in the literature.[50]

The MR ratio in the MSVs has been calculated taking the parallel configuration of electrode magnetizations as the reference, using the expression MR(%) = ((R_{AP} - R_P)/ R_P) where R_P and R_{AP} are the resistances in the parallel and antiparallel states, respectively. The LSMO contribution in the MR responses has been systematically subtracted from each experimental curve in order to get the net spin valve effect as explained in appendix B. For the MR measurements the chips are positioned between the poles of two coils controlled by a GMHW 231 HC source where magnetic fields up to 4 T can be reached. The voltage is applied and the electrical current is measured by means of a 6517A Keithley electrometer which supplies maximum 20 V and has a precision of hundreds of pA. Samples are kept in vacuum by a Varian pumping system. The thermal variation is reached thanks to a closed loop cryostat (C52045 F, ARS) and a He compressor (ARS). The temperature is controlled by a Cernox sensor and a 332 Temperature Controller (Lakeshore).

The magneto-optical characterization of the cobalt electrode was performed with a self-made Kerr magnetometer. A He-Ne laser with a wavelength of 633 nm and an output power of 12 mW was used as the light source producing a nearly linearly polarized light beam. This beam was passed through a Glan-laser calcite polarizer, which allowed for working with both s-polarized (electric eld perpendicular to the plane of incidence) and p-polarized (electric field parallel to the plane of incidence) configurations The design of the electromagnets and the cryostat allowed the u se

of longitudinal, polar, and transverse geometries. The external magnetic eld range in the polar configuration was $\pm$ 150 mT. The hysteresis loop of Co was measured at room temperature turning the sample upside down.

4.5 Bibliography

[1] E. Coronado and C. J. Gomez-Garcia. “Polyoxometalate-based molecular materials”. Chemical Reviews 98.1 (1998), pp. 273–296.

[2] D. L. Long, R. Tsunashima, and L. Cronin. “Polyoxometalates: building blocks for functional nanoscale systems”. Angewandte Chemie 49.10 (2010), 1736–1758.

[3] U. Kortz, A. Mueller, J. van Slageren, J. Schnack, N. S. Dalal, and M. Dressel. “Polyoxometalates: Fascinating structures, unique magnetic properties”. Coordination Chemistry Reviews 253.19 (2009), pp. 2315–2327.

[4] S. Herrmann, C. Ritchie, and C. Streb. “Polyoxometalate–conductive polymer composites for energy conversion, energy storage and nanostructured sensors”. Dalton Transactions 44.16 (2015), pp. 7092–7104.

[5] D. E. Katsoulis. “A survey of applications of polyoxometalates”. Chemical Reviews 98.1 (1998), pp. 359–388.

[6] J. M. Clemente-Juan, E. Coronado, and A. Gaita-Ariño. “Magnetic polyoxometalates: from molecular magnetism to molecular spintronics and quantum computing”. Chemical Society Reviews 41.22 (2012), pp. 7464–7478.

[7] J. M. Poblet, X. López, and C. Bo. “Ab initio and DFT modelling of complex materials: towards the understanding of electronic and magnetic properties of polyoxometalates”. Chemical Society Reviews 32.5 (2003), pp. 297–308.

[8] J. Keggin. “Structure of the crystals of 12-phosphotungstic acid”. Nature 132 (1933), pp. 351–351.

[9] D. Ciudad, M. Gobbi, C. J. Kinane, M. Eich, J. S. Moodera, and L. E. Hueso. “Sign control of magnetoresistance through chemically engineered interfaces”. Advanced Materials 26.45 (2014), pp. 7561–7567.

[10] S. S. Parkin, C. Kaiser, A. Panchula, P. M. Rice, B. Hughes, M. Samant, and S.-H. Yang. “Giant tunnelling magnetoresistance at room temperature with MgO (100) tunnel barriers”. Nature materials 3.12 (2004), pp. 862–867.

[11] Y. Zhou, C. Fuentes-Hernandez, J. Shim, J. Meyer, A. J. Giordano, H. Li, P. Winget, T. Papadopoulos, H. Cheun, J. Kim, et al. “A universal method to produce low–work function electrodes for organic electronics”. Science 336.6079 (2012), pp. 327–332.

[12] V. Dediu, L. Hueso, I. Bergenti, A. Riminucci, F. Borgatti, P. Graziosi, C. Newby, F. Casoli, M. De Jong, C. Taliani, et al. “Room-temperature spintronic effects in Alq_3-based hybrid devices”. Physical Review B 78.11 (2008), p. 115203.

[13] Y. Z. Wang, L. Cao, D. C. Qi, W. Chen, A. T. S. Wee, and X. Y. Gao. “Tuning the interfacial hole injection barrier between p-type organic materials and Co using a MoO_3 buffer layer”. Journal of Applied Physics 112.3 (2012), p. 033704.

[14] Y. Z. Wang, M. Yang, D. C. Qi, S. Chen, W. Chen, A. T. S. Wee, and X. Y. Gao. “A synchrotron-based photoemission study of the MoO_3Co interface”. Journal of Chemical Physics 134.3 (2011), pp. 1–7.

[15] A. Ulman. An Introduction to Ultrathin Organic Films: From Langmuir–Blodgett to Self–Assembly. Academic press, 1991.

[16] M. Clemente-Leon, B. Agricole, C. Mingotaud, C. Gomez-Garcia, E. Coronado, and P. Delhaes. “Toward new organic/inorganic superlattices: Keggin polyoxometalates in Langmuir and Langmuir- Blodgett films”. Langmuir 13.8 (1997), pp. 2340–2347.

[17] J. Qiu, G. Wang, D. Zeng, Y. Tang, M. Wang, and Y. Li. “Oxidative desulfurization of diesel fuel using amphiphilic quaternary ammonium phosphomolybdate catalysts”. Fuel Processing Technology 90.12 (2009), pp. 1538–1542.

[18] C. Rocchiccioli-Deltcheff, M. Fournier, R. Franck, and R. Thouvenot. “Vibrational investigations of polyoxometalates. 2. Evidence for anion-anion interactions in molybdenum (VI) and tungsten (VI) compounds related to the Keggin structure”. Inorganic Chemistry 22.2 (1983), pp. 207–216.

[19] N. Li, S. Yi, Z. Qian, J. Wang, N. Lei, and X. Chen. “Multicompartment-like aggregates formed by a redox-responsive surfactant encapsulated polyoxometalate in DMF/butanol mixed solvent”. RSC Advances 7.24 (2017), pp. 14631–14639.

[20] M. M. Duvenhage, M. Ntwaeaborwa, H. G. Visser, P. J. Swarts, J. C. Swarts, and H. C. Swart. “Determination of the optical band gap of Alq_3 and its derivatives for the use in two-layer OLEDs”. Optical Materials 42 (2015), pp. 193–198.

[21] J. Kalinowski. Organic light-emitting diodes: Principles, characteristics & processes. CRC press, 2004.

[22] R. Soulen, J. Byers, M. Osofsky, B. Nadgorny, T. Ambrose, S. Cheng, P. R. Broussard, C. Tanaka, J. Nowak, J. Moodera, et al. “Measuring the spin polarization of a metal with a superconducting point contact”. Science 282.5386 (1998), pp. 85–88.

[23] M. Bowen, M. Bibes, A. Barthélémy, J.-P. Contour, A. Anane, Y. Lematre, and A. Fert. “Nearly total spin polarization in La 2/3 Sr 1/3 MnO 3 from tunneling experiments”. Applied Physics Letters 82.2 (2003), pp. 233–235.

[24] C. Schneider, P. Bressler, P. Schuster, J. Kirschner, J. De Miguel, and R. Miranda. “Curie temperature of ultrathin films of fcc-cobalt epitaxially grown on atomically flat Cu (100) surfaces”. Physical Review Letters 64.9 (1990), p. 1059.

[25] J. Sierra, V. Pryadun, S. Russek, M. Garca-Hernández, F. Mompean, R. Rozada, O. Chubykalo-Fesenko, E. Snoeck, G. Miao, J. Moodera, et al. “Interface and temperature dependent magnetic properties in permalloy thin films and tunnel junction structures”. Journal of Nanoscience and Nanotechnology 11.9 (2011), pp. 7653–7664.

[26] J. Prieto-Ruiz, S. G. Miralles, H. Prima-García, A. Riminucci, P. Graziosi, M. Cinchetti, M. Aeschlimann, V. A. Dediu, and E. Coronado. “Controlling singlet-triplet ratio in OLEDs by spin polarised currents”. arXiv:1612.00633 (2016).

[27] H. Ishii and K. Seki. “Energy level alignment at organic/metal interfaces studied by UV photoemission: Breakdown of traditional assumption of a common vacuum level at the interface”. IEEE Transactions on Electron Devices 44.8 (1997), pp. 1295–1301.

[28] J. G. Simmons. “Generalized formula for the electric tunnel effect between similar electrodes separated by a thin insulating film”. Journal of Applied Physics 34.6 (1963), pp. 1793–1803.

[29] J. Jiang, J. Pearson, and S. Bader. “Absence of spin transport in the organic semiconductor Alq_3”. Physical Review B 77.3 (2008), p. 035303.

[30] S. Zhang, P. Levy, A. Marley, and S. Parkin. “Quenching of magnetoresistance by hot electrons in magnetic tunnel junctions”. Physical Review Letters 79.19 (1997), p. 3744.

[31] M. Kröger, S. Hamwi, J. Meyer, T. Riedl, W. Kowalsky, and A. Kahn. “P-type doping of organic wide band gap materials by transition metal oxides: A case-study on Molybdenum trioxide”. Organic Electronics 10.5 (2009), pp. 932–938.

[32] Y. Nakayama, K. Morii, Y. Suzuki, H. Machida, S. Kera, N. Ueno, H. Kitagawa, Y. Noguchi, and H. Ishii. “Origins of improved hole-injection efficiency by the deposition of MoO_3 on the polymeric semiconductor poly(dioctyifluorene-alt-benzothiadiazole)”. Advanced Functional Materials 19.23 (2009), pp. 3746–3752.

[33] M. Sessolo and H. J. Bolink. “Hybrid organic–inorganic light-emitting diodes”. Advanced Materials 23.16 (2011), pp. 1829–1845.

[34] K. Morii, M. Omoto, M. Ishida, and M. Graetzel. “Enhanced hole injection in a hybrid organic–inorganic light-emitting diode”. Japanese Journal of Applied Physics 47.9R (2008), p. 7366.

[35] J. Ma, Z. Liang, C. Jin, X. Jiang, and Z. Zhang. “Enhanced power efficiency for white OLED with MoO 3 as hole injection layer and optimized charge balance”. Solid State Communications 149.5 (2009), pp. 214–217.

[36] T. Matsushima, G.-H. Jin, and H. Murata. “Marked improvement in electroluminescence characteristics of organic light-emitting diodes using an ultrathin hole-injection layer of molybdenum oxide”. Journal of Applied Physics 104.5 (2008), p. 054501.

[37] C.-I. Wu, C.-T. Lin, G.-R. Lee, T.-Y. Cho, C.-C. Wu, and T.-W. Pi. “Electronic and chemical properties of molybdenum oxide doped hole injection layers in organic light emitting diodes”. Journal of Applied Physics 105.3 (2009), p. 033717.

[38] A. Droghetti, S. Steil, N. Grossmann, N. Haag, H. Zhang, M. Willis, W. P. Gillin, A. J. Drew, M. Aeschlimann, S. Sanvito, et al. “Electronic and magnetic properties of the interface between metal-quinoline molecules and cobalt”. Physical Review B 89.9 (2014), p. 094412.

[39] Y. Park, V. Choong, Y. Gao, B. R. Hsieh, and C. W. Tang. “Work function of indium tin oxide transparent conductor measured by photoelectron spectroscopy”. Applied Physics Letters 68.19 (1996), pp. 2699–2701.

[40] T. S. Sian and G. Reddy. “Optical, structural and photoelectron spectroscopic studies on amorphous and crystalline molybdenum oxide thin films”. Solar energy materials and solar cells 82.3 (2004), pp. 375–386.

[41] J. Devkota, R. Geng, R. C. Subedi, and T. D. Nguyen. “Organic spin valves: a review”. Advanced Functional Materials 26.22 (2016), pp. 3881–3898.

[42] D. Sun, E. Ehrenfreund, and Z. V. Vardeny. “The first decade of organic spintronics research”. Chemical Communications 50.15 (2014), pp. 1781–1793.

[43] M. Galbiati, C. Barraud, S. Tatay, K. Bouzehouane, C. Deranlot, E. Jacquet, A. Fert, P. Seneor, R. Mattana, and F. Petroff. “Unveiling Self-Assembled Monolayers’ Potential for Molecular Spintronics: Spin Transport at High Voltage”. Advanced Materials 24.48 (2012), pp. 6429–6432.

[44] T. D. Nguyen, E. Ehrenfreund, and Z. V. Vardeny. “Spin-polarized light-emitting diode based on an organic bipolar spin valve”. Science 337.6091 (2012), 204–209.

[45] E. Ehrenfreund and Z. V. Vardeny. “Organic spin-valves: from unipolar to bipolar devices”. Physical Chemistry Chemical Physics 15.21 (2013), pp. 7967–7975.

[46] P. Graziosi, M. Prezioso, A. Gambardella, C. Kitts, R. K. Rakshit, A. Riminucci, I. Bergenti, F. Borgatti, C. Pernechele, M. Solzi, et al. “Conditions for the growth of smooth $La_{0.7}Sr_{0.3}MnO_3$ thin films by pulsed electron ablation”. Thin Solid Films 534 (2013), pp. 83–89.

[47] B. Norgren, M. Somers, and J. De Wit. “Application of tougaard background subtraction to XPS spectra of passivated Fe–17 Cr”. Surface and Interface Analysis 21.6-7 (1994), pp. 378–381.

[48] I. Horcas, R. Fernández, J. Gomez-Rodriguez, J. Colchero, J. Gómez-Herrero, and A. Baro. “WSXM: a software for scanning probe microscopy and a tool for nanotechnology”. Review of Scientific Instruments 78.1 (2007), p. 013705.

[49] O. Andreyev, Y. M. Koroteev, M. S. Albaneda, M. Cinchetti, G. Bihlmayer, E. Chulkov, J. Lange, F. Steeb, M. Bauer, P. Echenique, et al. “Spin-resolved two-photon photoemission study of the surface resonance state on Co/ Cu (001)”. Physical Review B 74.19 (2006), p. 195416.

[50] X. Li, Z. Zhang, and V. E. Henrich. “Inelastic electron background function for ultraviolet photoelectron spectra”. Journal of electron spectroscopy and related phenomena 63.3 (1993), pp. 253–265.

5

Towards Light Emission: Design and Study of Spin-OLEDs

5.1 Introduction

The field of molecular spintronics was born when Alek Dediu and Carlo Taliani combined their expertise and knowledge with the objective of improving the organic light emitting diodes efficiency by magnetically controlling the population of singlets.[1,2] Despite the significant advances accomplished since then,[3] the isolation of a spin-OLED in which the spin polarization inside the organic semiconductor controls the singlet and triplet statistics, remains still a controversial subject.

A spin-OLED[4–7] is basically a light emitting spin valve where the intensity of the light emitted by the device is modulated in the presence of a magnetic field as a consequence of the spin polarization. The ferromagnetic electrodes vary the relative populations of spin-up and spin-down carriers increasing the population of singlets in

the antiparallel state up to 50 %. Thus, the spin-OLED maximum efficiency is double the efficiency limit of organic light emitting diodes.

Throughout history, different approaches have been pursued to fabricate spin-OLEDs. In 2004 Salis and coworkers[8] studied an OLED with ferromagnetic electrodes with the structure Ni / Alq_3 / STAD / NiFe. Unfortunately, the control experiments demonstrated that the increase in EL in the AP state was not caused by spin-polarized currents but by the stray fields generated by the electrodes.[1,9]

Later, in 2012 Nguyen and coworkers[7] reported 1 % of MEL effect in the device stack LSMO / D-DOO-PPV / LiF / Co. However, the MEL percentage was higher than the corresponding MR and, in addition, the effect measured has the opposite trend than expected since the electroluminescence emitted by the device decreased when the population of singlets is increased (and light intensity should increase). This seems to indicate that the variation of the EL signal measured was a consequence of the decrease in current, rather than a modification of the singlet-triplet ratio. Indeed their device can be considered a junction of a spin valve and an OLED.[10]

Recently, in our group,[11] a spin-OLED was assembled with the structure LSMO / N965 / F8BT / MoO_x / Co where it was carefully discarded that the EL modulation was caused by the electrodes. The maximum MEL effect measured in the device amounted to 1 %. However, the N965 monolayer needed to be synthesized, making the spin-OLED expensive to fabricate.

In this chapter we design and study a spin-OLED where all the layers are made from commercial materials. Spin statistics is changed by injecting electrons and holes with defined spin polarization, enabling the magneto-electro-optical multifunctionality. The most difficult task when designing a spin-OLED is to have spin-polarized currents and light emission at the same voltage and temperature. The turn on voltage of an OLED, that is the voltage at which light emission starts, increases with decreasing temperature. And the MR presents the highest values at low temperature but decreases with increasing voltage. Success depends fundamentally on the good alignment of energy levels between the layers.

5.2 Results and Discussion

5.2.1 Design of the Spin-OLED

In an OLED, charge carriers are injected from the electrodes to form an exciton in the emissive layer, typically a polymer or a molecular layer, and recombine resulting in the emission of light. In a regular OLED a low work function metal is responsible of electron injection whereas the electrode with high work function injects holes (see Section 1.1.2 in Chapter 1). However, our spin-OLED is based in a HyLED[12] rather than in an OLED. The fundamental difference between these two devices is that the cathode is a high work function metal in a HyLED. Consequently, the device is air stable and no capping layers to protect the electrodes are needed. The HyLED reverse configuration works thanks to two layers termed electron injection layer (EIL) and hole injection layer (HIL) which, as the name already indicates, help electron and hole injection respectively.

The first step to fabricate the spin-OLED is to replace the non-magnetic elec-

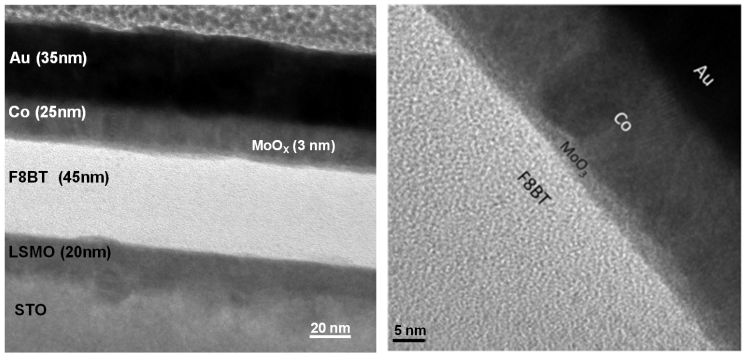

Figure 5.1 HRTEM images of the cross section of the spin-OLED with thicknesses LSMO (20 nm) / PEIE (∼1 nm) / F8BT (45 nm) / MoO_x (3 nm) / Co (25 nm) / Au(35 nm), where the high quality of the interfaces can be seen. Most importantly, there is no interpenetration of the top electrode in the organic layer.

trodes in a HyLED, a charge-only based device, by magnetic electrodes to introduce the spin as new degree of freedom. Thus, our device has the following configuration:

LSMO (20 nm) / PEIE ($\sim$1 nm) / F8BT (45 nm) / MoO_x (3 nm) / Co (25 nm)

The LSMO ($La_{0.7}Sr_{0.3}MnO_3$) electrode is deposited on a $SrTiO_3$ double-polished, transparent substrate enabling the light emitted to exit the device through it. As emissive layer, the organic conjugated polymer poly(9,9-dioctylfluorene-alt-benzothiadiazole) (F8BT)[13] has been employed. Its molecular structure is depicted in the inset of Figure 5.8b. Its bipolar character facilitates the establishment of a bipolar charge transport regime.[12]

Electrons are injected from the LSMO cathode into the LUMO of the F8BT, through a thin PEIE layer that acts as EIL by creating an interfacial dipole.[14] Holes are injected from the Co anode into the HOMO of the polymer, through the molybdenum oxide layer which is the HIL. Electron-hole recombination takes place in the F8BT giving rise to a yellow-green light emission. To protect the cobalt electrode from oxidation, a gold layer is evaporated on top of it. The high quality of the interfaces can be seen in the high-resolution transmission electron microscopy (HRTEM) image of Figure 5.1. The MoO_x barrier efficiently prevents the penetration of Co atoms into the organic layer, preventing the appearance of an ill-defined layer.

5.2.2 Interface Engineering

The energy levels of the layers in the device without the PEIE electron injector layer (EIL) and the MoO_x hole injection layer (HIL) are shown in Figure 5.2a, prior to layer contact. In this configuration the work functions of the LSMO and the cobalt are away from the LUMO and HOMO of the F8BT. To optimize the charge injection, two interfacial layers have been inserted to tailor the energy level alignment between the molecule frontier orbitals and the electrode work functions (see Figure 5.2). We used ultraviolet photoemission spectroscopy (UPS) to guide the choice of appropriate in-

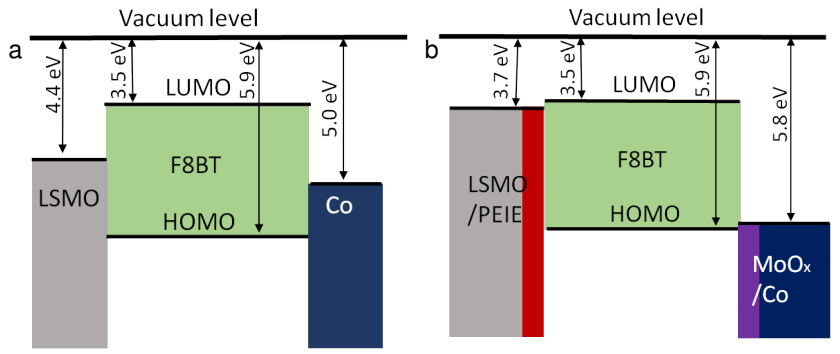

Figure 5.2 a) Energy level alignment in the device without using interfacial layers between the organic semiconductor (F8BT) and the ferromagnetic electrodes (LSMO and Co). b) Energy level alignment in the interface-engineered device. The work functions of the electrodes are modified energetically by the PEIE and MoO_x layers and approximated to the HOMO and the LUMO of F8BT. Consequently charge injection is facilitated.

terface layers. The MoO_x UPS study has been presented in the previous chapter and the PEIE UPS data will be shown in the following section.

5.2.3 Modification of the LSMO Work Function

The main challenge in the fabrication of spin-OLEDs lies in the coexistence of magnetoresistance and light emission at the same voltage and temperature. To that end, the LSMO cathode needs to meet a range of conditions. The devices do not emit light at low voltages if the RMS roughness of the LSMO layer is above 1 nm, probably because the PEIE layer is not properly formed. Figure 5.3 shows the AFM image, profile at medium high and histogram of a high quality LSMO substrate. The thermal dependence of the LSMO resistance is depicted in Figure 5.4 showing a metallic behavior.

The modification of the LSMO work function is done by the commercial polymer polyethylenimine ethoxylated (PEIE) that contains simple aliphatic amine groups

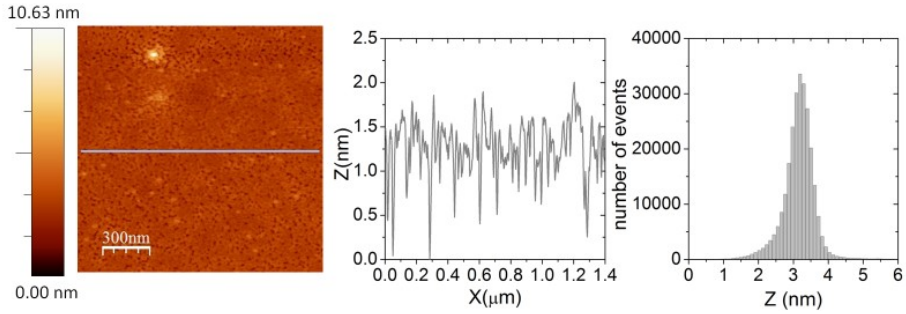

Figure 5.3 AFM image (left), profile at medium high (center) and histogram (right) of a good quality LSMO electrode ($\rho_{\text{peak to peak}}$ = 10.63 nm and ρ_{RMS} = 0.48 nm.). A RMS roughness below 1 nm is necessary for high quality PEIE-based spin-OLEDs. The peak to peak roughness is usually higher (above 10 nm) due to local high zones as seen in the top left of the topography image. The PEIE polymer is deposited gently on the LSMO if the RMS roughness is below 1 nm.

able to create a strong interface of molecular dipoles. The molecular structure of PEIE is depicted in the inset of Figure 5.6. This surface modifier has shown to substantially reduce the work function of the metallic electrodes in organic optoelectronic devices,[15] thus facilitating the injection of electrons to the LUMO of the organic semiconductor.[14]

The PEIE layer thickness is chosen so that the device works as spin valve, i.e., the current is spin polarized when it reaches the F8BT. This requirement does not need to be fulfilled by the optoelectronic devices and constitutes the main difference with molecular electronics where the optimum thickness of this layer is around 10 nm. For the fabrication of the spin-OLED, we have reduced progressively the PEIE thickness until the devices showed magnetoresistance. This has been achieved for an approximate PEIE thickness of 1 nm.

We determine the layer thickness by combining absorption measurements with AFM scratching. Initially, a PEIE layer was spin coated on a $Si-SiO_2$ substrate at 4500 rpm from a solution with a PEIE concentration of 0.4 % (see the experimental section at the end of the chapter for a detailed description). However, the film is too thin to be measured with a profilometer which has ha sensibility of 10 nm. Thus,

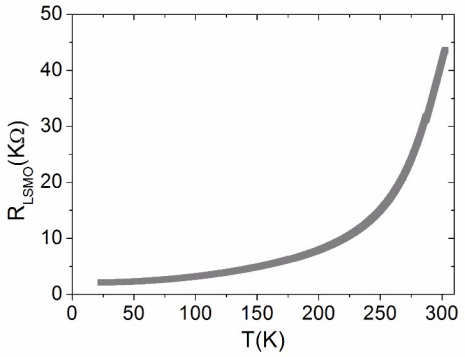

Figure 5.4 Thermal dependence of the resistance of the LSMO electrode employed for the fabrication of the spin-OLED. The resistance is measured along the LSMO stripe. The thermal decay of the resistance reveals the metallic behavior of the electrode.

to measure the film thickness we used the AFM scratching technique. Initially, the soft PEIE layer is scratched with a wooden toothpick and the surface is studied by atomic force microscopy (AFM). The upper panel of Figure 5.5 shows the vertical scratch. Clearly, two different heights are observed in the profile of the gray line seen on the right hand side of the figure. To provide a more accurate measurement of the PEIE layer thickness, we selected a good zone and zoomed in. The resulting image is shown in the lower panel of Figure 5.5 where the height is calculated by fitting the two peaks in the histogram to Gaussian curves. The fit of the peaks to $\exp[-(z-z_0)^2/(2\sigma)^2]$ gives z_0 = 10 nm for the pink peak and z_o = 19 nm for the purple peak (where σ is related to the width of the distribution and z_0 to the center of the Gaussian function). The difference, 9 nm, is approximately the height of the PEIE layer for a rotation speed of 4500 rpm and a concentration of 0.4 %.

However, the magnetic signal of the device appears for a PEIE concentration of 0.025 %. The thickness of this layer is obtained by comparing it to the 9 nm layer by means of absorption measurements and the Beer-Lambert law: $A(\lambda) = -\log_{10} \mathbf{T}(\lambda) = \alpha_a(\lambda)\, d$, where A is the absorbance, **T** is the transmittance, α_a is the absorption coefficient of PEIE, and d is the thickness of the film (see Figure 5.6a). The thickness

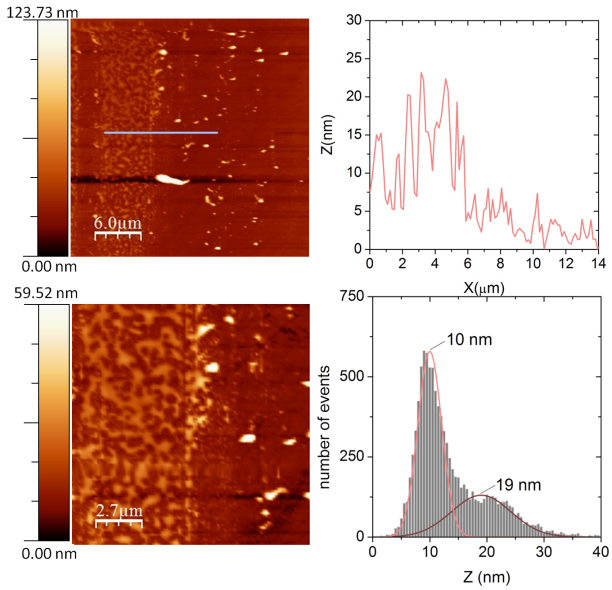

Figure 5.5 Upper panel: AFM image of a PEIE (0.4 %) layer deposited at 4500 rpm on $Si-SiO_2$ substrate. The PEIE thickness is determined by measuring the height of the groove created by a wooden toothpick scratch. On the right side, the profile of the gray line is shown where two different heights are observed. Lower panel: Zoom of the image in the upper panel and its histogram where two heights can be more accurately seen and estimated through Gaussian fits. The thickness of the PEIE layer amounts to $\approx$ 9 nm.

of the layer with initial PEIE concentration of 0.025 % is calculated from the slope of the curves $A_{0.4\%} = (d_{0.4\%}/d_{0.025\%}) \cdot A_{0.025\%}$ as seen in Figure 5.6b.The slope is 8.1 $\pm$ 0.1 and the obtained thickness for a PEIE concentration of 0.025 % is $d_1 \approx 1$ nm.

We performed photoemission spectroscopy measurements to evaluate the modification of the LSMO work function performed by the PEIE deposition. UPS measurements show that 1 nm of PEIE reduces the LSMO work function from -4.7 eV to -3.7 eV (see Figure 5.7). This value matches well with that of the LUMO of the F8BT that locates in -3.5 eV, hence the electron injection is considerably favored after the PEIE deposition.

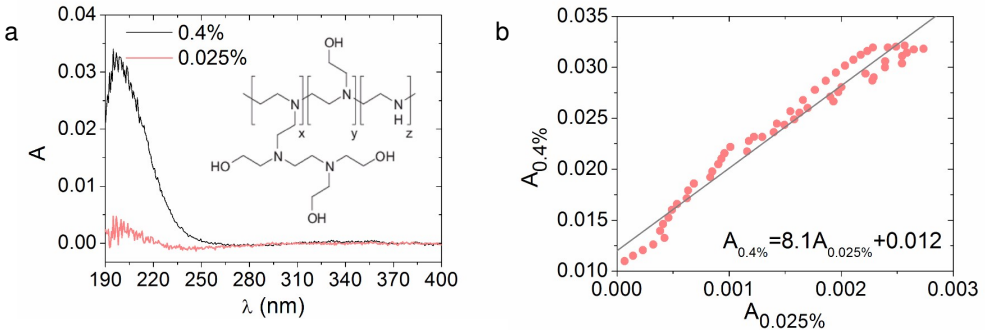

Figure 5.6 a) Absorbance curves of two PEIE films on quartz substrates deposited from solutions with PEIE concentrations of 0.4 % and 0.025 %. The molecular structure of PEIE is shown in the inset. b) Linear fit of the smoothed curves $A_{0.4\%} = (d_{0.4\%}/\ d_{0.025\%}) \cdot A_{0.025\%}$, with a slope 8.1 $\pm$ 0.1. The [PEIE] = 0.4 % film is 9 nm thick, consequently the [PEIE] = 0.025 % film is $\sim$1 nm thick.

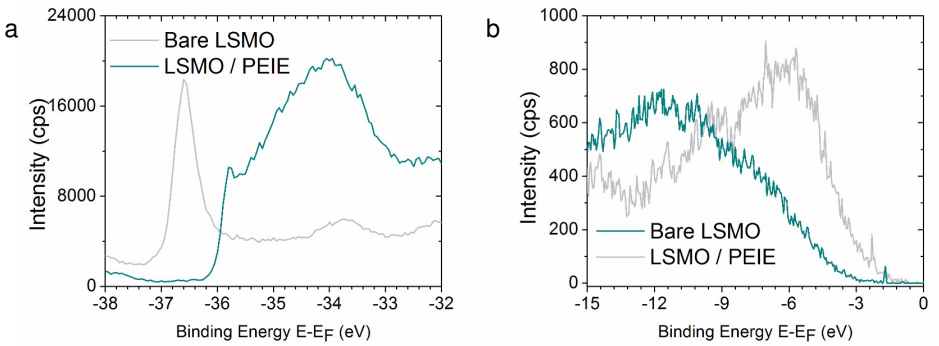

Figure 5.7 UPS spectra of LSMO and LSMO / PEIE ($\sim$1 nm). a) Cut-off region. b) Fermi level zone. The work function of bare LSMO is -4.4 ± 0.2 eV whereas the work function of LSMO / PEIE is -3.7 ± 0.2 eV.

5.2.4 Hole Injection Layer

Molecular electronics has widely used interfacial barriers to prevent the penetration of the evaporated metal in the molecular layer[16] or to change the electrode work function, thus improving the charge injection from the electrode to the molecular layer.[17,18] Molybdenum oxide is a popular barrier in the molecular electronics field. Apart, thick molybdenum oxide layers have been extensively used as hole injection layers in HyLEDs.[12] Here we alter the anode work function by means of a 3 nm MoO_x layer in the same way that it was done in the previous chapter, where it was shown how MoO_x increased the work function of the cobalt electrode from -5.0 to -5.8 eV, thus reducing the hole injection barrier from the electrode to the HOMO of the F8BT. In addition, up to a nominal MoO_x thickness of 3 nm, the spin polarization close to the Fermi level is virtually unaffected by the presence of this interfacial barrier.[19]

5.2.5 Charge Transport

The conductive mechanism in this multifunctional interface-engineered device implies a bipolar charge transport regime involving injection from the electrodes to the F8BT frontier orbitals and subsequent hopping through this semiconductor. This is supported by the high temperature dependence and non-linearity of the IV curves (see Figure 5.8a) and, more clearly, from the observation of the F8BT electroluminescence spectrum for all the temperature range studied (from 20 K to 300 K). The electroluminescence spectrum of the spin-OLED at room temperature is shown in Figure 5.8b and the molecular structure of the F8BT polymer is illustrated in the inset.

The major challenge when designing a spin-OLED is to have light and magnetic effects at the same voltage and temperature. On one side, the magnetization of the LSMO increases with decreasing temperature and also the magnetoresistance is higher.[20,21] On the other, as we cool down the device, the current also decreases since transport is thermally activated. And besides, due to the semiconducting char-

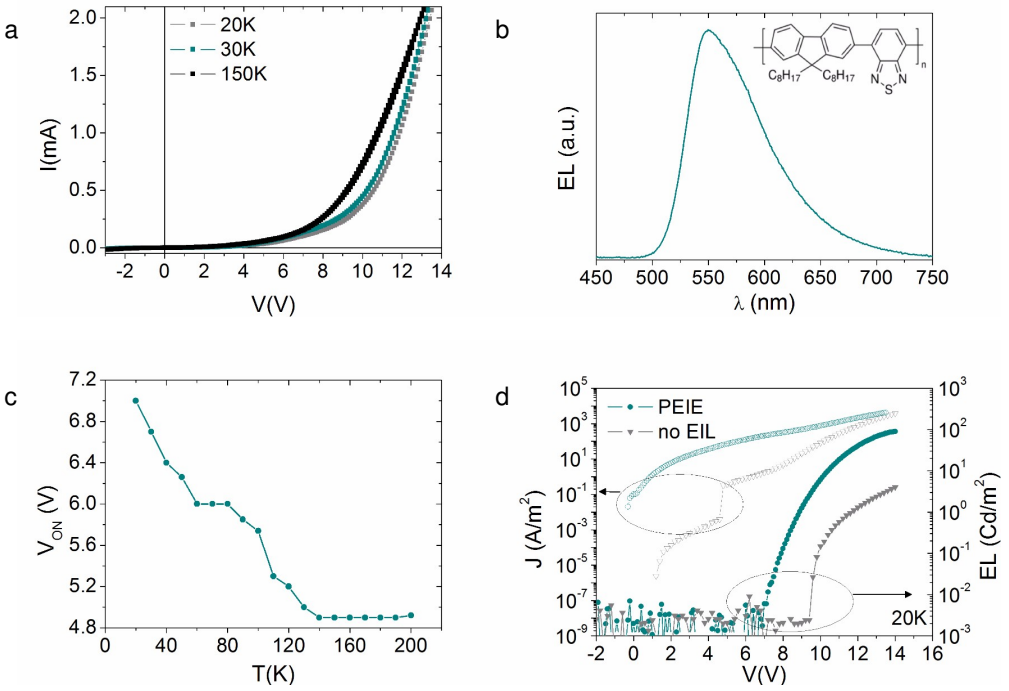

Figure 5.8 a) Current-voltage curves for the spin-OLED LSMO (20 nm) / PEIE (∼1 nm) / F8BT (45 nm) / MoO_x (3 nm) / Co (25 nm) at different temperatures. b) Electroluminescence spectrum of the device at room temperature. The molecular structure of F8BT is illustrated in the inset. c) Thermal dependence of the turn-on voltage for light emission (V_{ON}). At room temperature $V_{ON} = 3.7$ V. d) IVL recorded at 20 K varying the bias voltage from -2 to 14 V. For the SO fabricated with PEIE ($V_{ON} = 7$ V) and without electron injection layer ($V_{ON} = 9.5$ V).

acter of F8BT, the voltage at which light emission starts (V_{ON}) is higher (see Figure 5.8c where V_{ON} = 3.7 V at room temperature and V_{ON} = 7 V at 20 K).

The effect of the PEIE electron injection layer on the electroluminescence of the device can be clearly seen in Figure 5.8d. At low temperatures (20 K), the presence of PEIE significantly decreases the V_{ON} value from 9.5 V to 7 V, while the luminance increases by more than one order of magnitude. This is related with the modification

of the LSMO work function shown in Figure 5.7. The electron injection is enhanced and less bias voltage is necessary to emit light.

5.2.6 Magneto-Electroluminescence

As far as the spintronic properties of the multifunctional device are concerned, we observe that the field dependence of the resistance exhibits the typical features of a spin valve, indicating that the current passing through the device is able to preserve its spin-polarization. Thus, two different resistance states are observed depending on the relative magnetic alignment of the two magnetic electrodes. The AP state of the electrodes shows the high resistance state and then the MR measured is positive.

Figure 5.9 shows the magnetoresistance of the device measured at different voltages and temperatures. This MR response is hysteretic and follows the coercive fields of the electrodes (see Figure 5.11). It is remarkable that the spin valve response is maintained up to voltages of 14 V, which are well above the turn-on voltage of the OLED. The spin polarized current is preserved up to $180 - 200$ K which is the temperature at which the ferromagnetic properties of our manganite dwindle.[21]

The MR response is maintained at high bias voltages as depicted in Figure 5.10. This feature is quite unusual for molecular spin valves,[4,16,22–24] which, in general, show a complete degradation of their spin-polarization signal for voltages above 1 V as pointed out in the previous chapter. One of the reasons is that for most molecular spin valves the spin injection does not take place through the frontier orbitals of the organic semiconductor, but through a trap or impurity band located in the HOMO$-$LUMO gap.[25] In our case, we have shown that, through a careful interface engineering, the energy-level alignment between the molecules frontier orbitals and the electrode's work functions can be optimized in such a way that polarized charges are injected in an efficient way at the HOMO and LUMO levels of the F8BT, thus maintaining the spin-polarization at high voltages. This result is also favored by the fact that in our device these charges recombine to emit light for $V > V_{ON}$. Thus,

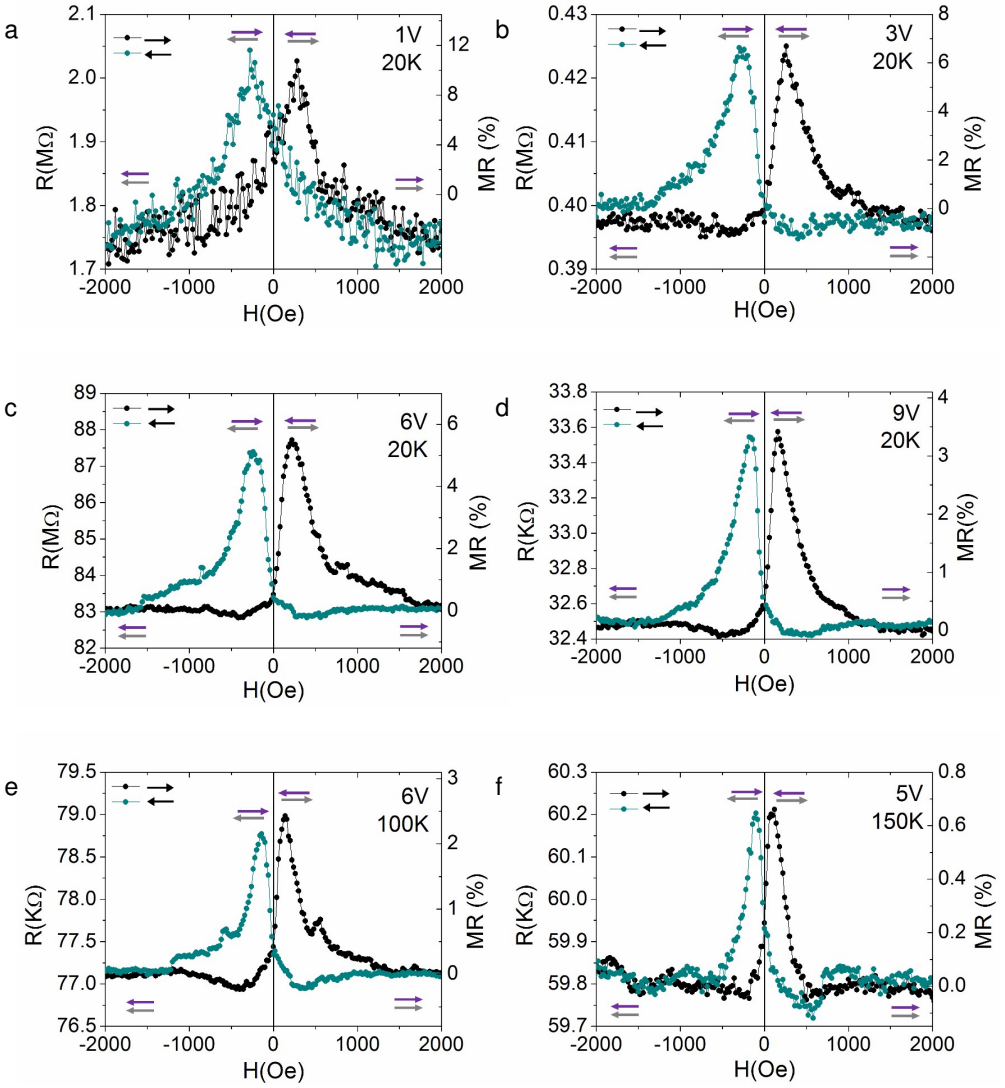

Figure 5.9 Magnetoresistance curves at different voltages and temperatures. a) MR = 9.5 % at 1 V and 20 K. b) MR = 6.9 % at 3 V and 20 K.c) MR = 5.4 % at 6 V and 20 K. d) MR = 3.4 % at 9 V and 20 K. e) MR = 2 % f) MR = 0.67 % 6 V 100 K. The black curve is the forward sweep while the gray curve is the backward sweep. The purple and gray arrows indicate the magnetization direction of the electrodes

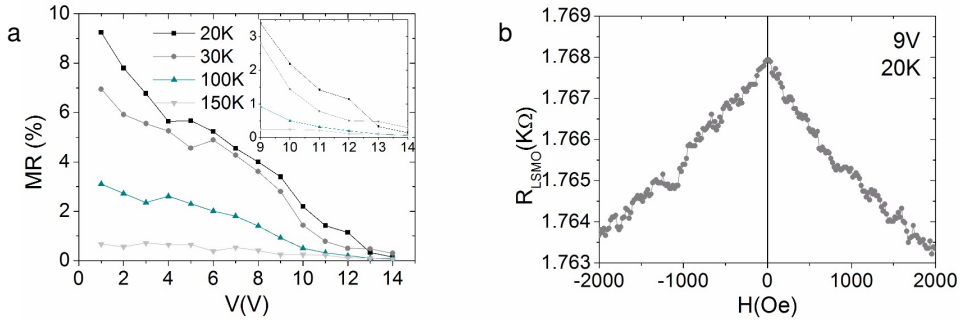

Figure 5.10 a) Voltage dependence of the magnetoresistance of the spin-OLED at different temperatures. b) Variation of the resistance of the LSMO electrode in a magnetic field at 9 V and 20 K (MR = $(R_{2000\,Oe} - R_{H=0})/R_{H=0} = 0.25$ %). The signal of the LSMO electrode has been systematically subtracted from every MR and MEL curve as described in appendix B.

at these high voltages there is a significant reduction of charge density in the F8BT that may contribute to reduce spin-spin scattering processes, leading to a reduction of the spin relaxation rate.[26]

Concerning light emission, one expects that for electrodes with random spin polarization the singlet-to-triplet ratio is 1:3, which leads to maximum efficiency of 25 % in a regular OLED.[27] This ratio increases to 1:1 for the antiparallel configuration in a spin-OLED.[4,28,29] In contrast, when the external magnetic field induces a parallel configuration in the electrodes, triplet states will be formed with a correspondent reduction in the light emission.[29] In this case, the external magnetic field does not represent a direct input but is used to manipulate the magnetization of electrodes, the latter fully responsible for the spin polarization.

The stabilization of a spin-polarized current in the same range of voltage and temperatures where light emission is the necessary condition to detect a MEL response in the hybrid device. The MEL response is defined by:

$$MEL(\%) = \frac{EL_{AP} - EL_P}{EL_P} \tag{5.1}$$

being EL_{AP} and EL_P the electroluminescence in the antiparallel and parallel states of the magnetization of the electrodes, respectively.

In the present case, MEL is indeed observed showing a maximum value of 2.4 % in the AP state at 9 V and 20 K (see Figure 5.11a). The absolute value of the MEL effect for different voltages follows the same trend as the magnetoresistance as shown in Figure 5.11. Furthermore, it is observed for voltages below 14 V and it decreases when the temperature is increased being clearly observed up to 100 K (see Figure 5.11). This MEL effect gives rise to an enhancement of the EL in the AP state, in agreement with the presence of spin-polarized charge carriers in the F8BT. Equivalently to the MR, the MEL response follows the Hc of the electrodes as shown in Figure 5.11f.

At 12 V and 20 K, a measurable intrinsic organic magneto-electroluminescence (OMEL) dominates the MEL effect (see Figure 5.12). This last effect is opposite to the previous one and leads to a minimum value of the EL at zero field. As the temperature is progressively increased, the OMEL effect is enhanced leading to a screening of the MEL signal related to the spin valve performance of the device. The OMEL effect stems from the influence of the external magnetic field on polaron pairs (PP).[9,30] When electron and hole are close enough but still on different molecules and the exciton has not yet formed, the carriers can flip their spins by intersystem crossing (ISC). The possible energy eigenstates of a spin 1/2 split up in the presence of an external magnetic field, what is known as Zeeman splitting. In the absence of field, the singlet state and the entire triplet manifold can mix by hyperfine interaction. In the presence of a high enough field there is no degeneracy of the triplet energies and S_0 can only mix with T_0. Hence, the external magnetic field regulates the intersystem crossing rates and then also the recombination rates that lead to light emission change. At zero field, the electroluminescence is lower because the singlet can transform into triplets and "become dark" since the radiative rate of these is much smaller. The magnetic field influences polaron pairs but once excitons are formed, H has no effect on them. However, if triplet excitons do not annihilate or singlet excitons do not recombine, they can dissociate in PP and ISC can happen.[30]

A MEL response following the coercive fields of the electrodes (see Figure 5.11f)

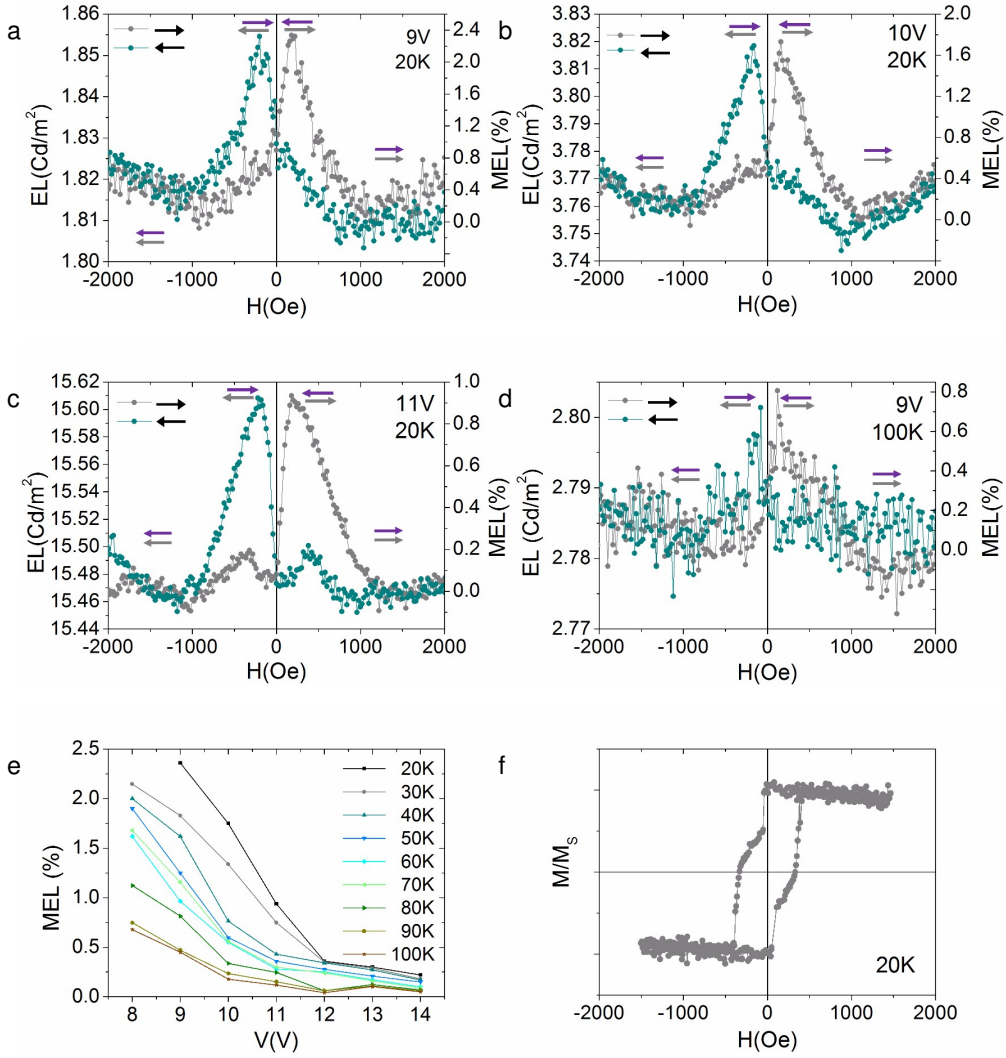

Figure 5.11 a) MEL response at 9 V and 20 K exhibiting a maximum enhancement of light emission of 2.4 % in the AP state. b) MEL effect at 20 K and 10 V. c) MEL effect at 11 V and 20 K. d) MEL response at 9 V and 100 K. e) MEL response dependence on voltage for different temperatures. f) Hysteresis loop of the SO measured at 20 K. The electroluminescence switches coincide with the coercive fields of the ferromagnetic electrodes (H_c(Co) = 385 Oe, H_c(LSMO) = 35 Oe). Black arrows indicate the sweep direction while purple and gray arrows point the Co and LSMO magnetization direction respectively.

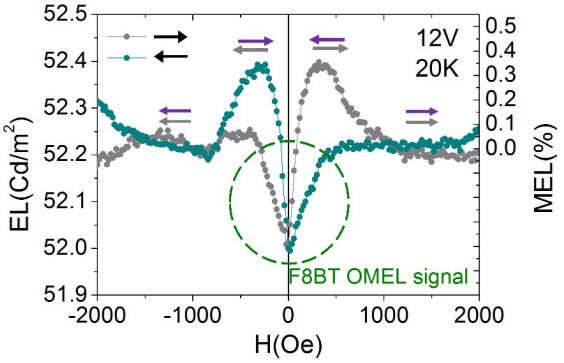

Figure 5.12 MEL response at 12 V and 20 K showing the appearance of an important OMEL contribution due to the organic F8BT polymer

is a first indication that a spin valve effect is the responsible of this behavior. However, a systematic study has been performed in order to discard that this light modulation comes from artifacts induced by the electrodes in the structure, which could mimic spin dependent processes of the injected carriers.

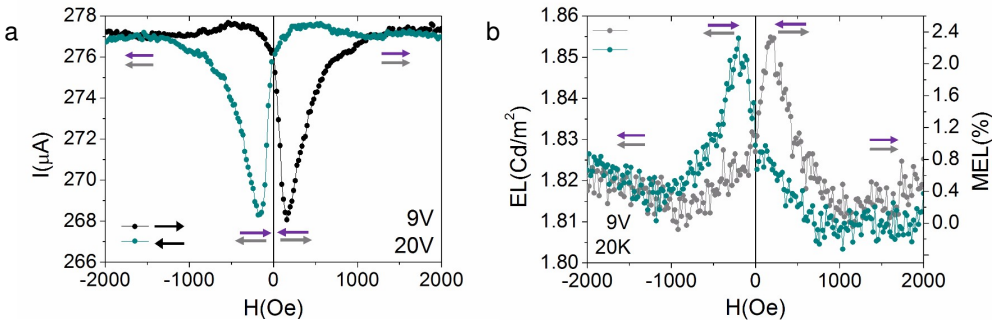

Figure 5.13 Current (a) and electroluminescence (b) variation in a magnetic field at the same voltage and temperature. The current decreases in the AP state while the EL increases. The EL modulation cannot be caused by the variation of current since they are opposite effects.

The first artifact is the coupling of the current with light emission. For devices

showing positive MR the current decreases in the AP state while the population of singlets increases. In the case of devices presenting negative MR the situation is reversed.

We observe the correct trend in our devices: an enhancement of the light emission when the current is reduced by the spin valve effect in the AP state (see Figure 5.13). This result supports the spin-polarization effect as responsible for the light modulation[4,28,29] in clear contrast with previous reports.[7] In our case, in the antiparallel state the current shows its low state while the intensity of the light is in the high state. Therefore we can rule out that the measured MEL effect is caused by a modulation in current.

A second artifact may be induced by the stray fields of the ferromagnetic electrodes.[8] The electrodes can induce a hysteretic response of the EL under sweeping of an external magnetic field, which would not be related to the spin valve effect in the device. In order to discard this situation three reference devices were fabricated (without ferromagnetic electrodes, with Co as single FM electrode and with LSMO as single FM electrode) and studied in the same conditions than the spin-OLED (see Figure 5.14). In the three cases no hysteretic features were observed and the EL response had an opposite sign with respect to the MEL effect observed in the spin-OLED.

A third artifact may be related with the effects of resistive ferromagnetic electrodes on the current and light emission responses under the application of external magnetic fields. We have discarded possible artifacts in the measured MR and MEL signals caused by high resistances of the ferromagnetic electrodes by using a simple 1 D resistor model.[31] Concerning the MR measurements, the resistance of the Co can be neglected and the LSMO cannot induce any artifact since the device is 10 times more resistive than this electrode and furthermore its MR shows the same sign as the device (the 1 D resistor model predicts inverse signs for the MR of the device and the electrode).

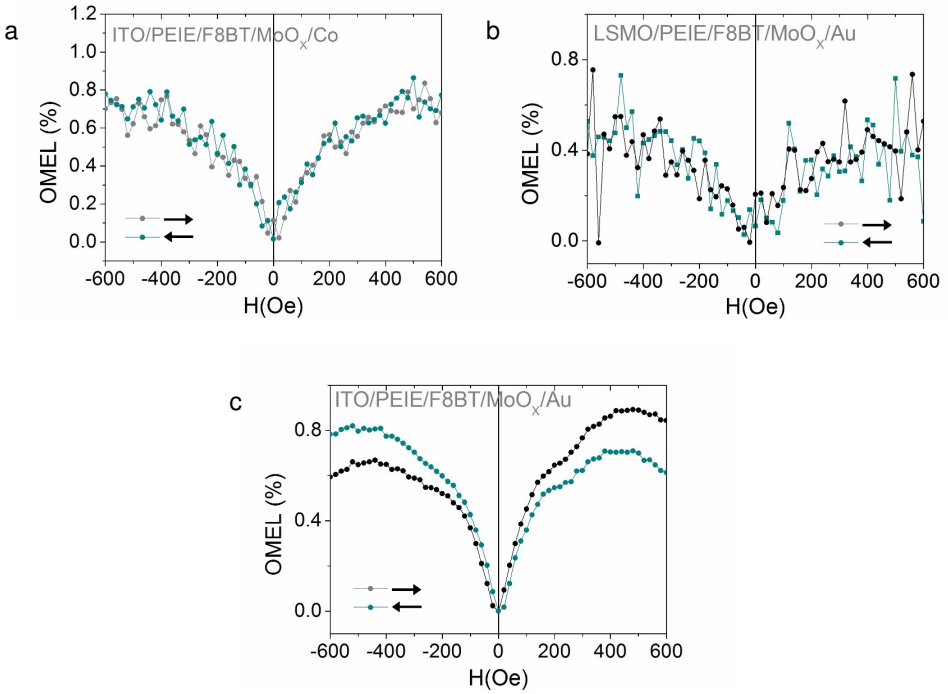

Figure 5.14 The light emission response of the reference devices under sweeping of an external magnetic field show no hysteretic effects. a) ITO cathode and a Co anode as Co-reference. b) LSMO cathode and Au anode reference sample. c) No ferromagnetic electrodes being used ITO as cathode and Au as anode. Measurements registered at 9V and 20 K.

5.3 Conclusions and Perspectives

In summary, we have fabricated a spin-OLED based on an inverted OLED structure and commercial materials. The device presents a maximum MEL response of 2.4 % at 20 K. After studying the MR and MEL effects in the device, we checked that the light modulation is not created by any artifact and therefore its origin lies in the variation of singlet and triplet populations controlled by the external magnetic field.

This constitutes the first definite demonstration of spin polarization in the HOMO and LUMO levels of the organic semiconductor, a question amply debated in molecular spintronics.

We optimized the device of Prieto-Ruiz and coworkers[11] by replacing the ruthenium-based electron injection layer, named N965,[32] by a fully organic PEIE[14] layer. One very important benefit of the PEIE polymeric layer is that it is a commercial compound contrary to the N965 that needs to be synthesized. Furthermore, our PEIE-based spin-OLED shows better values in terms of MR (9.5 % compared to 6 % at 20 K and 2 V) and maximum MEL signal (2.4 % compared to 1 %). The low spin-orbit coupling of the organic PEIE layer may be the reason of the better performance of the PEIE-based spin-OLED compared to the N965-based device, as the N965 contains Ru.

This approach opens the way for preparing new types of multifunctional spintronic devices showing a synergy between spin and a second functionality such as light emission, electrical memory or photovoltaics. The next step would be to design a spin-OLED with MEL response at room temperature. This might be achieved by the replacement of the LSMO cathode by a high Curie temperature such as permalloy.

5.4 Experimental Details

All materials were used as received without further purification. The spin-OLED under study was fabricated by combining solution processing methods and evaporation techniques.

LSMO electrodes with a thickness of 20 nm were grown by channel spark ablation (CSA)[33] on (100) oriented double-sided polished $SrTiO_3$ substrates, and employed as the cathode and spin injector electrode of the structure.

As EIL, polyethylenimine 80 % ethoxylated (PEIE) (Mw = 70,000 g/mol), was dissolved in H_2O with a concentration of 35−40 % wt. 1 % when received from

Aldrich. Then it was further diluted with 2-methoxyethanol to a weight concentration of 0.025 %. The solution was spin coated on top of the substrates at a speed of 5000 rpm for 1 min and an acceleration of 1000 rpm/s. Spin-coated PEIE films were annealed at 100 ℃ for 10 min on a hotplate in air. The thickness of the PEIE layers was determined to be around 1 nm by combining AFM scratching technique and absorption measurements as described in the text.

After the deposition of the EIL, a 45 nm film of the light emitting conjugated polymer poly(9,9-dioctylfluorene-alt-benzothiadiazole) named as F8BT was deposited by spin-coating from a chlorobenzene solution in a concentration 14 mg /mL. After the polymer deposition, the sample was annealed at 100 ℃ during 30 min inside a glove box.

Subsequently, the sample is transferred to a thermal evaporator placed inside the glove box where a 3 nm MoO_x layer was evaporated on top of the F8BT layer. A new shadow mask in a cross-bar configuration respect to the LSMO was used for the deposition of 25 nm of Co by thermal evaporation. Without breaking the vacuum, a final gold layer of 35 nm thickness was prepared to protect the Co electrode. The active area amounts to 1500 μm x 500 μm.

The high resolution TEM (HRTEM) experiments were performed in a Tecnai F30 (FEI Company) operated at 300 KV at the Advanced Microscopy Laboratory at the Nanoscience Institute of Aragón (INA). The sample is previously cryogenized to avoid the damage of the organic layer. High angle annular dark field (HAADF) images, energy dispersive X-rays spectra (EDS) and electron energy loss spectra (EELS) were obtained using a HAADF detector, an EDAX detector and a Tridiem (Gatan) Energy Filter respectively in Scanning Transmission Electron Microscopy mode (STEM): The sample is scanned with a small probe (diameter $\approx$0.5 nm), obtaining an image and a spectrum in the whole range of Energy in order to obtain 1D composition profiles or 2D maps for each of the elements.

An Avantes luminance spectrometer was used to measure the EL spectrum of the device. The absorbance of the films deposited on quartz substrates has been measured with a Cary 300 UV-Vis spectrometer. AFM images were recorded by

means of a Nanoscope IV atomic force microscope from Veeco. The images were acquired in tapping-mode in air at room temperature with Si tips (frequency 300 kHz and K 40 Nm^{-1}). Image processing was done with the WSxM[34] software developed by Nanotec Electronics.

The MR ratio in the spin-OLEDs has been calculated taking the antiparallel configuration of electrode magnetizations as the reference, using the expression MR(%)= $((R_{AP}-R_P)/ R_P)$ where R_P and R_{AP} are the resistances in the parallel and antiparallel states, respectively. The LSMO contribution in the MR responses has been systematically subtracted from each experimental curve in order to get the net spin valve effect as it was done for each MEL signal (see appendix B). The magneto-electroluminescence intensity was detected by employing a Si-photodiode coupled to a Keithley 6485 picoamperometer. The photocurrent was calibrated using a Minolta LS100 luminance meter.

The UPS measurements were recorded at the University of Kaiserslautern in collaboration with prof. Mirko Cinchetti from the Ultrafast Phenomena at Surfaces research group at the Department of Physics and research center OPTIMAS. To detect the work function at the interface LSMO / PEIE we have used UPS in a setup similar to the one described in the work.[35] The excitation source is a VUV5000 monochromatized vacuum ultraviolet lamp (Scienta), operated at the He II line ($h\nu$ = 40.8 eV). The light incident angle is 45°. The photoelectrons were collected at normal emission using a hemispherical energy analyzer for parallel energy and momentum detection (SPECS Phoibos 150). All presented measurements were performed at room temperature.

5.5 Bibliography

[1] V. Dediu, M. Murgia, F. Matacotta, C. Taliani, and S. Barbanera. “Room temperature spin polarized injection in organic semiconductor”. Solid State Communications 122.3 (2002), pp. 181–184.

[2] Editorial. “Why going organic is good”. Nature Materials 8.691 (2009).

[3] D. Sun, E. Ehrenfreund, and Z. V. Vardeny. “The first decade of organic spintronics research”. Chemical Communications 50.15 (2014), pp. 1781–1793.

[4] V. A. Dediu, L. E. Hueso, I. Bergenti, and C. Taliani. “Spin routes in organic semiconductors”. Nature Materials 8.9 (2009), pp. 707–716.

[5] J. Camarero and E. Coronado. “Molecular vs. inorganic spintronics: the role of molecular materials and single molecules”. Journal of Materials Chemistry 19.12 (2009), pp. 1678–1684.

[6] E. Ehrenfreund and Z. V. Vardeny. “Organic spin-valves: from unipolar to bipolar devices”. Physical Chemistry Chemical Physics 15.21 (2013), pp. 7967–7975.

[7] T. D. Nguyen, E. Ehrenfreund, and Z. V. Vardeny. “Spin-polarized light-emitting diode based on an organic bipolar spin valve”. Science 337.6091 (2012), 204–209.

[8] G. Salis, S. Alvarado, M. Tschudy, T. Brunschwiler, and R. Allenspach. “Hysteretic electroluminescence in organic light-emitting diodes for spin injection”. Physical Review B 70.8 (2004), p. 085203.

[9] F. Macía, F. Wang, A. D. Harmon N. J.and Kent, M. Wohlgenannt, and M. Flatté. “Organic magnetoelectroluminescence for room temperature transduction between magnetic and optical information.” Nature Communications 5 (2014), p. 3609.

[10] X. Sun, M. Gobbi, A. Bedoya-Pinto, O. Txoperena, F. Golmar, R. Llopis, A. Chuvilin, F. Casanova, and L. E. Hueso. “Room-temperature air-stable spin transport in bathocuproine-based spin valves”. Nature Communications 4 (2-013).

[11] J. P. Prieto-Ruiz. “Molecular spintronics: from magnetic materials to light emitting spintronic devices”. PhD thesis. 2015.

[12] M. Sessolo and H. J. Bolink. “Hybrid organic–inorganic light-emitting diodes”. Advanced Materials 23.16 (2011), pp. 1829–1845.

[13] L. L. Chua, J. Zaumseil, J. F. Chang, E. C. W. Ou, P. K. H. Ho, H. Sirringhaus, and R. H. Friend. “General observation of n-type field-effect behaviour in organic semiconductors”. Nature 434.7030 (2005), pp. 194–199.

[14] Y. Zhou, C. Fuentes-Hernandez, J. Shim, J. Meyer, A. J. Giordano, H. Li, P. Winget, T. Papadopoulos, H. Cheun, J. Kim, et al. “A universal method to produce low–work function electrodes for organic electronics”. Science 336.6079 (2012), pp. 327–332.

[15] B. A. Courtright and S. A. Jenekhe. “Polyethylenimine interfacial layers in inverted organic photovoltaic devices: Effects of ethoxylation and molecular weight on efficiency and temporal stability”. ACS Applied Materials & Interfaces 7.47 (2015), pp. 26167–26175.

[16] V. Dediu, L. Hueso, I. Bergenti, A. Riminucci, F. Borgatti, P. Graziosi, C. Newby, F. Casoli, M. De Jong, C. Taliani, et al. “Room-temperature spintronic effects in Alq_3-based hybrid devices”. Physical Review B 78.11 (2008), p. 115203.

[17] Y. Z. Wang, L. Cao, D. C. Qi, W. Chen, A. T. S. Wee, and X. Y. Gao. “Tuning the interfacial hole injection barrier between p-type organic materials and Co using a MoO_3 buffer layer”. Journal of Applied Physics 112.3 (2012), p. 033704.

[18] Y. Z. Wang, M. Yang, D. C. Qi, S. Chen, W. Chen, A. T. S. Wee, and X. Y. Gao. “A synchrotron-based photoemission study of the MoO_3Co interface”. Journal of Chemical Physics 134.3 (2011), pp. 1–7.

[19] J. P. Prieto-Ruiz, S. G. Miralles, N. Grossmann, M. Aeschlimann, M. Cinchetti, H. Prima-García, and E. Coronado. “Design of molecular spintronics devices containing molybdenum oxide as hole injection layer”. Advanced Electronic Materials (2017).

[20] J. Devkota, R. Geng, R. C. Subedi, and T. D. Nguyen. “Organic spin valves: a review”. Advanced Functional Materials 26.22 (2016), pp. 3881–3898.

[21] J. Prieto-Ruiz, S. G. Miralles, H. Prima-García, A. Riminucci, P. Graziosi, M. Cinchetti, M. Aeschlimann, V. A. Dediu, and E. Coronado. “Controlling singlet-triplet ratio in OLEDs by spin polarised currents”. arXiv:1612.00633 (2016).

[22] Z. Xiong, D. Wu, Z. V. Vardeny, and J. Shi. “Giant magnetoresistance in organic spin-valves”. Nature 427.6977 (2004), pp. 821–824.

[23] C. Barraud, P. Seneor, R. Mattana, S. Fusil, K. Bouzehouane, C. Deranlot, P. Graziosi, L. Hueso, I. Bergenti, V. Dediu, et al. “Unravelling the role of the interface for spin injection into organic semiconductors”. Nature Physics 6.8 (2010), pp. 615–620.

[24] X. Zhang, S. Mizukami, T. Kubota, Q. Ma, M. Oogane, H. Naganuma, Y. Ando, and T. Miyazaki. “Observation of a large spin-dependent transport length in organic spin valves at room temperature”. Nature Communications 4 (2013), p. 1392.

[25] Z. G. Yu. “Impurity-band transport in organic spin valves”. Nature Communications 5 (2014), p. 4842.

[26] G. Szulczewski, S. Sanvito, and M. Coey. “A spin of their own”. Nature Materials 8.9 (2009), pp. 693–695.

[27] M. Reufer, M. J. Walter, P. G. Lagoudakis, A. B. Hummel, J. S. Kolb, H. G. Roskos, U. Scherf, and J. M. Lupton. “Spin-conserving carrier recombination in conjugated polymers”. Nature Materials 4.4 (2005), pp. 340–346.

[28] M. Yunus, P. Ruden, and D. Smith. “Spin injection effects on exciton formation in organic semiconductors”. Applied Physics Letters 93.12 (2008), p. 354.

[29] I. Bergenti, V. Dediu, E. Arisi, T. Mertelj, M. Murgia, A. Riminucci, G. Ruani, M. Solzi, and C. Taliani. “Spin polarised electrodes for organic light emitting diodes”. Organic Electronics 5.6 (2004), pp. 309–314.

[30] V. Prigodin, J. Bergeson, D. Lincoln, and A. Epstein. “Anomalous room temperature magnetoresistance in organic semiconductors”. Synthetic Metals 156.9 (2006), pp. 757–761.

[31] A. Riminucci, M. Prezioso, P. Graziosi, and C. Newby. “Electrode artifacts in low resistance organic spin valves”. Applied Physics Letters 96.11 (2010), p. 112505.

[32] H. J. Bolink, E. Baranoff, M. Clemente-León, E. Coronado, A. Lopez-Muñoz, D. Repetto, M. Sessolo, and M. K. Nazeeruddin. “Molecular ionic junction for enhanced electronic charge transfer”. Langmuir 25.1 (2008), pp. 79–83.

[33] P. Graziosi, M. Prezioso, A. Gambardella, C. Kitts, R. K. Rakshit, A. Riminucci, I. Bergenti, F. Borgatti, C. Pernechele, M. Solzi, et al. “Conditions for the growth of smooth $La_{0.7}Sr_{0.3}MnO_3$ thin films by pulsed electron ablation”. Thin Solid Films 534 (2013), pp. 83–89.

[34] I. Horcas, R. Fernández, J. Gomez-Rodriguez, J. Colchero, J. Gómez-Herrero, and A. Baro. “WSXM: a software for scanning probe microscopy and a tool for nanotechnology”. Review of Scientific Instruments 78.1 (2007), p. 013705.

[35] M. Cinchetti, S. Neuschwander, A. Fischer, A. Ruffing, S. Mathias, J. P. Wüstenberg, and M. Aeschlimann. “Tailoring the spin functionality of a hybrid metal-organic interface by means of alkali-metal doping”. Physical Review Letters 104.21 (2010), p. 217602.

6

Spin Precession in Spin-OLEDs: Study of the Hanle Effect

6.1 Introduction

Notwithstanding the large number of studies reported on molecular spin valves, there is still controversy over whether the current is spin polarized in the molecular materials (with injection of spin carriers in their HOMO and LUMO orbitals), or the devices behave as magnetic tunnel junctions.

Magnetoresistance in molecular spin valves does not prove spin injection in the molecular material since GMR and TMR are indistinguishable. The low resistances[1,2] that have been reported in several MSVs seem to indicate that the molecular layer is very thin, much thinner than the nominal thickness due to the interpenetration of the top ferromagnetic electrode.

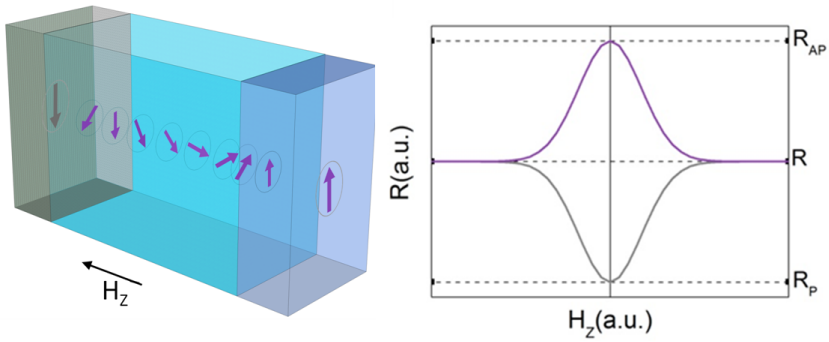

Figure 6.1 Illustration of the spin precession (Hanle effect) in a molecular spin valve. If the Hanle effect occurs, the non-collinear field H_z randomizes the spins and quenches the MR. The spins precess around the magnetic field H_z at the Larmor frequency so that the resistance is no longer the resistance of the antiparallel state (R_{AP}). An analogous situation is encountered by the parallel state.

As pointed out in section 1.4.1, this occurs because typically the second electrode is evaporated at high temperatures impacting strongly on the soft molecular layer, which is affected and reduced, resulting in what is known as an ill-defined layer.[3] For low thicknesses, commonly below 5 nm, charge carriers tunnel through these locally thin regions.[4] Even when the molecular spin valve shows a high resistance value, this does not imply that the charge carriers travel in the orbitals of the molecular material, since a pinhole could be mimicking the high resistance of a molecular layer due to its small area. Furthermore, MR is measured in most MSVs at low voltages and it typically quenches around 1 V, a voltage too low to inject charge in the HOMO and LUMO of the molecular layer indicating that charge transport may be taking place in a trap band located in the gap.[5]

Although it has been demonstrated that spin injection is possible in a molecular material using low-energy muon spin rotation[6] and two-photon photoemission[7] techniques, no Hanle effect has been measured in a molecular spin valve so far. The Hanle effect is considered the litmus test of spin injection in MSVs and the conclusive evidence with regard to the spin polarized currents as the source of MR.[8]

In the case of incoherent transport, the effect is measured in the depolarization

of the electrical current by an out-of-plane magnetic field (H_z). The Hanle effect occurs if the spins precess as they traverse the molecular material by the action of the magnetic field applied non-collinear to the orientation of the electrodes. When the spins reach the spin detector electrode, they have lost the initial spin polarization and the resistance of the device no longer corresponds to either the parallel or the antiparallel state resistances (see Figure 6.1). The GMR is proportional to $\cos^2\theta$, where θ is the angle between the applied magnetic field and the spin polarization.[9,10]

A spin-OLED embodies a powerful tool for the investigation of spintronic effects in molecular materials,[3,11–13] in particular for the study of spin precession or Hanle effect.[14,15] Thanks to a careful engineering of the interfaces, in a spin-OLED, carriers are injected in the HOMO and LUMO of the emissive layer and not only the resistance depends on the magnetization of the electrodes but also the light intensity is modulated in a sweep of magnetic field, which is known as MEL effect. The spin-OLED is the ideal device for making Hanle effect measurements since the device emits the electroluminescence spectrum characteristic of the emissive layer showing that charge transport occurs indubitably in the HOMO and LUMO of the molecular layer. Hence, the doubt as to whether the Hanle effect can not be measured because there is no transport in the molecular material disappears.

6.2 Results and Discussion

6.2.1 Design of the Spin-OLED

We report the fabrication of a spin-OLED based on a hybrid organic-inorganic inverted HyLED structure[16] using the green light-emitting polymer F8BT and LSMO and Co as ferromagnetic electrodes acting as cathode and anode, respectively. The device is very similar to the spin-OLED described in the previous chapter. However, the PEIE layer at the electron injection bottleneck is substituted by a bilayer formed by ZnO and N965.[17] Indeed, the design closely resembles the spin-OLED studied

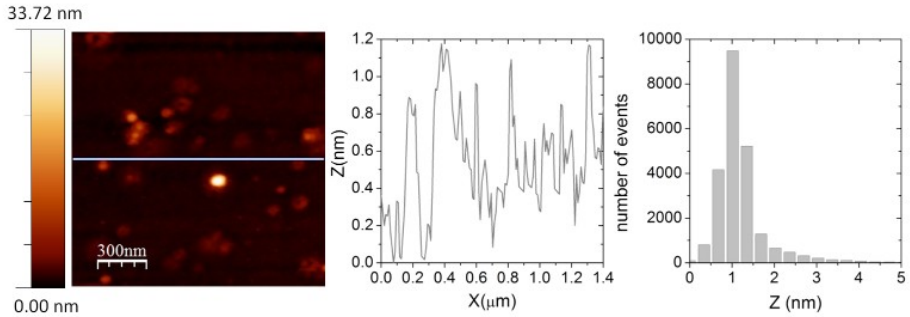

Figure 6.2 AFM topography image (left), profile at medium height (center) and histogram (right) of a 20 nm LSMO electrode deposited on a double polished $SrTiO_3$ substrate. The surface quality of the electrode is not optimal for PEIE or N965 only devices since the peak to peak roughness is high (33.72 nm) and the RMS roughness amounts to 1.47 nm ($>$ 1 nm).

previously in our group,[18] in which we implemented the thin ZnO layer that improved considerably the statistics and stability of the samples, fundamental skills to study spin precession. The spin-OLED is assembled in the configuration:

LSMO (20nm)/ ZnO (1.8nm)/ N965 (1ML)/ F8BT (65nm)/ MoO_x (3nm)/ Co (15nm)

The work function of the LSMO cathode is initially located at -4.4 eV but the ZnO and N965 layers modify it approximating it to the LUMO of F8BT. Both help to confront the difficulty in the electronic injection that is the bottleneck in these devices.[16] Indeed, they act as a tandem electron injection layer. On the other side of the device, the cobalt electrode injects holes in the HOMO of the F8BT aided by molybdenum oxide. As usual, the electron-hole pair recombines near the cathode and photons exit the device through the LSMO side.

There might be various reasons for the enhancement of the stability and reproducibility of the spin-OLEDs with the ZnO/N965 tandem of electron injection layers, when comparing to the PEIE and N965 spin-OLED devices reported in Prieto-Ruíz et al.[14]

First, the ZnO/N965 tandem has allowed us to use LSMO electrodes with roughness profiles above 1 nm but still obtaining high quality devices, contrary to the PEIE or N965-based spin-OLEDs. It should be taken into account that LSMOs with roughness profiles below the nanometer are not easy to fabricate without compromising the magnetic properties or the electrical conductivity. Figure 6.2 depicts the AFM image of the LSMO used for the device reported in this chapter. Presumably, the ZnO spin coated layer may smooth the surface providing a better substrate surface for the anchorage of the N965 monolayer (ML).

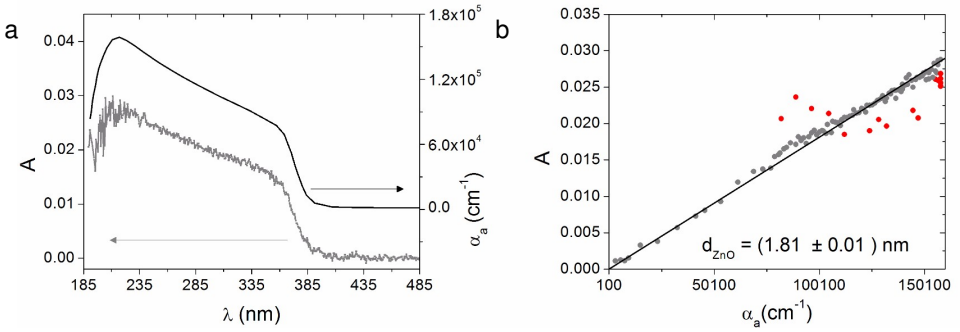

Figure 6.3 a) Absorbance curve for the ZnO layer on quartz compared with the absorbance coefficient curve extracted from the work of Khan and coworkers[19] b) Linear fit of $A(\lambda) = d_{ZnO}\ \alpha_a(\lambda)$ depicted in (a) to obtain a ZnO thickness of $d_{ZnO} = (1.81 \pm 0.01)$ nm. The red points have been excluded from the fit.

In addition, the conduction band of ZnO is slightly closer to the LUMO of the F8BT than the work function of the LSMO ($CB_{ZnO} = -4.2$ eV, $\phi_{LSMO} = -4.4$ eV) so the starting point is better in the ZnO case (the LUMO of F8BT is located at -3.5 eV).

Besides, ZnO presents high electron mobility and low light absorption.[20] These are positive characteristics in optoelectronic devices such as OLEDs[21] or solar cells.[22,23] ZnO has a band gap of 3.4 eV and a valence band located at -7.8 eV. Thin layers of ZnO are easily manufactured by means of several deposition techniques like sol-gel[24] or electrodeposition.[25] In some cases, the as-deposited metal oxide film needs an annealing at high temperatures to optimize the crystalline structure. In our case,

the layer of ZnO is spin coated on the LSMO surface and subsequently annealed in a protected atmosphere during 1 hour at 400 ºC (see the experimental section for a complete description of the ZnO deposition method).[17]

The thickness of the ZnO is maximized so that the spin polarization is not lost. At a later stage, the chosen thickness is determined by dividing the absorbance curve by the absorption coefficient curve by means of the Beer-Lambert law ($A(\lambda) / \alpha_a(\lambda) = d$, where A is the absorbance, α_a is the absorption coefficient and d is the thickness of the ZnO layer). Figure 6.3a depicts the absorption measurement for the ZnO layer compared to the absorption coefficient dependence on wavelength extracted from the study of Khan and coworkers.[19] The dependence of the absorbance with the absorption coefficient is shown in Figure 6.3b. The slope of the linear fit is an estimation of the thickness of the ZnO layer in the device: $d_{ZnO} = (1.81 \pm 0.01)$ nm.

On top of the ZnO layer, we deposit a monolayer of a single ionic molecular layer named N965, which contains a Ru atom. Its structure is depicted in the inset of Figure 6.4a, and its synthesis is described somewhere else.[17]

This ruthenium-based compound has the ability to enhance the electron injection into the organic semiconductor. Ions rearrange when an external voltage is applied and an strong field is induced at the interface.[17] As a consequence, the turn on voltage for light emission of the spin-OLED decreases. N965 is deposited through the Langmuir-Blodgett technique, as illustrated in Figure 6.4a, since it anchors to oxygen atoms. The molecule has one hydrophilic side and another side that is hydrophobic. This characteristic makes it to organize on a water surface. To check the proper deposition of the monolayer, we perform contact angle measurements. Since the alkyl chains in N965 are hydrophobic, if the film is well-formed, the contact angle is higher than 75° as seen in the picture on the bottom in Figure 6.4b.

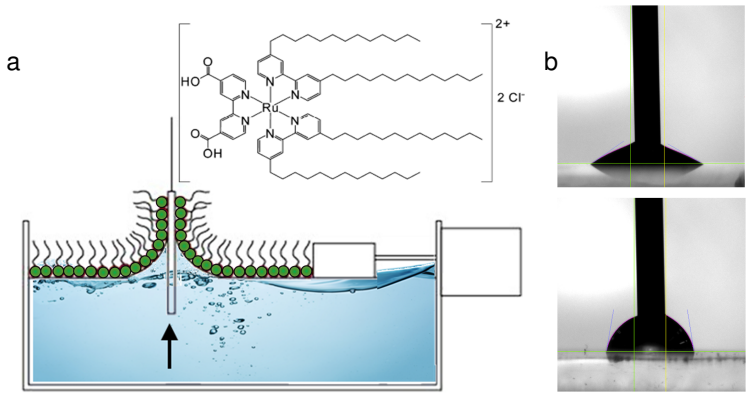

Figure 6.4 a) N965 molecular structure and illustration of Langmuir-Blodgett technique used to deposit the N965 monolayer. b) Contact angle of 30° before (top) and 80° after (bottom) the deposition of the N965 monolayer on the LSMO/ZnO surface.

6.2.2 Electric and Magnetic Characterization

The electric characterization of the spin-OLED is shown in Figure 6.5. The current-voltage and electroluminescence curves at different temperatures are shown in 6.5a and 6.5b respectively. The devices show an electroluminescence spectrum characteristic of the F8BT polymer layer with a maximum emission at the wavelength $\lambda = 560$ nm (green light). The spectrum registered at room temperature is shown in Figure 6.5c.

The spin-OLED presents a turn-on voltage (V_{ON}) of 3.2 V at room temperature (see Figure 6.5d). As the sample is cooled down, the V_{ON} is higher as expected (it shifts up to 8.3 V, at T = 40 K), because the transport inside the organic semiconductor is less effective, since it is thermally activated. At low temperature, the surface polarization of the LSMO electrode is higher and the MR shows the highest values.

The resistance of the spin-OLED calculated from the IV curves at different voltages in the temperature range studied is shown in Figure 6.5e, where the two differ-

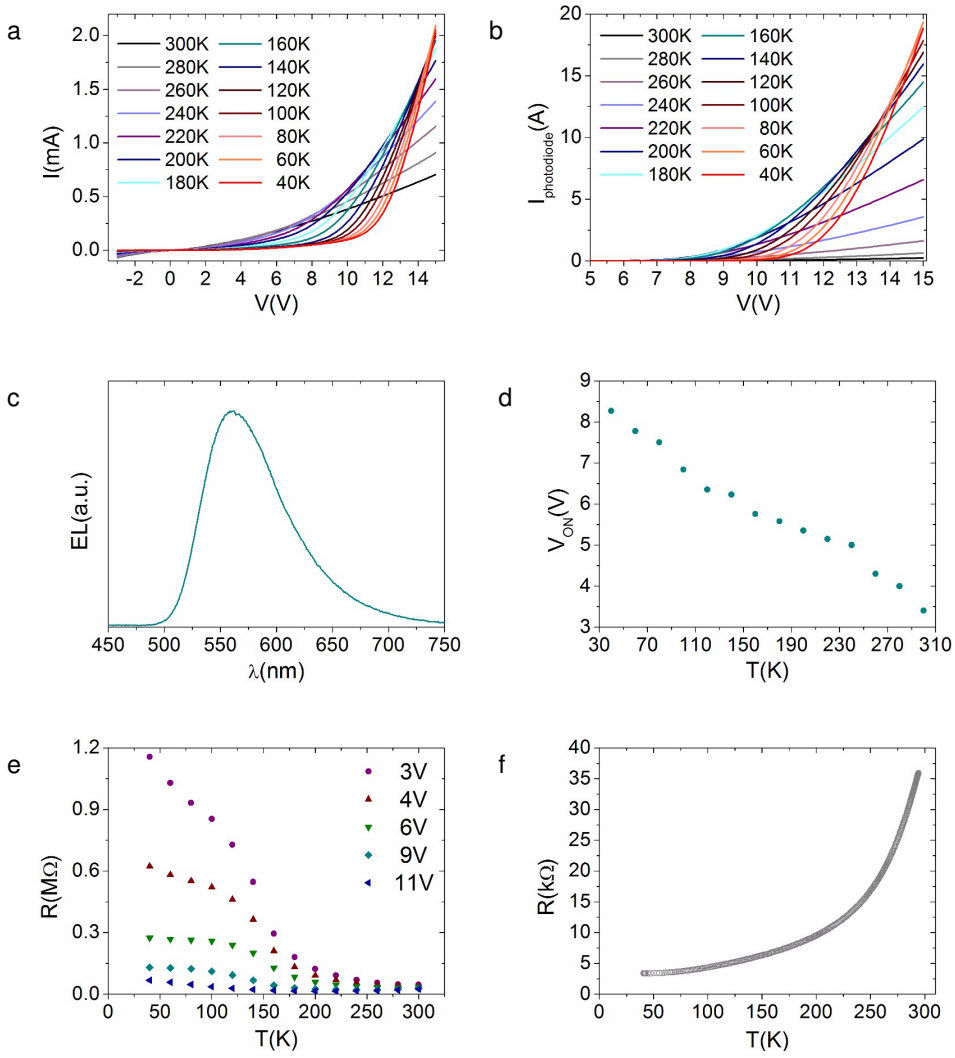

Figure 6.5 a) Current-voltage curves and b) light intensity registered in the photodiode of the spin-OLED at different temperatures. c) Electroluminescence spectrum of the spin-OLED measured at room temperature. d) Thermal dependence of the turn on voltage for light emission (V_{ON}). e) Resistance of the spin-OLED at different voltages as a function of the temperature calculated from the IV curves in (a). g) Thermal dependence of the resistance of the LSMO cathode showing a metallic behavior.

ent regimes that can be qualitatively seen in the IV curves of Figure 6.5a are here clearly appreciated. Although the dependence of the resistance with the temperature is in both cases weak, the spin-OLED shows a stronger dependence for the high resistance values.

The thermal dependence of the resistance of the LSMO electrode depicted in 6.5b reveals its metallic behavior. Besides, at low temperature the resistance of the electrode is low compared to the resistance of the spin-OLED and thus, the voltage drop at the electrode is negligible.

As usual, the MR is measured by sweeping an external magnetic field while applying a constant voltage to the device at a fixed temperature. Depending on the relative orientation of the magnetization of the electrodes the resistance reaches the antiparallel state (AP) and the parallel state (P).

The MR of the LSMO / ZnO / N965 / F8BT / MoO_x / Co spin-OLED shows, in general, lower values compared to the N965 based spin-OLED[18] or the PEIE spin-OLED.[14] In fact, the ZnO layer improves stability but depolarizes the current. Figure 6.6a shows the 7.2 % MR measured at 40 K and 3 V whereas Figure 6.6b depicts the 1 % MR measured at 3 V and 100 K. The MR signal is hysteretic and follows the coercive fields of the electrodes as seen in Figure 6.6d.

Figure 6.6c shows the voltage dependence of MR at 40 K for the LSMO electrode and the spin-OLED. This dependence exhibits the usually reported decay[2,12,13] but the MR signal is conserved up to very high voltages (MR $\approx$ 0.2 % at 13 V), probably due to the good energy alignment between layers and the charge recombination (radiative and non-radiative). The MR signal at high voltage is a necessary condition for the device operation since the most difficult task when fabricating a spin-OLED is the coexistence of MR and light emission at the same applied voltage and working temperature.

The light registered in the magnetic field sweep varies its intensity depending on the singlet:triplet ratio.[14] A MEL response of $\approx$ 0.9 % has been observed (Figure 6.6e), with an EL modulation that follows the coercive fields of the ferromagnetic

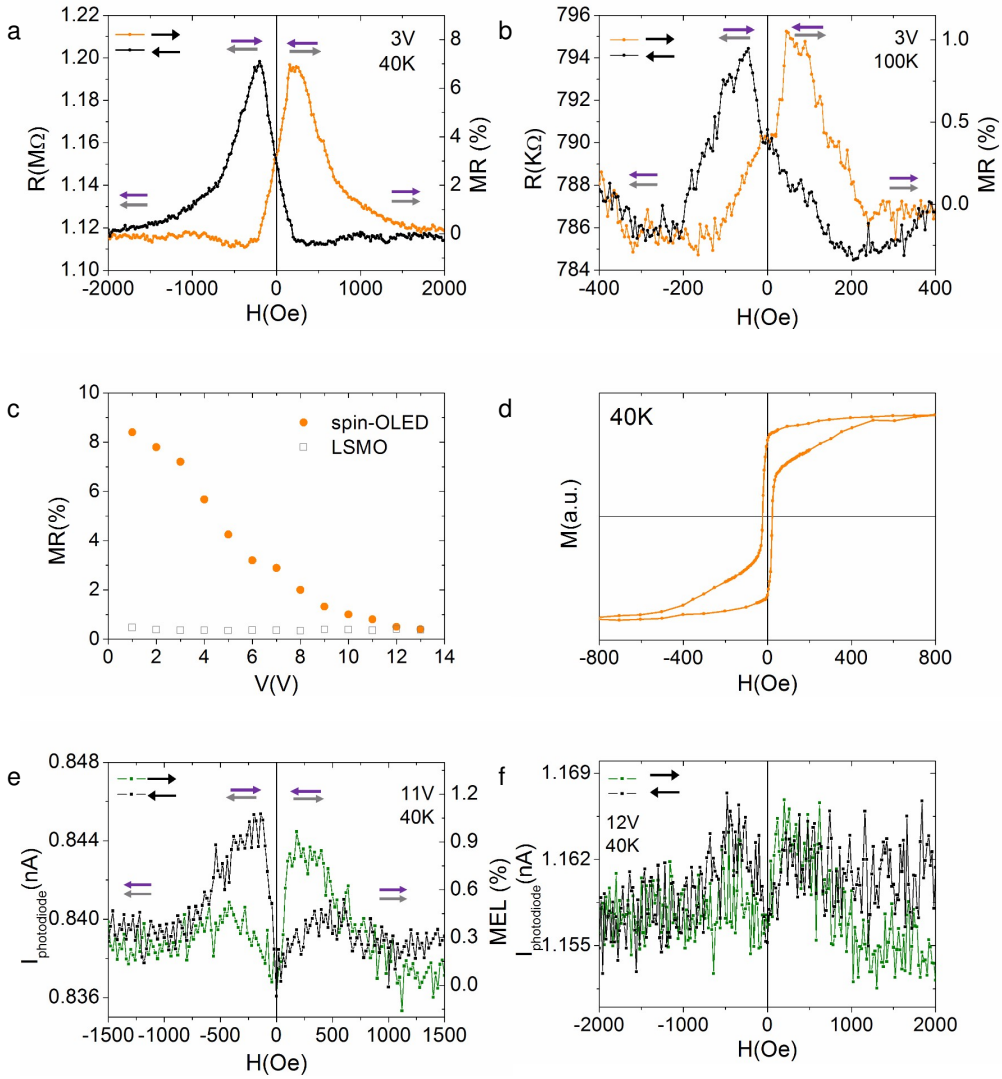

Figure 6.6 a) Magnetoresistance MR = 7.2 % of the spin-OLED at 3 V and 40 K. b) MR = 1 % at 100 K and 3 V. c) Magnetoresistance percentage of the spin-OLED (filled orange circles) and LSMO electrode (gray empty circles) as a function of applied voltage at 40 K. d) Hysteresis loop of the spin-OLED at T = 40 K with H_c(Co) = 400 Oe and H_c(LSMO) = 25 Oe. e) Maximum 0.9 % MEL signal measured at 40 K and 11 V in the spin-OLED. f) MEL effect at 12 V and 40 K.

electrodes (see Figure 6.6d). At 13 V the OMEL of the F8BT masks the MEL signal whereas at 12 V the MEL percentage decreases (Figure 6.6f). Consequently, only at 11 V there is a good signal to noise ratio. These will be the appropriate conditions for the Hanle measurements.

After the electrical and magnetic characterization of the LSMO / ZnO / N965 / F8BT / MoO_x / Co spin-OLED, the following section is devoted to the Hanle effect. These measurements are slow, mainly because of the waiting time for the electric current to stabilize. In addition, the sample is stressed because high voltages are applied for long periods of time. It is on this point where the stability and robustness of the sample is important. In fact, we didn't succeed in the Hanle measurements until the ZnO layer was incorporated to the spin-OLED.

The spin-OLED is considered the ideal system to study the Hanle effect since the light emitted from the organic emissive layer ensures that charge transport takes place across the frontier molecular orbitals (HOMO and LUMO) of the semiconductive layer, allowing to exclude any conduction through pinholes or thin areas and any tunneling magnetoresistance.

6.2.3 Study of Hanle Effect in the MR

The rationale of the Hanle is based on the rotation of the spin carriers in the molecular layer by the force exerted by a magnetic field.

We perform Hanle effect measurements in the spin-OLED as follows.[26] The device is initially prepared in the AP or P state by applying an in plane magnetic field ($\theta = 0$, where $0° < \theta < 90°$ is the angle between the magnetization direction of the FM electrodes and the field that sweeps). Then, a constant voltage is applied to the device and the current is stabilized for approximately 20 minutes. Later, the magnets were rotated $-\theta$ degrees, which is equivalent to rotate the sample θ degrees. At this point, the current is measured in a sweep of magnetic field (H_z), a field interval small enough to guarantee that the coercive fields of the electrodes are not reached, and

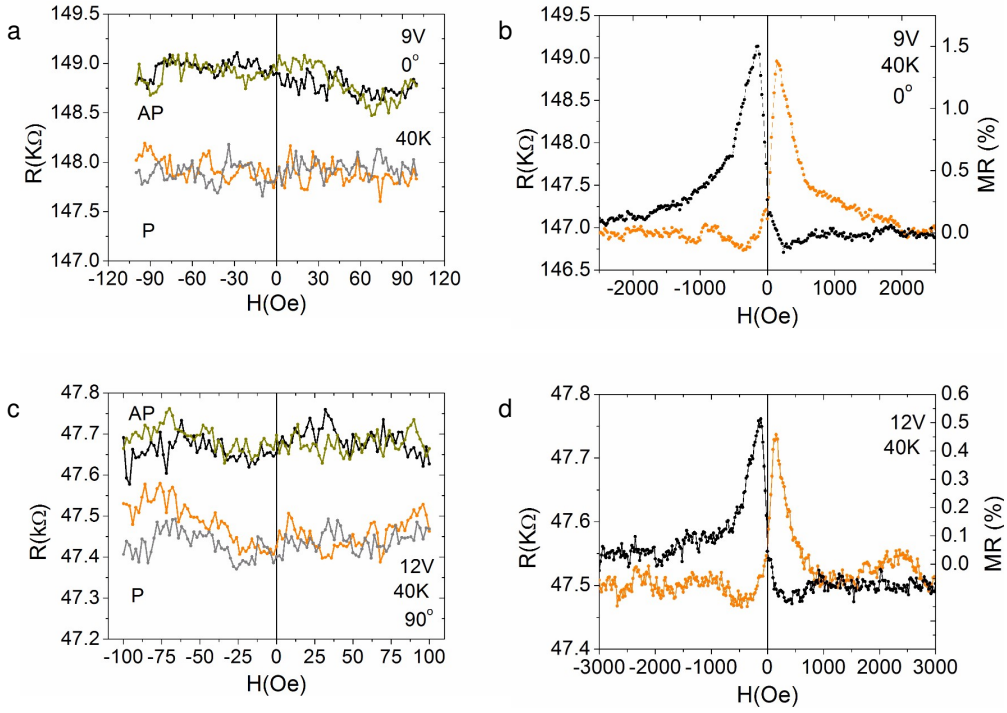

Figure 6.7 Hanle effect measurements at different voltages at 40 K. a) 9 V. b) 12 V. In both cases the resistance of the AP and P states are different and the Hanle effect is not observed. The loops at $\theta = 0°$ are shown on the right hand side.

big enough to overcome the hyperfine field.[27] First, the AP sweep is measured and subsequently the P sweep. Afterwards, the AP sweep is measured again to discard the influence of a drift in current into the measurement.

In the non-collinear magnetic field (H_z) the spins will precess in the emissive layer at the Larmor frequency ($\omega_{Larmor} = egH_z/(2m_e)$). The GMR is proportional to $\cos^2\theta$ according to the Johnson and Silsbee model.[28] For a perpendicular H_z ($\theta = 90°$) the spins will be randomly oriented when reaching the spin detector and consequently, the GMR will be quenched (see Equation 1.12 in the Chapter 1).

The Hanle measurements performed in the spin-OLED at different 9 and 12 V at 40 K are shown in Figure 6.7. On the left, the Hanle measurements for initial P and AP states are shown. The curve expected should be similar to the right hand side of Figure 6.1. However, in all cases, two separated horizontal lines were registered showing that the spin dephasing is not achieved. On the right of Figure 6.7, the complete magnetic field sweep at $\theta = 0°$ is shown (the signal of the LSMO electrode has been subtracted from the MR curves on the right hand side of the figures, the method used for the slope subtraction is explained in Appendix B).

Moreover, the absence of Hanle effect is also observed for different angles (see Figure 6.9) and higher temperatures (see Figure 6.8).

With the absence of Hanle effect in the spin-OLED, shown at different voltages, angles and temperatures, two opposite scenarios are most likely to unfold: in the first, the Hanle curve is too narrow,[29] while in the second scenario the curve is too broad[8] precluding the measurement of the effect in both situations.

In the first case, the spin memory is lost as consequence of the time that the spin carriers spend in the trap sites while hopping between molecules according to the model described by Roundy et al.[29] As a result, the Hanle curve is flat, except at low field. If this narrow zone is smaller than 1 Oe (which constitutes the minimum resolution set by the Earth's magnetic field) the width of the Hanle curve is smaller than the measurement resolution and consequently it is not detectable. In this case, the time that the spins need to cross the molecular layer ($t_{transit}$) is higher than the time they need to precess, related to the Larmor frequency ($t_{transit} >> 2\pi/\omega_L \Rightarrow$ Hanle curve narrowing).

In the second case, the spin carriers travel by pure spin currents,[8,30] generated by exchange between neighboring molecules, and are decoupled from electrons or holes. Spin transport is fast and there is not enough time for the spins to rotate while they travel in the molecular layer. Therefore, the Hanle curve is broadened and to measure the Hanle effect, the H_z field should be much more intense in order to increase the Larmor frequency. However, a more intense non-collinear field would modify the magnetization of the electrodes, which makes the measurement impos-

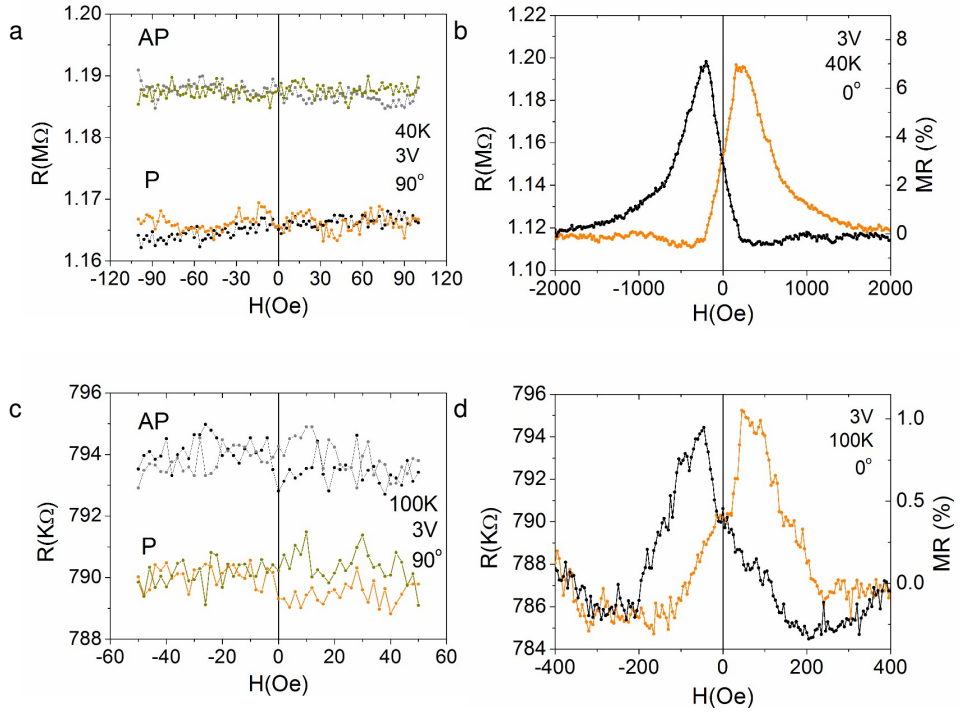

Figure 6.8 Temperature study. Resistances of the parallel and antiparallel states of the spin-OLED at 3 V and 40 K and 100 K with H_z applied at 90° (left). There is no quenching of the MR. On the right the MR at 0° is shown.

sible. In this case, the transit time is much smaller than the time that the spins need to precess ($t_{transit} << 2\pi/\omega_L \Rightarrow$ Hanle curve broadening.)

In order to find out the origin of the absence of Hanle effect in our spin-OLED, we calculate the time that the carriers need to traverse the F8BT layer and compare it to the time that they need to precess in the presence of H_z loosing their spin polarization.

The charge carrier mobility (μ) of holes in the case of the F8BT polymer, is one order of magnitude higher than the electronic mobility.[31] Thus, we consider that elec-

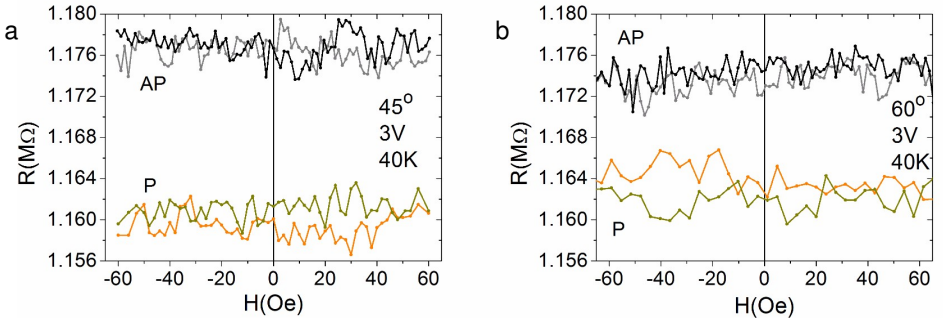

Figure 6.9 Angular study. Hanle effect measurements at different angles at 3 V and 40 K. a) $\theta = 45°$. b) $\theta = 60°$.

trons stay near the cathode while holes traverse the device. We can obtain the hole mobility by means of pulsed electroluminescence techniques.

In the measurements, a pulsed voltage is applied to the device and the light is registered in a time window that allows us to obtain the transient electroluminescence curves (see Figure 6.10). Figure 6.11a shows the transient electroluminescence curves at different temperatures of the device in a time window of 2500 ns after applying a voltage pulse of 5 V during 1000 ns. The delay time of the electroluminescence onset with respect to the application of the V pulse is related to the time of flight (ToF) as seen in Figure 6.11a. The drifting holes transit time can be measured as the time interval between the onset of the V pulse and the arrival time of the first photons in the transient electroluminescence signal.

In fact, light emission takes place once an exciton is formed (i.e. when an electron and a hole, injected from opposite electrodes drift under the electric field and bind together on the same site of the F8BT polymer chain) and radiatively decays. The assumption to use the onset of EL to determine the ToF value is valid if the exciton lifetime (of the order of nanoseconds) is negligible with respect to the observed transit time (of the order of hundreds of nanoseconds). By collecting electroluminescence transients and by measuring the ToF for holes at various temperatures, the thermal dependence of the hole mobility is calculated from T = 300 K down to T =

15 K (Figure 6.11b). The mobility is related to the velocity ($v = \mu_h \cdot E$) and calculated from:

$$\mu_h = \frac{x^2}{ToF \cdot V} \tag{6.1}$$

The transit time is inversely proportional to the applied voltage; thus, the mobility does not depend on the electric field ($E = dV/dx$).

We calculate the transit time, i.e., the time that the holes need to transverse the device at different voltages through:

$$t_{transit} = \frac{x^2}{\mu_h V} \tag{6.2}$$

With $\mu_h = 4 \times 10^{-5}$ cm^2/Vs at 40 K, the transit time for voltages applied in the Hanle curves are: $t_{transit}$ (3 V) = 352 ns, $t_{transit}$ (6 V) = 176 ns, $t_{transit}$ (9 V) = 117 ns, $t_{transit}$ (11 V) = 96 ns and $t_{transit}$ (12 V) = 88 ns.

The time that the carriers need to lose their spin polarization (t_L) can be obtained from the Larmor frequency:

$$t_L = \frac{2\pi}{\omega_L} = \frac{4\pi m_e}{egH_z} \tag{6.3}$$

For $H_z = 100$ Oe, the Larmor frequency amounts to 2 x 10^9 Hz, and $t_L \approx 1$ ns. Thus, the transit time is much longer than the precession time and, in principle, there is plenty of time to depolarize the current at all voltages applied.

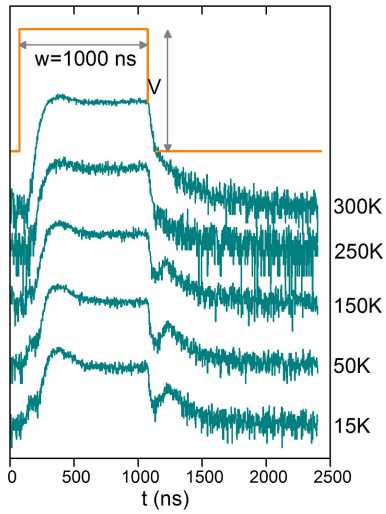

Figure 6.10 Temperature dependence of the the transient electroluminescence of the ITO (100 nm) / ZnO (1.8 nm) / N965 (1ML) / F8BT (65 nm) / MoOx (3 nm) / Au (35 nm) device, as collected at $\lambda = 560$ nm (maximum of F8BT emission spectrum), biasing the device by a pulsed voltage (indicated in orange, V = 5 V and pulse width of 1000 ns)

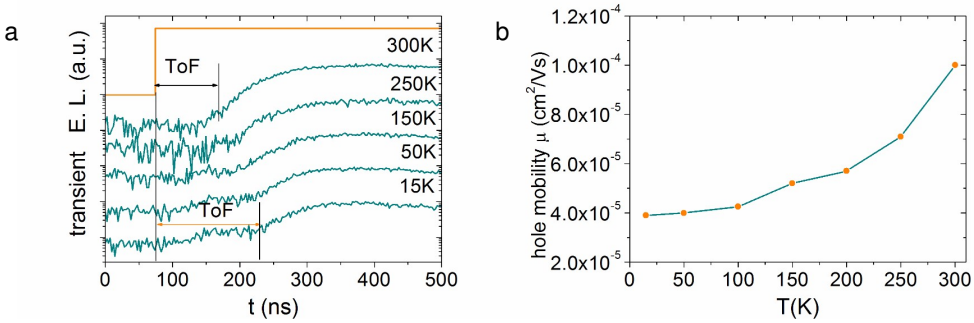

Figure 6.11 Time of flight and mobility. a) Transient electroluminescence at different temperatures at $\lambda = 560$ nm, following the application of a voltage pulse (orange line, V = 5 V, and a pulse width of 1000 ns). b) Temperature dependence of F8BT hole mobility, calculated from the transit times extracted from curves shown in (a).

6.2.4 Study of Hanle Effect in the MEL

The magnetic field not only influences the resistance of the device but also modifies the light intensity in a spin-OLED.[14] In the case of the MR, charge carriers are scattered with more or less intensity upon reaching the second electrode, depending on the relative orientation of the magnetization of the electrodes. But the case of the MEL is different, since the AP state increases the population of singlets and therefore the intensity of light. It is interesting to see if there is Hanle effect in the light emitted by the spin-OLED. As illustrated in Figure 6.12, if a field perpendicular to the direction of magnetization of the electrodes is applied, the electron and the hole would precess at the Larmor frequency as long as they are free charges or polaron pairs, but when the exciton is formed the magnetic field has no effect on them.[32]

Because of the low mobility of electrons compared with holes in F8BT, recombination electron-hole and light emission takes place near the LSMO cathode.[33] At 40 K, the V_{ON} is 8.3 V but a good signal to noise ratio in EL signal is still observed at 11 V, where the OMEL is not seen. Nevertheless, there is no Hanle effect in the light emitted by the device as seen in Figure 6.13.

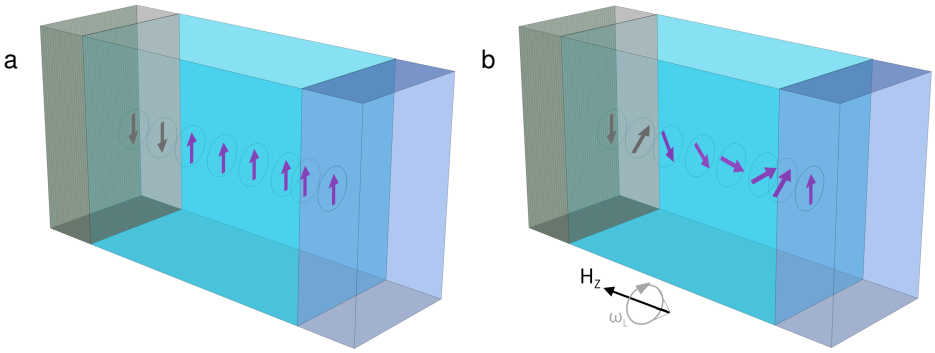

Figure 6.12 Sketch of the Hanle effect in the light emitted by the spin-OLED. The spins injected from the electrodes precess in the molecular layer due to H_z. When the exciton is formed, the spins have already flipped and the light intensity is not enhanced in the antiparallel state.

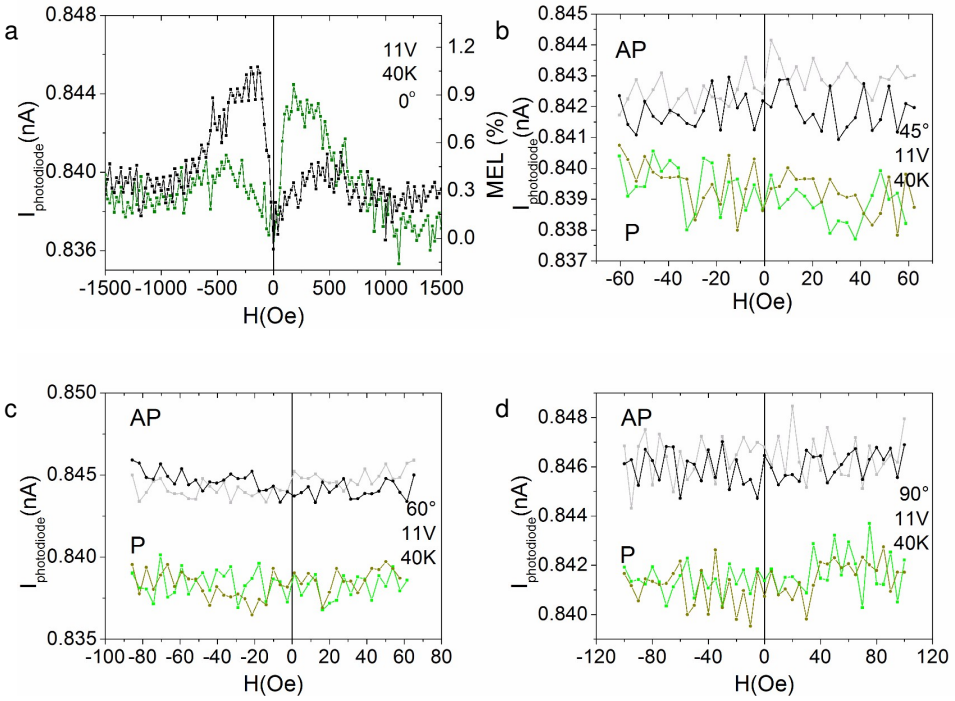

Figure 6.13 a) MEL effect of the spinOLED at 11 V and 40 K. Absence of Hanle effect in the light emitted by the spin-OLED. The non-collinear magnetic field is positioned at the angles: b) $\theta = 45°$. c) $\theta = 60°$. d) $\theta = 90°$.

Finally, control samples have been studied to discard the influence of the electrodes in the measurements. The roughness of the ferromagnetic electrodes might create local fields in the molecular material leading to an inhomogeneous spin accumulation and a broadening of the Hanle curve.[34] To test that this is not our case, we measured the Hanle curves in two devices with only one ferromagnetic electrode: ITO (100 nm) / ZnO (1.8 nm) / N965 (1 ML) / F8BT (65 nm) / MoO_x (3 nm) / Co (25 nm) / Au (35 nm) and LSMO (20 nm) / ZnO (1.8 nm) / N965 (1 ML) / F8BT (65 nm) / MoO_x (3 nm) / Au (35 nm). Figure 6.14 shows the Hanle measurements at 40 K and 11 V where no Hanle curve is observed in these devices. The noise of the recorded signal is lower than the expected MEL response (in the ITO−Co curve the noise is

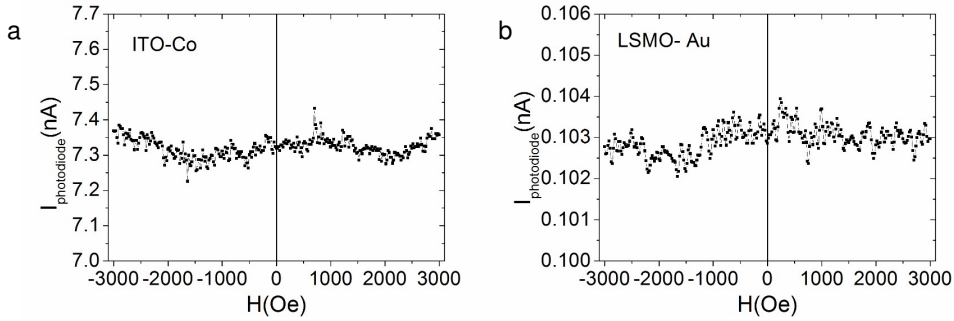

Figure 6.14 Hanle measurements in the control samples with only one ferromagnetic electrode. a) ITO / ZnO / LB / F8BT / MoO_x / Co / Au at 11 V and 40 K. b) LSMO / ZnO / LB / F8BT / MoO_x / Au at 11 V and 40 K.

0.7 % and in the LSMO−Au curve it is 0.5 %).

6.3 Conclusions and Perspectives

In this chapter we have studied the spin precession in a new spin-OLED where two EILs were used. The device showed high stability and a maximum MEL response of 1 % at 11 V at 40 K. The spin-OLED solved two problems that were encountered when studying the Hanle effect with molecular spin valves (MSVs). First, the light functionality ensures that the devices are not behaving as MTJs. Second, the charge transport takes place without question in the HOMO and LUMO of the molecular semiconductor, contrary to MSVs where the low voltages at which MR is measured imply that charge transport occurs in an intermediate trap band.[5]

The absence of Hanle effect in molecular spin valves has been modeled by Yu.[8] While hopping can lead only to charge transport, both hopping and exchange can transport the spin. Both mechanisms compete and depending on the local density of carriers, one dominates the other since hopping takes place between one charged and one neutral molecule whereas exchange occurs between neighboring occupied

molecules.[8]

Consequently, only for high local density of polarons, the exchange dominates over hopping in the molecular layer. However, the density of carriers obtained in our spin-OLED from the drift current ($j = e \cdot n \cdot \mu \cdot E$) amounts only to 10^{15} cm^{-3} at 3 V and 10^{16} cm^{-3} at 11 V. The model predicts that the exchange becomes significant for density of carriers $n > 10^{17}$ cm^{-3}. Thus, the exchange transport may be taking place thought small regions with high carrier density.

However, the most interesting part in this study concerns the absence of Hanle effect in the MEL signal. The theoretical framework of these experiments is being developed nowadays in collaboration with Dr. Zhi-Gang Yu. For electrons and holes with different g-factors, the spin diffusion-precession equations can be solved to obtain the spin polarization of electrons and holes in the organic material in the presence of H_z.

To conclude, the absence of Hanle effect in the spin-OLED strongly suggests that the spin transport in the emissive layer is due to electron exchange (pure spin currents).[8,30,35] In contrast to what happens to inorganic materials, in molecular materials spin and charge transport may travel decoupled.

6.4 Experimental Details

The devices have been manufactured in a class 10000 clean room that is shielded from UV radiation. The 20 nm thick LSMO spin-OLED cathode was grown by channel-spark ablation (CSA)[36] on (100) oriented double-side polished $SrTiO_3$ substrates. In the OLED devices, the cathode is formed by the commercial substrate glass-ITO (100 nm) received from Naranjo Substrates. A 3 x 3 cm glass / ITO substrate is diced in squares with area 0.8 mm x 0.8 mm. In both cases, substrates are cleaned manually with a solution of the alkaline soap Mucasol, from Sigma-Aldrich, in distilled water. Subsequently, they are sonicated in a mixture of Mucasol and distilled water, distilled water and isopropanol during 10 minutes in each of the three solu-

tions. Thereupon, substrates are dried in a nitrogen gas flow and placed during 5 minutes inside a UV lamp cleaner.

A Nanoscope Multimode (Veeco) atomic force microscope (AFM) in tapping mode operation was used in the morphological study of the LSMO electrode. The images were acquired in tapping-mode in air at room temperature with Si tips (frequency 300 kHz and K 40 Nm^{-1}). Image processing was done with the WSxM software developed by Nanotec Electronics.[37]

The ZnO layers were spincoated from a solution of $C_4H_{10}O_6Zn$ in H_2O-EtOH-CH_3COOH (5:1:1). The solution is kept under stirring overnight at 40 ℃. The films are deposited by spin coating and annealed during one hour in a laminar flow cabinet at 400 ℃.[38] The absorbance of ZnO the films deposited on quartz substrates has been measured with a Cary 300 UV-Vis spectrometer. The absorbance coefficient curve from reference[19] has been extracted by means of the Web Plot Digitizer software version 3.11.

A monolayer of the molecule bis(4,4‘-tridecyl-2,2‘-bipiridine)-(4,4‘-dicarboxy-2,2‘-bipiridine)-ruthenium-(II)-bis(chloride), named N965, was deposited on top of ZnO layer by means of the Langmuir-Blodgett technique using a KSV 300. The solution of N965 diluted in chloroform ($CHCl_3$) was spread on the water surface and an aqueous subphase of KPF_6. After 10 minutes the solvent $CHCl_3$ was evaporated. As the solvent was evaporated an organized monolayer of the N965 molecules was formed on the water surface. The monolayer was compressed within two barriers. This gives rise to an ordered 2D structure on the surface of water. The Langmuir film was transferred onto the substrate by dipping the substrate up and down through the monolayer. The transfer to the substrate was done at 27 mN/m. The synthesis of this ruthenium complex is described elsewhere.[17] The proper transfer to the substrate was checked by contact angle measurements using a Ramé-Hart Model 200 Standard Goniometer with Dropimage Standard v2.3 equipped with an automated dispensing system.

The light emitting polymer F8BT (poly(9,9-dioctylfluorene-alt-benzothiadiazole)- is spin coated from a chlorobenzene solution in a concentration 14 mg /ml, that is

previously placed under stirring and at 60 ℃ during 12 h. After the deposition at 2000 rpm during 40 s, films are annealed at 100 ℃ during 30 minutes inside a glove box (O_2 and H_2O concentrations $<$ 0.1 ppm). The F8BT layer thickness is measured with an Ambios-Technology profilometer model XP-1, placed on a vibration isolation table. Photoluminescence has been measured with an integrated sphere spectrophotometer.

The 3 nm MoO_x layer is sublimated in a thermal evaporator placed in a glove box, with oxygen and water concentrations below 0.1 ppm. The evaporation rate is kept at 0.05 nm /s at a pressure of 10^{-6} mbar. The gold electrode is thermally sublimated from effusion cells and using shadow masks at a base pressure of 10^{-6} mbar and a deposition rate of 0.01 nm/s. The spin-OLED active area amounts to 1.5 mm x 500 μm.

The MR and MEL are calculated as MR $=$ 100·(R_{AP} - R_P) / R_P and MEL $=$ 100·(EL_{AP} - EL_P) / EL_P, where AP and P indicate the antiparallel and parallel states. The magneto-transport properties were characterized via the standard two-probe method using a bespoke MEL set-up which is able to work in a temperature range of [18, 400] K. Magnetic fields up to 1 T can be applied and the electrical conductivity measurement is done by means of a Keithley 6517A electrometer, while light is detected with a Si photodiode and a Keithley 6485 picoammeter. The photocurrent was calibrated using a Minolta LS100 luminance meter. An Avantes luminance spectrometer was used to measure the EL spectrum of the device.

The time-resolved measurements were performed at ISMN-CNR Bologna in close collaboration with Dr. Lunedei. In time resolved electroluminescence, a pulsed bias was applied to the light emitting device by an Agilent 8114A-100 (100 V / 2 A) Pulse Generator, triggering in the same time the light detection system, based on a Hamamatsu H7422-20 photosensor module, whose output signal was fed into a TimeHarp-100 (time window up 150 ns) or into a NanoHarp250 (time window up to 2.15 s), both from Picoquant, Absolute intensity was measured by International Light Technologies ILT-1700 Research Radiometer. In low temperature electro/optical measurements, the sample was fixed on a cold finger at the end of the second stage in a dual-stage Helium close circuit refrigerator-cooled cryostat (Leybold, RDK 10-

320), that allows to control the sample temperature from 330 K down to 12 K. All the instruments are controlled by home-made software.

6.5 Bibliography

[1] H. Vinzelberg, J. Schumann, D. Elefant, R. Gangineni, J. Thomas, and B. Büchner. “Low temperature tunneling magnetoresistance on (La,Sr)MnO_3/Co junctions with organic spacer layers”. Journal of Applied Physics 103.9 (2008), p. 093720.

[2] Z. Xiong, D. Wu, Z. V. Vardeny, and J. Shi. “Giant magnetoresistance in organic spin-valves”. Nature 427.6977 (2004), pp. 821–824.

[3] D. Sun, E. Ehrenfreund, and Z. V. Vardeny. “The first decade of organic spintronics research”. Chemical Communications 50.15 (2014), pp. 1781–1793.

[4] J. Jiang, J. Pearson, and S. Bader. “Absence of spin transport in the organic semiconductor Alq_3”. Physical Review B 77.3 (2008), p. 035303.

[5] Z. G. Yu. “Impurity-band transport in organic spin valves”. Nature Communications 5 (2014), p. 4842.

[6] A. J. Drew, J. Hoppler, L. Schulz, F. Pratt, P. Desai, P. Shakya, T. Kreouzis, W. Gillin, A. Suter, N. Morley, and V. Malik. “Direct measurement of the electronic spin diffusion length in a fully functional organic spin valve by low-energy muon spin rotation”. Nature Materials 8.2 (2009), pp. 109–114.

[7] M. Cinchetti, K. Heimer, J.-P. Wüstenberg, O. Andreyev, M. Bauer, S. Lach, C. Ziegler, Y. Gao, and M. Aeschlimann. “Determination of spin injection and transport in a ferromagnet/organic semiconductor heterojunction by two-photon photoemission”. Nature Materials 8.2 (2009), pp. 115–119.

[8] Z. G. Yu. “Suppression of the Hanle effect in organic spintronic devices”. Physical Review Letters 111.1 (2013), p. 016601.

[9] M. Johnson and R. Silsbee. “Coupling of electronic charge and spin at a ferromagnetic-paramagnetic metal interface”. Physical Review B 37.10 (1988), p. 5312.

[10] S. P. Dash, S. Sharma, R. S. Patel, M. P. de Jong, and R. Jansen. “Electrical creation of spin polarization in silicon at room temperature”. Nature 462.7272 (2009), pp. 491–494.

[11] I. Zutic, J. Fabian, and S. D. Sarma. “Spintronics: Fundamentals and applications”. Reviews of Modern Physics 76.2 (2004), p. 323.

[12] V. A. Dediu, L. E. Hueso, I. Bergenti, and C. Taliani. “Spin routes in organic semiconductors”. Nature Materials 8.9 (2009), pp. 707–716.

[13] J. Devkota, R. Geng, R. C. Subedi, and T. D. Nguyen. “Organic spin valves: a review”. Advanced Functional Materials 26.22 (2016), pp. 3881–3898.

[14] J. Prieto-Ruiz, S. G. Miralles, H. Prima-García, A. Riminucci, P. Graziosi, M. Cinchetti, M. Aeschlimann, V. A. Dediu, and E. Coronado. “Controlling singlet-triplet ratio in OLEDs by spin polarised currents”. arXiv:1612.00633 (2016).

[15] T. D. Nguyen, E. Ehrenfreund, and Z. V. Vardeny. “Spin-polarized light-emitting diode based on an organic bipolar spin valve”. Science 337.6091 (2012), 204–209.

[16] M. Sessolo and H. J. Bolink. “Hybrid organic–inorganic light-emitting diodes”. Advanced Materials 23.16 (2011), pp. 1829–1845.

[17] H. J. Bolink, E. Baranoff, M. Clemente-León, E. Coronado, A. Lopez-Muñoz, D. Repetto, M. Sessolo, and M. K. Nazeeruddin. “Molecular ionic junction for enhanced electronic charge transfer”. Langmuir 25.1 (2008), pp. 79–83.

[18] J. P. Prieto-Ruiz. “Molecular spintronics: from magnetic materials to light emitting spintronic devices”. PhD thesis. 2015.

[19] Z. R. Khan, M. S. Khan, M. Zulfequar, and M. S. Khan. “Optical and structural properties of ZnO thin films fabricated by sol-gel method”. Materials Sciences and Applications 2.05 (2011), p. 340.

[20] D. C. Look. “Recent advances in ZnO materials and devices”. Materials Science and Engineering B 80.1 (2001), pp. 383–387.

[21] K. Zilberberg, J. Meyer, and T. Riedl. “Solution processed metal-oxides for organic electronic devices”. Journal of Materials Chemistry C 1.32 (2013), pp. 4796–4815.

[22] H. Y. Park, D. Lim, K.-D. Kim, and S. Y. Jang. “Performance optimization of low-temperature-annealed solution-processable ZnO buffer layers for inverted polymer solar cells”. Journal of Materials Chemistry A 1.21 (2013), pp. 6327–6334.

[23] D. Liu and T. L. Kelly. “Perovskite solar cells with a planar heterojunction structure prepared using room-temperature solution processing techniques”. Nature Photonics 8.2 (2014), pp. 133–138.

[24] Y. Sun, J. H. Seo, C. J. Takacs, J. Seifter, and A. J. Heeger. “Inverted polymer solar cells integrated with a low-temperature-annealed sol-gel-derived ZnO film as an electron transport layer”. Advanced Materials 23.14 (2011), pp. 1679–1683.

[25] S. Schumann, R. Da Campo, B. Illy, A. Cruickshank, M. McLachlan, M. Ryan, D. Riley, D. McComb, and T. S. Jones. “Inverted organic photovoltaic devices with high efficiency and stability based on metal oxide charge extraction layers”. Journal of Materials Chemistry 21.7 (2011), pp. 2381–2386.

[26] A. Riminucci, M. Prezioso, C. Pernechele, P. Graziosi, I. Bergenti, R. Cecchini, M. Calbucci, M. Solzi, and V. Alek Dediu. “Hanle effect missing in a prototypical organic spintronic device”. Applied Physics Letters 102.9 (2013), p. 092407.

[27] P. Bobbert, W. Wagemans, F. Van Oost, B. Koopmans, and M. Wohlgenannt. “Theory for spin diffusion in disordered organic semiconductors”. Physical Review Letters 102.15 (2009), p. 156604.

[28] M. Johnson and R. H. Silsbee. “Interfacial charge-spin coupling: Injection and detection of spin magnetization in metals”. Physical Review Letters 55.17 (1985), p. 1790.

[29] R. C. Roundy and M. E. Raikh. “Spin transport with dispersive traps: Narrowing of the Hanle curve”. Physical Review B 90.24 (2014), p. 241202.

[30] S. Jiang, S. Liu, P. Wang, Z. Luan, X. Tao, H. Ding, and D. Wu. “Exchange-Dominated Pure Spin Current Transport in Alq_3 Molecules”. Physical review letters 115.8 (2015), p. 086601.

[31] D. Kabra, L. P. Lu, M. H. Song, H. J. Snaith, and R. H. Friend. “Efficient single-layer polymer light-emitting diodes”. Advanced Materials 22.29 (2010), pp. 3194–3198.

[32] V. Prigodin, J. Bergeson, D. Lincoln, and A. Epstein. “Anomalous room temperature magnetoresistance in organic semiconductors”. Synthetic Metals 156.9 (2006), pp. 757–761.

[33] B. H. Wallikewitz, D. Kabra, S. Gélinas, and R. H. Friend. “Triplet dynamics in fluorescent polymer light-emitting diodes”. Physical Review B 85.4 (2012), pp. 22–25.

[34] S. P. Dash, S. Sharma, J. Le Breton, J. Peiro, H. Jaffrès, J.-M. George, A. Lematre, and R. Jansen. “Spin precession and inverted Hanle effect in a semiconductor near a finite-roughness ferromagnetic interface”. Physical Review B 84.5 (2011), p. 054410.

[35] Z. G. Yu. “Spin transport and the Hanle effect in organic spintronics”. Nanoelectronics and Spintronics 1.1 (2015), pp. 1–18.

[36] P. Graziosi, M. Prezioso, A. Gambardella, C. Kitts, R. K. Rakshit, A. Riminucci, I. Bergenti, F. Borgatti, C. Pernechele, M. Solzi, et al. “Conditions for the growth of smooth $La_{0.7}Sr_{0.3}MnO_3$ thin films by pulsed electron ablation”. Thin Solid Films 534 (2013), pp. 83–89.

[37] I. Horcas, R. Fernández, J. Gomez-Rodriguez, J. Colchero, J. Gómez-Herrero, and A. Baro. “WSXM: a software for scanning probe microscopy and a tool for nanotechnology”. Review of Scientific Instruments 78.1 (2007), p. 013705.

[38] H. J. Bolink, E. Coronado, D. Repetto, and M. Sessolo. “Air stable hybrid organic-inorganic light emitting diodes using ZnO as the cathode”. Applied Physics Letters 91.22 (2007), p. 223501.

Outlook

The research carried out during the PhD thesis and described in this manuscript belongs to the field of molecular spintronics. The field can be divided into two major branches: single-molecule spintronics, where the objective is the device miniaturization to the molecular size and molecular-based spintronics also known as organic spintronics, where molecular materials are incorporated in spintronic devices. The work described in this manuscript was focused in the latter area.

The research herein described was motivated by the desire to delve into the understanding of the physics underlying the molecular spin valve and spin-OLED devices.

The most studied molecule in this field is the aluminum (III) tris-8-hydroxyquinoline complex, a sublimable molecular compound very well-known by the OLED community. Motivated by its widespread use, not only in optoelectronics but also in molecular-based spintronics, a new family of quinoline-based compounds was studied in the Chapter 2 of this dissertation, based on lanthanoids. The five quinoline-based complexes have the chemical formula: A[Ln(5,7Cl_2q)$_4$] (where A = Na^+, $NEt_4{}^+$, $K_{0.5}(NEt_4)_{0.5}{}^+$, Ln = Y^{III}, Tb^{III}, Dy^{III}, 5,7Cl_2q = 5,7-dichloro-8-hydroxiquinoline, $NEt_4 = N(CH_2CH_3)_4$. For simplicity the compounds were named NaYClq, NaDyClq, NaTbClq, NEtDyClq and KNEtDyClq. The synthesis was motivated not just because they are molecular complexes similar to Alq_3, but also because they posses a magnetic nature. In fact, the Tb or Dy derivatives behave as single ion magnets. A comprehensive study was carried out to determine which compounds are sublimable with

the aim of fabricating thin films and incorporating them in heterostructures. An initial thermogravimetric analysis estimated the sublimation temperatures. Thereafter, we compared elementary analysis, infra-red and mass spectrometry analysis of all compounds in bulk and in films. The combination of these techniques indicated that only the Na derivatives compounds are thermally stable remaining intact upon sublimation. Finally, we checked by ac magnetometry that the single molecule magnet behavior is also observed in the films.

The molecular spin valve (MSV) and the magnetic tunnel junction (MTJ) are the typical devices in molecular-based spintronics. Basically they are formed by three layers: two ferromagnetic electrodes and a molecular spacer. The differences between them rely on the type of charge transport. In a MSV, the spin polarized charge is injected and transported through the molecular material whereas in a MTJ the charge carriers tunnel between electrodes. The electrodes, which have different coercive fields, change their relative magnetization orientation in a magnetic field sweep. The device shows a high or low resistance state depending on the scattering that the carriers undergo at the second electrode. Thus, in a typical device if the magnetization of the electrodes is in the same direction, the resistance is low; conversely, if the electrodes are in anti-parallel configuration the resistance is high. The dependence of the resistance with the magnetic field is termed magnetoresistance (MR). This phenomenon is the main topic of Chapters 3 and 4. In a typical MSV, MR is positive, which means that when the electrodes are in the antiparallel configuration the resistance is higher than in the parallel one.

The NaDyClq and NaYClq sublimable compounds of Chapter 2 were implemented as molecular layers in spintronic devices in chapter 3. The MSVs structure were Co / lb (1 nm) / NaLnClq ($8-15$ nm) / NiFe, where the lb is a thin partially oxidized aluminum seed layer. Interestingly, in this case MR is reversed with respect to a typical MSV. Thus, we measured negative MR, which means that when the electrodes are in the parallel (antiparallel) configuration the resistance is in the high (low) state. This is explained by the fact that one of the interfaces makes spin filtering inverting the polarization of the majority carriers. The molecule / ferromagnet interface that flips the spins is known as spinterface. We were able to identify the spinterface

by isolating the molecular material from the electrode, which resulted in a positive MR. The structure of the spin valve with the ferromagnetic electrodes swapped was NiFe / Ib (1 nm) / NaLnClq (25 nm) / Co. Finally, we measured the edges of the molecular atoms by X-ray absorption spectroscopy which allowed us to discard the chemical reaction and identify the hybridization states.

In Chapter 4 we introduced the polyoxometalates (POMs) into the molecular spintronics field for the first time. They are anionic compounds with three-dimensional structure formed mainly by oxygen and transition metals. We studied molecular spin-valves based on the $[PMo_{12}O_{40}]^{3-}$ Keggin anion. The robustness of the POM-based layers allowed us to design a MSV without any kind of oxide barrier. We compared two kind of devices in the configurations: LSMO (20 nm) / POM (100 nm) / Co (25 nm) and LSMO (20 nm) / POM (80 nm) / MoO_x (3 nm) / Co (25 nm). The energy level alignment was studied by means of UPS measurements and the appropriate MoO_x thickness was extracted from the spin-polarized UPS analysis. Surprisingly, the MSV with MoO_x showed magnetoresistance at high voltages (above 3.5 V), which is something quite unusual in this type of devices that typically loose the signal at voltages around 1 V.

Chapters 5 and 6 were devoted to spin-OLEDs which are multifunctional devices that behave at a time as OLEDs and MSVs. In an OLED, quantum statistics rules the formation of 3 triplets and 1 singlet, all with equal probability $1/4$. The singlets are the main responsible of light emission in organic semiconductors, limiting the maximum electron to photon conversion to 25 %. This theoretical limit is doubled in a spin-OLED which can reach a value of 50 %. Two ferromagnetic electrodes modify the singlet-triplet relative populations, since they inject polarized charges. In the antiparallel configuration only the singlet and 1 out of the 3 triplets can be formed and thus the limit is increased 50 %. The equivalent to the MR measurement is the magneto-electroluminescence (MEL) effect where the light intensity is modulated by an external magnetic field.

In Chapter 5 we designed the spin-OLED: LSMO / PEIE (1 nm) / F8BT (45 nm) / MoO_x (3 nm) / Co, where PEIE $=$ polyethylenimine ethoxylated and F8BT $=$ poly(9,9-dioctylfluorene-alt-benzothiadiazole). The UPS data demonstrated that both

PEIE and MoO_x modify the electrode's work functions and help electrode and hole injection in the HOMO and LUMO respectively of the emissive F8BT polymer layer. This device broke the record of MEL effect with 2.4 % at low temperature, what allowed us to study the MEL effect in a wide range of temperatures and voltages. Besides, all the layers assembled were made from commercial materials and the major components were deposited by solution techniques. Both features reduce the production costs and facilitate the scaling in large areas. Finally, this spin-OLED device has demonstrated for the first time that a spin polarization from the ferromagnetic electrodes to the frontier orbitals of the organic material is possible.

Parallel to the study carried out in the previous chapter, spin precession was studied in a very similar spin-OLED, described in chapter six, by means of the Hanle effect. The effect is considered the litmus test to demonstrate that the spin injection in molecular materials is at the origin of the magnetoresistance. So far it has not been measured in a functional molecular spin valve. The objective of the Hanle effect experiment is to depolarize the current in the molecular semiconductor by means of a non-collinear magnetic field and enforce the quenching of the magnetoresistance. So far, the reason of the absence of Hanle effect in a MSV remained unclear since it was not possible to discern whether the charge was being injected into the molecular semiconductor, or the carriers tunnel between electrodes through pinholes or thin areas.

Therefore the spin-OLED constitutes the ideal device for studying spin precession since the emission of light ensures charge transport through the molecular material. The spin-OLED used for this experiment had the structure: LSMO / ZnO (1.8 nm) / N965 (1 ML) / F8BT (45 nm) / MoO_x (3 nm) / Co. This spintronic device showed a high reproducibility and stability, both fundamental characteristics necessary to study spin precession. Remarkably, we measured the absence of Hanle effect not only in the resistance but also in the light emitted by the spin-OLED at 40 K. We concluded, with the help of a theoretical framework, that our measurements point to separate channels for spin and charge transport. As electrons and holes traverse the molecular layer by hopping, the spin crosses it by exchange which is much faster.

In summary, the research carried out has tried to address some hot topics in the field of molecular spintronics such as the spinterface, the magnetoresistance at high voltage and charge and spin transport mechanisms in MSVs and spin-OLEDs.

The perspectives in each of the studied lines are several. Regarding the first part of the thesis, it will be interesting to assemble MSVs with several families of quinoline-based molecules that have recently been synthesized in our group. They would shed light on the role of the central lanthanide atom and whether it is possible to polarize the SIM layers through the ferromagnetic electrodes. For this it would be necessary to have hopping transport, contrary to what happened in our devices which were in the tunneling regime. One of the possible problems in carrying out this objective is that HOMO and LUMO in the quinoline-based molecules are located spatially on the ligands and they are very similar in all the compounds of the different family members. However, it would not be surprising that carriers were affected by the magnetism of the central lanthanide despite being traveling around the periphery of the molecules.

As far as polyoxometalates are concerned, our deposition method can be used to deposit many other compounds of this large family. The comparison between them can be very interesting when it comes to understand the mechanisms that govern molecular spin valves. Besides, molybdenum oxide has allowed us to build a spin valve with magnetoresistance at high voltage, which is a necessary condition when incorporating these devices into the technology. A further exploration of this kind of devices will be worthwhile to understand the reasons that bring magnetoresistance to high voltages.

As for the spin-OLEDs, it would be good to change the LSMO electrode by NiFe to have MEL signal at room temperature. In addition, it would also be very appealing to design a spin-OLED based on perovskites, that have already shaken optoelectronics, and hopefully will work very well in this type of devices.

Finally, the Hanle effect resistance measurements rely on a robust model, but a theoretical framework is needed to describe the absence of Hanle effect in the light emitted by the spin-OLED. This modeling would allow us to better understand how

the spin transport in molecular materials takes place.

In general, molecular spintronics is a very young field and it is expected that it will revolutionize in the future the magnetic information storage technology with the incorporation of molecular spintronics devices into consumer electronics.

A

NaDyClq AC Susceptibility Measurements

The single ion magnet behavior of the compound NaDyClq has been experimentally checked by applying an ac magnetic field at different frequencies superimposed to a small dc field that avoided the quantum tunneling relaxation.

The Cole-Cole plots indicate a single dominant relaxation mechanism through the low alpha values (see Equation 2.1), with no indication of a secondary mechanism, so that all available experimental data can be rationalized by assuming a Raman (see Equation 2.3) or an Orbach relaxation mechanisms. The latter is described by an Arrhenius law (see Equation 2.2). The data shown in this appendix has enabled us to obtain the extrapolation of the U_{eff} and B_{Raman} parameters at $H_{dc} = 0$ as seen in Figure 2.12 in Chapter 2.

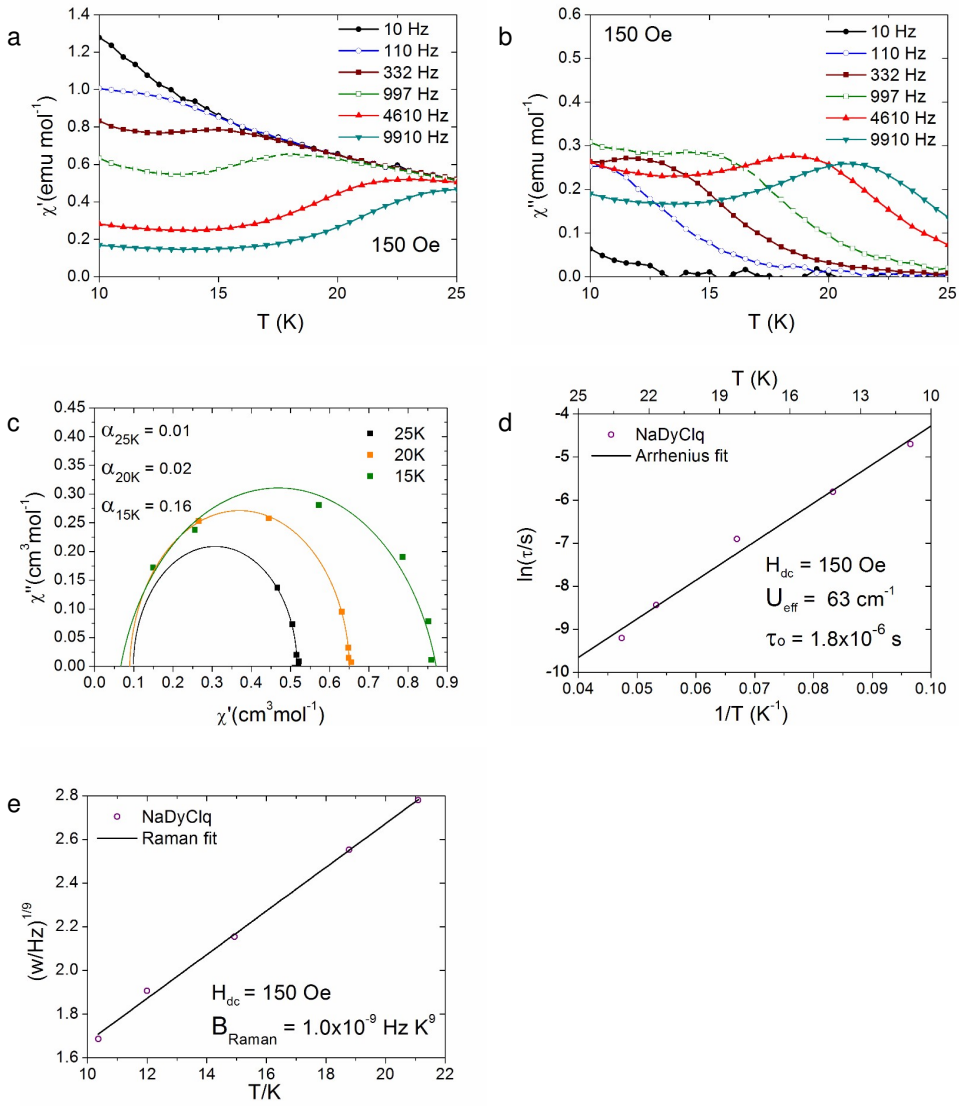

Figure A.1 ac measurements and fits of bulk NaDyClq at $H_{dc} = 150$ Oe. a) Magnetic susceptibility in phase. b) Magnetic susceptibility out of phase. c) Cole-Cole plots. The points represent the data constructed from the χ' and χ" experimental curves whereas the lines are the fits to equation 2.1. d) Arrhenius fit with an effective energy barrier $U_{eff} = 63$ cm^{-1}, and a pre-exponential factor $\tau_0 = 1.8 \cdot 10^{-6}$ s. e) Raman fit with $B_{Raman} = 1.0 \cdot 10^{-9}$HzK^9.

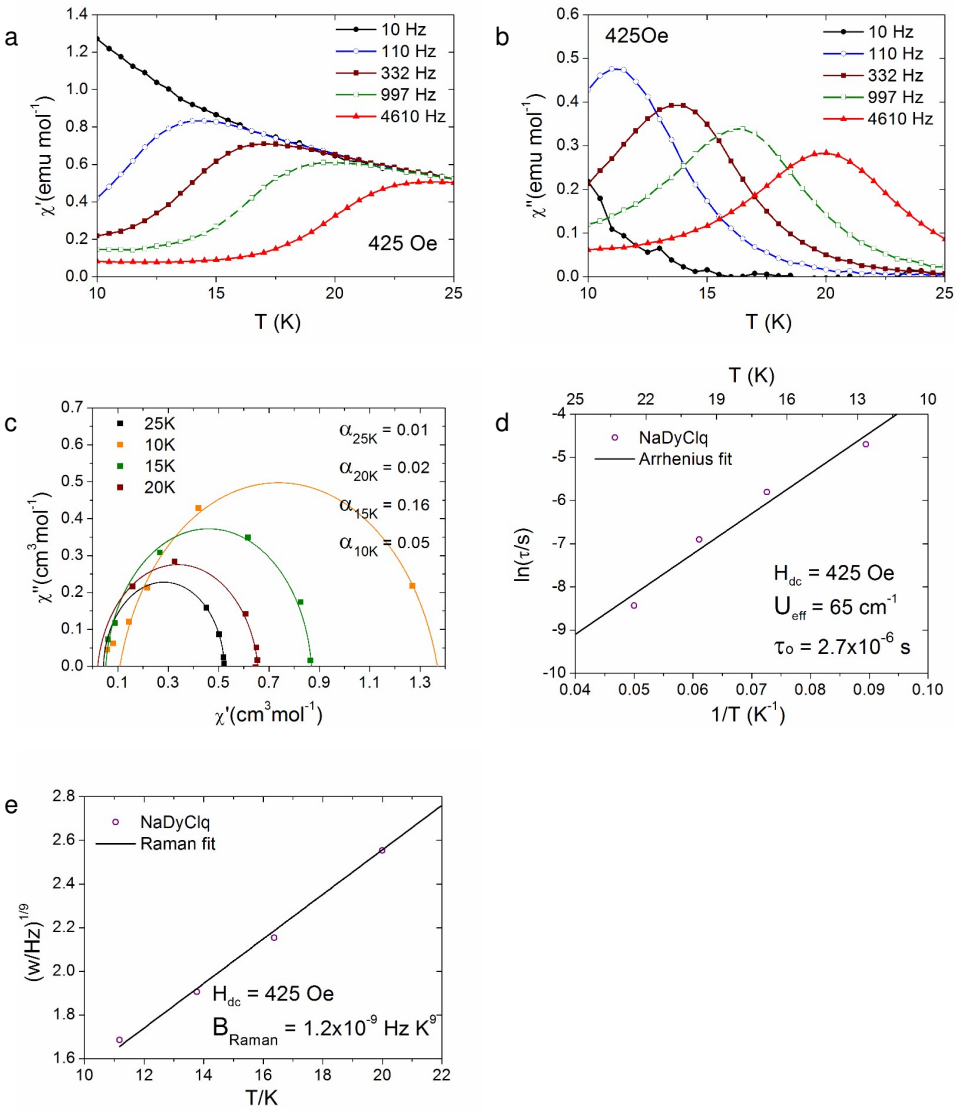

Figure A.2 ac measurements and fits of bulk NaDyClq at $H_{dc} = 425$ Oe. a) Magnetic susceptibility in phase. b) Magnetic susceptibility out of phase. c) Cole-Cole plots. The points represent the data constructed from the χ' and χ" experimental curves whereas the lines are the fits to equation 2.1 from where the α values are obtained. d) Arrhenius fit with an effective energy barrier $U_{eff} = 65$ cm^{-1}, and a pre-exponential factor $\tau_0 = 2.7 \cdot 10^{-6}$ s. e) Raman fit with $B_{Raman} = 1.2 \cdot 10^{-9}$HzK^9.

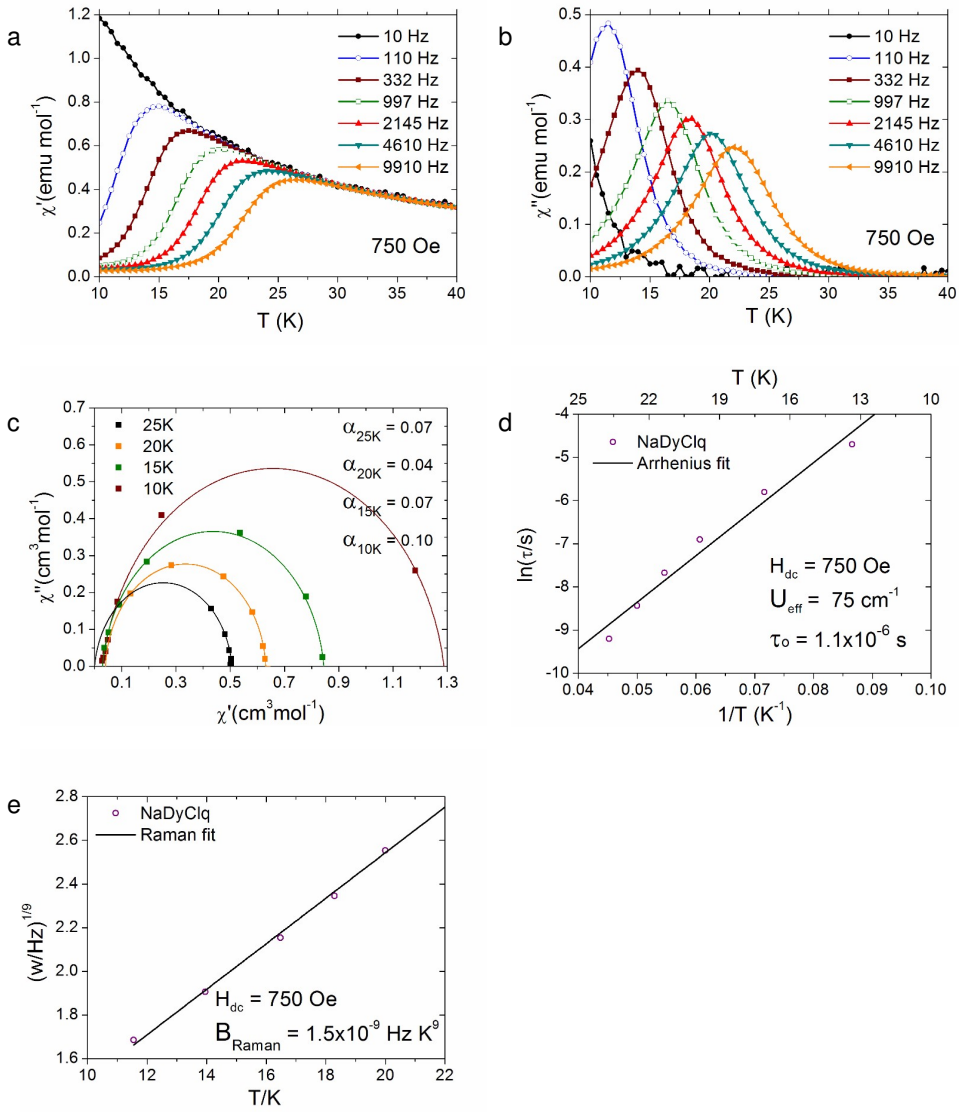

Figure A.3 ac measurements and fits of bulk NaDyClq at $H_{dc} = 750$ Oe. a) Magnetic susceptibility in phase. b) Magnetic susceptibility out of phase. c) Cole-Cole plots. The points represent the data constructed from the χ' and χ" experimental curves whereas the lines are the fits to equation 2.1. d) Arrhenius fit with an effective energy barrier $U_{eff} = 75$ cm^{-1}, and a pre-exponential factor $\tau_0 = 1.1 \cdot 10^{-6}$ s. e) Raman fit with $B_{Raman} = 1.45 \cdot 10^{-9}$HzK^9.

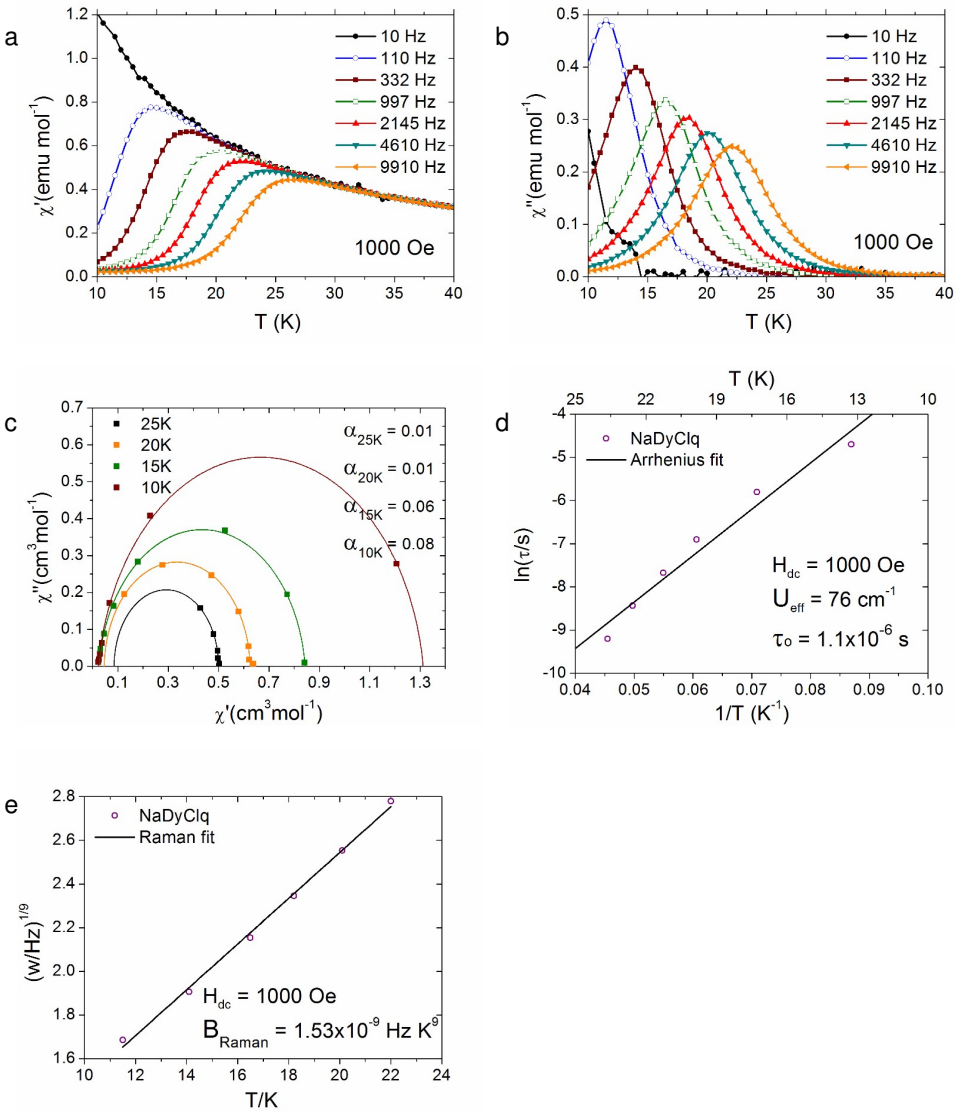

Figure A.4 ac measurements and fits of bulk NaDyClq at $H_{dc} = 1000$ Oe. a) Magnetic susceptibility in phase. b) Magnetic susceptibility out of phase. c) Cole-Cole plots. The points represent the data constructed from the χ' and χ" experimental curves whereas the lines are the fits to equation 2.1. d) Arrhenius fit with an effective energy barrier $U_{eff} = 76$ cm^{-1}, and a pre-exponential factor $\tau_0 = 1.1 \cdot 10^{-6}$ s. e) Raman fit with $B_{Raman} = 1.53 \cdot 10^{-9}$HzK^9.

B

MR and MEL Signal Processing

In the MR and MEL curves described in this manuscript the contribution of the LSMO electrode has been subtracted, if indicated, using a local regression,[1,2] as described below.

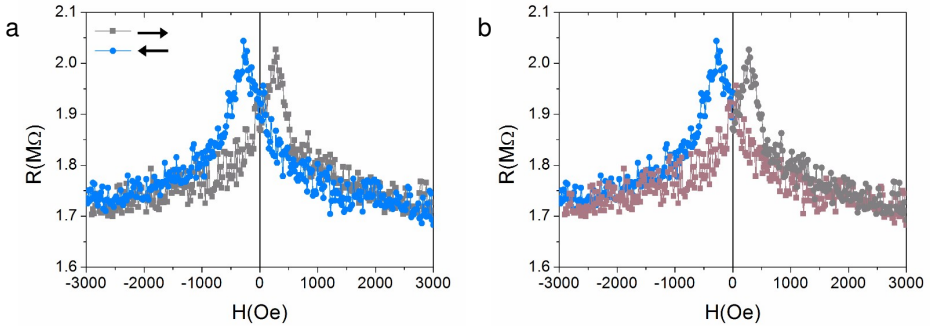

Figure B.1 Example of MR signal processing. a) Raw data. b) Contribution of the LSMO electrode highlighted in brown.

Figure B.1 shows an example of MR signal processing executed. The as-obtained signal is depicted in Figure B.1a. The baseline of the MR and MEL responses would be flat in the absence of the electrode contribution (see Figures 1.4 or 1.11 in Chapter 1). Thus, we assume that the brown curve in Figure B.1b corresponds to the LSMO electrode. This contribution is fitted locally to straight lines. Then, the process consists on subtracting the electrode contribution to the MR signal. In the example of Figure B.1b, the brown curve is subtracted from itself, the gray and blue curves. The MR curve obtained is shown in Figure B.2.

The electrode contribution curve is formed by a data set of pairs (H_i,R_i) where the resistance can be described as a function (f) of the field (H) plus an error term (ϵ):

$$\begin{aligned} R_i^{for} &= f^{for}(H_i^{for}) + \epsilon_i \\ R_i^{back} &= f^{back}(H_i^{back}) + \epsilon_i \end{aligned} \tag{B.1}$$

for and back refer to the forward ($\rightarrow$) and backward ($\leftarrow$) magnetoresistance curves in the magnetic field sweep.

For a fitting point H, we choose a bandwidth h(H) that defines a smoothing window (H $-$ h(H), H $+$ h(H)). The h(H) is chosen as the minimum distance, where the distance is d(H, H_i) $=$ |H $-$ H_i|, required to include 70 % of the data points in the smoothing window. Only the data points H_i included in the smoothing window are used to estimate f(H_i). Within the smoothing window around H, f can be approximated by the Taylor's series:

$$f(x) \approx a_0 + a_1(x - H) + \frac{1}{2}a_2(x - H)^2 \tag{B.2}$$

whenever |x - H| $<$ h(H).

The coefficients a_0, a_1 and a_2 can be estimated numerically by minimizing the locally weighted sum of squares:

$$\sum_{i=1}^{n} w_i(H)(R_i - f(H_i)) \tag{B.3}$$

$$\sum_{i=1}^{n} w_i(H)\left(R_i - \left(a_0 + a_1(H_i - H) + \frac{1}{2}a_2(H_i - H)^2\right)\right)$$

Besides, the data points are weighted according to:

$$w_i(H) = W\left(\frac{H_i - H}{h(H)}\right) \tag{B.4}$$

where W(x) is a weight function that assigns largest weights to points close to H:

$$W(x) = (1 - |x|^3)^3 \tag{B.5}$$

Thus, the local regression estimate at the fitting point H is the estimation of the coefficient a_0:

$$f(H) = a_0 \tag{B.6}$$

Finally, once we have the estimation for f^{for} and f^{back}, the corrected signal ($\widetilde{R}$) is:

$$\widetilde{R}_i^{for}(H_i^{for}) = \begin{cases} R_i^{for} - f^{back}(H_i^{for}), & H_i > 0 \\ R_i^{for} - f^{for}(H_i^{for}), & H_i < 0 \end{cases} \tag{B.7}$$

$$\widetilde{R}_i^{back}(H_i^{back}) = \begin{cases} R_i^{back} - f^{back}(H_i^{back}), & H_i > 0 \\ R_i^{back} - f^{for}(H_i^{back}), & H_i < 0 \end{cases} \tag{B.8}$$

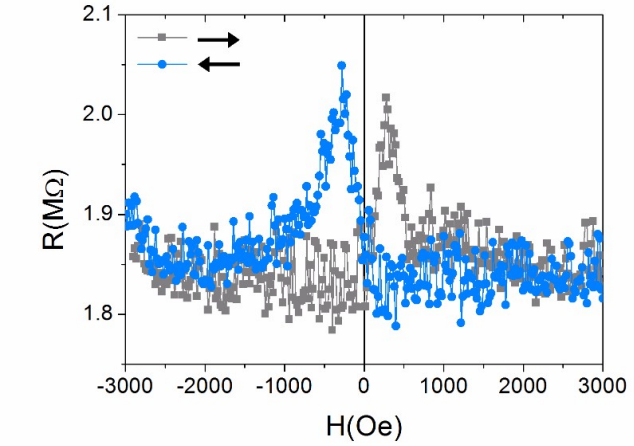

Figure B.2 Processed MR curve.

Bibliography

[1] C. Loader. Local Regression and Likelihood. New York: Springer, 1999. 290 pp.

[2] C. Loader. locfit: Local Regression, Likelihood and Density Estimation. R package version 1.5-9.1. 2013.

C

Experimental Techniques and Equipment

AFM

Atomic force microscopy (AFM) is a type of scanning probe microscopy that reveals the topography of samples in the range of microns. In the atomic force microscope, a tip of a pair of microns in length and less than 100 Å in diameter located at the end of a flexible cantilever scans the surface of the sample. The van der Waals forces between the tip and the surface causes the cantilever to bend. A detector measures the flection and the topography is imaged. A piezoelectric scans the motion and a reflecting laser monitories the interaction between the tip and the sample, which then is collected by a photodiode. The voltage differences in the four zones of the photodiode determine accurately the changes in amplitude of the tip oscillation.

AFM images were obtained using the tapping mode in air at room temperature

with Si tips. The processing and analysis of the images were carried out using the Nanotec WSxM software. The peak to peak roughness ($\rho_{\text{peak to peak}}$) is defined as the difference between the maximum and minimum heights. whereas the root mean square roughness (ρ_{RMS}) is defined as $\rho_{RMS} = \sqrt{\frac{1}{N}\sum_{i=1}^{N} z_i^2}$, where z_i are the height values.

In the Cic-Nanogune facilities the atomic force microscopy images were recorded by means of an AFM 5500 Agilent-Nano Observer CSI Instruments equipment, while in the ICMol facilities, a Nanoscope IVa atomic force microscope from Veeco was used in tapping mode.

C-H-N Elemental Analysis

The percentage of the light elements carbon, hydrogen and nitrogen in the samples was determined by C-H-N analysis. The technique consists in oxidizing completely the sample through combustion. Subsequently, the combustion products are separated by a chromatographic column and registered by the thermal conductivity detector, which gives an output signal proportional to the concentration of the individual components.

Carbon, hydrogen and nitrogen contents were determined by micro-analytical procedures using an EA 1110 CHNS-O Elemental Analyzer from CE at the SCSIE technical facilities of the University of Valencia.

Clean Room

Spin-OLEDs and POM-based spin valves were fabricated in a class 10000 clean room of 50 m^2, shielded from UV radiation coming from illumination to protect sensitive materials during the whole fabrication process.

EDX Analysis

The energy dispersive X-ray (EDX) analysis uses a high-energy beam of charged particles, such as electrons, to determine the atomic proportions in a sample. Electrons impact on the material and excite electrons in inner atomic orbitals. Then, electrons in higher atomic orbitals fill these holes and the difference in energy is released in the form of X-rays. The energies of the X-rays are characteristic of each element, thus elemental analysis of the surface is obtained. In the scanning electron microscopy (SEM) equipment used we obtained a reliable signal for elements from Na onwards in the periodic table.

The percentage of Y, Dy, Tb, Cl, Na and K in the samples was estimated by electron probe microanalysis performed with a Philips SEM XL30 equipped with an EDAX DX-4 microprobe. Neat samples were prepared on $Si-SiO_2$ substrates (films) or on carbon tape (compounds), placed under general 10^{-6} mbar pressures and analysed with a 20 kV electron beam at a working height of 10 cm.

ESI-MS

Electrospray ionization mass spectrometry (ESI-MS) is an analytical technique that provides structural information of molecules. The sample is diluted and delivered through a capillary tube to which a high electric potential is applied. At the exit of the tube, the solution is dispersed in small charged drops, which evaporate. The ionized drops are accelerated in a magnetic field where the trajectory depends on their mass and charge. During detection, the variable potentials cause instability in the trajectories of the ions to distribute them in the axial direction as a function of their m / z ratio giving rise to the mass spectrum.

For the ESI-MS studies, a QTOF Premier instrument with an orthogonal Z-spray-electrospray interface (Waters, Manchester, UK) was used. The drying and cone gas was nitrogen set to flow rates of 300 and 30 L/h, respectively. A capillary voltage

of 3.5 kV was used in the positive scan mode, and the cone voltage was set to Uc = 10 V to control the extent of fragmentation. The isotopic distributed patterns were simulated using the mMass software (v. 5.5.0).

The ESI-mass spectra were obtained with a Waters Micromass ZQ spectrometer at the technical facilities of the University of Castellón.

Evaporators

In the Cic-Nanogune facilities the molecular spin valves were assembled by layer sublimation in a Theva ultra-high vacuum dual evaporator. In the dual chamber metals are e-beam sublimated while molecules thermally evaporated from conventional effusion cells. The base pressure is 10^{-11} mbar.

In metallic layers deposited by electron beam, the contamination levels are lower compared to thermal evaporation, allowing the formation of high quality films. Besides, adhesion is believed to be better. In e-beam evaporation, an electron beam is generated by applying an electric current to a filament which is subjected to a high electric field. The electrons scape from the filament while are focused by magnets to form a beam. This beam is directed to the crucible that contains the metal. The energy of the beam is transferred to the material, allowing its evaporation.

In the ICMol facilities the layers were thermally sublimated in an evaporator placed in a glove box from conventional effusion cells, with a base pressure of 10^{-6} mbar. The thickness is monitored with an Edwards FTM7 film thickness monitor.

Infrared Spectroscopy

Infrared (IR) spectroscopy is based on the fact that molecules absorb IR radiation at the characteristic frequencies of their structure.

Infrared spectra were collected on a Nicolet 5700 FT-IR spectrometer. Compound spectra were recorded from solid products prepared in the form of KBr compressed pellets.

Glove Box

A globe box from MBRAUN allowed the manipulation of sensitive materials in an inert N_2 atmosphere with H_2O and O_2 concentrations < 0.1 ppm.

Langmuir-Blodgett

The molecular compounds suitable for the formation of films deposited by the Langmuir-Blodgett (LB) technique are formed by a hydrophilic and a hydrophobic moieties. The molecules are placed at an air-water interface. The hydrophilic heads point to the water phase, opposite to the hydrophobic tails. A teflon barrier compresses the molecule and then, molecules are transferred to a substrate by dipping it in the liquid.

A bespoke computer controlled Langmuir-Blodgett instrument for molecule deposition onto solid substrates was used.

MALDI-TOF

The matrix-assisted laser desorption-ionization time of flight mass spectrometry technique is suitable for films. The sample is placed in UHV where short laser pulses impact on it. The absorption of energy by the sample leads to excitation and ionization, giving rise normally to monocharged species which are analyzed by the ToF detector. This analyzer allows the determination of the ion mass by a very precise measurement of the time interval between the acceleration of the ions at the source

and their impact on the detector.

MALDI-TOF measurements were performed on a 5800 MALDI-TOF (ABSciex) in negative (and positive) reflection mode in a mass range of [1000, 3000] m/z. The isotopic distributed patterns were simulated using the mMass software (v. 5.5.0).

The MALDI-TOF measurements were performed in the Proteomics Unit of SCSIE that belongs to ProteoRed a the University of Valencia.

MEL Set-Up

Spin-OLEDs and POM-based MSV were characterized in the magneto-electroluminescence and magneto-transport set-up in a two-probe configuration. The MEL set-up allows to measure the current and light emitted by a sample while applying a bias voltage and a magnetic field sweep, under vacuum conditions and a thermal variation in the range [8, 350] K.

The bespoke equipment keeps the sample at a pressure of 10^{-6} mbar by the pumping system Mini Task AG8. The voltage is applied and the electrical current is measured by means of a Keithley electrometer model 6517A. The light emitted by the spin-OLEDs is measured by a Si photodiode that is coupled to the cryostat window and registered by a picoammeter model Keithley 6485. The intrinsic response of the Si photodiode under the influence of external magnetic fields has been discarded through the analysis of reference samples. The temperature of the sample is measured by a Cernox sensor screwed on the sample holder in every measurement. Besides, the temperature is varied by in the close loop cryostat model C52045 F from ARS, by a He compressor also from ARS and controlled by a temperature controller model 332 from Lake Shore. The magnetic fields up to 1 T are generated by two electromagnets that are controlled by the source GMHW 231 HC. The MEL set-up is controlled by a bespoke Visual Basic program.

MOKE Set-Up

The magneto-optic Kerr effect (MOKE) and magneto-optical characterization of the cobalt electrode was performed with a self-made Kerr magnetometer.

The magneto-optic Kerr effect describes polarization and intensity changes of the light reflected by a magnetic material. The origins rely on the non-diagonal components of the dielectric tensor which describe the anisotropic permittivity. The speed of light in the sample depends on the permittivity, thus causing fluctuations in the phase of the polarized incident light.

In the MOKE set-up a λ = 633 nm He-Ne laser with an output power of 12 mW was used as the light source which constitutes a nearly linearly polarized incident light beam. The light passes through a Glan-laser calcite polarizer, which allows both s-polarized (electric field perpendicular to the plane of incidence) and p-polarized (electric field parallel to the plane of incidence) congurations. The set-up allows the use of longitudinal, polar, and transverse geometries. The external magnetic field range in the polar conguration is $\pm$ 150 mT.

PPMS

The single ion magnets response to an ac field is studied through the complex susceptibility (χ' + iχ"). The real susceptibility is in phase with the applied ac field, while the imaginary component is out of phase. The χ" is related to the energy absorbed by the sample from the ac field.

The ac magnetometry at high frequencies was performed in a Quantum Design Physical Property Measurement System (model PPMS-9). The magnetic field (H_{ac} = H_0cos(ωt)) was applied with an amplitude of H_0 = 5 Oe. The H_{ac} is superimposed to an H_{dc} field which has been indicated in every measurement. The dependent magnetic moment induced in the sample is: M_{ac} = H_{ac}sin(ωt)· dM / dT.

Probe-Station

The electric and magnetic characterization of the NaLnClq-based spin valves was performed with a Lake Shore Probe Station.

The Lake Shore Model CRX-EM-HF is a cryogen-free closed cycle refrigerant probe station with a $\pm$ 0.6 T horizontal, in-plane electromagnet. A bespoke software based on Labview was used. Transport measurements were made in four probe configuration where two probes supply current and the other two are used to measure the voltage. In this way, the voltage drop in the electrodes is not taken into account. This arrangement is especially useful when the resistance of the electrodes is similar to the resistance of the junction.

Profilometry

Layer thicknesses were measured by means of profilometry. Initially, the layers were scratched with a glass pipette. Then, the equipment quantifies the height difference between the groove and the surface.

An Ambios Technology XP-1 profilometer placed on a vibration isolation table was employed. The profilometer sensibility is 10 nm.

Spin-Coating

One of the techniques used to deposit thin films of molecular layers was spin coating. Usually, a small amount of the molecular compound in solution is placed on the center of the substrate and then the substrate is rotated. The centrifugal force spreads the coating material creating thin and uniform films with a thickness depending on the initial concentration and rotation speed.

A Chemat Technologies model KW-4A was used.

SQUID Magnetometry

A SQUID (superconducting quantum interference device) has been used to measure the coercive fields of some devices and the ac susceptibility at low frequencies of some single molecular magnets.

The SQUID is a high sensibility magnetometer based on Josephson junctions. The magnetometer contains two parallel Josephson junctions which consist of two superconductors separated by thin isolating films. Cooper pairs tunnel between the superconductors and the electric current is very sensitive to the presence of magnetic fields.

Hysteresis loops and dc and ac magnetometry curves were measured with a Quantum Design MPMS XL-5 SQUID magnetometer operating in the thermal range [1.7, 400] K and the frequency range []0.1, 1000] Hz.

TGA

TGA (Thermogravimetric analysis) measures the weigh loss of a compound by means of a high-precision balance while temperature is increased.

Thermogravimetric analysis curves were registered on a thermogravimetric and differential thermal analyzer model Mettler Toledo TGA/SDTA 851e that operates in the range [25, 1100] ℃ with a sensibility of 0.1 μg. A typical load of 3 mg of neat material was employed. The standard runs were performed at a 10 ℃ / min scan rate and with an air flow of 30 mL / min.

Time-Resolved Electroluminescence

The time-resolved technique was employed to determine the hole mobility of the F8BT polymer.

The photoluminescence excitation experiments were carried on by scanning a 250 W tungsten lamp (or a 75 W Xe lamp) via a 150 mm (alternatively a 300 mm) Princeton Instruments monochromator Acton Spectra Pro SP2155 (SP2300i) to select a bundle of light spanning the chosen wavelength range. In steady-state luminescence spectroscopy, the emitted light was detected by means of a Peltier-cooled Hamamatsu H7422-20 photosensor module (or by a Hamamatsu R928 Photo Multiplier Tube), across a triple-turret 300 mm Princeton Instruments monochromator (Acton Spectra Pro SP2300i). In ns-time resolved fluorescence experiment the sample was excited by a λ = 400 nm, 70 ps FWHM, pulsed solid-state laser diode head (LDH-P-C-400, Picoquant), driven by PDL-800B Pulsed Laser Driver (Picoquant) operating at a repetition rate in the frequency range ν = 180 kHz $-$ 3 MHz. Fluorescence spectra were collected by the previously indicated detector and monochromator as a component of an inverted start-stop detection system (Picoquant, TimeHarp-100) with 36 ps/channel time resolution.

Steady-state electroluminescence (EL) spectroscopy was carried on by biasing the device under test, in vacuum, by a Keithley 2400 Source Measurement Unit and by detecting the light emitted by the device via the above described detection system or by a Hamamatsu C7041 (Multichannel Detector Head with Back-Tinned CCD). In time resolved electroluminescence, a pulsed bias was applied to the light emitting device by an Agilent 8114A-100 (100 V / 2 A) Pulse Generator, triggering in the same time the light detection system, based on the Hamamatsu H7422-20 photosensor module, whose output signal was fed into a TimeHarp-100 (time window up 150 ns) or into a NanoHarp250 (time window up to 2.15 s), both from Picoquant. Absolute intensity was measured by International Light Technologies ILT-1700 Research Radiometer. In low temperature electro/optical measurements, the sample (film or device) was fixed on a cold finger at the end of the second stage in a dual-stage Helium close circuit refrigerator-cooled cryostat (Leybold, RDK 10-320), that

allows to control the sample temperature from 330 K down to 12 K. Measurements in magnetic field were carried on placing the sample under test between to poles of an GMW-3470 electromagnet driven in current by a Bipolar Operational Power supply BOP 72-6M.4886 ($\pm$ 72 V, $\pm$ 6°) (Kepco). In current transient experiments a GDS-200 Digital Storage Oscilloscope (GwINSTEK) has been used. All the instruments are controlled by home-made softwares.

Time-resolved measurements were performed in collaboration PhD. Eugenio Lunedei from the Istituto per lo Studio dei Materiali Nanostrutturati at ISMN-CNR in Bologna.

UPS

Ultraviolet photoemission spectroscopy or UPS is based on the photoelectric effect in which high energy photons extract electrons from the surface of a metal or semiconductor. The technique has been used to determine the work function of the HOMO of some materials.

The UPS spectra were calibrated in a way that the Fermi level is at the origin of binding energy. The E_F is manifested as a step since it separates filled from empty states. The technique works only with occupied states which have electrons to be emitted (states above the Fermi level are empty and do not emit electrons). The measurements were done inside an ultrahigh vacuum chamber with a base pressure of 10^{-10} mbar. The photo emission spectra were obtained by an Omicron HIS 13 vacuum ultra-violet lamp (VUV) at room temperature; the HeI or HeII lines of Helium were used (21.2 eV or 40.8 eV). The light angle of incidence was 45 ° and the spectra were recorded with a commercial cylindrical sector analyzer (Focus CSA 300) equipped with a spin detector based on spin polarized low-energy electron diffraction (Focus SPLEED).

The UPS measurements were performed in collaboration with prof. Mirko Cinchetti from the Technische Universität Dortmund and the Surfaces Research Group at the

University of Kaiserslautern.

XAS

The spinterface was studied by means of X-ray absorption spectroscopy (XAS). The technique shows a very high sensitivity to the local structure of the samples. The data is obtained by tuning the incident photon energy to a range where core electrons are excited by means of a monochromator. The nomenclature of the edges indicates the core level (n = 1, 2, and 3, correspond to the K-, L-, and M-edges, respectively).

X-ray absorption spectroscopy preliminary data were obtained at MAX-lab synchrotron radiation laboratory in Lund (Sweden). Beamline I1011 2 is a soft X-ray beamline, covering the energy range 200 to 2000 eV. The final X-ray spectra were obtained at the Boreas line in the ALBA Synchrotron (Barcelona). Both lines are equipped with a preparation chamber where the NaDyClq/metal layers were prepared in-situ. Besides, the molecules were grown with the effusion cells and the NiFe and Co metals were deposited via e-beam evaporation, under the same conditions as in the device fabrication. The X-ray absorption measurements were taken in total electron yield mode both in normal and grazing incidence of the photon beam with linearly polarized X-rays; the spectra were normalized to the incident photon flux measured by a freshly evaporated Au-grid inserted in the X-ray path before the sample.

XPS

The oxidation states in the MoO_x samples were studied by means of X-ray photoelectron spectroscopy (XPS) which is based on the photoelectric effect. A source of X-rays irradiates the sample and the kinetic energy and number of photoelectrons emitted are analyzed.

A XPS, K-ALPHA Thermo Scientific was used to analyze the films. It has a beam

size of less than 300 μm. Spectra were collected using Al - Kα radiation (1486.6 eV) with a twin crystal monochromator and yielding a focused X-ray spot (elliptical in shape with a major axis length of 400 μm) at 3 mA C and 12 kV. The alpha hemispherical analyzer was operated in the constant energy mode with survey scan pass energies of 200 eV to measure the whole energy band and 50 eV in a narrow scan to selectively measure the particular elements. The Avantage software was used to analyze the spectra. Besides, all spectra were calibrated using the adventitions C1s peak with a fixed value of 284.5 eV. After calibration, the background was subtracted from all spectra using a Shirley-type background in order to remove most of the extrinsic loss structure.

The X-ray photoelectron spectroscopy (XPS) data were obtained from the Universidad de Alicante technical facilities.

Resumen

La investigación llevada a cabo durante el periodo de tesis doctoral y que se describe en este manuscrito pertenece al campo de la espintrónica molecular. Ha sido motivada por el deseo de incorporar nuevos materiales moleculares a dispositivos espintrónicos y ahondar en la comprensión de la inyección y el transporte de espín en este tipo de capas, a través del estudio de dispositivos como la válvula de espín molecular y el spin-OLED.

En 1988 Albert Fert y Peter Grünberg descubrieron que la resistencia eléctrica de unas multicapas de Fe-Cr variaba considerablemente en función de la magnetización de las láminas. El efecto se conoce hoy en día como magnetoresistencia gigante o GMR, por sus siglas en inglés, y su hallazgo se considera el nacimiento de la espintrónica basada en materiales inorgánicos. La GMR supuso un gran avance tecnológico al triplicar la densidad de almacenamiento de datos en los discos duros y facilitar la incorporación de estos a la electrónica de consumo. Cabe destacar que solamente transcurrieron nueve años desde el descubrimiento de la GMR y el lanzamiento por IBM del primer disco duro basado en esta tecnología en 1977. Rara vez ha habido una trasferencia tan rápida entre investigación y tecnología. Veinte años después el Premio Nobel de Física 2007 fue otorgado conjuntamente a Albert Fert y Peter Grünberg por este descubrimiento.

Actualmente la espintrónica inorgánica, que diseña dispositivos que tienen en cuenta tanto las propiedades eléctricas como las propiedades magnéticas de los electrones, tiene múltiples aplicaciones. Toda ella está construida sobre el desequi-

librio en la densidad de estados para las bandas *spin-up* y *spin-down* a nivel de Fermi característico de los materiales ferromagnéticos. Este desequilibrio hace posible que la corriente eléctrica inyectada por un ferromagnético esté polarizada en espín, de manera que se añade un grado de libertad a los dispositivos optoelectrónicos.

Dentro del campo destacan la válvula de espín y la unión magnética de efecto túnel. Ambas están formadas básicamente por tres capas: dos electrodos ferromagnéticos y un espaciador. Éste último es un metal o un semiconductor en el caso de la válvula de espín y un aislante en el caso de la unión magnética de efecto túnel. El espaciador no es un material magnético y su función es desacoplar los electrodos. Éstos tienen diferentes campos coercitivos y cambian la orientación de su magnetización relativa en función del valor del campo magnético aplicado. Los dos dispositivos espintrónicos muestran un estado de resistencia alto o bajo dependiendo de la dispersión que sufren los electrones al entrar en el segundo electrodo. Normalmente ocurre que cuando la magnetización de los electrodos es paralela, la resistencia es baja y al contrario, si los electrodos están en configuración antiparalela, la resistencia es alta. En el caso de la válvula de espín, el espaciador transporta la corriente polarizada de un electrodo a otro, mientras que en las uniones magnéticas de efecto túnel el espaciador es una barrera aislante en la que no hay transporte de carga y los electrones atraviesan el dispositivo por efecto túnel. Por tanto, la disparidad en el transporte de carga es lo que diferencia a ambos dispositivos.

Las principales aplicaciones de estos son las siguientes. Por una parte, las cabezas de lectura de los discos duros llevan incorporada una válvula de espín y están basadas en el efecto GMR. Uno de los materiales ferromagnéticos es lo que se conoce como imán blando y es el que va cambiando la dirección de su magnetización a medida que lee ceros o unos en la pista de datos. El otro electrodo ferromagnético tiene un campo coercitivo alto y su magnetización no se ve afectada. La resistencia muestra un estado alto o bajo dependiendo de lo que se lee (0 ó 1), de manera que la corriente eléctrica informa del valor del bit en la pista de datos.

La segunda aplicación que cabe destacar es la MRAM o memoria de acceso aleatorio magnética que constituye una memoria permanente basada en uniones

magnéticas de efecto túnel, usada hoy en día como memoria de trabajo en los ordenadores para el sistema operativo y la mayor parte del software. Cada unión magnética de efecto túnel almacena un bit de datos. Tal y como ocurría en las cabezas de lectura de los discos duros, una de las capas ferromagnética es un imán duro y su magnetización se mantiene constante y la otra capa mantiene su estado magnético siempre que no se reescriba, de forma que la información sigue almacenada en ausencia de corriente eléctrica.

Siguiendo la revolución que sufrió la electrónica cuando se incorporaron los materiales moleculares, una rama de la espintrónica estudia dispositivos en los que se incorporan moléculas. Las principales ventajas que tienen los materiales moleculares frente a los semiconductores inorgánicos son su flexibilidad, bajo coste económico, ligereza y facilidad de producción. Además, se pueden sintetizar y diseñar a demanda y tienen una alta versatilidad química. Por otro lado, los materiales moleculares se caracterizan por tener bajo acoplamiento espín órbita e interacción hiperfina, ya que están que están compuestos principalmente por carbono y elementos ligeros, siendo estos dos fenómenos las fuentes principales de despolarización de espín. Por lo tanto, se espera que los tiempos de vida de spin y las longitudes de difusión de spin sean mayores en la espintrónica molecular en comparación con los semiconductores inorgánicos utilizados en espintrónica.

A su vez la espintrónica molecular, de manera análoga a la electrónica molecular, se divide en dos ramas principales: la espintrónica de una sola molécula, donde el objetivo es la miniaturización del dispositivo hasta el límite molecular o un conjunto pequeño de moléculas, y la espintrónica basada en materiales moleculares, en la que se incorporan estos materiales en dispositivos espintrónicos. El trabajo descrito en esta tesis doctoral se centra en esta última área.

En líneas generales, dos temas diferentes han sido desarrollados durante el periodo de tesis agrupados en dos bloques y seis capítulos. El primer capítulo de este manuscrito constituye el capítulo de introducción y en él se describen los conceptos básicos de la espintrónica molecular haciendo hincapié en aquellas ideas que han sido parte fundamental en la investigación llevada a cabo. El primer bloque lo conforman los capítulos dos, tres y cuatro que corresponden al estudio y fabricación

de válvulas de espín moleculares con nuevos materiales. El segundo bloque está formado por los capítulos cinco y seis y allí se describe la fabricación y el estudio de spin-OLEDs que son dispositivos capaces de aumentar la eficiencia de los OLEDs en presencia de un campo magnético externo.

La molécula más usada en el campo de la espintrónica molecular es el tris(8-hidroxiquinolinato)aluminio conocida como Alq_3; un compuesto muy usado también en optoelectrónica, particularmente en la fabricación de OLEDs. Recientemente, y motivados por el uso generalizado del Alq_3 en estos campos, se sintetizó en nuestro grupo una familia de compuestos muy similares y también basados en las quinolinas. En el segundo capítulo de este manuscrito se realiza un estudio de sublimación de estos nuevos compuestos y su deposición sobre sustratos, con el objetivo de discernir cuáles de ellos son óptimos para su incorporación a dispositivos espintrónicos en forma de capas delgadas. Los cinco compuestos estudiados son: $Na[Y(5,7Cl_2q)_4]$, $Na[Tb(5,7Cl_2q)_4]$, $Na[Dy(5,7Cl_2q)_4]$, $NEt_4[Dy(5,7Cl_2q)_4]$, y $K_{0.5}(NEt_4)_{0.5}[Dy(5,7Cl_2q)_4]$, donde $5,7Cl_2q$ = 5,7-dicloro-8-hidroxiquinolinato. Para simplificar los hemos llamado: NaYClq, NaTbClq, NaDyClq, NEtDyClq and KNEtDyClq, especificando el catión usado y el lantánido central.

Algunos miembros de esta familia de compuestos, al contrario que el Alq_3, son imanes moleculares o SIMs, por sus siglas en inglés. Este comportamiento magnético SIM tiene su origen en el lantánido (Tb^{III} y Dy^{III}) que posee orbitales f semillenos que lo dotan de gran momento orbital. Los ligandos de la molécula aíslan el espín central de las moléculas vecinas evitando efectos cooperativos entre ellas y permitiendo que los efectos cuánticos se manifiesten. Cuando un SIM se magnetiza, los electrones desapareados se alinean el campo magnético, comportándose como un superparamagneto. A bajas temperaturas, si se retira el campo la magnetización permanece durante algún tiempo, lo que se conoce como relajación lenta de la magnetización que puede ser cuantificada midiendo la susceptibilidad en fase y fuera de fase del compuesto. Ésta última muestra una dependencia con la frecuencia del campo aplicado. Al realizar estas medidas hemos comprobado que todos los compuestos basados en Dy y Tb se comportan como SIMs. Además, hemos podido demostrar que la molécula NaDyClq relaja su magnetización por un solo mecanismo

tipo Raman a través de un nivel virtual.

Posteriormente nos hemos valido de diferentes técnicas experimentales para averiguar si los compuestos conservan la estructura molecular y las propiedades magnéticas al ser sublimados y por tanto son aptos para formar capas y ser incluidos en dispositivos. Este conjunto de técnicas está formado por: termogravimetría, espectroscopía infrarroja, análisis elemental mediante microscopía electrónica de barrido y espectroscopía de masas. Inicialmente, mediante el análisis termogravimétrico hemos estimado la temperatura de sublimación lo que nos ha permitido evaporar los compuestos sobre sustratos. Seguidamente, al comparar los espectros de infrarrojo de las capas y los compuestos, hemos podido comprobar que el ligando estaba intacto en todos ellos después de ser evaporados. Además, el análisis elemental ha mostrado que la proporción entre átomos en los compuestos y las capas era la correcta en todos los compuestos excepto en el KNEtDyClq. Por último, los patrones en análisis de espectroscopía de masas solamente aparecen para los compuestos basados en Na. Y por último, en el caso del NaDyClq se ha comprobado que la capa delgada conserva el comportamiento magnético mediante medidas de susceptibilidad magnética ac. Algo que no ha sido posible para el compuesto NaTbClq debido a su baja temperatura de bloqueo (< 2 K).

A partir del análisis de los resultados obtenidos de las diferentes técnicas, concluimos que solamente los compuestos basados en sodio subliman correctamente. Se han depositado capas delgadas sobre diferentes sustratos y estudiado su morfología mediante microscopía de fuerza atómica observando un buen recubrimiento del sustrato y una baja rugosidad. Por último, se han estudiado bicapas formadas por un metal ferromagnético y una película delgada molecular donde hemos podido observar que el metal polariza la molécula.

Los capítulos tres y cuatro tienen como tema principal las válvulas de espín moleculares (MSVs) que constituyen el dispositivo más estudiado en la espintrónica molecular. Las capas finas de materiales moleculares, que forman parte de las MSVs, principalmente se fabrican por dos métodos: bien evaporando las moléculas o bien partiendo de una disolución molecular. En el capítulo tres se hace uso de la evaporación para las capas de NaYClq y NaDyClq mientras que en el capítulo cua-

tro se deposita la capa de polioxometalato a partir de disolución mediante la técnica de spin coating.

Las MSVs básicamente están formada por tres capas: dos electrodos ferromagnéticos y un espaciador molecular. El dispositivo muestra un estado de resistencia alto o bajo dependiendo de la dispersión que sufren los portadores al entrar en el segundo electrodo y esta dependencia de la resistencia con el campo magnético es lo que se conoce comúnmente como magnetoresistencia (MR) y que se estima a partir de $MR(\%) = (R_{AP} - R_P)/\ R_P$, donde R_{AP} y R_P son las resistencias de los estados antiparalelo y paralelo respectivamente.

En el capítulo tres se describe el estudio de válvulas de espín moleculares fabricadas con dos de las tres moléculas sublimables del capítulo dos. Las MSVs se han fabricado con la molécula diamagnética NaYClq y NaDyClq que se comporta como imán molecular. Inicialmente, el objetivo ha sido estudiar si la capa que se comporta como imán molecular al polarizarse en presencia de los electrodos ferromagnéticos influía en el transporte de espín diferenciándose de la válvula de espín fabricada con la capa diamagnética. La configuración de dos tipos de dispositivos estudiados es Co / AlO_x / NaYClq / NiFe y Co / AlO_x / NaDyClq / NiFe. En ambos casos, sobre el electrodo de abajo se ha depositado una barrera parcialmente oxidada de aluminio que facilita el crecimiento de la capa molecular y reduce la probabilidad de cortocircuito. La distancia HOMO-LUMO o *gap* óptico de ambas moléculas en disolución se ha determinado mediante medidas de absorción obteniendo 2.78 eV para NaYClq y 2.73 eV para NaDyClq.

El grosor real de la capa molecular suele ser menor que el grosor evaporado debido a la interpenetración del segundo electrodo en el proceso de deposición. A partir del formalismo de Simmons hemos estimado los grosores reales de las capas de NaYClq y NaDyClq que resultan ser menores a 5 nm. En este rango, y como también se puede ver a partir de la dependencia sutil que muestran las curvas corriente-voltaje con la temperatura, inferimos que los electrones viajan por efecto túnel en el dispositivo. Mediante la dependencia de la corriente con el grosor hemos podido averiguar que los electrones atraviesan la capa molecular haciendo dos o tres paradas intermedias solamente.

En las curvas de magnetoresistencia no hemos encontrado diferencias significativas entre los dos tipos de dispositivos. Pero curiosamente, ambas MSV han mostrado magnetoresistencia negativa a baja temperatura. Es decir, cuando los electrodos están en la configuración paralela (antiparalela) la resistencia es alta (baja). Esto implica que una de las interfaces está filtrando el espín e invirtiendo la polarización de los portadores mayoritarios. Esta interfaz formada entre el metal ferromagnético y la molécula que invierte la polarización se conoce como *spinterface* y es un efecto basado en el solapamiento orbital entre el metal y la molécula propio de los materiales moleculares que no tiene análogo en los semiconductores inorgánicos.

Además, hemos podido identificar qué interfaz es la que invierte la polarización al aislar el material molecular y el NiFe y obtener magnetoresistencia positiva en la configuración NiFe / AlO_x / NaLnClq / Co. Finalmente, se han realizado medidas de espectroscopía de absorción de rayos X en las diferentes interfaces y se ha observado que la interacción entre la molécula NaDyClq y los dos ferromagnéticos es diferente. Por un lado el NiFe modifica notablemente el C *k-edge* mientras que el Co hace lo propio con el N *k-edge*. En ambos casos aparecen estados híbridos nuevos en los espectros que contribuyen al transporte electrónico. Los estados híbridos responsables de la inversión se han identificado a 281 eV y 282 eV en el C *k-edge*.

En el capítulo cuatro se detalla el estudio de dos MSVs basadas en polioxometalatos (POMs). Los POMs son una familia muy amplia de complejos tridimensionales con alto grado de simetría formados por cationes metálicos y oxo-aniones. El potencial de estos compuestos en el campo de la espintrónica molecular reside en su amplia variabilidad y versatilidad química. Nosotros hemos introducido por primera vez este tipo de compuestos en el campo mediante la fabricación y el estudio de válvulas de espín moleculares basadas en el anión fosfomolibdato ($[PMo_{12}O_{40}]^{3-}$).

Se han estudiado estas dos configuraciones de MSV diferentes: LSMO (20 nm) / POM-DODA (100 nm) / Co (25 nm) y LSMO (20 nm) / POM-DODA (80 nm) / MoO_x (3 nm) / Co (25 nm). La capa molecular formada por $DODA_3PMo_{12}O_{40}$, donde DODA $=$ dimetildioctadecilamonio, muestra una distancia HOMO-LUMO de 3.36 eV. Además, mediante medidas de espectroscopia electrónica ultravioleta (UPS) hemos podido referenciar el HOMO de esta capa que se encuentra a -7.1 eV respecto del

nivel de vacío, lo que nos ha permitido un mejor diseño del dispositivo. Además, hemos incorporado una capa de óxido de molibdeno que tiene una banda de conducción profunda y se usa normalmente como inyector de huecos en dispositivos optoelectrónicos. El grosor de la capa de óxido de molibdeno en las MSVs ha sido elegido en base a las medidas de UPS polarizadas en espín. El grosor elegido, 3 nm, está modificando la función de trabajo del cobalto (-5 eV), y acercándola al HOMO de la capa de POM (-5.8 eV) sin despolarizar significativamente la corriente.

La MSV sin MoO_x muestra 7.5 % de MR a 50 K y 0.1 V. La señal MR a 50 K se pierde alrededor de 1 V, tal y como suele ocurrir en las MSVs. Por otro lado, la MSV con MoO_x muestra un porcentaje de MR menor (6 %), tal y como se espera. Sin embargo, la señal MR no desaparece más allá de 3.5 V. Aunque no tenemos claro cuál es el origen de esta MR a alto voltaje, la comparación de ambas válvulas de espín indica que está relacionado con el alineamiento energético, que es mucho mejor en la MSV con MoO_x. Esto es algo que se había conseguido en nanoindentaciones pero no en dispositivos funcionales con áreas en el rango de los cientos de micras.

Los capítulos cinco y seis están dedicados al diseño y estudio de spin-OLEDs que son dispositivos multifuncionales que se comportan como válvula de espín molecular a la vez que como diodo orgánico de emisión de luz u OLED. En un OLED, los electrodos inyectan electrones y huecos con orientaciones de espín aleatorias (tres tripletes y un singlete) y todas ellas tienen igual probabilidad de formación. Además, los singletes son los principales responsables de la emisión de luz, y por consiguiente, la conversión de electrones a fotones es máximo del 25 %. Este límite teórico se duplica en un spin-OLED porque los dos electrodos ferromagnéticos modifican la probabilidad de formación de singletes y tripletes al inyectar carga polarizada en espín. Cuando ambos electrodos están alineados magnéticamente de forma antiparalela, teóricamente solo se pueden formar el singlete y uno de los tres tripletes. Por lo tanto, el límite teórico de eficiencia cuántica en un spin-OLED es del 50 %. El equivalente a la medida magnetoresistencia en la luz en lugar de en la corriente eléctrica es el efecto MEL, donde la intensidad de la luz es modulada en un barrido de campo magnético y que se calcula como $\mathrm{MEL}(\%) = (\mathrm{EL}_{\mathrm{AP}} - \mathrm{EL}_{\mathrm{P}})/$

EL_P, donde EL es la electroluminiscencia. Una de las mayores dificultades a la hora de tener éxito en la fabricación este tipo de dispositivos es que magnetoresistencia y emisión de luz deben coexistir a la misma temperatura y voltaje.

En el capítulo cinco se describe cómo hemos fabricado un spin-OLED a partir de materiales comerciales. La configuración del dispositivo estudiado en este capítulo es la siguiente: LSMO (20 nm) / PEIE (1 nm) / F8BT (45 nm) / MoO_x (3 nm) / Co (25 nm), F8BT = poli(9,9- dioctilfluoreno-alt-benzotiadiazol), PEIE = polietilenimina etoxilada. El alineamiento energético de todas las capas es muy bueno, lo que facilita la inyección de electrones en el LUMO (-3.5 eV) del F8BT por parte del LSMO y de huecos en el HOMO (-5.9 eV) por parte del cobalto. Las medidas de UPS han demostrado que la capa del polímero alifático PEIE (polietilenimina etoxilada) modifica la función de trabajo del cátodo hasta los -3.7 eV, manteniendo alta la polarización de espín de la corriente eléctrica. Y lo mismo ocurre con el MoO_x, que modifica la función de trabajo del Co, mediante la transferencia de carga, hasta los -5.8 eV. La recombinación de electrón y hueco para dar fotón tiene lugar en la capa emisora del polímero F8BT y su extracción se realiza a través del cátodo.

Nuestro spin-OLED establece un nuevo récord de efecto MEL con un 2.4 % a 20 K. Esta mejora nos ha permitido estudiar dicho efecto en un amplio rango de temperaturas y voltajes. Además, todas las capas utilizadas están hechas de materiales comerciales y los componentes principales se han depositado desde disolución. Ambas características reducen los costes de producción y facilitan su escalado industrial en grandes áreas. Además, este dispositivo ha demostrado que la corriente polarizada en espín puede ser inyectada desde los electrodos ferromagnéticos en el HOMO y el LUMO del material molecular.

Paralelamente a la fabricación de este spin-OLED se ha estudiado la precesión del espín en un dispositivo muy parecido al anterior a través del efecto Hanle, lo que constituye el tema principal del capítulo seis.

El efecto Hanle está considerado la prueba definitiva para demostrar que la magnetoresistencia que muestran las válvulas de espín moleculares tiene su origen en corrientes polarizadas de espín. En estos dispositivos no es posible discernir, me-

diante las curvas de magnetoresistencia, si hay inyección de espín en el semiconductor molecular o si los portadores pasan por efecto túnel de un electrodo a otro a través de pequeños agujeros o zonas delgadas. Esto se debe a que la capa molecular reduce su grosor considerablemente al evaporar el segundo electrodo.

El experimento consiste en hacer girar los espines mientras viajan en el material molecular mediante la aplicación de un campo magnético pequeño en dirección perpendicular a la polarización de los electrodos ferromagnéticos. Si efectivamente hay transporte de espín en la capa molecular, este campo despolarizaría la corriente de espín y por tanto eliminaría la magnetoresistencia. Entonces se demostraría que en efecto, la capa molecular transporta el espín. Sin embargo, no se ha podido medir el efecto Hanle hasta ahora en una válvula de espín molecular funcional. Llegados a este punto, pueden estar ocurriendo dos cosas: que las válvulas de espín moleculares se comporten en realidad uniones magnéticas de efecto túnel o que el transporte de espín en los materiales moleculares ocurra de una forma distinta a los semiconductores inorgánicos, tal y como sucede con el transporte de carga.

Un spin-OLED constituye un dispositivo idóneo para estudiar el efecto Hanle ya que la emisión de luz asegura que la carga está siendo transportada a través del semiconductor molecular permitiendo descartar la primera posibilidad. El dispositivo espintrónico estudiado tiene la configuración: LSMO (20 nm) / ZnO (1.8 nm) / N965 (1 nm)/ F8BT (65 nm) / MoO_x (3 nm) / Co (15 nm). Se trata de un spin-OLED que muestra alta estabilidad y reproducibilidad, ambas características necesarias para el estudio de precesión, además de un buen alineamiento energético entre capas. El óxido de zinc y la monocapa del complejo de rutenio N965 modifican la función de trabajo del cátodo, acercándola al LUMO del F8BT y mejorando la inyección electrónica. Los grosores de las capas se han determinado mediante diferentes técnicas como medidas de absorción y perfilometría. Previamente al estudio del efecto Hanle, se ha realizado una caracterización eléctrica y magnética del spin-OLED y también del electrodo de LSMO. Destacamos que el dispositivo muestra MR y un efecto MEL del 1 % a 40 K, aunque ambos efectos son menores que el dispositivo presentado en el capítulo cinco. Seguramente esto es debido a una mayor despolarización ejer-

cida por el tándem ZnO / N965 comparado con la capa de PEIE. Además de que el grosor del tándem es mayor, también lo es su acoplamiento espín órbita.

Las medidas de efecto Hanle las hemos realizado de la forma siguiente. El spin-OLED se prepara en el estado paralelo (P) o antiparalelo (AP), esto es, con las magnetizaciones de LSMO y Co alineadas en el mismo sentido o en sentido contrario. Posteriormente, se aplica una diferencia de potencial fija entre los electrodos, se estabiliza la corriente y se giran los imanes hasta la posición perpendicular (θ = 90 °). En este punto se miden la corriente eléctrica y la intensidad de la luz variando el campo magnético H_z. El campo magnético perpendicular hace girar los espines en la capa de F8BT a la frecuencia de Larmor ($\omega_L = egH_z/(2m_e)$, donde e es la carga del electrón, g el g-factor y m_e la masa del electrón en reposo). La MR en esta posición es proporcional al $\cos_2\theta$, según el modelo de Johnson y Silsbee, y debería anularse. Sorprendentemente, hemos medido que no hay efecto Hanle no sólo en la corriente que atraviesa el dispositivo sino tampoco en la luz emitida por el spin-OLED. Se ha comprobado también que este efecto no lo causan los electrodos mediante la medida de dos muestras de control con la configuración: LSMO / ZnO / N965 / F8BT / MoO_x / Au y ITO / ZnO / N965 / F8BT / MoO_x / Co ya que ninguna de las dos ha mostrado efecto Hanle.

Mediante la comparación del tiempo que tardan los portadores en atravesar la capa molecular con el tiempo que tardan en girar asociado a la frecuencia de Larmor, hemos inferido que los espines viajan mucho más rápido de lo que tardan en girar y que por tanto la curva Hanle, al estar ensanchándose, necesitaría de campos H_z mucho más intensos. Sin embargo estos campos interferirían con los campos coercitivos de los electrodos y por lo tanto esto imposibilita la medida.

Nuestras medidas indican que probablemente los materiales moleculares transporten el espín de forma diferente a los materiales inorgánicos. Todo apunta a que no es que la carga no sea inyectada en el material emisor, sino que carga y espín viajan por canales separados. Mientras que el electrón atraviesa la capa molecular por *hopping*, el espín la cruza por *exchange*. Éste es mucho más rápido y hace que el giro inferido por H_z no sea significativo.

En resumen, en la investigación llevada a cabo durante esta tesis doctoral se han intentado abordar varios temas actuales del campo de la espintrónica molecular como son la *spinterface*, la magnetoresistencia a alto voltaje, los mecanismos de transporte en las válvulas de espín, el transporte en el HOMO y el LUMO del material molecular en los spin-OLEDs y el estudio de los mecanismos de transporte de espín mediante el efecto Hanle.

Las perspectivas de futuro en cada una de las líneas estudiadas son varias. Por un lado, recientemente se han sintetizado en el grupo varias familias más de moléculas basadas en las quinolinas. El estudio de válvulas de espín basadas en ellas podría arrojar luz sobre cuál es el papel del lantánido central y si es posible polarizar la capa mediante los electrodos ferromagnéticos. Para ello sería necesario que los portadores viajaran por la capa molecular por *hopping* y no a través del efecto túnel, tal y como ocurría en nuestros dispositivos. Uno de los posibles problemas a la hora de llevar a cabo este objetivo es que HOMO y LUMO se sitúan espacialmente sobre los ligandos que son muy parecidos entre todos los compuestos de las diferentes familias. Sin embargo, no sería de extrañar que los portadores se vieran afectados por el magnetismo del lantánido central a pesar de estar viajando por la periferia de la molécula.

En lo que a los polioxometalatos (POMs) se refiere, sería muy interesante diseñar dispositivos con otro tipo de POMs aprovechando su gran versatilidad. Nuestro método de deposición puede ser utilizado para depositar otros compuestos de esta gran familia y formar capas delgadas. La comparación entre los diferentes dispositivos puede ayudar a entender los mecanismos que gobiernan las válvulas de espín moleculares.

En cuanto a los spin-OLEDs, sería bueno cambiar el electrodo del LSMO por NiFe para poder tener señal MEL a temperatura ambiente. Además, sería también muy interesante intentar construir un spin-OLED basado en perovskitas, que ya han revolucionado la optoelectrónica, ya que es de esperar que funcionen muy bien también en este tipo de dispositivos.

Por último, las medidas de efecto Hanle tienen un apoyo teórico en lo que a la

corriente eléctrica se refiere, pero falta un modelo que describa qué ocurre con la luz y que nos permita entender mejor cómo es el transporte de espín en los materiales moleculares.

En general, la espintrónica molecular es un campo todavía muy joven y del que se espera que revolucione en el fututo el almacenamiento de información con la incorporación de sus dispositivos a la electrónica de consumo.